Imperial College London
Department of Materials

The Influence of Temperature on the Mechanical Behaviour of Ceramics in $Ti_{1-x}Al_xN$ System

Constantin Ciprian Ciurea

Submitted in part fulfilment of the requirements for the degree of

Doctor of Philosophy in Department of Materials

Imperial College London

Declaration of Originality

I hereby declare in the lieu of oath that I have myself composed this doctoral thesis and the work contained therein is my own, except were stated.

January 2014

To my parents Dumitru and Maria for their
unlimited contribution to my education
and for their endless love

Abstract:

High temperature nanoindentation has been employed to study the influence of temperature on mechanical properties of ceramics in $Ti_{1-x}Al_xN$ system. The temperature had a strong effect on the hardness of the bulk single crystal TiN (TiN_{bulk}), leading to a drop from 21.4 ± 0.4 GPa at 22 °C to 13.7 ± 0.4 GPa at 350 °C. Plastic deformation of TiN_{bulk} mainly occurred along the (110) crystallographic planes, over the temperature range 22 °C – 350 °C, suggesting that the drop in hardness with the temperature was attributed to a change of ease of plastic slip. Hardness of magnetron sputtered $Ti_{0.66}Al_{0.34}N$ coatings dropped with temperature in a similar manner to TiN_{bulk}, although from a higher starting value. Approaching the compositional atomic ratio Al : Ti = 1:1, maximum hardness was reached and the thermal stability of hardness improved. It was proposed that the high hardness stability with the temperature of magnetron sputtered coatings is linked to the presence of the two crystallographic domains, fcc TiN and stabilized fcc AlN. The small difference between the lattice parameters of these phases seems to be accommodated by distortion of lattices, in order to form coherent boundaries between domains. It has been shown that stabilised fcc AlN formed during deposition and remained in the structure after annealing at 600 °C.

Aluminium addition increased the activation energy for slip from 0.75 eV for TiN_{bulk} to 1.26 eV for $Ti_{0.48}Al_{0.52}N$ coatings. These values indicate the deformation took place by lattice controlled dislocation glide mechanism.

The hardness of industrial cathodic arc $Ti_{0.4}Al_{0.6}N$ films decreased with temperature in a similar way to TiN_{bulk}, although at higher values. High deposition energies promoted fcc AlN alongside fcc TiN, and a change of growing direction from (200) to (111). The differences in structure and mechanical properties attributed to different physical vapour depositions are presented.

Acknowledgments

My gratitude is no manner aligned to the acknowledgements listing below, but since there is no other way to list, I express a very special and humble thank you to all who have helped me along the doctoral studies.

I would like to thank my wife, my children and my mother in law. They have borne the brunt of my absences from home (and occasionally the brunt of my presence). My doctoral success would have not been possible without their help, encouragement, advice and persistence.

I have been fortunate to have as my direct supervisor Dr. Finn Giuliani and, as co-supervisor Prof. Neil Alford. The pragmatism of the first combined with the enthusiasm of the second was invaluable during this three-year experience. Thank you for the confidence you have placed in me, for your patience in answering my questions, for your receptivity concerning all aspects related to my research work and for guiding me through the achievement of this work.

I am also indebted to Dr. Vineet Bhakhri for offering many helpful suggestions, for sharpening my nanoindentation knowledge, for reviewing my entire manuscript and for encouraging me at difficult times.

Beside my supervisors, the remaining members are all acknowledged for their help during my three-year of doctoral studies, and for their pertinent criticism that allowed me to improve the quality and readability of the thesis manuscript. Many thanks to: Dr. Luc Vandeperre, Prof. Eduardo Saiz Gutierrez, Dr. Barbara Shollock, Dr. Mahmoud Ardakani, Dr. Ecaterina Ware, Richard Sweeney, Richard Chater, Dr. Jianye Wang, Dr. Tayyab Subhani, Dr. Naeem Ur-Rehman and Dr. Peter Petrov.

Contents

NOMENCLATURE

Roman symbol	Description
A	Contact area between the indenter tip and the sample [nm^2]
b	Burgers vector [nm]
C	Compliance [nm/N]
C_f	Frame compliance [nm/N]
C_s	Specimen compliance [nm/N]
E	Young's modulus [GPa]
E_r	Reduce modulus [GPa]
fcc	Face central cubic
ΔG^0	Gibbs free energy [kJ/mol]
H	Hardness [GPa]
h	Depth of penetration [nm]
h_c	Contact depth [nm]
h_f	Final depth [nm]
h_s	Elastic deflection of the surface [nm]
hex	Hexagonal
K	Boltzmann's constant [J/K]
P	Load [N]
Q	Activation energy [J]
S	Stiffness [N/m]
t	Time [s]
T	Temperature [K]
T_m	Melting point [K]
V	Activation volume [m^3]

Greek symbol	Description
λ	Electron wave-length [nm]
λ	X-ray wave-length [nm]
τ	Shear stress [MPa]
τ_p	Peierls stress [GPa]
ρ_m	Density of mobile dislocation
v	Dislocation velocity
Δ	Defocus
v	Attempt frequency

$\Delta \varphi$	Electron phase shift
v	Poisson's ration
μ	Chemical potential [J/mol]

Abbreviations	**Description**
Al	Aluminium
AlN	Aluminium nitride
BF	Bright field
CDF	Enter dark field
Co	Cobalt
DAF	Diamond area function
DF	Dark field
EDX	Energy dispersive X-Ray analysis
FIB	Focused ion beam
MgO	Magnesium oxide
NaCl	Sodium chloride
PVD	Physical vapour deposition
SADP	Select area diffraction pattern
SEM	Scanning electron microscope
TEM	Transmission electron microscopy
Ti	Titanium
TiN	Titanium nitride
TiAlN	Titanium aluminium nitride
WC	Tungsten carbide
XRD	X-Ray diffraction

List of Figures

List of Tables

1 Introduction

1.1 Background and motivation

The selection, processing and utilization of materials have been part of human culture since its beginning. Human ability to fabricate, develop and use tools to manufacture goods laid the foundation for a further progress, allowing technological and cultural development. Since the Industrial Revolution materials with excellent properties have been manufactured. The successful utilization of materials depends on their properties, such as: thermal, mechanical, physical and chemical properties, which in turn are the result of the synthesis and processing methods used.

Despite technological advances, during machining of hard materials, the cutting tools still face challenges: a requirement for constantly increased operating temperatures, higher impact forces and increased wear resistance. During dry high-speed machining of hard materials, the temperature at the contact point between the cutting tool and the working piece usually reaches values in excess of 900 °C [1-2]. In order to protect the tool and to improve its performance, a protective coating is applied on the tool.

The ability to increase the thermal stability of protective coatings under work load has been the subject of numerous investigations in recent years. The focus has been primarily on the design of coating compositions with improved mechanical properties at the temperature of application. Due to lack of adequate equipment, the fundamental mechanical properties of hard ceramic films have often been investigated at room temperature, either in as deposited state or after heat treatment. Although this approach is useful, it is sensible to test materials at or close to their service temperature, at which point the intrinsic material properties may be expected to change. Various types of hard coatings have been developed to protect the base material of cutting tools. This work is focused on coatings from TiN and TiAlN systems.

TiN and $Ti_{1-x}Al_xN$ are ceramic materials widely used as protective coatings due to their extreme hardness, excellent adhesion to substrates, high chemical inertness

and a low coefficient of friction with most workpiece materials. TiN is the first generation of physical vapour deposition (PVD) hard coatings and from the early 1980s it has been widely used, making it the most applied protective coating in industry applications where the abrasive wear is a major problem; for example: cutting, drilling, extrusion, stamping, forging and casting [3-6]. Some cutting tools coated with TiN film are presented in Figure 1-1 (a). However, the usage of TiN is not restricted to protective coatings for cutting tools. It is also used in electronics as a diffusion barrier [7-9] and in decorative applications (see Figure 1-1 (b)) [10] due to its golden colour [3]. In addition, because nitrided titanium surfaces have good biocompatibility, TiN is a potential implant material, particularly for components subjected to wear erosion conditions [11-15].

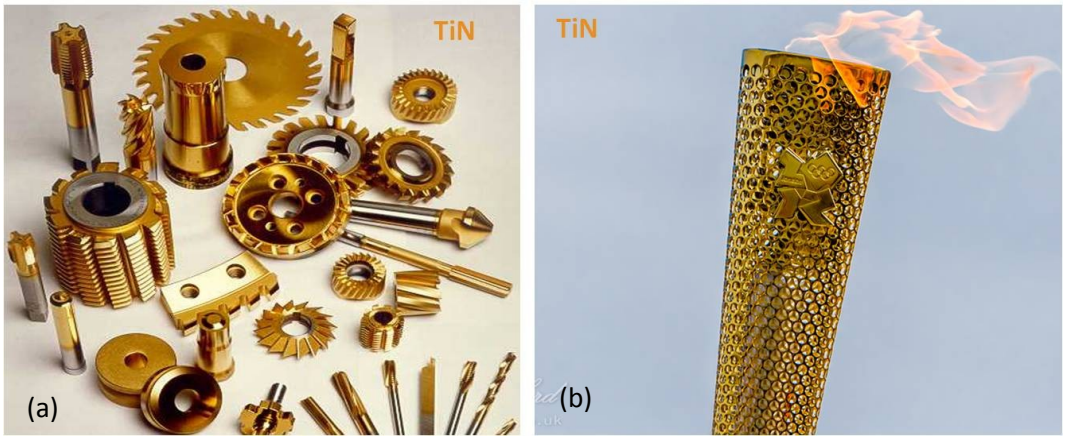

Figure 1-1 Various objects coated with TiN: (a) cutting tools (image courtesy SECO Tools Sweden) [16] and (b) the 2012 London Olympics Games torch [17].

Nevertheless, limited oxidation resistance at high temperatures represents a major drawback of TiN coatings, with oxidation initiating above 500 °C, leading to the formation of TiO_2 [3, 18-21]. One way to improve oxidation resistance is by replacing titanium atoms in titanium nitride lattice with aluminium atoms, thereby forming $Ti_{1-x}Al_xN$ ceramics [3, 22-27]. Aluminium is used as it forms a stable aluminium oxide layer on top of $Ti_{1-x}Al_xN$ coatings at elevated temperatures. This oxide layer prevents further oxidation of the underlying material [5].

Alongside improved oxidation resistance, the cubic structure of $Ti_{1-x}Al_xN$ ceramics exhibits a significantly higher hardness at room temperature [3, 5, 26]. These dark greyish-colour coatings are primarily used in high temperature environments above the limits of TiN usage [3, 27]. During high-speed machining

of hard materials, $Ti_{1-x}Al_xN$ coated tools perform better and last longer than those coated with TiN. The improved performance suggests the high temperature hardness of ternary coatings is higher than the TiN one. This allows $Ti_{1-x}Al_xN$ coated tools to be used at significantly higher cutting-speeds and feed rates for machining hard materials [3, 5, 28-29]. The good performance at high temperatures has been linked to the fact that, the fcc $Ti_{1-x}Al_xN$ structure decomposes spinodaly at high temperatures into two coherent fcc nanodomains, which correspond to TiN and stabilised AlN (AlN_{fcc}) crystallography, resulting in a highly stressed crystallographic structure [27, 30]. In addition, another factor that might contribute to the high temperature performance improvement of these ternary coatings could be attributed to the different critical resolved shear stresses of TiN and AlN_{fcc} phases. For dislocations to glide across nanodomains interfaces, a critical shear stress that is large enough to overcome the resistance caused by interface–dislocation interactions is required. This critical shear stress is a function of the shear-modulus difference between alternate nanodomains and the smallest angle between slip planes and nanodomains interfaces [31]. However, AlN_{fcc} is a metastable phase and it has been obtained in nanometre domains only, which makes it difficult to determine its mechanical properties. Nevertheless, such a hypothesis should not be excluded from analyses.

$Ti_{1-x}Al_xN$ coatings annealed in controlled atmosphere at high temperature (800 °C onwards) exhibit higher room temperature indentation hardness, a phenomenon which has also been related to spinodal decomposition [27, 30].

However, most of these indentation experiments were carried out at room temperature. In-situ studies of these materials at elevated temperatures are very rare. Furthermore, studies which treated this subject have not linked the high temperature hardness to the structure and chemistry of the coatings.

In this work, instrumented nanoindentation was employed to study the influence of temperature on mechanical properties of a wide compositional range of $Ti_{1-x}Al_xN$ coatings deposited by magnetron sputtering and cathodic arc evaporation deposition techniques. Although it is desirable to investigate these materials at temperatures encountered in their applications (values in excess of 900 °C [1-2]), the temperature at which a reliable investigation could be performed was limited

to 350 °C, due to capability of the equipment. The factors which limited the experimental temperature are discussed in detailed in the experimental chapter.

Transmission electron microscopy, focus ion beam and X-ray analyses were employed for a comprehensive comparative study of mechanical behaviour of these coatings. The investigation started with the analyses of the bulk single crystal (001) TiN (TiN_{bulk}) as it represents the simplest and the purest system related to the $Ti_{1-x}Al_xN$ films, followed by magnetron sputtered TiN coatings, which have a more complex structure and a higher density of defects. The research carried on with the investigation of magnetron sputtered $Ti_{1-x}Al_xN$ coatings (x = 0.34, 0.52, 0.62) and cathodic arc evaporated $Ti_{1-x}Al_xN$ industrial coatings (x = 0.44, 0.6, 0.7), the latter ones being deposited at three biases (20, 40 and 60 V).

The influence of aluminium addition in TiN matrix was examined based on deformation kinetics analysis. A set of fundamental deformation parameters as activation volume, activation energies and Peierls stress were determined.

The motivation for the work has been the desire to understand how and why the amount of aluminium, the applied substrate bias and the deposition technique alter the mechanical properties of these films at moderately elevated temperatures. A better understanding of these phenomena could lead to the improvement of these types of coatings or even to the creation of new high temperature hard coatings.

1.2 Structure of the thesis

This work is focused on characterising mechanical properties of coatings in the TiN and TiAlN systems. As these materials are ceramics, a review of various techniques for determining mechanical properties of brittle materials at room and elevated temperatures was done and is presented in Chapter 2. An analytical model used for determining the fundamental deformation parameters is also presented in this chapter.

Chapter 3 discusses the chemistry and structure of TiN and $Ti_{1-x}Al_xN$ coatings. The chemistry and the structure are strongly related to the manufacturing

technique of these materials, materials which are synthesised in the form of thin films (coatings). Because of that, an overview of film deposition techniques and how deposition parameters influence the structure of thin coatings are also presented in this chapter.

Chapter 4 summarises the literature data regarding the mechanical properties of TiN and $Ti_{1-x}Al_xN$ coatings and briefly shows how the mechanical properties of these thin coatings are affected by various deposition conditions.

Chapter 5 describes the materials studied and the experimental techniques employed for structural and mechanical analysis.

Chapter 6 presents the results and their analysis. Finally, Chapter 7 summarises the achievements and presents the further work.

2 Measurement of plastic properties of brittle materials

Plastic deformation in crystalline ceramics can occur, as with metals, by the motion of dislocations. However, lattice resistance in ceramics is much higher than in metals due to the nature of atomic bonding, which, in the majority of ceramics (e.g. carbides, nitrides, borides of transitional metals) consists of a mixture of covalent and ionic components [32-33]. The covalent and ionic components of the bonding increase the Peierls stress for dislocation glide and in the most of ceramics determine the slip system for dislocation movement. The requirement for charge neutrality (due to the ionic component of the atomic bonding) imposes dislocations to move only on certain crystallographic planes and directions within those planes in order to prevent the proximity of the like charges [34-35]. In addition to the above considerations, the covalent component of the bonding makes dislocation movement even more difficult; because in these materials covalent bonds are stronger than ionic ones [34, 36].

All the above mentioned factors explain the limitation of the number of active slip systems in ceramics at room temperature; limitation which restricts the freedom of dislocation motion required for a general homogeneous deformation by crystallographic slip. Von Mises (1928) showed that five active independent slip systems are necessary for general plastic deformation of polycrystals by

crystallographic slip. In the absence of enough active slip systems, the force applied to the material is not released by plastic deformation, but it is stored in the volume. In addition, the lattice resistance, which denotes the stress required to break the atomic bonds to allow for a dislocation movement from one atomic position to the next (along the close pack direction), is large in ceramics. The lack of required number of independent slip systems, coupled with large lattice resistance, leads to a yield strength much higher than fracture strength at ambient temperature [34]. Therefore, when a high enough force is reached to break the atomic bonds, rapid subsequent propagation of the crack is driven by the large accumulated stresses [37]. Hence, the brittleness of ceramic materials is explained by the reduced number of active independent slip systems and the high Peierls stress values. The deformation resistance of each distinct slip system can vary significantly, resulting in exceedingly high stresses that are required to plastically deform a crystal in certain orientations, particularly in crystals of low symmetry [38].

Therefore, alongside the nature of the atomic bonding, the structure of crystalline materials may determine the elements most susceptible to deformation, such as slip, cleavage and twin planes, together with their directions. Changes in physical environment (temperature, pressure, strain rate) in combination with crystal structure may act to suppress or favour changes of certain slip systems, thus altering the mechanical response of the material [39-41].

An important factor which should be taken in consideration in determining plastic properties is the strain rate. The plastic flow of the material with regards to the applied strain rate is influenced by the lattice resistance. At low and moderate temperatures, increasing the strain rate results in a decreased probability for the thermal activation of dislocations over impeding obstacles and hence leads to increased flow stress [42]. In the case of hard ceramics, which possess a high Peierls barrier, an increase in the strain rate can be translated as an increase in the lattice resistance.

A secondary effect of the strain rate over the plastic flow in brittle materials could be described by a process similar to work hardening in metals. When the load is applied (either during indentation or tensile/compression test) a plastic zone is

usually created due to the movement/formation of dislocations. On one hand, during a low loading rate, dislocations have time to move and arrange in low energy configuration, forming a plastic zone of a certain size. On the other hand, during a high loading rate, the same amount of plastic deformation has to be created in much less time; a high rate of plastic deformation means a faster movement of dislocations. Because of that, dislocations do not have enough time to rearrange themselves in low energy configuration, but they get entangled and pinned at grain boundaries, leading to high stresses (work hardening). These stresses are released either by nucleation of internal cracks or by opening/extending existing surface flows.

During room temperature testing, a brittle material would fail by fracture in the elastic region. This behaviour is attributed to the crack development from the microcracks and other defects present in the structure, particularly on or in the proximity of the surface. Because of that, the plastic properties at room temperature of brittle materials are hard to measure. However, a number of practical solutions have been developed in order to extract the plastic properties of brittle materials. These solutions are briefly discussed next and include: application of confining pressure during compressive tests, compressive and/or tensile experiments at elevated temperatures, micropillar compression and indentation at small scale (nanoindentation).

2.1 Compressive testing under confining pressure

The majority of brittle materials fail in compression by cone fracture (Figure 2-1 a) noted by Coulomb in eighteenth century or by axial splitting (Figure 2-1 b) [37]. Von Karman showed that a powerful technique to control the crack development during compressive tests of brittle materials at room temperature is the application of lateral pressure, which has shown to dramatically increase compressive strength [43]. High confining pressure inhibits both, the growth and nucleation of cracks. When the applied compressive stress is sufficiently high, dislocations may be generated at the stress concentrated crack tips since the cracks cannot propagate to relax the high stresses at the tips [44]. Therefore, the initial deformation of brittle materials under a high confining pressure is expected to be governed by plastic flow.

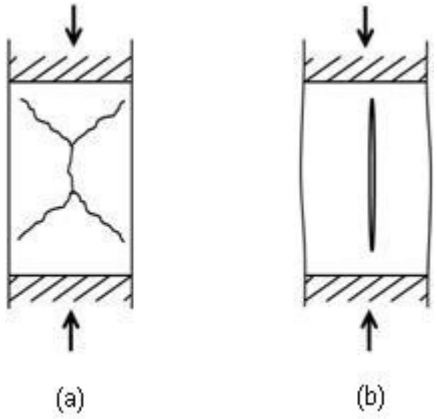

Figure 2-1 Compression failure of brittle materials by: (a) cone fracture, and (b) axial fracture, from [45]

Typically, multi-axial stress/strain experiments for studying plasticity at room temperature are performed using a modified Kolsky (split Hopkinson) pressure bar, in which a cylindrical brittle specimen is placed between two metallic bars. Confinement of the specimen is achieved by installing a shrink fit metal sleeve on the lateral surface of the cylindrical ceramic specimen [44]. The inner diameter of the sleeve is slightly smaller than the specimen diameter. In order to mount the sleeve around the specimen, the sleeve is heated to expand the inner diameter and enable the specimen to slide into it. After the assembly is cooled, shrinkage of the sleeve provides confinement pressure on the lateral surface of the specimen. The magnitude of the confining pressure can be varied by using different materials and thickness for the sleeves.

Experiments conducted using a servo-hydraulic load frame, in which the samples were confined laterally using shrink-fit metal sleeves, were performed on various types of polycrystalline BeO, Al_2O_3 and AlN ceramics. With increasing confining pressure up to 1.25 GPa, AlN and BeO exhibit a transition from brittle fracture to plastic deformation. Furthermore, their compressive failure strength and ductility strongly increased at moderate confining pressure. In the same time, Al_2O_3 seemed to exhibit brittle fracture behaviour up to the highest pressure investigated, 1.25 GPa. TEM analyses on plastically deformed samples show that the dominant deformation mechanism during compressive test is plane slip by dislocation motion, with attendant pile-up at grain boundary [41].

Increase in strength of brittle materials (including SiC and Al_2O_3) and brittle to ductile transition behaviour under confining pressure have been subject of numerous research projects [37, 45-48]. They confirmed that with increasing

confining pressure, the contribution to inelastic deformation by microcracking decreases while that by plastic flow increases.

2.2 High temperature mechanical testing

High temperature mechanical testing is the most common means to measure the plastic properties of brittle materials. With increasing temperature, the high Peierls-Nabarro force (intrinsic lattice resistance to dislocation movement) decreases and the number of active independent slip-systems increases, allowing for plastic deformation by dislocation motion to take place. The main techniques used to measure plastic deformation at elevated temperatures are: indentation, tensile and compression tests.

Indentation hardness at temperature up to 2000 °C was performed by Atkins and Tabor to determine the plasticity of a range of refractory materials (carbides, nitrides, oxides, borides and Si_3N_4). The experimental set up consisted in a graphite resistance furnace, inside which the material and the indenter (which were mounted at the end of graphite bars) were brought in contact at a controlled pressure and atmosphere. Few indenter materials are sufficiently hard and chemically stable above 1000 °C. Because of that, the indenter was made from the tested material itself (mutual indentation). The authors noticed that the most rapid fall in hardness occurred at temperatures above half of the absolute melting point, T_m. However, the hardness of TiC and WC drops off rapidly at temperatures between 0.2 - 0.4 T_m. With the increase in temperature the materials pass through a brittle – ductile transition. Around 0.3 - 0.4 T_m the deformation becomes primarily ductile [49].

Yamamoto et al. have studied the mechanical properties of fine-grain polycrystalline TiN by mean of compression at temperature ranging from 800 to 1550 °C and strain rates from $2x10^{-5}$ to $5x10^{-3}$ s^{-1}. Compression tests were carried out in vacuum or nitrogen gas using an Instron testing machine. Experiments have shown that polycrystalline TiN is still brittle at 1100 °C, whereas at 1500 °C it becomes fully ductile because five independent slip systems are available [40]. TEM analyses from plastically deformed samples revealed that the primary slip system of TiN is {110} ⟨110⟩.

Veyssiere et al. used compression under imposed hydrostatic pressure at elevated temperature to compare the plastic deformation of equimolar $MgAl_2O_4$ spinel along various slip systems. They found out that at temperatures up to 600 °C, the critical resolved shear stresses CRSS for {110} <1-10> slip system are about half of those for { 111 } < 110 > and { 100 } < 110 > [50].

Wakai et al. were the first who clearly showed the superplastic behaviour in structural ceramics by conducting uniaxial tensile tests at temperatures up to 1500 °C of 3 mol % Y_2O_3 tetragonal ZrO_2 polycrystals [51] and of Y-TZP/Al_2O_3 (20%) [52]. With the right combination of temperature and strain rate, the former material plastically elongated more than 120% whereas the latter material reached 200% permanent elongation.

Plastic deformation of Al_2O_3 polycrystals with grain sizes between 1 and 15 microns was investigated by bend-test experiments at temperatures and stresses between 1200 °C and 1750 °C and 1.4 MPa and 310 MPa, respectively [53]. In addition, compression tests on high density alumina cylinders were conducted at 1450 °C to investigate possible texture development [54]. Both studies revealed that several deformation mechanisms simultaneously contribute to the overall plastic deformation of alumina, in which diffusional creep dominates and that both lattice and grain boundary sliding (Nabarro-Herring and Coble creep, respectively) are important. Grain boundary sliding can be accommodated either by diffusion or by slip in those grains which are favourably oriented. TEM analysis revealed that non-accommodated grain boundary sliding leads to the development of cavities at triple point junctions. Basal slip was observed on all tested conditions but does not significantly affect the plasticity dynamics. Grain boundaries are the primary source for the basal dislocations and the deformation by basal slip is favoured by high stresses. These results are in line with Folweiler's [55] and Cannon's et al. findings [56], in which they showed that plastic deformation of polycrystalline Al_2O_3 with a grain size up to 100 microns does not occur by basal slip but by a diffusional creep process as described by Nabarro and Herring. However, for the coarse grain-specimens (65 μm) the creep appears to be related to a dislocation mechanism [56].

Waku et al. investigated the high-temperature tensile strength of unidirectional solidified $Al_2O_3/Y_3Al_5O_{12}$ eutectic composite, which is a candidate for high-temperature structural materials [57]. The tensile tests were conducted at temperature up to 1750 °C in an argon atmosphere at a strain rate of 10^{-4} s^{-1}. During tensile tests at room temperature to 1600 °C, the ceramic exhibit brittle behaviour, with fracture in the elastic region. However, stress-displacement curves from tensile tests performed at 1650 °C onwards revealed that the eutectic composite exhibit plasticity. SEM images of the microstructure after plastic deformation caused by tensile testing at 1600 °C and 1650 °C showed the presence of microcracks. Therefore, on this temperature regime, ductile to brittle transition takes place in this ceramic. TEM analysis confirmed that, alongside microcracks the yield phenomenon occurs by dislocation motion, which intensifies with increase in temperature [57].

2.3 Microindentation

The issue of plasticity in brittle materials has been most directly addressed by indentation testing, from which indentation hardness can be determined quite easily. Hardness is a measure of a material resistance to permanent deformation of its surface. There are several types of hardness measurements, depending on the form of surface disturbance: scratch hardness, impact hardness and indentation hardness. Conventional hardness technique (indentation) involves applying and removing a specific load onto a flat-smooth surface via an indenter probe, which could be either a hard sphere (Brinell hardness), a cone (Rockwell hardness) or a pyramid (Vickers or Knoop hardness). The load applied to the indenter divided by either the unit area of plastic deformation (Brinell, Vickers) or to the projected area of the indentation impression in the plane of the surface (Meyer, Knoop) represents the respective hardness. The results are different and relate to the used method [58].

Transmission Electron Microscopy (TEM) of the area under the indent has shown that multiple slip dislocation activity is directly responsible for initial permanent deformation in hard ceramics. Hockey showed that during Vickers microindentation performed at room temperature on single crystal and polycrystalline Al_2O_3, plastic deformation occurred by both slip and mechanical

twinning [59]. TEM cross-sectional images of indents provided direct evidence that a high density of dislocations is produced under the Vickers indenter. Confirmation of similar prolific plastic flow associated with room temperature indentation was subsequently obtained for other brittle ceramics, including ZnS, Si, Ge, Al_2O_3 - ZrO_2 and SiC [60]. Nakano et al. studied the plastic anisotropy in borides: TiB_2, HfB_2, ZrB_2 by means of Knoop microindentation. The plastic flow during indentation on basal plane of ZrB_2 was lower than the plastic flow associated with the indentation performed on a prismatic plane. In other words, the hardness of ZrB_2 is higher on the basal plane. In TiB_2, HfB_2, contrary to mechanical behaviour to ZrB_2, the plastic flow was greater on the basal planes; therefore, the indentation performed on the prismatic planes yielded higher hardness [61].

The occurrence of plastic deformation during indentation in these normally brittle materials is considered to be a consequence of the nature and magnitude of the local stresses developed under pointed indenters. The factor which permits the abundant plastic flow is the intense confining pressure induce within the elastic surround. However, stresses apparently associated with the heads of dislocation piles-ups blocked by grain boundaries are relaxed by the nucleation of inter-granular cracks [62-63]. Once the cracks appear and develop to a certain size, the plastic flow is concentrating on opening these cracks. Higher indentation load results in an increased volume of the plastic zone, which may extend over an increased number of grains and pores present in the material. Therefore, bigger indentation impressions would normally exhibit larger cracks. However, in order to suppress the formation of cracks, indentation technique at a smaller scale (nanoindentation) is performed.

It is well known that cracking is a scale-dependent process [64] and it may be suppressed completely if the sample is sufficiently small [37, 65-66]. Recent advances in experimental capabilities such as instrumental nanoindentation and ion milling have enabled examining the mechanical behaviour of materials at nanometre scale. Two of the techniques that have recently been widely used to study the effects of sample size in plasticity are micropillar compression and instrumental nanoindentation, and they are presented next.

2.4 Micropillars compression

Indentation is commonly used for studying plasticity in materials, particularly in macroscopically brittle materials, due to the ease of varying the load–displacement parameters and the high resolution of data obtained from this experimental technique. However, in materials with complex crystal structures, typical of many brittle materials, the flow required to accommodate the multi-axial stress field created during indentation may cause deformation on both hard and soft slip systems and renders such data difficult to interpret [67]. Therefore, the deformation behaviour during indentation might reflect that of the harder slip system.

To circumvent the strain gradients inherent in conventional indentation experiments, a "simple" uniaxial compression technique of micron-size uniform cross-section columns milled on the surface of examined materials can be used. Focused ion beam is used to fabricate the micro-pillars which remain attached to the bulk substrate at one end. Samples are tested in uniaxial compression using nanoindenter equipment outfitted with a flat-punch tip. The response of interest from a compression test is a stress–strain curve. The conversion of the load-displacement data from the nanoindenter to a stress–strain curve is analogous to calculating a stress–strain curve for a macroscopic compression sample. The technique can be used to examine the plastic response and dimensional size effects of samples of different sizes that are from the same bulk of polycrystalline material or from single crystals. The only significant difference is that SEM images are used to measure the dimensions of the micro-sample.

Theoretical analyses backed by experimental results on fused silica and polymethylmethacrylate showed that brittle materials should deform plastically rather than by cracking if samples are small enough [37, 65]. These findings have been confirmed for other materials as well.

Uchic et al. showed that the mechanical behaviour of single crystal of nickel changes with the size of the micropillar [68-69]. Whereas the bulk samples and pillars larger than 20 microns showed a smooth transition from elastic to plastic flow and a steady rate of work hardening, samples of 5 microns or less in diameter display large strain bursts in the elastic region and an increase in the work hardening. Decreasing in the pillar diameter resulted in a significant increase in

the yield strength. This phenomenon was confirmed by Volkert et al., who showed that the yield stress increases strongly with the decreasing column diameter during micropillar compression tests on a gold crystal [70].

Recently, it has been shown that micropillars of materials normally considered brittle (GaAs, MgO) can be deformed plastically at room temperature [71-73] and the measured yield stress and its variation with temperature is similar to that observed in tests on large crystals [74].

Ductile to brittle transition in micropillar compression at room temperature of brittle materials depends on the dimensions of the pillar and the direction of the applied stress with respect to the active slip systems [66, 75]. Compression of GaAs micropillars occurs by formation of slip bands which propagate inside the pillar and intersect. Axial compression splitting follows from the intersection of slip bands. It has been shown that, for materials which exhibit a similar plasticity to GaAs, axial cracking becomes more difficult as the sample gets smaller [66].

Soler et al. have done an analysis in which concluded that the size - effect relationship in micropillar technique depends on the lattice resistance. Materials with a small Peierls stress, as fcc metals, show a strong size effect due the variation of the dislocation density with the pillar size; the mechanical behaviour of the pillar is governed by the dislocation density and dislocation sources density. In contrast, solids with very high Peierls stress (high bulk yield stress) exhibit insignificant size - effect on the flow stress [75].

Korte and Clegg performed micropillar compression on ceramics at elevated temperature up to 400 °C [74]. Micropillars were made on [001] facet of a single crystal $MgAl_2O_4$ spinel and their compression was carried out using a nanoindenter with a hot stage. Whereas micropillar compression performed at room temperature resulted in a negligible amount of plastic deformation followed by brittle fracture, micropillars compressed at 200 °C and 400 °C exhibit significant plastic deformation along the operating slip system {110} <1-10>. The same slip system was operative in compression of bulk single crystals of $MgAl_2O_4$ spinel under confining pressure [50].

2.5 Instrumented nanoindentation

Instrumented nanoindentation is an experimental technique used to determine mechanical properties (most often hardness and elastic modulus) of small volumes

at room and moderately elevated temperatures [76]. It is the most viable experimental technique to determine the mechanical properties of thin films. In addition, nanoindentation could be used to determine the mechanical properties of individual grains in polycrystalline materials, providing that the grains have a reasonable size.

Furthermore, due to its high-resolution load-displacement data, nanoindentation has been employed in studying discrete events such as dislocation source activation [77-78], shear instability initiation [79-80], phase transformation [81-82], fracture toughness [83] and creep [84-85]. Some of these phenomena are depicted in Figure 2-2.

Fundamental deformation rate-controlling parameters such as activation volume, activation energy and Peierls stress can be determined by extending the data obtained from nanoindentation [86].

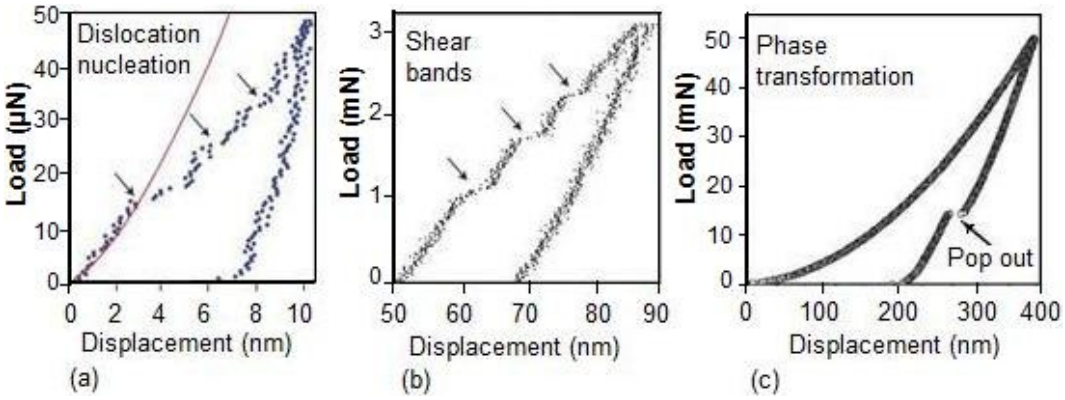

Figure 2-2 Discontinuities in the load-displacement curves which are attributed to: (a) dislocation nucleation in (110) single-crystal Pt [78], (b) shear localization into shear bands [80], (c) phase transformation in Si with a significant volume increase, from [82].

High-temperature nanoindentation is a relatively new additional capability of this technique. However, a reliable nanoindentation analysis performed at elevated temperatures must overcome technical issues such as heat management, thermal drift and sample oxidation [87-88].

Instrumented nanoindentation was the primary experimental technique used to determine the mechanical properties of materials in the present work. The technique is discussed in detail in the chapter which presents the experimental part of this research.

2.6 Kinetics of deformation

The kinetics of deformation is interpreted in terms of fundamental deformation rate-controlling parameters such as the activation energy of the obstacles controlling the deformation rate process, the apparent activation volume and the Peierls stress. These parameters were measured and compared at various length-scales and temperatures for various materials.

Plastic deformation of crystalline materials at ambient and moderately elevated temperatures takes place by generation and movement of dislocations. The energy required for dislocation motion comprises of two components: (1) thermal component, which is responsible for the vibration of atoms and, (2) mechanical component, which is the mechanical energy that is supplied externally to the dislocation by the shear stress. The energy addition of these two components forms the total activation energy, which is the energy required by a dislocation to overcome the rate controlling obstacles. A glide resistance diagram which illustrates the energies involved in the motion of dislocations is shown in Figure 2-3. The total activation energy is represented by the total area beneath the force – distance curve.

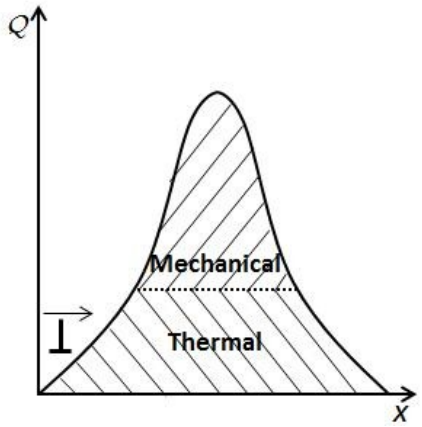

Figure 2-3 Schematic representation of the energies required for a dislocation glide over an idealised obstacle [42].

The lattice resistance (Peierls stress) for hard materials, such as hard ceramic coatings, is very high. Therefore, it is reasonable to assume that the plastic deformation mechanism responsible for the high hardness is dislocation glide controlled by the lattice resistance. In this mechanism, the movement of a dislocation by a single step through the crystallographic lattice is the strain rate controlling step. A simple model for the relation between the effective strain rate

in the plastic volume beneath the indenter, $\frac{d\gamma}{dt}$, and shear flow stress, τ, can easily be developed [86]. The procedure starts/originates from Orowan's equation which relates the plastic strain rate, the density of mobile dislocations, ρ_m, the magnitude of the Burgers vector of dislocations producing the shear strain, b, and the dislocation velocity, v:

$$\frac{d\gamma}{dt} = \rho_m \cdot b \cdot v$$

where the v can be estimated using a standard approach for a stress activated process:

$$v = \nu \cdot b \cdot \left\{ \exp\left[- \frac{(\tau_p - \tau) \cdot V}{kT} \right] - \exp\left[- \frac{(\tau_p + \tau) \cdot V}{kT} \right] \right\}$$

where ν is the attempt frequency, τ is the applied shear stress, V is the activation volume, T is the absolute temperature in Kelvin, k is the Boltzmann's constant and τ_p is the lattice resistance or the Peierls stress, which is the stress required to move a dislocation through the lattice in the absence of any thermal energy (at zero Kelvin). Activation volume is widely recognised in the literature as a measure of the Burgers vector multiplied by the area swept out by dislocations during the process of thermal activation.

The first term in the square brackets is associated to the dislocations moving in the direction of the applied shear stress, whereas, the second term is associated to the dislocations jumping backwards. It is reasonable to assume that the number of dislocations moving backwards is much smaller than the number of dislocation moving forwards. Therefore, the second term in the square brackets could be neglected; and assuming further the activation volume can be treated as a constant, the expression can be simplified to:

$$\tau = \tau_p + \frac{kT}{V} \ln \frac{d\gamma}{dt} - \frac{kT}{V} \ln (\rho_m \cdot b^2 \cdot \nu)$$

A plot of shear flow stress, τ, versus the natural logarithm of strain rate, $\ln \frac{d\gamma}{dt}$, at a particular temperature, should yield a straight line with the slope $\frac{kT}{V}$. Therefore, the activation volume, V, can be obtained from the slope of the graph. Similarly, a

plot of shear flow stress against temperature at a fixed strain rate should result in a linear relationship, with the slope $[\frac{k}{V} \ln \frac{\frac{d\gamma}{dt}}{\rho_m \cdot b^2 \cdot \nu}]$. By extrapolating the straight line to zero Kelvin, the intercept with the shear stress axes should provide the value corresponding to the Peierls stress, τ_p.

This way the activation energy, Q, can be determined from the following relation:

$$Q = \tau_p \cdot V$$

2.7 Methods of hardening in ceramics

Plastic deformation in crystalline ceramics occurs, as with metals, by the multiplication and motion of dislocations, followed by initiation and/or growth of microcracks and eventually fracture. Virtually all strengthening techniques rely on controlling the multiplication and mobility of dislocations; that is, greater mechanical forces will be required to initiate plastic deformation. This can be achieved in various ways known from metallurgy, such as the work, solution and grain boundary hardening [89].

The work hardening consists of introducing a high number of defects in the structure (dislocations, point defects, grain boundary etc) similar to traditional work hardening in a ductile material. The increased number of defects constitutes obstacles for motion of dislocation. That might lead to an increase in the applied stress required for movement of dislocations. In this way the strength and hardness of ceramic material can be increased.

The introduction of a secondary phase, such as precipitates, could impede the dislocation motion. Systems with a limited solid solubility between two or more elements (eg $Ti_{1-x}Al_xN$) exhibit a heterogeneous microstructure, consisting of two or more phases at thermodynamic equilibrium. The distribution of phases in a heterogeneous microstructure can be described by two models illustrated in Figure 2-4. The second phase particle can be on the order of the grain size of the matrix (a), or can be dispersed in the matrix, so that each particle is completely surrounded by the matrix (b) [34, 90].

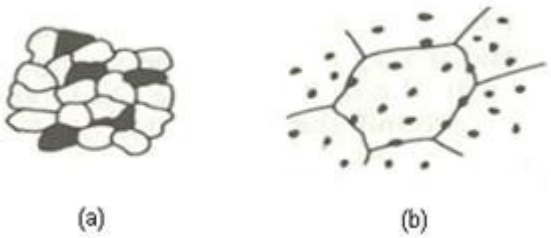

Figure 2-4 Two phase microstructure; (a) aggregate structure; (b) dispersed structure, from [34]

Not all second phase particles enhance the hardness; for strengthening to occur, there must be a strong particle-matrix bond. Strengthening from a second-phase depends on a number of factors, which include: crystallographic fit between the phases, the bonding and energy of the interfaces, the size, strength, shape, number and distribution of the particles and coherency stresses [34, 90].

If a stronger phase is in small percentage and surrounded by matrix, the deformation takes place in the softer phase, around the particles. Increasing the percentage of the stronger phase up to the point where the softer phase no longer forms a continuous matrix, forces the deformation to take place in both phases [34, 90].

Other ways to increase the hardness of ceramics are by strengthening the grain boundaries alongside controlling the dislocation motion. This can be achieved by creating heterostructures or superlattice structures which can be either (1) of nonisostructural phases, (2) epitaxial layers or (3) nanocrystalline biphase. In the case of the former, the different phases will exhibit different slip systems that will prevent the dislocation from moving easily through the interfaces between the phases [91]. For epitaxial layers, the strain resulted from the distortion of the lattices, distortion required to form homogeneous boundaries between the layers, creates a stress field which impedes the dislocation motion, leading to an increase in the hardness [31, 92]. Nanocrystalline biphases are nanocomposites with coherent grain boundaries between the nanodomains (nanograins), which form a continuous two phase system. Similar to the strengthening mechanism in epitaxial layers, a strain field is created by the distortion of lattices which form coherent grain boundaries. The strong grain boundaries inhibit the grain boundary sliding alongside the dislocation motion [93-94].

3 Structure and chemistry of TiN and $Ti_{1-x}Al_xN$

3.1 Structure and chemistry of TiN

TiN exists as a solid solution containing nitrogen in the range 37.5-53 at.%, as can be seen in the binary diagram presented in Figure 3-1 (a) [95]. It has a high melting point of 2947 °C [96], a density of 5.4 g/cm^3 and a cubic B1 NaCl crystal structure [97] (see Figure 3-1 (b)) with a mean lattice parameter of 4.2417 Å [98]. Each type of atom binds to form an intermixed octahedral structure. However, due to the size of the atoms (Ti_r=147 pm, N_r=74 pm), it could be considered that, the main matrix is formed by the titanium atoms and the smaller nitrogen atoms occupy the octahedral sites. The complete filling of the octahedral sites would result in a stoichiometric compound, with the chemical formula TiN [99].

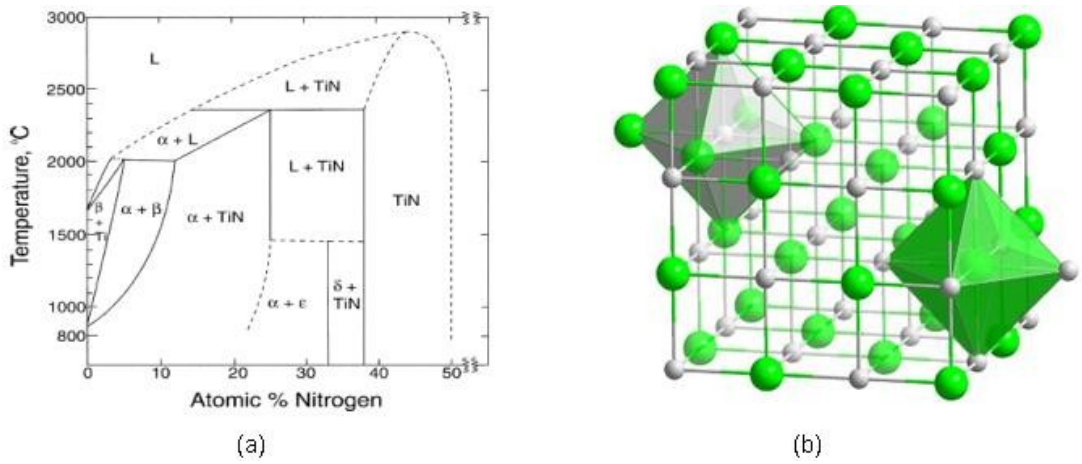

Figure 3-1 (a) Equilibrium phase diagram of Ti-N binary system, from [95], and (b) schematic of TiN lattice structure, from [100].

The colour of TiN films was found to be related to deposition bias and nitrogen flow rate which is translate in the film stoichiometry [101-102]. For a stoichiometric TiN (atomic ratio Ti:N = 1) the colour is gold, when it is under-stoichiometric (atomic ratio Ti:N > 1) the colour changes towards silver and when over-stoichiometric (atomic ratio Ti:N < 1) the colour becomes reddish, similar to copper. The increase in bias enhances the golden colour. Based on its colour, the TiN layer has the function of wear detection, that is, to allow the operator to distinguish between a used and a new cutting edge [6].

TiN has a low room temperature electrical resistivity (18 – 150 μΩ·cm), which means it is electrically conductive [18, 101, 103], and an isotropic Poisson ratio of 0.25 [104].

The morphology of the TiN films deposited by PVD methods can generally be characterised as being composed of columnar grains elongated along the growth direction [97]. The length of grains can extend to a few microns, which means that many crystallites grow through the whole thickness of the coating. Depending on the deposition process parameters, either equiaxed or crystallographically aligned columnar grains or a mixture of the two can occur with varying levels of coating porosity [4].

The deposition method has a strong influence on texture of the coatings and crystallographic orientation. It has been shown that CVD coatings exhibited relatively larger, defect-free grains, whereas, PVD coatings possessed finer grains with a high density of defects [2]. In addition, moderate {200} and {220} textures were found in magnetron sputtered films as opposed to the very predominant {111} texture exhibited by vacuum arc evaporated coatings. O'Hern et al. have shown that the crystallographic orientation is influenced by the stoichiometry, as well. Increasing the concentration of nitrogen, the films changed their preferential orientation from (111) to (200) and at high concentrations of nitrogen the (220) orientation developed [105].

Deposition bias has an overwhelming effect on the morphology of polycrystalline hard coatings. Generally, high energetic particle bombardment is known to suppress columnar growth structure, resulting in an increase in the number of nucleation sites and a smaller grain size, which lead to denser and harder coatings. The unbiased coatings exhibit an open columnar morphology with large voids, which results in low hardness and poor wear resistance [2, 106-109].

3.2 Structure and chemistry of $Ti_{1-x}Al_xN$

$Ti_{1-x}Al_xN$ is a metastable structure. At thermodynamic equilibrium the $Ti_{1-x}Al_xN$ system splits into a two phase structure consisting of cubic [NaCl] TiN and hexagonal [wurtzite] AlN [30, 110]. From the TiN-AlN phase diagram presented in Figure 3-2 (b), which is taken as a quasibinary phase diagram from the ternary system Ti–Al–N shown in Figure 3-2 (a), it could be seen that, the solubility of

AlN in TiN is extremely low; basically non-existent under 1800 °C. Therefore, a large single crystal or bulk $Ti_{1-x}Al_xN$ cannot be synthesized.

However, by using various deposition techniques, an aluminium supersaturated metastable $Ti_{1-x}Al_xN$ solid solution can be obtained. During deposition, aluminium, titanium and nitrogen ions arrive at the surface of the growing film with energies above the lattice displacement energies, breaking the bonds between atoms at the surface. Each atom in the coating comes at rest with large amplitude vibrations around its new site, making it possible to synthesize a structure at conditions far from thermodynamic equilibrium [111]. Severe kinetic restraints on the mobility of ad-atoms enable the incorporation of aluminium atoms in TiN lattice. The substitution of Ti atoms with smaller Al atoms leads to a decrease of the lattice parameter of the fcc $Ti_{1-x}Al_xN$ [3, 5, 103]. The deposition processes will be discussed in more detail in the next chapter.

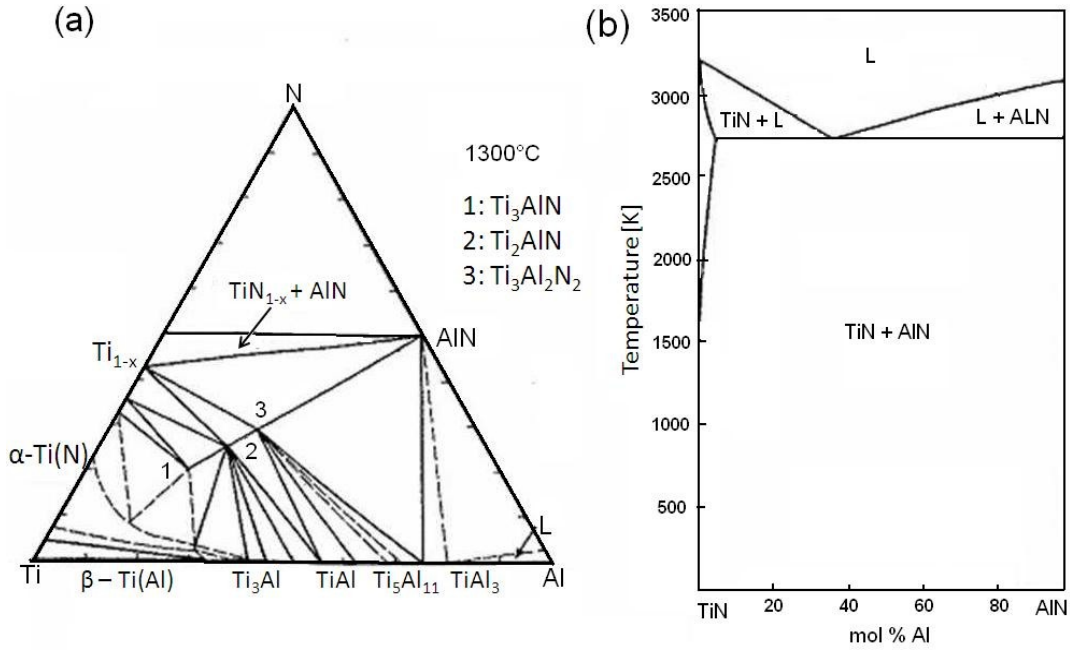

Figure 3-2 (a) Isothermal section at 1300°C in ternary phase diagram of Ti - Al – N and (b) calculated quasi - binary TiN - AlN phase diagram, from [112]

In as-deposited condition, depending on the amount of aluminium and processing parameters, $Ti_{1-x}Al_xN$ could either have a B1 cubic [NaCl] crystallographic structure or a wurtzite hexagonal crystallographic structure, as can be seen in Figure 3-3. However, in certain conditions a two phase coating consisting of cubic and hexagonal structures can be obtained [30, 103, 109].

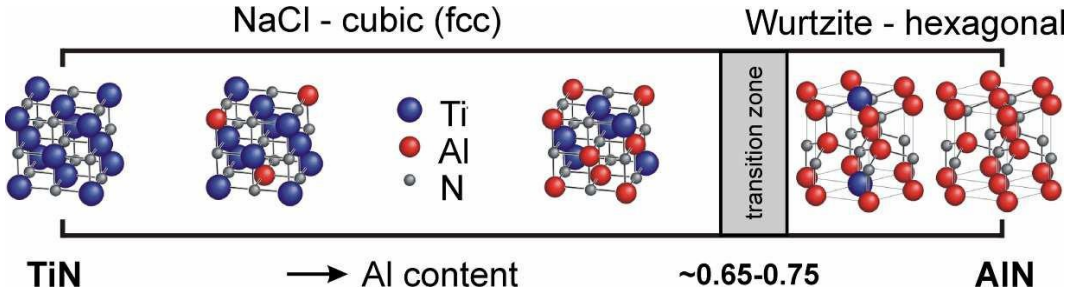

Figure 3-3 Changes in lattice structure in $Ti_{1-x}Al_xN$ with varying Al content, from [113]

During high energy depositions, $Ti_{1-x}Al_xN$ can retain the TiN crystallographic structure for an aluminium content $x \leq 0.65$. Both crystallographic phases, cubic TiN and hexagonal AlN, could be present in a film when $0.65 \leq x \leq 0.75$. For a rich aluminium composition with $x > 0.75$, $Ti_{1-x}Al_xN$ exhibits only a hexagonal structure corresponding to wurtzite AlN [30, 103, 114]. Out of these three $Ti_{1-x}Al_xN$ lattice structures, cubic $Ti_{1-x}Al_xN$ is of most industrial importance due their excellent mechanical properties, which make them suitable for cutting tools coating applications. Because of that, the present research has mainly focused on $Ti_{1-x}Al_xN$ compositions with cubic crystallography.

As mentioned, due to the synthesis condition at low temperatures, far from thermodynamic equilibrium, the TiN and AlN are frozen in a single phase cubic solid solution corresponding to cubic $Ti_{1-x}Al_xN$. High temperature thermal treatment was shown to lead to spinodal decomposition, a process during which cubic $Ti_{1-x}Al_xN$ splits into a two phase structure consisting of face central cubic TiN and face central cubic AlN (AlN_{fcc}) [27, 115]. A further increase in temperature leads to the onset of the formation of hexagonal wurtzite AlN (AlN_{hcp}) from cubic AlN. The spinodal decomposition process is described in more detail in next chapter.

The applied negative substrate bias has a strong influence on the morphology and microstructure of $Ti_{1-x}Al_xN$ films [116-118]. Films grown at low deposition energies (< 80 V) exhibit a (200) preferred columnar structure, as well as significant intragrain porosity. At high substrate bias (140 and 200 V) the films exhibit a smaller grain size and a high crystallographic defect concentration, structure which exhibits high internal stresses and high hardness values. Increased bias promotes a (111) oriented columnar texture with an interrupted columnar structure and a higher lattice parameter.

Aluminium addition has been shown to lower the thermal conductivity of TiN [119]. This is beneficial for tool tip as much of the heat generated during machining would be carried away by the chip [120].

3.3 Oxidation of TiN

The performance of coating depends on not only mechanical properties, but also corrosion resistance. TiN coatings suffer from a limited oxidation resistance, starting to oxidize around 500 °C [3, 18-20, 116]. The oxidation reaction of titanium nitride follows the equation:

$$2TiN + 2O_2 \rightarrow 2TiO_2 + N_2$$

The oxidation mechanism of TiN films was found to be controlled by the diffusion of oxygen and nitrogen through the TiO_2 surface layer. The oxygen from the atmosphere diffuses inwards to the reaction interface as the nitrogen desorption from the reaction interface towards the surface takes place. The difference in the molar volume of TiN (11.4 cm^3) and TiO_2 (18.8 cm^3) is large enough to induce substantial compressive stresses in the oxide layer. The large volume expansion that accompanies the oxidation of TiN to TiO_2 is shown in the Figure 3-4. As the oxidation process develops the magnitude of the stresses increase with the increase in the oxide layer thickness. The thickness of the TiO_2 reaches a threshold value, beyond which the oxide spalls [20, 116].

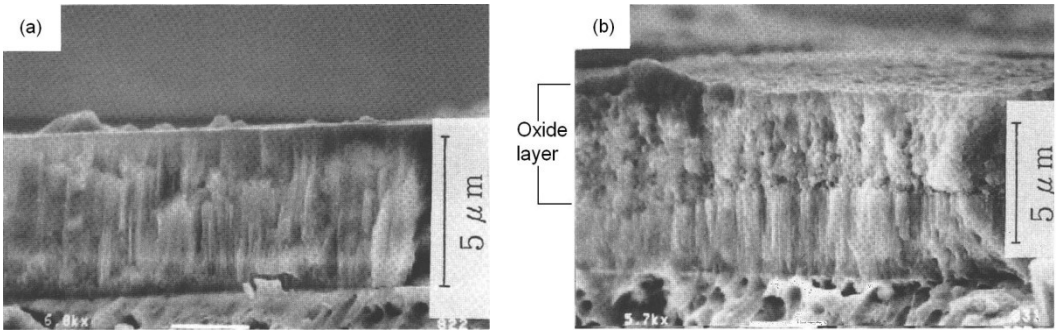

Figure 3-4 SEM micrographs of the fracture cross-section of The TiN film (a) before oxidation, (b) after oxidation, from [20]

3.4 Oxidation of $Ti_{1-x}Al_xN$

The oxidation resistance of TiN films is improved by the addition of aluminium in TiN matrix [3, 5]. This improvement is attributed to the formation of a highly

adhesive, stable and dense protective Al_2O_3 surface layer, which prevents the diffusion of atomic species in and out of the coating [3]. An important practical feature of Al_2O_3 is that, it has a dissolution rate four orders of magnitude lower than that of TiN. The chemical stability was shown by Kramer and Judd, who did experimental tests in ferrous work-pieces at 900 °C. Therefore, substituting titanium with aluminium imparts higher chemical stability through the formation of a stable Al_2O_3 surface layer at high temperatures [119].

A number of researchers observed that the surface-oxide layer formed in sputter deposited titanium rich films consists of two partially crystalline oxide layers; the upper one Al-rich and the lower one rutile-structure Ti-rich [20, 116]. With increasing temperature the degree of crystallinity of the aluminium oxide ceramic upper layer increases. As the Al_2O_3 layer wears, it continuously reforms by oxidation of the aluminium present in the coating [3, 116, 121-123]. Therefore, $Ti_{1-x}Al_xN$ compositions with higher content in aluminium provide a better, longer oxidation resistance [3, 27, 103, 116, 124]. This is of special importance in the area of high-speed and dry cutting processes, and where high tribological load are employed.

Better oxidation resistance of $Ti_{1-x}Al_xN$ can be attributed to the difference in the values of the Gibbs free energy for oxides formation. At 500 °C, temperature over which TiN starts to oxidise, aluminium oxide is much more stable than titanium oxide, with $\Delta G^0_{Al_2O_3}$= - 954 kJ mol^{-1} and $\Delta G^0_{TiO_2}$ = - 765 kJ mol^{-1} [125].

It was also shown that, a higher bias improves the oxidation behaviour of $Ti_{1-x}Al_xN$. Films deposited on stainless-steel at 0 V bias have an open columnar structure with large voided regions between the grains. Furthermore, these films developed cracks when annealed at 700 - 900 °C for 0.5 h. The cracks were generated upon heating due to the differences in the thermal expansion coefficients of film and substrate. The cracks and voids accelerate the oxidation process by providing free pathways for oxygen not only at the crack surfaces but at the film-substrate interface as well. A high bias (- 150 V) reduces the porosity and generates enough internal compressive stresses in the film to prevent crack formation. Therefore, the oxidation behaviour of $Ti_{1-x}Al_xN$ can be improved by the presence of a substrate bias during deposition [3, 116].

Munz showed that for arc ion-plated $Ti_{1-x}Al_xN$ coatings a protective Al_2O_3 film started to develop at temperatures as low as 600 °C, but without further effects at temperatures above 700 °C [3]. $Ti_{1-x}Al_xN$ can withstand elevated temperatures up to 800 °C. At higher temperatures the oxidation intensifies, especially for samples deposited without a substrate bias [116, 122-123].

These findings were confirmed by Ichimura and Kawana who studied the oxidation behaviour of $Ti_{1-x}Al_xN$ (x = 0.1 and 0.4) films deposited onto stainless steel substrates. The oxidation process was analysed in the range of temperature from 650 °C to 900 °C. They confirmed that, with increase in Al content, the oxidation rate decreased, and the activation energies of oxidation reaction increased. In the initial stages of oxidation the surface oxide layer made of Al_2O_3 and TiO_2 retained the original columnar structure of the nitride film [20, 116]. This process is governed by the oxygen diffusion from the surface into the already formed oxide scale (Al_2O_3, TiO_2) and Al atoms diffusion towards the surface.

The next step of oxidation is characterised by oxygen diffusion through the pores in the outer layer, towards the interface between the oxide layer and $Ti_{1-x}Al_xN$ film. The activation energy of the later oxidation stage has smaller values due to the lower concentration in Al. Data regarding the activation energies of oxidation and diffusion for a number of nitride composition is presented in Table 3-1 [20].

Table 3-1 Activation energies of oxidation and diffusion for various compositions related to $Ti_{1-x}Al_xN$, from [17]

Oxidation process	E (kJ/mol)
Oxidation of TiN (standard)	136
Oxidation of TiN (columnar)	122
Oxidation of $Ti_{0.9}Al_{0.1}N$	185
Oxidation of $Ti_{0.6}Al_{0.4}N$ (initial)	456
Oxidation of $Ti_{0.6}Al_{0.4}N$ (later)	265
Oxidation of CVD TiN	195
Oxidation of hot pressed TiN	190
Oxidation of $Ti_{0.51}Al_{0.49}N$	419
Oxidation of Ti metal	231
Oxidation of TiO_2	251
Oxidation of Al_2O_3	460
Oxidation of TiO_2	257
Oxidation of Al_2O_3	477

Knoteck et al. showed that sputtered ion plated $Ti_{1-x}Al_xN$ films from Ti:Al 50:50 targets start to oxidize at temperatures from 700 °C to 750 °C. The oxidation behaviour was studied and compared in Figure 3-5 with oxidation behaviour of other hard compound coatings [5, 26].

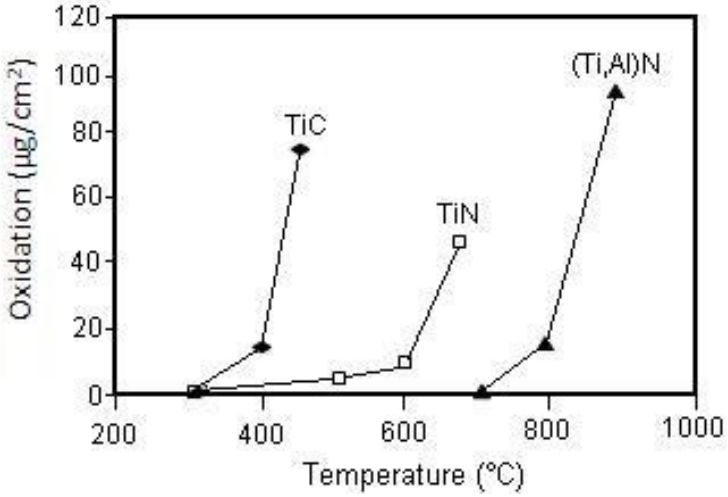

Figure 3-5 Oxidation of hard compound coatings with the temperature, from [26].

3.5 Spinodal decomposition

In any metastable structure there is a driving force for rearrangement of the atoms to form a structure which minimises the free energy of the systems. The transformation of a metastable to a thermodynamically stable structure requires activation energy. For $Ti_{1-x}Al_xN$ coatings this energy might be supplied by high temperatures encountered at the contact surface between the coated tool and the work-piece during machining. When the required energy is supplied, the $Ti_{1-x}Al_xN$ transforms through spinodal decomposition into thermodynamically stable face central cubic lattice (fcc) TiN and metastable fcc AlN phases, as can be seen in Figure 3-6. A further energy supply triggers the transformation of fcc AlN into thermodynamically stable AlN wurtzite structure [27, 30, 126].

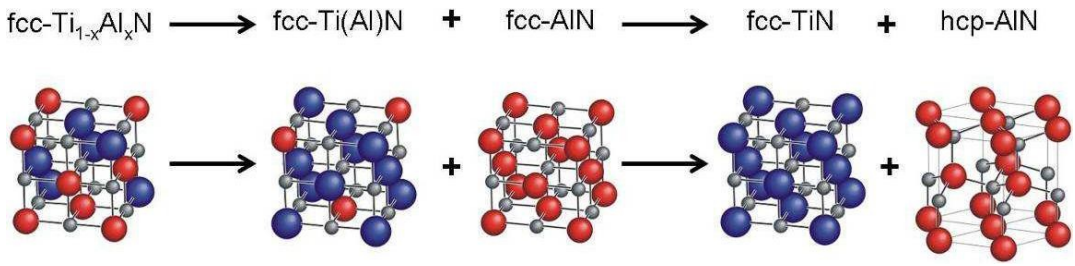

Figure 3-6 Crystallographic changes during spinodal decomposition, from [113]

The structural rearrangement in a solid is made by atomic movement (atomic diffusion). The reason why this process occurs is always so to produce a decrease in the Gibbs free energy [127]. The binary diagram (Figure 3-2 (b)) shows that AlN is insoluble in TiN below 1800 °C. This corresponds to a binary system with a miscibility gap, system in which the components (TiN and AlN) repel each other.

An important contributor to the internal energy of the system is kept by the bonds between different atoms in the film. Furthermore, a considerable amount of internal energy is stored in crystal defects as: vacancies, dislocations, stacking faults, twin boundaries, voids, grain boundaries, inclusions and free surfaces. The most efficient way of minimizing the total free energy is to reach a minimum in interfacial energy and a maximum in interatomic energy. Depending on these factors (interatomic bonding, whether the constituent atoms attract or repel each other, energy carried by defects) an ordering or decomposition of the solid solution may occur [127].

Figure 3-7 (a) and (b) illustrates a schematic of the most common case for a binary system, in which the free energy decreases due to diffusion of chemical species, in order to eliminate the concentration difference. The free energy will decrease towards G4 which represents the minimum energy of the homogeneous alloy. Thus, A and B atoms diffuse down the concentration gradients, from regions of high concentration to ones of low concentration [127].

However, if the system contains a miscibility gap the free energy curves can have a negative curvature at low temperatures as in Figure 3-7 (c) and (d). The compositional domain which is characterised by a negative curvature of the free energy, which is mathematically described by a negative second derivative, $\frac{d^2G}{dX^2} < 0$, is called chemical spinodal domain (see Figure 3-8). Any composition in

this domain may exhibit spinodal decomposition. Therefore, A and B atoms will diffuse up the concentration gradients, towards the regions with high concentration as shown in Figure 3-7 (c) and (d). This is a natural process from the energy point of view, as it reduces Gibbs energy from G3 to G4 [127].

However, it is better to express the driving force for diffusion in terms of a chemical potential gradient (μ). Figure 3-7 (e) shows that, when $\mu_A^2 > \mu_A^1$ A atoms move from (2) to (1); when $\mu_B^1 > \mu_B^2$ B atoms move from (1) to (2). Figure 3-7 (f) shows that, when $\mu_A^1 > \mu_A^2$ A atoms move from (1) to (2); when $\mu_B^2 > \mu_B^1$ B atoms move from (2) to (1). Therefore, A and B atoms diffuse down the chemical potential in both cases [127].

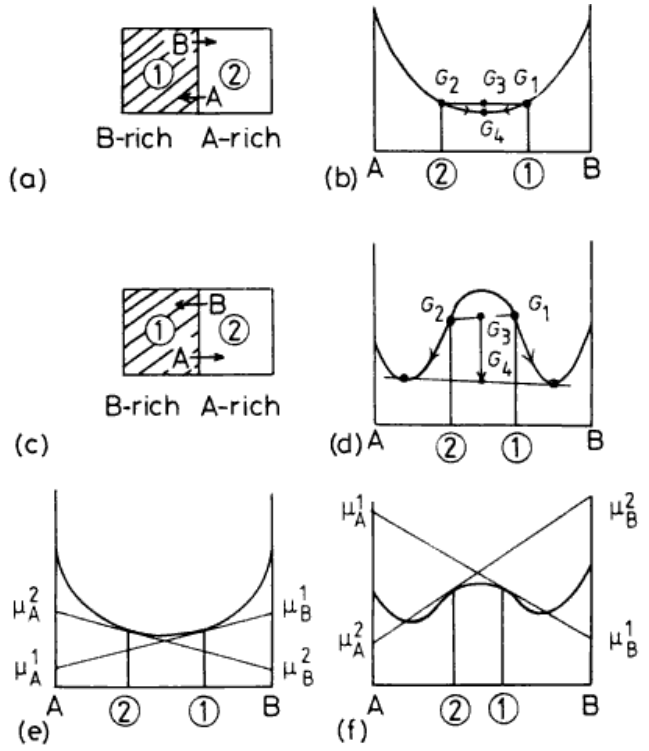

Figure 3-7 Free energy and chemical potential variation during diffusion; (a) and (b) down-hill diffusion, the homogeneously mixture is thermodynamically stable; (c) and (d) up-hill diffusion, the Gibbs free energy of the system is minimal when the atomic species are separated; (e) and (f) diffusion down the chemical potential gradients, from [127]

When a quenched homogeneous phase within miscibility gap is annealed, it becomes unstable with respect to phase separation into two phases with different compositions. The process takes place through spontaneous amplification of compositional fluctuation. Since the new phases form by a continuous process, interfaces between themselves and the parent matrix remain coherent during the

separation process. Therefore, spinodal decomposition is a process distinctly different from the nucleation-and-growth mechanism.

For the $Ti_{1-x}Al_xN$ solid solutions, a total energy gain results when thermal activation of the metastable state leads to decomposition. This is schematically represented in Figure 3-8 for the composition X_0. Any composition outside the spinodal domain lowers its free energy by the normal process of nucleation-and-growth through down-hill diffusion [113, 127].

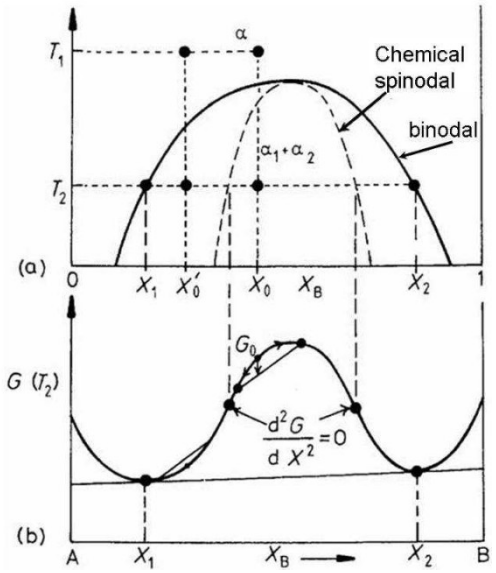

Figure 3-8 Binary phase diagram (a) with a miscibility gap and (b) corresponding free energy curve and chemical spinodal domain, from [127]

Spinodal decomposition in $Ti_{1-x}Al_xN$

Spinodal decomposition of $Ti_{1-x}Al_xN$ was reported in a number of papers [110, 118, 126, 129-130], which have shown that the wurtzite AlN_{hex} phase precipitates by phase decomposition. Recent research suggests that this process takes place in the volume of the $Ti_{1-x}Al_xN$ films at high temperatures, resulting in an increase in hardness of the film [27, 30, 126]. The temperature over which this decomposition process takes place is greatly influenced by the composition of the film [130-131]. With increase in Al content the phase separation process is initiated at lower temperatures; the $Ti_{0.75}Al_{0.25}N$ composition did not exhibit any sign of spinodal decomposition up to 1030 °C, whereas the $Ti_{0.34}Al_{0.66}N$ composition started decomposing at 900 °C after 120 min [27, 131]. Up to this temperature residual

stresses, which contribute significantly to the film hardness at low temperatures, relax. Despite this thermal relaxation, an increase in room temperature hardness is observed for $Ti_{0.34}Al_{0.66}N$ films annealed around 900 °C. The increased hardness seems to be attributed to coherency strains arising from lattice mismatch between TiN and AlN_{fcc} nanodomains [30, 130-131], strains that hinder the dislocation motion. If the annealing temperature is increased above a threshold value, the metastable AlN_{fcc} transforms into the thermodynamically-stable [wurtzite] AlN_{hex} structure. The transition AlN_{fcc} to AlN_{hex} is accompanied by an approximated 20% [132-134] increase in the unit cell volume. This increase triggers a sharp drop in the coating hardness [30]. Whereas, films with high aluminium content have a better (prolonged) oxidation resistance, they exhibit a lower transition temperature of metastable AlN_{fcc} to AlN_{hex}.

The crystallographic development with the temperature for plasma-assisted vapour deposited $Ti_{0.46}Al_{0.54}N$ was observed by atom probe investigations [126]. Figure 3-9 presents atom probe tomography images of spinodal decomposition and phase transformation.

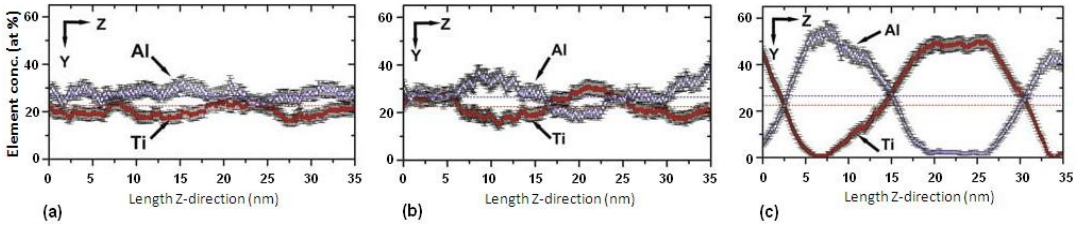

Figure 3-9 Ti and Al concentration profile with the increase in temperature for $Ti_{0.46}Al_{0.54}N$ composition; (a) as-deposited $Ti_{0.46}Al_{0.54}N$ exhibits a random distribution of Ti and Al atoms, with local fluctuations of the Ti and Al atoms in the opposite direction. (b) at 900 °C, Ti and Al started to separate, beginning to form an interconnected network of Ti and Al rich nanometre domains (cubic structure confirmed by XRD) separated by diffuse boundaries. (c) at 1350 °C a coarsened network of TiN and AlN suggests diffusion against the concentration gradient (uphill diffusion). XRD investigations revealed a completely decomposed structure with c-TiN and h-AlN and no c-$Ti_{1-x}Al_xN$ matrix, from [126].

3.6 Bulk TiN processing methods

Bulk single crystals TiN can be processed by direct nitridation of pure titanium, employing a zone annealing technique [135]. Bars of titanium (purity 99.9 %) of 6 millimetres thickness were passed through a heating-coil in the presence of nitrogen gas 99.9 % purity at a pressure of 2 MPa. The maximum temperature of the heating zone was approximately 2600 °C. Titanium bars were held vertically

in holders of boron nitride and travelled downwards relative to the heating coil. The growth rate, define as the moving rate of the specimen through the coil, was between 2 to 9 mm/h. The whole process takes place in a single operation. Large single crystal grains with the composition $TiN_{0.83}$ were obtained.

TiN polycrystalline bulk can be process from TiN powders, powders which are commonly produced by nitridation of titanium with nitrogen [136] or ammonia [137]. By sublimation-recondensation technique Du et al. produced TiN bulk crystals on tungsten substrates, with a stoichiometry of the crystals N/Ti ratio of 0.99 [138]. Graziani et al. processed polycrystalline TiN by hot pressing sintering of TiN powders. They showed that addition of metal dopants allows TiN to densify at lower temperature and in a reduced sintering time [139].

3.7 Thin film processing methods

As mention in the previous chapter, TiN ceramics have found industrial applications only in the form of thin films and $Ti_{1-x}Al_xN$ ceramics can be synthesised only by film deposition techniques. Because of that an overview of film deposition techniques is presented next.

Ceramic coatings can be synthesised by a wide range of deposition processes, which allow the deposited films to be tailored for their respective applications. The microstructure of coatings depends on how atoms are incorporated into the structure. During initial stages of film deposition at low energies a series of arrangement-reactions takes place at the substrate surface, processes which lead to the formation of clusters and nuclei; these processes are illustrated in Figure 3-10. The next adatoms adhere at the already formed clusters and nuclei, leading to an expansion of them. Clusters touch and coalesce to form islands. Monomers absorb on fresh exposed area leading to further nucleation till the surface is covered by the first layer of the film. Arrival of further atoms on top of the already deposited ones lead to growth of the film [140].

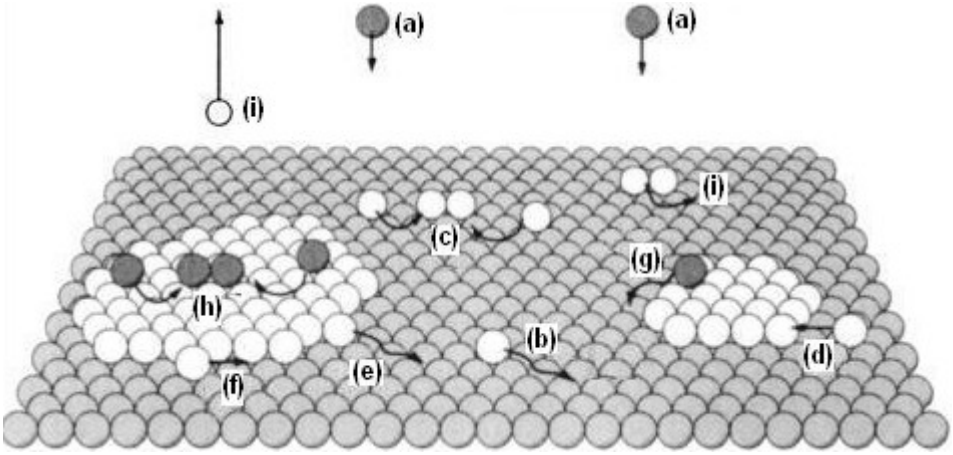

Figure 3-10 Typical atomistic processes during initial stages of epitaxial growth. (a) arriving atom at the substrate surface, (b) and (d) atoms diffuse along the surface to adhere to other atoms or to clusters, (c) adatoms form a dimmer, (e)(f) adatoms at the end of a cluster, from [140]

Structure Zone Models

The microstructure of deposited films is greatly influenced by the atomic diffusion of the deposited species, which is controlled by the substrate temperature. To correlate the resulting microstructure of films with deposition parameters, structure zones models (SZM) were developed [140].

Movchan and Demchishin introduced the SZM for vacuum deposited films [141]. They proposed three structure zones, each with its own characteristic structure and physical properties, depending on the ratio T_s/T_m; were T_s is substrate temperature and T_m is the melting temperature of the deposited material. Thornton improved the model by adding another deposition parameter, inert gas pressure. As the pressure of the sputtering gas is decreased in zone 1, a new zone, named T-zone, which makes the transition to zone 2, emerges. For deposition at high inert gas pressure, the adatom energy is diminished due to an increased number of collisions with the gas atoms along its path towards the substrate [142]. Figure 3-11 highlights the physical processes which govern each zone in Thornton's SZM.

Zone 1 is characterised by preferential growth on elevated regions, growth which results in a columnar microstructure of the deposited material, with open boundaries, due to surface roughness and geometrical shadowing. Tapered crystallites with high density of dislocations, pores and voids between dome shape crystals are present in this region. By increasing the substrate temperature, zone T

develops, which exhibits a dense columnar structure, a lower porosity and fibrous grains.

A further increase in the substrate temperature enhances the atomic surface diffusion. Zone 2 is dominated by the surface diffusion, which leads to a denser structure with coarser columnar grains.

In zone 3 the bulk diffusion has a dominant influence, leading to formation of large equiaxed grains. Recrystallization processes and polymorphic phase changes take place in this region [142-143].

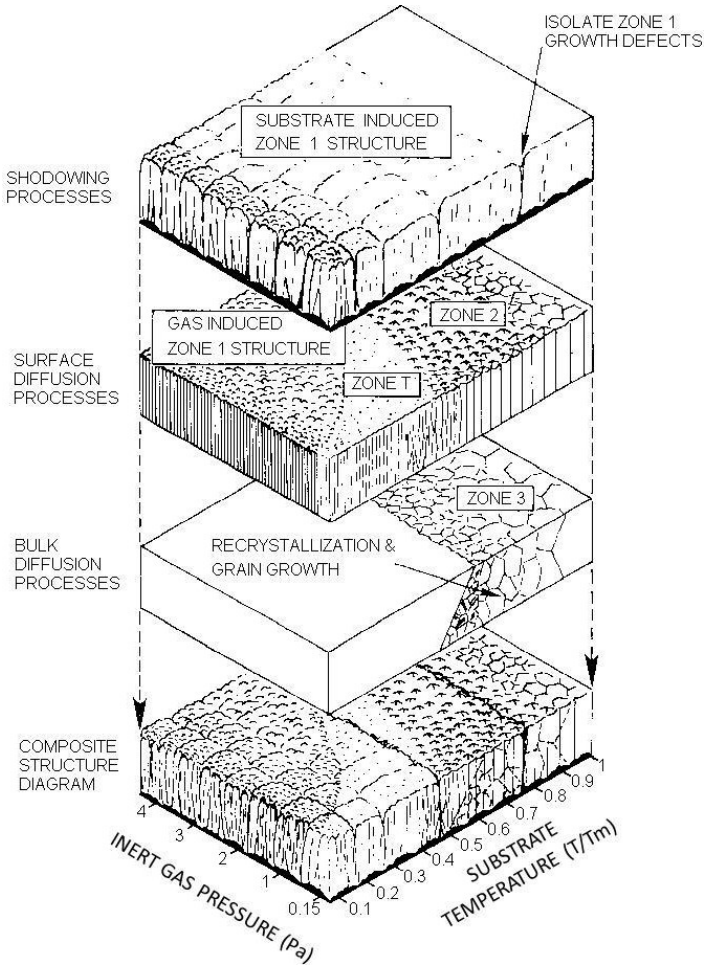

Figure 3-11 Thornton's structural zones models, from [142]

Messier et al. revised Thornton's SZM. The bombardment-induced mobility of the ionised deposited species was found to be a fundamental parameter which affects the film crystallography. It was shown that, a higher substrate bias increases the adatom surface diffusion, leading to a more compact structure. Consequently, a

new SZM model, which takes in consideration the substrate bias (V_s), emerged. The effects which result from the combination of varying the bias substrate and the inert gas pressure would lead towards a linear 1-T boundary, as can be seen from Figure 3-12 [144].

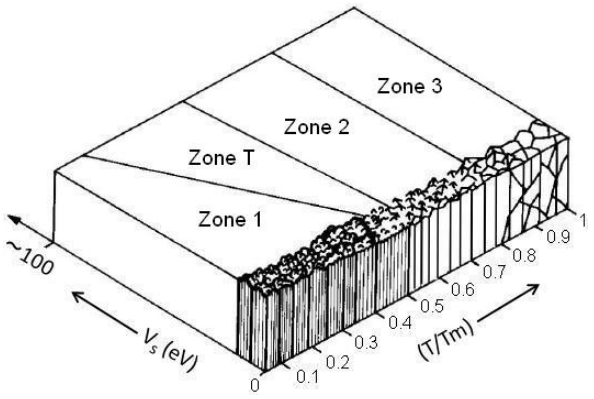

Figure 3-12 The effects of substrate bias (Vs) and thermal-induced mobility over the structure (SZM) of deposited films, from [144]

A more detailed discussion about thin film deposition techniques used for the synthesis of materials studied in this work is presented in the next chapter.

3.8 PVD coating deposition techniques

Physical vapour deposition (PVD) is a general term used to describe a variety of methods to deposit thin films by condensing a vaporized form of a material onto various surfaces called substrates. These thin-film deposition techniques involve controlled physical processes such as evaporation, condensation, sputtering, melting, implantation, etc.; processes which make it possible to synthesize structures at conditions far from thermodynamic equilibrium [111].

TiN and $Ti_{1-x}Al_xN$ coatings for high speed steel applications are commonly processed by PVD [6]. Pure titanium and aluminium are evaporated-sublimated in a flux of neutral and/or ionized atoms and reacted with nitrogen in a "high-energy vacuum" environment before deposition on a substrate. PVD techniques differ with respect to the type of evaporation process of the metallic components (which are deposited) and the plasma conditions employed during the deposition process [145].

An overview of the most employed PVD methods of processing titanium nitride coatings is shown in Table 3-2 where typical characteristics and the percentage of the ionised target atoms are compared. It is noticed that the cathodic arc evaporation process generates the highest quantity of ionized cathode atoms [145].

Table 3-2 Characteristics of various PVD processes, from [145-146]

Parameters	Processes			
	Magnetron sputtering	Anodic arc ion planting	Electron beam ion planting	Cathodic arc evaporation
Evaporation tool	Sputter effect	Electron beam	Electron beam	Thermal arc
Phase transformation	Solid-vapour	Solid-vapour	Liquid-vapour	Solid-vapour
Geometry of target/cathode	Flexible	Limited	Limited	Flexible
Ionised target atoms (%)	1-5	5-40	< 1	50 – 100
Additional ionization	Aimed	Unusual	Aimed	Not necessary
Inert gasses necessary	Yes	No	Variable	No

3.8.1 Cathodic arc evaporation

Cathodic arc evaporation deposition is a process in which a high current low voltage electric arc is used to vaporize material from a cathode (target), which is made from the elements to be deposited (Ti and Al in the present research). The place where the electric arc strikes is a highly energetic emitting area which is called the cathode spot. As a result, high velocity (10 km/s) [111] jets of vapourised cathode material are ejected from the target, leaving a crater behind on the cathode surface [147] as is shown in Figure 3-13.

To evenly erode the entire surface of the target, either the arc is rapidly moved by an applied electromagnetic field [148], or the cathodes are rotated during deposition [149]. The vaporized material is guided and accelerated towards the substrate by a negative bias applied to the substrate, which attracts positively charged ions [3, 150]. The whole system is kept in a vacuum chamber in order to allow the particles to travel as freely as possible [145, 151]. The first ionised particles to be deposited traverse the surface of the uncoated material breaking the

bonds between the atoms of the substrate surface. This process is known as plasma immersion ion implantation [111]. By forming a metallurgical bond to the substrate, the cathodic arc deposited films will not flake, blister, chip or peel [111]. During the deposition of the next layers, the already deposited atoms in the film suffer new series of knock-on which provide the accommodation and redistribution of atoms in the coating. This atomic accommodation, combined with fully ionised plasma and a low substrate temperature, offers the possibility to incorporate large fractions of Al atoms into the TiN structure.

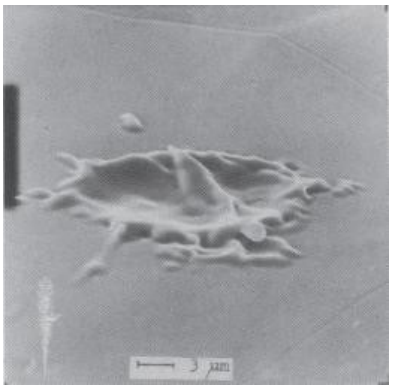

Figure 3-13 Crater on a Mo cathode formed within 10 ns since the electric arc strikes the target, from [152]

Each atom in the coating and at the film-substrate interface comes to rest with large amplitude vibrations around its new site, making it possible to synthesize structure at conditions far from thermodynamic equilibrium [111]. In addition, since particles are guided to follow a straight path, films deposited by physical means are commonly directional.

Whereas the applied field does not have a great influence over the atoms in the evaporated material (atoms are neutral from electric point of view), it has a strong influence over the ions, influence translated on the growth and morphology of the film. This is why the degree of plasma ionisation is a key parameter in the PVD processes.

A schematic representation of cathodic arc equipment is shown in Figure 3-14. If the vacuum chamber is fed with reactive gases (eg. nitrogen) during the evaporation process, dissociation, ionization and excitation can occur during interaction with the ion flux and compounds of the vaporised metal are formed on the path towards the substrate. When these vapour-state compounds get in contact

with the low-temperature substrate, condensation process takes place, forming a highly adherent thin film. The substrates are rotated in order to obtain a uniform thickness of the deposited material.

A drawback of the industrial cathodic arc deposition is that, the plasma beam ejected from the surface of the cathode target contains, among the ionised particles, some larger clusters of atoms or molecules (so called macro-particles or droplets), which prevent the deposited film from being useful for some applications [151-152]. These macro-particles affect the structure and the smoothness of the deposited films [150]. For small processes which require high quality production, magnetic field-filtering techniques are employed in order to minimize the presence of droplets [148]. Whereas, atoms and molecules do not respond to a magnetic field (because they have no charge), ionised particles exhibit a strong response. When plasma stream is bent by a magnetic field, atoms and relatively massive particles move along almost straight trajectories, exiting plasma flow. This way the droplets are removed from the plasma and are not deposited.

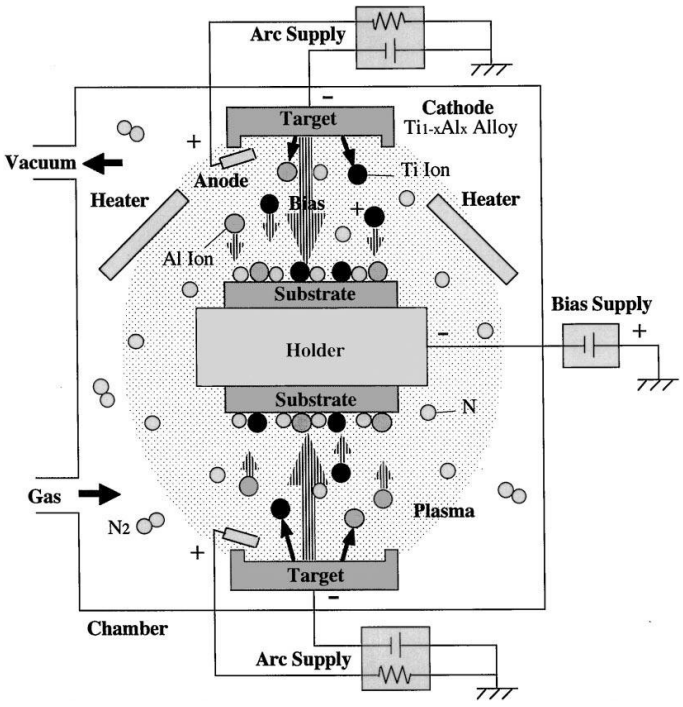

Figure 3-14 Section of a cathodic arc evaporation deposition chamber, from [114]

A filter that has been widely used in cathodic arc process is schematically shown in Figure 3-15. It consists of a 90° curved tube (the 'duct') which is surrounded by

magnetic field coils generating a curved axial field. The plasma transport and filter efficiency are improved by biasing the duct positively. New concepts and designs are under development, including twist-filters, electrostatic filters, and stroboscopic filters [148, 153-154].

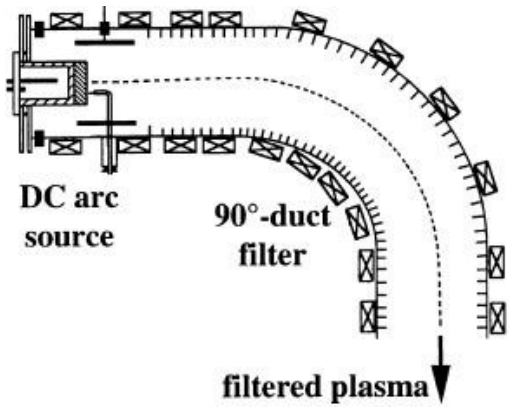

Figure 3-15 Aksenov's duct filter used to remove the neutral particles from the ionised stream during cathodic arc evaporation deposition, from [148]

3.8.2 Magnetron sputtering

Sputtering is a process of ejecting particles from a solid source, by means of collisions with incident ions of a working gas, e.g. Ar^+. In magnetron sputtering deposition process a discharge is established, in an argon plus nitrogen gas, between the anode and the cathode (target). The gas is ionised by electrons supplied by the cathode, following an applied anode-to-cathode voltage. Gas ions are accelerated to the target where sufficient momentum transfer enable sputtering away and ionising of the cathode material. The sputtered material lands on the substrate (anode), which faces the target at a distance of a few centimetres. The whole system is under vacuum. By introducing a reactive gas, e.g. nitrogen, in the deposition chamber, a wide range of coating compositions can be synthesized [155-156]. Increasing the gas pressure triggers a higher ionization rate at the expense of the deposition efficiency, which decreases as a result of the increased number of collisions (a decrease in the mean free electron path) and target poisoning. Therefore, the gas pressure (partial or total) has a great influence on the deposition rate, which in turn may affect the composition and structure of the film. A negative potential, known as the bias, might be applied to the substrate.

The bias raises the flux and energy of deposited particles, strongly affecting the coating growth, adhesion and structural density [157].

A magnetron component of a sputtering process is achieved by permanent magnets placed behind the target. These magnets create magnetic field lines, which restrain and guide the sputtering ions on cyclonical paths. Therefore, the sputtering is most intense in this region, resulting in a circular target erosion zone, as presented in Figure 3-16. Due to this plasma confinement the sputtering rate increases up to a factor ten, since only charged particles (and not ejected neutral atoms) are influenced by the magnetic field. This process allows the gas pressure to be lower, leading to a longer mean free path. Therefore, by using magnetron magnetic fields, the same deposition rate is achieved for a lower gas pressure [155, 158].

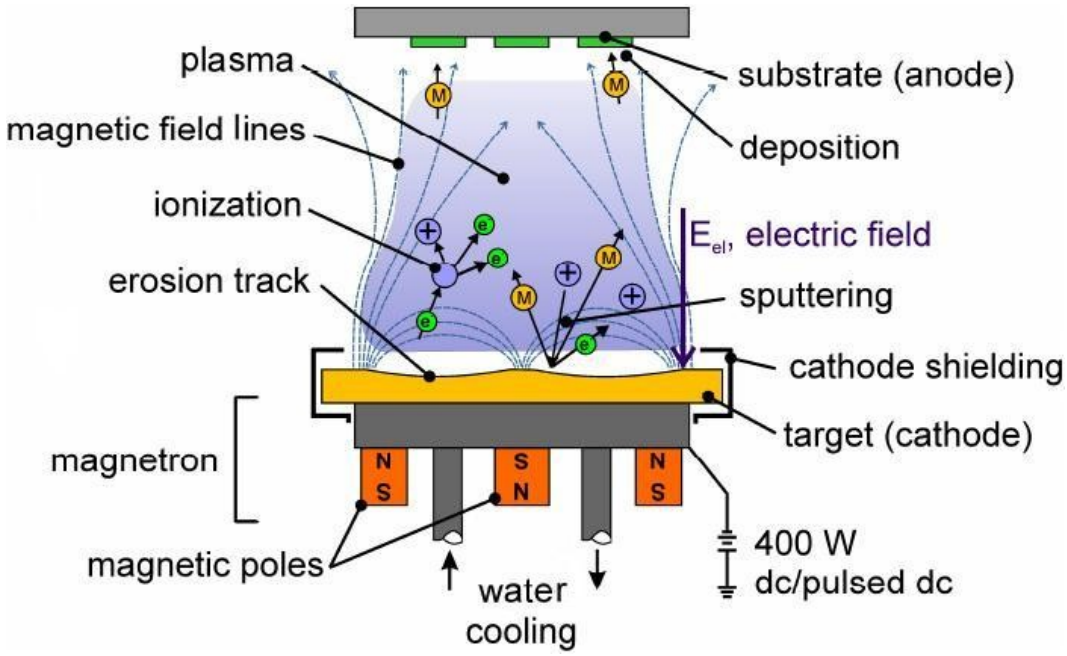

Figure 3-16 Schematic representation of magnetron sputtering system, from [113]

3.8.3 Chemical vapour deposition

Chemical vapour deposition (CVD) is a coating process in which chemical reactions take place at the substrate surface. Generally, this coating technique uses low pressure gas-phase precursors, often a halide or hydride of the elements to be

deposited [159-160]. An important distinction between CVD and PVD methods is the activation process required for the film growth and its consequent effects on the resulting microstructure. A CVD process employs heating the substrate to high temperature (~ 1000 °C), to facilitate the chemical reaction at the substrate. The film grows at thermodynamic equilibrium conditions by classical nucleation and grain growth, leading to a larger grain size with strong high angle grain boundaries and defect free grain interiors. Therefore, CVD deposited coatings are expected to have a morphology similar to bulk polycrystalline materials with well-defined grains, as observed in [2].

4 Properties of TiN and $Ti_{1-x}Al_xN$

The mechanical properties of TiN and $Ti_{1-x}Al_xN$ coatings are dependent on the morphology and the composition of the films, which, in turn, are governed by the process parameters [109]. Since different techniques and various deposition conditions are used for processing nitride films, the mechanical properties reported in literature spread over a wide range of values and the comparison of results can be difficult. Furthermore, it is clear the properties of these materials are very sensitive to deposition parameters. The main factors which influence the properties of these coating materials can be summarised as:

- Chemical composition (nonmetal-to-metal ratio).
- Crystallography (lattice type and lattice parameter).
- Morphology (columnar structure, epitaxial growing, density and distribution of voids and vacancies, grain size).
- Homogeneity of coatings (droplets, crystallographic domains).
- Internal stresses (compressive in-plane stresses, mismatch between the thermal expansion coefficient of the coating and the substrate material).
- Impurity concentration (especially argon and oxygen).

What is expected in the following chapter is knowledge of the characterisation problem, a reasonable attempt to understand the mechanical properties of TiN and $Ti_{1-x}Al_xN$ coatings and the way in which these properties are influenced by various deposition parameters.

4.1 Deformation of bulk polycrystalline TiN

Ductile to brittle behaviour of bulk polycrystalline TiN versus temperature was studied by Yamamoto and collaborators. Based on the electronegativity of atomic species they compared the deformation behaviour versus temperature for TiN, TiC and MgO; all three materials have the same cubic crystallographic structure. Up to around 1373 K TiN (obtained by isostatically pressed 30 nm diameter TiN powder) exhibits brittle fracture. This is explained by crack-extension from pre-existing flaws and by the absence of a sufficient number of independent slip systems. At a higher temperature, up to 1773 K TiN exhibits a quasi-brittle fracture. The combination of grain-boundary sliding and the $\{110\} < 110 >$ primary slip system allows a limited plastic deformation. This deformation leads to stress concentration (sharp cracks), stress that cannot be accommodated due to insufficient number of independent slip systems. Above the latter temperature, five independent slip systems are active; TiN becomes fully ductile, with the plastic deformation controlled by diffusion of nitrogen ions. This behaviour is shown in Figure 4-1. The Burgers vector of active dislocations in TiN was confirmed as $\frac{1}{2} < 110 >$ and the primary slip system $\{110\} < 110 >$ [40].

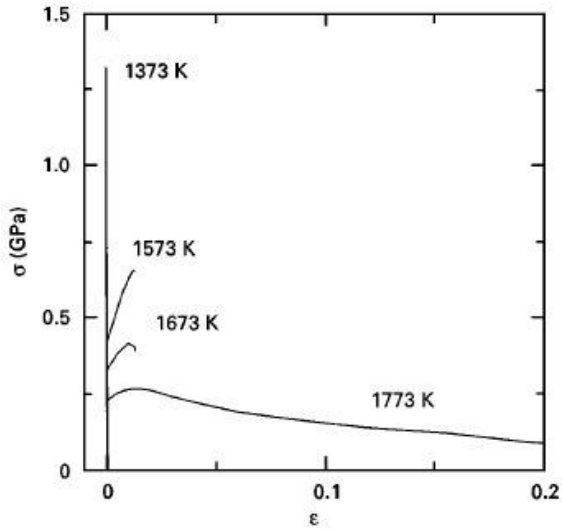

Figure 4-1 Stress versus plastic strain of polycrystalline TiN at various temperatures, from [40]

4.2 Mechanical properties of Single crystal TiN

The literature data regarding mechanical properties of bulk single crystal TiN seems to be very scarce. However, for the sake of comparison to the mechanical properties of $Ti_{1-x}Al_xN$ coatings, concise TiN film literature data is presented.

Mechanical properties of epitaxial (001), (011), and (111) oriented magnetron sputtered TiN films grown on single-crystal MgO wafers were determined [104]. Measured hardness values increased in the order (011) < (001) < (111). The authors explained the higher hardness of (111) orientation compared to (001) and (011) by considering the shear stress (τ) resolved on the primary slip system {110} < 1-10 >. The shear stress is directly related to Schmid factor through formula: $\tau = \sigma \cos \Phi \cos \lambda$, where σ is the applied stress which is approximately normal to the surface; the product $\cos \Phi \cos \lambda$ is the Schmid factor. Schmid factor values for TiN are 0, 0.25, and 0.5 for loading along (111), (011), and (001), respectively. "Thus, for plastic flow to occur in TiN (111) loaded normal to the surface, slip has to occur on a secondary slip system, which increases the hardness" [104]. However, the flow required to accommodate the multi-axial stress field created during indentation may cause deformation on both hard and soft slip systems and renders such data difficult to interpret [67]. Therefore, the above interpretation of TiN hardness should be treated with care, as it is difficult to isolate and investigate a slip system by nanoindentation.

4.2.1 The influence of nitrogen partial pressure on mechanical properties of TiN

The variation in chemical composition of films is translated in differences in mechanical properties. Torok et al. found that the elastic modulus of TiN films increases gradually with nitrogen content, reaching the maximum values at the stoichiometric composition [161]. O'Hern et al. showed a similar trend for elastic modulus with nitrogen content, whereas, TiN hardness does not exhibit a similar direct correlation with the stoichiometry. However, maximum hardness values were registered around Ti:N atomic ratio 1 [105]. These findings were confirmed by Shojaei and Karimi et al. in [106, 108], where a modification of the nitrogen partial pressure from 0.11 to 0.09 Pa enhances the hardness and elastic modulus of magnetron sputtered TiN films by about 30 %. However, these improvements in elastic properties are strongly affected by the deposition bias, as it is illustrated in

Figure 4-2 for two films deposited at different nitrogen partial pressure. Over-stoichiometric composition (Ti:N < 1) leads to lower hardness and elastic modulus values. Coarse grains with voids in the grain boundaries and, therefore, a lower internal stress, are promoted by the presence of too much nitrogen [106].

4.2.2 The influence of deposition bias on mechanical properties of TiN

The deposition bias has a significant importance in affecting the hardness of polycrystalline hard coatings. Generally, high energetic particle bombardment is known to suppress columnar growth structure resulting in an increase in the number of nucleation sites and a smaller grain size, which lead to denser and harder coatings [2, 106-109], [162]. The unbiased coatings exhibit an open columnar morphology with large voids, which results in low hardness and poor wear resistance.

It is well established that PVD TiN coatings, due to the nature of deposition process, can be in residual compressive stresses [163]. These stresses are a result of the shot peening events which proceed on an atomic scale by energetic particle bombardment during the growth of the PVD coatings. Therefore, internal compressive stresses build up in dense coatings synthesized at high deposition energies, whereas, in unbiased films the internal compressive stresses do not reach high values due to the presence of voids at the grain and columnar boundaries. Quinto showed that an increase in residual compressive stresses from -1 to -4 GPa led to an increase in microhardness toughness of PVD TiN coatings, from 2 to 8 MPa $m^{1/2}$, respectively. This was expected, since the residual compressive stresses counteract the tensile stresses required to generate and propagate a type I crack [163].

Residual compressive stresses increase up to a maximum value with increasing the negative bias. A further increase in the bias triggers a drop in residual compressive stresses, as shown in Figure 4-2 [106, 164]. Davis suggested that the apparent relaxation of the stress with increasing deposition energy over a threshold value is due to the defect annihilation processes occurring in the collision cascade in the growing film surface [165]. Alongside high hardness, increased deposition energy has a positive contribution towards the adhesion of

the film to substrate, due to the plasma immersion ion implantation process at the interface [111]. However, too large compressive stresses can cause delamination of the film [117].

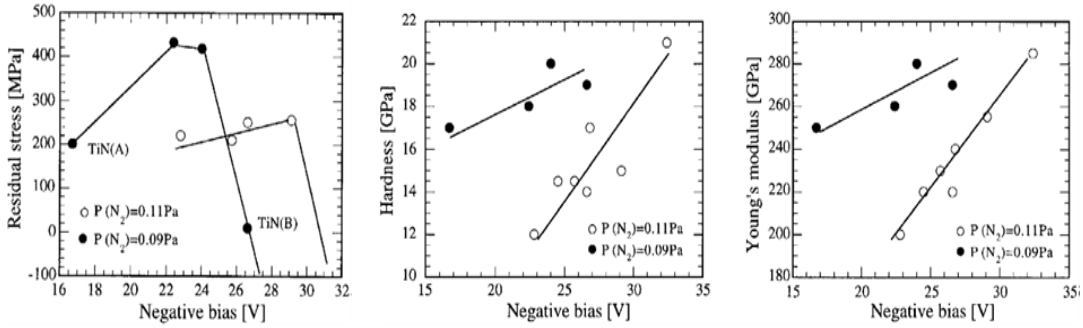

Figure 4-2 Variation of the residual stress, hardness and Young's modulus as a function of the substrate bias for two series of TiN films deposited at nitrogen partial pressure of 0.09 Pa and 1.1 Pa, from [106]

4.2.3 High temperature hardness of polycrystalline TiN

While it is convenient to measure the microhardness of materials at room temperature, it is often the corresponding high temperature microhardness which is more relevant in practical application. The industrial applications in which TiN and $Ti_{1-x}Al_xN$ coatings are employed encounter high temperatures. The cutting tool edge temperatures usually exceed 900 °C in continuous high speed dry cutting operations on hard materials [1-2]. Higher hardness at room temperature for this type of films is generally associated with a higher amount of residual stresses, which arise from two main sources: (1) high concentration of internal defects, (2) the thermal mismatch between film and substrate. These films are deposited at high temperatures and, upon cooling, thermal stresses develop due to difference in the thermal expansion coefficients of film and substrate.

With the increase in temperature, the residual stress in a film is known to relax through annihilation of deposition-induced lattice defects. In addition, the thermal stress present in the film is expected to diminish. Therefore, increasing the temperature should trigger a decrease in hardness values. Furthermore, the intrinsic material properties at elevated temperature are expected to change. Hence, it is sensible that, materials which encounter high temperatures in their applications to be studied at elevated temperatures. However, the limited literature data regarding the mechanical properties of TiN and $Ti_{1-x}Al_xN$ coatings at

elevated temperature suggests that very little research focused on this matter has been carried out.

Quinto et al. compare the high temperature hardness of CVD TiN coating and three PVD TiN coatings deposited by ion planting (IP), high rate magnetron sputtering (MS) and vacuum arc evaporation (AE) processes [2]. The hardness values dropped drastically with the increase in temperature, following an almost linear descending trend for all coating. At room temperature IP and MS deposited coatings exhibited hardness values of 23 GPa, compared to CVD and AE which measured 17 GPa. The difference in hardness values disappeared with increase in temperature, with all coating exhibiting only 5 GPa at 1000 °C. Interestingly, the substrate hardness at 1000 °C was also measured as 5 GPa.

However, a number of factors have to be taken into account when analysing these findings, and some of these factors are summarised next. The hardness of coatings was usually measured on a Vickers microhardness tester, based on the principle of penetration depth of a hard tip into the tested material. In order to remove the substrate influence on the hardness of the film, the penetration depth of the indenter must be less than one-tenth of the coating [166-167], which was not possible for most coatings when measured on a conventional microhardness tester. Nowadays high-accuracy nanoindentation equipment is on the market, which is able to precisely measure the hardness of sub-micron thick coatings.

Quinto and co-workers considered the true coating hardness being independent of the substrate hardness when the thickness of the coating is greater than Vickers indentation diagonal [163]. As the temperature increases the indentation depth increases as well. The nominal thickness of the tested films was between 8 and 16 μm and the hardness measurements were made using a 50 gf (490 mN) indentation load. At this load the indents are quite big and the substrate has a major influence on the hardness measurements. Furthermore, based on these micro-indentation experiments, the authors determined the fracture toughness of the coatings, K_{IC}, making use of the type I microcracks which emanate from the corners of the Vickers indents during indentation. As soon as a crack forms, the stress applied by the indenter is concentrated at the tip crack. Therefore, the measured hardness values did not reflect the real hardness of the coatings, but the hardness of the system coating-substrate. Furthermore, Bull et. al. showed that the

microcracks can already be present on indents performed on TiN coatings at only 15 gf [168].

4.3 Mechanical properties of $Ti_{1-x}Al_xN$

4.3.1 The influence of aluminium content on mechanical properties of $Ti_{1-x}Al_xN$ films

The amount of Al present in the film has a strong influence on the morphology and mechanical properties of these materials. Hardness is probably the most important property of $Ti_{1-x}Al_xN$ coatings for machining applications. Since the films are grown using various techniques and processes, the hardness of $Ti_{1-x}Al_xN$ coatings reported in the literature varied widely with values between 9.8 GPa [118] to 47 GPa [129]. The substitution of Ti atoms with Al atoms in the non-equilibrium cubic $Ti_{1-x}Al_xN$ structure leads to an increase in the hardness [30, 114, 125, 169]. This has been attributed to a change in the bonding character. The difference in the electronegativity between atomic species of titanium and nitrogen is 1.47, whereas between aluminium and nitrogen is 1.43. Therefore, replacement of Ti with Al leads to an increase in the covalent component of bonding in $Ti_{1-x}Al_xN$ compositions [103], which could explain the increase of indentation hardness.

Hardness values reach a maximum for an aluminium content around x = 0.6. A further addition of aluminium, leads to a decrease in hardness, as illustrated by the Figure 4-3 [114]. The cubic structure of cathodic-arc deposited $Ti_{1-x}Al_xN$ changed to a wurtzite structure around x = 0.6 - 0.7. This structural change triggers a sharp decrease in the hardness values. Similar results were found by Tanaka [125]. He also confirmed the change in the crystallographic structure from cubic B1 to hexagonal wurtzite when x increases over 0.6.

Superhard $Ti_{1-x}Al_xN$ unbalanced DC magnetron deposited films were processed by Musil and Hruby [129]. They measured hardness greater than 40 GPa for composition x = 0.5 - 0.6. The hardest films (47 GPa) have a composition of about 20 at.% Ti, 25 at.% Al and 55 at.% N, (111) preferential orientated grains with a size of approximately 30 nm. These films exhibit an AlN phase, precipitated along the grain boundary of cubic $Ti_{1-x}Al_xN$ (111) preferential orientated. For higher grain size, a loss in texture was noticed and the hardness decreased.

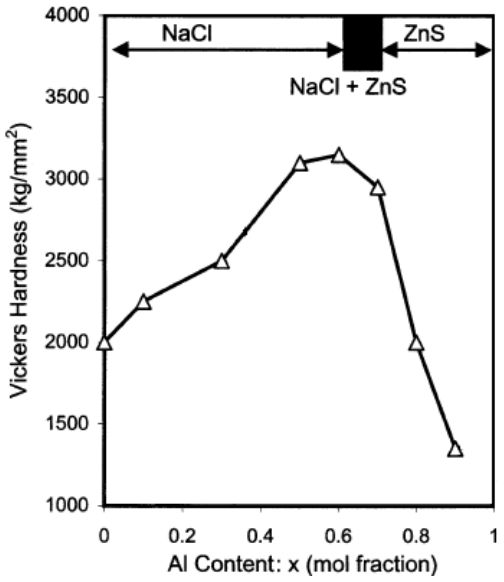

Figure 4-3 Variation of $Ti_{1-x}Al_xN$ hardness as a function of aluminium. For an aluminium content x = 0 – 0.6 the film has an fcc structure and hardness increases with the aluminium content. Beyond x = 0.7 the hexagonal wurtzite structure becomes more stable and hardness drops, from [170]

4.3.2 The influence of deposition bias on mechanical properties of $Ti_{1-x}Al_xN$ films

The applied negative substrate bias has a strong influence on the morphology and microstructure of $Ti_{1-x}Al_xN$ films [116-118]. Low deposition energies (< 80 V) led to a (200) preferred columnar structure with significant intragrain porosity, whereas, high substrate bias (140 V and 200 V) led to a smaller grain size and an interrupted columnar structure with a high defect density. In addition, high bias promotes a higher lattice parameter and a (111) growth orientation [117, 171-173]. Increasing the lattice parameter with bias has been reported in the literature to be attributed to the implantation of gas atoms in the interstices of the lattice [5, 103, 114]. Because of that, films synthesized at higher deposition energy are denser and exhibit higher internal compressive stresses, which in turn promote a higher hardness, compared to films synthesized at low deposition energies [117, 174]. In the same time, the change in orientation with the deposition bias seems to be also linked to the interstices of the lattice. The (111) growth orientation has been shown to exhibit the highest volume of interstitial voids, which accommodate the implanted gas atomic species in the structure [175].

One example regarding the correlation bias - properties for films with approximately the same atomic composition is presented (in values) in Table 4-1.

Table 4-1 Properties of $Ti_{1-x}Al_xN$ similar compositions films at various substrate bias values, from [117]

Substrate bias (V)	Hardness (GPa)	Young's Modulus (GPa)	Composition (at. %)		Lattice parameter (nm)	Residual stress (GPa)	Thickness (μm)
			Ti	Al			
40	33.8 ± 0.5	493 ± 12	26.6	23.6	0.4173	-1.69 ± 0.04	3.2
70	37.0 ± 2.3	445 ± 29	25.8	23.3	0.4225	-4.37 ± 0.22	3.0
100	35.9 ± 1.4	454 ± 15	26.0	23.1	0.4231	-5.05 ± 0.21	3.0
140	36.2 ± 1.7	446 ± 39	26.9	23.1	0.4231	-5.08 ± 0.06	1.6
200	**	**	27.0	24.0	0.4219	-5.59 ± 0.47	1.8

4.3.3 Effect of thermal treatment on hardness of $Ti_{1-x}Al_xN$

It has been shown that rich ternary coatings $Ti_{1-x}Al_xN$ exhibit a slight increase in room temperature hardness following an annealing treatment at high temperatures. This phenomenon was attributed to spinodal decomposition process during which, the single phase cubic $Ti_{1-x}Al_xN$ splits into two face central cubic crystallographic phases: TiN and stabilised AlN [176], resulting in a highly stressed crystallographic structure [177].

Horling et al. showed that room temperature hardness (~37 GPa) and texture of the as-deposited cathodic arc $Ti_{0.34}Al_{0.66}N$ coatings were retained after annealing at 950 °C for 2 hours [30]. The retention of hardness was attributed to the competing mechanisms between softening by residual stress relaxation through lattice defect annihilation and, hardening by the formation of a coherent nanocomposite structure of c-TiN and c-AlN. Further increases in the annealing temperature to 1100 °C for 2 hours lead to the formation of the softer hexagonal phase AlN. The hardness values taken after annealing at various temperatures are plotted inFigure **4-4**.

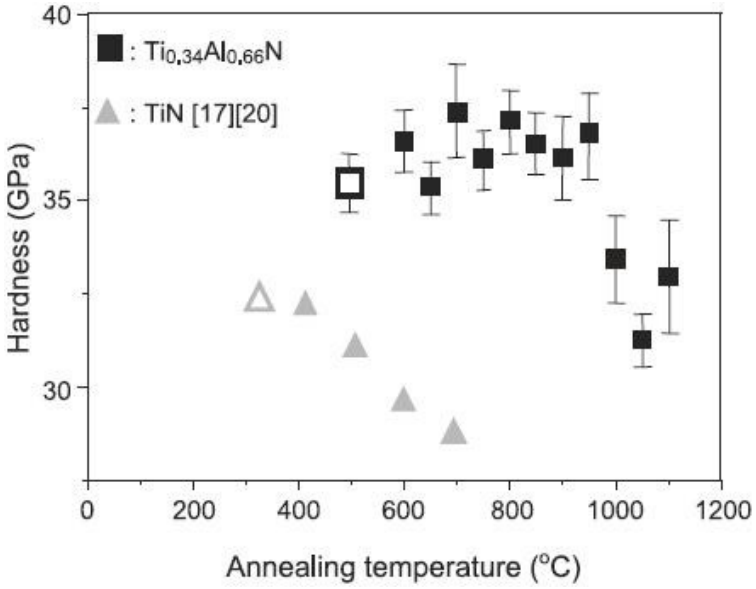

Figure 4-4 Hardness of $Ti_{0.34}Al_{0.66}N$ and TiN coatings versus thermal annealing temperature. Open symbols refer to as-deposited samples, from [30]

4.3.4 High temperature hardness of $Ti_{1-x}Al_xN$

Quinto et al. showed that the hardness values of magnetron sputtered $Ti_{1-x}Al_xN$ coatings (with x=0.25 and x=0.5) significantly dropped with the increase in temperature, following an almost linear descending trend [2]. The higher aluminium content exhibited slightly higher room temperature hardness than low aluminium composition. However, this difference disappeared with increase in temperature, and the hardness of coatings converged to the hardness corresponding to the substrate, of 5 GPa at 1000 °C. The nominal thickness of the tested films was 8 to 16 μm and the hardness measurements were made using a 50 gf (490 mN) indentation load. In addition, as the temperature increases the indentation depth increases.

In [168] it is shown that indents performed in TiN coating exhibits cracks at loads of 15 gf. Therefore, one might expect that at 50 gf loads the indents are quite big, the cracking of the coating is quite probable and the substrate has a major influence. Therefore, the measured hardness values probably did not reflect the real hardness of the coatings, but the hardness of the system coating-substrate.

Jindal et al. compared the behaviour of magnetron sputtered $Ti_{0.55}Al_{0.45}N$, TiN and TiCN films at various temperatures up to 1000 °C. The studied compositions

exhibited a decrease in hardness with the increase in the temperature, as can be seen in the Figure 4-5 [1]. The lower room temperature hardness exhibited by $Ti_{0.55}Al_{0.45}N$ film (compared to literature data) might be attributed to lower values of residual stress. However, the nominal thickness of the tested films was 3-3.5 μm and the hardness measurements were made using a 50 gf (490 mN) indentation load. As mention earlier, at these high loads the measured hardness values, probably, did not reflect the real hardness of the coatings.

However, since the substrate material was the same for all the tested films, the observed difference could be ascribed to the mechanical behaviour of the coatings. It was shown that titanium alloy nitride coatings exhibit higher microhardness than TiN coatings over the temperature range tested (25 °C to 1000 °C) [1].

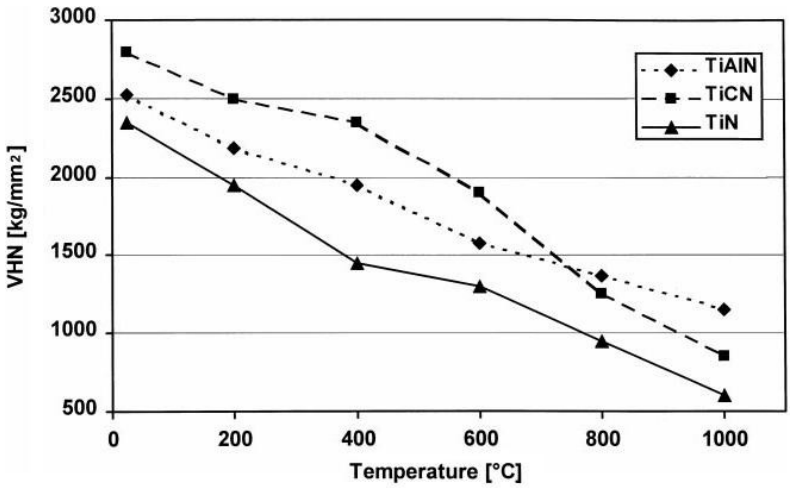

Figure 4-5 Vickers microhardness as function of temperature from 25 °C to 1000 °C for $Ti_{0.55}Al_{0.45}N$, TiN and TiCN, from [1]

A significant drop in hardness of cathodic arc ion-planting deposited $Ti_{0.50}Al_{0.50}N$ films with rising in temperature was registered by Beake et al. [178]. The films were deposited to a thickness of 3 - 3.5 μm on WC–Co cemented carbide. The indentation load was chosen to prevent substrate influence. Measurements at 500 °C revealed a hardness value of 15.4 GPa, corresponding to a 48 % drop in the room temperature hardness of $Ti_{0.50}Al_{0.50}N$ films.

5 Experimental techniques

In order to determine mechanical properties (hardness and elastic modulus) and to investigate the influence of temperature on the mechanical behaviour of studied materials, depth-sensing nanoindentation at moderately elevated temperatures was employed. To correlate the data from nanoindentation to crystalline structure and morphology of the films, and to gain a better understanding of the influence of deposition technique and processing parameters on properties of studied coatings, a combination off cross sectional TEM (XTEM), high resolution TEM (HRTEM), X-ray diffraction (XRD) and SEM imaging was performed.

5.1 Materials

The **bulk single crystal TiN** (TiN_{bulk}) was kindly provided by Prof. Dr. Leif Johansson, Linköping University, Sweden and it was prepared by zone-annealing technique presented in [135], from pure titanium and nitrogen, with crystal growth occurring in a single operation. The crystallographic orientation of the crystal was determined by EBSD analyses.

Magnetron sputtered $Ti_{1-x}Al_xN$ films were kindly provided by Prof. Dr. Paul Mayrhofer, Mountanuniversität Leoben, Austria. They were deposited on (001) magnesium oxide (MgO) single crystal, in a lab-scale magnetron sputter deposition plant to a thickness between 2 and 4 microns. MgO was chosen as a substrate because it is a high melting point hard material (Tm_{MgO}=2852 °C [179]) and has a comparable thermal expansion coefficient to TiN ($a_{TiN}=9.4x10^{-6}$ K^{-1} and $a_{MgO}=13x10^{-6}$ K^{-1} [180]), which allows for dimensional stability of the interface over various temperatures and therefore, preventing the exfoliation of the coating due to dilatation/contraction phenomena. Furthermore, MgO has the same crystal structure as TiN (cubic NaCl structure), with a good lattice constant match (a_{MgO}=0.4213 nm [181]), which allowed for the TiN to be epitaxially grown on MgO. The substrates samples (provided by CrysTec) were size 10x10x1 mm^3 and polished on both sides. They were ultrasonically cleaned for 10 minutes in acetone, then in ethanol to remove any residues of acetone before film deposition. The chemical composition of the coatings was determined by energy-dispersive X-ray spectroscopy (EDX) and the nominal compositions were: $Ti_{0.66}Al_{0.34}N$ (low

content Al film), $Ti_{0.48}Al_{0.52}N$ (intermediate Al film) and $Ti_{0.38}Al_{0.62}N$ (rich Al film). The standard deviation of these chemistries determined by EDX was less than 1 at %. The latter film was synthesised using a 50:50 Ti:Al target. To achieve the other two compositions, Ti pieces of 99.99% purity were physically added to the target. The target was cleaned, to insure there is no oxide layer on its surface, by pre-sputtering against a shutter, before every deposition process. The crystallinity of deposited films increases with increase in temperature, because thermal energy promotes surface and bulk diffusion, which allows for atoms to rearrange in low energy configurations [101, 142]. To promote an epitaxial growth of magnetron sputtered coatings to MgO substrates, the depositions were carried at 500°C. Hultman et al. have successfully deposited $Ti_{1-x}Al_xN$ coatings at similar temperature [94]. In order to facilitate a reliable comparison of samples, the applied substrates bias during deposition of $Ti_{1-x}Al_xN$ coatings (x = 0.34; 0.52; 0.62) was the same, – 60 V. TiN coating was deposited at a substrate bias of – 40 V. The base pressure before and after deposition was in the range of $5x10^{-6}$ mbar and $2x10^{-6}$ mbar, respectively. The working gas pressure was $0.4x10^{-2}$ mbar.

Industrial cathodic arc coatings were provided by SECO AB Sweden. They had a thickness of around 6 microns and were deposited on WC - 6% Co insertions, in an industrial plant. This substrate was chosen because WC - 6% Co is widely used in the bulk form as tool steel, and its dimensions were 13 x 13 x 5 mm^3. The industrial cathodic arc $Ti_{1-x}Al_xN$ coatings investigated in this work have three nominal compositions, x = 0.44; x = 0.6; x = 0.7, and they were determined by energy-dispersive X-ray spectroscopy (EDX). Each composition was deposited at three substrate biases: 20, 40 and 60 V. The temperature of the substrate was maintained at 500 °C during deposition of cathodic arc coatings. $Ti_{1-x}Al_xN$ specimens of 4 mm x 4 mm were cut by using a disk with diamond insertions.

5.2 Nanoindentation

Hardness is a measure of a material resistance to permanent deformation of its surface. There are several types of hardness measurements, depending on the form of surface disturbance: scratch hardness, impact hardness and indentation hardness. Conventional hardness technique (indentation) involves applying and removing a specific load onto a flat-smooth surface via an indenter probe, which

could be either a hard sphere (Brinell hardness), a cone (Rockwell hardness) or a pyramid (Vickers or Knoop hardness). As a consequence, an indent impression which has its area optically measured is left in the probed surface. The load applied to the indenter divided by either the unit area of plastic deformation (Brinell, Vickers) or to the projected area of the indentation impression in the plane of the surface (Meyer, Knoop) represents the respective hardness. The results are different and relate to the used method [58].

Nanoindentation (also known as depth-sensing indentation) is a relatively new technique used for characterising mechanical properties at a small scale (usually under micrometer size). For practical reasons, other means than direct observation of the hardness impressions were needed to measure contact areas since imaging very small indentations is both time-consuming and difficult. Pethica, Hutchings and Oliver suggested a method for determining hardness and the elastic modulus by nanoindentation without the need for measuring the indent areas by direct imaging [182]. The technique was subsequently improved by Oliver and Pharr [76] and is based on measured indentation load-displacement curves and a knowledge of the indenter geometry.

During experiment, the penetration depth of the indenter, the applied load and the elastic response of the material are continuously measured, yielding the load-displacement curve as shown in Figure 5-1.

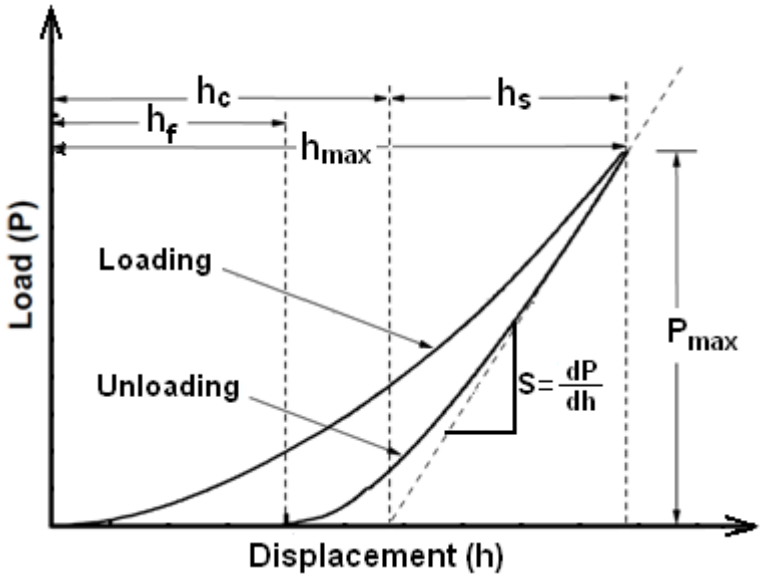

Figure 5-1 Typical load-displacement curve obtained from an instrumented nanoindentation experiment performed with a Berkovich indenter, showing important analysis parameters, from [76]

The indenter tip geometry represents a critical parameter in analytical procedure and it is characterised by the indenter area function, which is the cross sectional area of the indenter as a function of the distance from its tip. Even though the diamond has the highest hardness of all materials, tip blunting occurs during indentation experiments due to mechanical wear and/or the oxidation events occurring at elevated temperatures. Therefore, the geometry of the Berkovich diamond tip must be checked regularly.

Oliver and Pharr highlighted a few important observations from Stillwell's and Tabor's work [183]. Experiments performed with a spherical indenter produced an impression with a slightly larger radius than the radius of the indenter, and the impression formed by a conical indenter is still conical but with a larger included tip angle. During indentation loading the indenter sinks into the sample leading to elastic followed by plastic deformation of the specimen surface. During unloading, it is assumed that only the vertical elastic displacements recover, leaving a permanent impression in the material surface, as it is illustrated in Figure 5-2. The initial part of the unloading curve corresponds to the elastic recovery at which stage the diamond indenter is in constant contact area with the material and it was thought to be linear. Therefore, it represents the Hooke's law and allows one to calculate the corresponding elastic modulus. However, Oliver and Pharr showed that the unloading curve is not linear even in the initial stages, and its deviation from linearity should be accounted for. The unloading curve was fitted to a power low and the initial unloading slope could be determined by analytically differentiating this power low and evaluating the derivative at the maximum load/displacement points.

Other important observations include: (1) whereas the depth of the impression made by a conical indenter recovers during unloading, the diameter of the contact impression in the surface remains constant; (2) the contribution from non-rigid indenters on the load-displacement behaviour can be effectively accounted for by defining a reduced modulus, E_r, through the equation;

$$\frac{1}{E_r} = \frac{(1 - \upsilon^{\,2})}{E} + \frac{(1 - \upsilon_i^2)}{E_i} \tag{1}$$

where E, E_i are the elastic moduli of specimen and diamond; υ, υ_i, are the Poisson's ratio of specimen and diamond. In order to determine the elastic modulus of the tested material (E) from this relation, υ is presumed to be known and the E_r has to be determined.

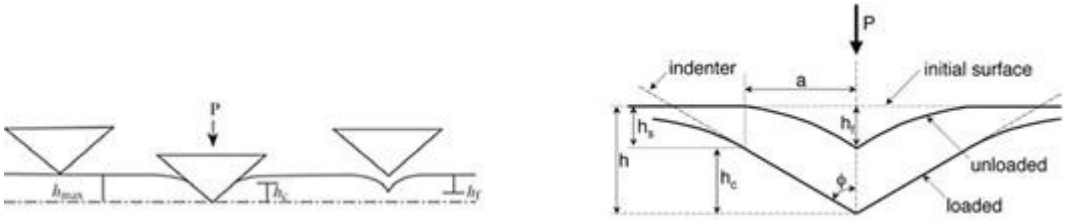

Figure 5-2 Schematic representation of the deformation geometry during indentation process [76]

The events occurring during the indentation cycle are schematically described by the load-displacement curve shown in Figure 5-1. The elastic-plastic response of the indented material, coupled with a functional relationship between the displacement of the indenter and the contact area, make possible the calculation of the hardness and elastic modulus. The data is analysed according to the following equations:

$$S = \frac{dP}{dh} = \beta \frac{2}{\sqrt{\pi}} E_r \sqrt{A} \tag{2}$$

The unloading stiffness (also known as the contact stiffness), S is defined as the slope of the initial portion of the unloading curve. P is the applied load, h is the indentation depth at P load, A is the projected contact area between the indenter and the specimen, β is a parameter which accounts for the deviation in stiffness corresponding to various indenter geometries. In order to calculate E_r the unloading stiffness and contact area must be determined.

An early model, proposed by Doerner and Nix [184], used a linear fit, as would be expected during indentation with a cylindrical punch indenter, to the upper part of the unloading curve to determine the stiffness [185]. However, Oliver and Pharr observed that the unloading response during indentations made by sharp-tip self-similar (conical/pyramidal) indenters is rather well described by the power law relation;

$$P = \alpha (h - h_f)^m \tag{3}$$

where h_f is the final residual depth of the indent impression. α and m are fitting constants and are determined by a least squares fitting exercise, which implies an initial guess for α, m and h_f. Then, an iterative procedure provides the best fit values for these parameters. The obtained relationship can then be differentiated to obtain the initial unloading slope (stiffness).

The contact area represents the cross-sectional area of the indenter as a function of the distance from its tip.

$$A = F(h_c) \tag{4}$$

where h_c is the contact depth between the indenter and the material. The function F is experimentally determined (prior or after experiment) and it accounts for the deviations from the ideal Berkovich indenter. For a perfect Berkovich geometry, the area function would be:

$$A(h_c) = 24.5h_c^2 \tag{5}$$

In order to determine the projected contact area, A, the contact depth, h_c, needs to be determined.

h_c can be calculated from the unloading stiffness. From Figure 5-2 it is noted that, h_c represent the intercept between the extrapolation (dotted line) of the initial unloading stiffness (determined from equation 3) and the displacement axes.

Alongside the elastic modulus, the hardness of the tested material can be determined by using the relation

$$H = \frac{P_{max}}{A(h_c)} \tag{6}$$

5.2.1 Sources of error in nanoindentation

Room temperature nanoindentation has become a ubiquitous technique for obtaining reliable mechanical properties measurements from micro-scale amount of material, including thin films. However, due to the sensitivity of the nanoindentation equipment, which allows for the investigation of mechanical

properties at depth of penetrations as small as several tens of nanometers, any kind of measurement errors could have a significant impact on the results. Because of that sources of errors should be taken in consideration. The main sources of error during nanoindentation tests could be classified in two categories:

(a) errors attributed to the stability and accuracy of measuring device, such as: initial depth of penetration, thermal drift, load and depth measurement, the indenter tip shape and the compliance of the measuring system, noise in the system, elastic constants of the indenter;
and
(b) errors attributed to the specimen, such as: surface roughness, sink-in/pile-up effects, artefacts and scatter of material properties.

In the following, a succinct discussion about main errors in nanoindentation is presented.

Initial depth of penetration

The first step in the determination of a reliable indentation stress-strain curve from the measured load displacement data is an accurate estimation of the point of effective initial contact. Every indentation test starts after the indenter makes contact with the surface of the specimen. If the tip is very sharp, the initial contact force (which is the minimum force detected by the instrument) causes the indenter to penetrate slightly into the specimen, penetration which is not measured by the equipment. This initial penetration depth is very small and can usually be neglected for large indents. However, for indents of around tens of nanometre depth the inaccuracy of surface detection becomes significant and should be taken into account [187]. One way to determine the initial penetration is by fitting a suitable regression curve to a number of initial points of the load-displacement curve and extrapolating it to zero load [188].

Surface roughness

Due to the very small surface deflections associated with nanoindentation, the roughness of the surface is a key factor affecting the analyses [189]. A smooth flat surface large enough to perform several indents is required in order to gather enough data to make statistically significant quantitative evaluation of the film

mechanical properties. Therefore, films which are not smooth should undergo a polishing treatment, with a minimum material removal. Nevertheless, even the best polishing will leave small asperities of several nanometers high. Furthermore, while reducing the surface roughness, the polishing may well induce a substantial modification of the surface of the specimen due to strain-hardening or cold-working, especially in metals [190-191]. Langitan and Lawn found that the flaw size resulted from polishing glass microscope slide is always a little less than the nominal size of the abrading particles [192].

Sink-in/pile-up of indented surface

Even if the surface is flat, the deflection of the surface during indentation should be taken in consideration. The contact area depends not only on the shape of the indenter but also on the elastic response of the material being indented. In some cases the volume of material displaced by the indenter pushes out to the side of the indenter and forms a pile-up of the material [188, 193-194]. The contact height increases above the sample surface. That results in some unaccounted area of contact supporting the load and a contact depth smaller than would be in the case without uplift [193-194]. For other cases, the displaced volume of material is accommodated by far-field elastic displacements, producing a sink-in of the surface in the indenter proximity. In this case the contact area is less than the cross-sectional area of the indenter tip at a certain depth. For materials that exhibit pile-up or sink-in, a correction parameter must be determined [194]. This parameter takes the form

$$\alpha = \frac{A_c}{A_i} \tag{7}$$

where A_c refers to the actual projected contact area, and A_i represents the cross-sectional area of the indenter at the depth recorded by the equipment. For pile-up indentation $\alpha > 1$, whereas, for sink-in indentation $\alpha < 1$. For ceramic materials the deflection takes the form of a sink-in and this is taken into account as shown in Oliver and Pharr analytical method [76]. Accounting for the pile-up induced error is difficult without a priori knowledge of the mechanical properties and work hardening behaviour of the material. An effective solution for determining the

actual projected contact area (A_c) is SEM imaging of the residual contact impression [194].

The indenter tip shape and DAF

As already mentioned, a significant source of error is represented by the deviation of the Berkovich diamond tip shape from the ideal pyramidal geometry. This is because the tip of any real indenter is rounded on a nanometer scale, with the effective radius of the order of tens of nanometers [187]. As a consequence, there is always a difference between the real penetration depth and the depth corresponding to an ideally sharp indenter. This difference is more significant for small indents. The initial stage of an indentation at very small loads with a blunt tip results in large elastic response of the material followed by plastic deformation. In extreme cases, a perfect elastic response can be obtained from the tested material, which is translated as an infinite hardness. This shortcoming is overcome by having a good knowledge of the indenter shape and this knowledge is incorporated in the DAF. If this function does not represent the indenter shape precisely enough, erroneous results can be obtained.

The procedure used for determining the DAF involves making indents over a wide range of depths in fused quartz. This material is chosen as it does not deform by dislocation motion, and, therefore, it does not exhibit indentation size effect. In addition, it is an elastically isotropic material; its elastic modulus is well known and independent of indentation depth. The contact areas and contact depths are then determined using equations (2)

$$S = \beta \frac{2}{\sqrt{\pi}} E_r \sqrt{A}$$

Contact stiffness S is the inverse of the specimen compliance (C_s) during elastic contact

$$S = \frac{1}{C_s} \tag{8}$$

and

$$C_s = C - C_f \tag{9}$$

where C is the total measured compliance and C_f is the loading frame compliance, which is usually provided by the maker of the equipment. However, if C and C_f are not known, a procedure for calculating them is presented in the next chapter.

By combining equations (2), (8) and (9) the total compliance becomes

$$C = C_f + \frac{\sqrt{\pi}}{2E_r}\frac{1}{\sqrt{A}} \tag{10}$$

E_r and A are the only unknown parameters. However, using the elastic constants of fused silica (E = 72 GPa, υ = 0.17) in conjunction with elastic constants of the diamond indenter E_i = 1141 GPa and υ_i = 0.07, the value of E_r can be determined from equation (1), which has the form

$$\frac{1}{E_r} = \frac{(1-\upsilon^{\,2})}{E} + \frac{(1-\upsilon_i^2)}{E_i}$$

The contact area and contact depth are then determined at various depths (using a range of applied loads) from equations (7) and (10), the latter one taking the form

$$A = \frac{\pi}{4}\frac{1}{E_r^2}\frac{1}{(C-C_f)^2} \tag{11}$$

To finally establish the area function, the A vs h_c data are plotted in a graph and an equation describing the graph if fitted to it.

The compliance of the measuring system

The frame compliance of the measuring system could represent a source of errors as well. The total displacement, h_t, recorded by the capacitor during indentation is the sum of the displacements in the specimen, h, and the total compliance of the system C. Therefore, the penetration depth of the indenter at any load, P, can be written:

$$h = h_t - C * P \tag{12}$$

If the apparent compliance of the system is higher than its true value, the penetration depth appears to be smaller. As a consequence, the calculated values of hardness and elastic modulus are higher than the real ones. Therefore, the value

of the system compliance should be precisely determined. Considering equation (10),

$$C = C_f + \frac{\sqrt{\pi}}{2E_r}\frac{1}{\sqrt{A}}$$

it is noted that, a graph of C vs $\sqrt{A}$ is linear for a given material, and the intercept of the graph with the vertical axes represents C_f. If the DAF is not known, the C_f can still be determined by following the technique developed by Oliver and Pharr [76]. They showed that, the best approximation of C_f can be obtained when $\sqrt{A}$ is big, which corresponds to large indents. For large indents the area function for a perfect Berkovich indenter can be used to provide a first estimate of the contact area. This way an initial estimate of the C_f is obtained, estimate which is inserted in equation (10) to determine the contact areas for a range of indentation loads. Then an initial guess of the DAF is made by plotting A against h_c and fitting them to the relationship

$$A(h_c) = 24.5\, h_c^2 + C_1 h_c^{10} + C_2 h_c^{\frac{1}{2}} + C_3 h_c^{\frac{1}{4}} + \cdots + C_8 h_c^{\frac{1}{128}} \qquad (13)$$

where C_1 through C_8 are constants which in conjunction with h_c^x describe deviations from the ideal Berkovich geometry due to blunting at the tip. The new value of A is inserted in equation (10) and a new C_f is obtained. The process is iterated till convergence is achieved.

Thermal drift analysis

When measuring the mechanical properties at such a small scale, the influence of the thermal drift should be accounted for. Thermal expansion or contraction of various parts of the loading frame results in a moving frame of reference, which is translated into thermal drift and subtracted from the final load-depth response. Therefore, common to all instrumented nanoindentation experiments is the need to minimise thermal and electronic drift. These artefacts superimpose the nanoindentation data in such a way that it is difficult to distinguish them from the response of the material and hence, it leads to miscalculations of material properties. In order to account for the thermal drift, measurements of

displacement at constant load are performed before and during the experiment. The displacements from these measurements are attributed to the thermal drift.

Depth and load calibration

The accuracy of load and displacement measurements is usually high in nanoindentation. However, the electronic components are sensitive and it is good practice to calibrate the equipment at regular times. There are two main calibrations in a nanoindenter, load and depth.

Load calibration establishes the forces which can be applied at the diamond tip during measurements. This calibration is performed by placing a set of known weights at the lower end of a vertical pendulum (Figure 5-3). An amount of electric current required by an electromagnetic actuator (located at the top end of the pendulum) to pull the pendulum in the vertical position is measured corresponding to each known mass. This way a linear relationship between the applied current and the load is established.

The depth calibration relates the change in capacitance to a known movement (displacement) of the sample in contact with the pendulum. The calibration routine involves moving a stiff reference sample in contact with the pendulum to known gradual displacements by a DC encoder motor. Corresponding change in capacitance signal is determined by a Wheatstone bridge arrangement with three known capacitances. A linear interpolation method is used to generate a calibration curve from the Capacitance versus Encoder displacement measurements. A capacitive transducer comprising of aluminium plates is used as a displacement gauge, therefore its calibration is very sensitive to the temperature fluctuations and surrounding environment (humidity, vibrations). The equipment is housed in a temperature and vibrations controlled chamber.

Artefacts and scatter of material properties

Due to the high sensitivity of the system, noise and various artefacts can influence the accuracy of the data, especially at the beginning of unloading, when a tortuous unloading curve could be obtained. Such an unloading response could be attributed to specimen creep or relaxation, phenomena which take place during the first few seconds of each unloading stage. Non-constant coefficient of friction and

stick-slip effects between the indenter and specimen could cause unevenness in the unloading curves, as well. These effects are mostly random in character and can never be totally excluded for such precise measurements, and at any loading or unloading step they can cause an error of several nanometers in depth determination. Taken in consideration that the tested volumes in these experiments are in the nanometer/micrometer range, these artefacts can mask the data in such a way that it becomes very hard to distinguish the real material response from these measurements.

The indenter tip properties

The elastic modulus of a material is calculated from the measured composite modulus, which is a function of both the specimen and the indenter modulus (equation(1)). An error in the indenter modulus thus causes an error in the specimen modulus, especially for materials with a high elastic modulus [187-188].

5.2.2 The equipment

The experiments were performed using a Nanotest Platform 2 instrument manufactured by Micromaterials Ltd, Wrexham, UK, equipped with a diamond Berkovich indenter, which is three sided pyramid geometry. This shape is chosen for its nominal geometric self-similarity, which makes for relatively simple analysis using the methods of continuum mechanics. Another advantage of this geometry is that the facets of a triangular pyramid meet in one point, resulting is a sharper indenter than a Vickers indenter, in which the four facets will always lead to a chisel shape at the tip. Due to the fine scale of indentation tests, a sharper indenter is desired.

A schematic representation of the equipment is presented in Figure 5-3. The main component of the nanoindenter is a pendulum based device that applies the load horizontally. The indenter tip is fixed to the lower end of the pendulum, which swings around of a frictionless pivot. The movement of the indenter tip is assumed, from geometrical considerations, to be in a straight line. A coil is mounted on the top of the pendulum and placed next to a permanent magnet. When the coil is supply with current it is attracted towards the permanent magnet and thus produces a motion of the pendulum which pushes the indenter into the sample surface.

The displacement of the diamond indenter tip is measured by a sensitive capacitive transducer with a resolution of 0.4 nm. The applied force is measured by the current supplied to the coil, with a resolution of 0.3 μN.

The equipment incorporates a dual heater arrangement, which comprises of a high temperature sample stage and a heated indenter. This type of arrangement was shown to significantly reduce the amount of the thermal drift in the measured indentation depth signal, compared to nanoindenters which have only the sample stage heated [88]. The temperature is measured by separate thermocouples. The indenter thermocouple is located approximately 1 mm from the indenter tip and the sample stage thermocouple is placed approximately 2 mm from the surface on which the sample was mounted with high temperature adhesive (FortaFix). A thermal shield is placed between the high-temperature sample stage and the loading head in order to minimise the heat transfer towards electronics. In order to further minimize the influence of temperature on the experiments, the temperature in the cabinet is maintained constant by means of a heater.

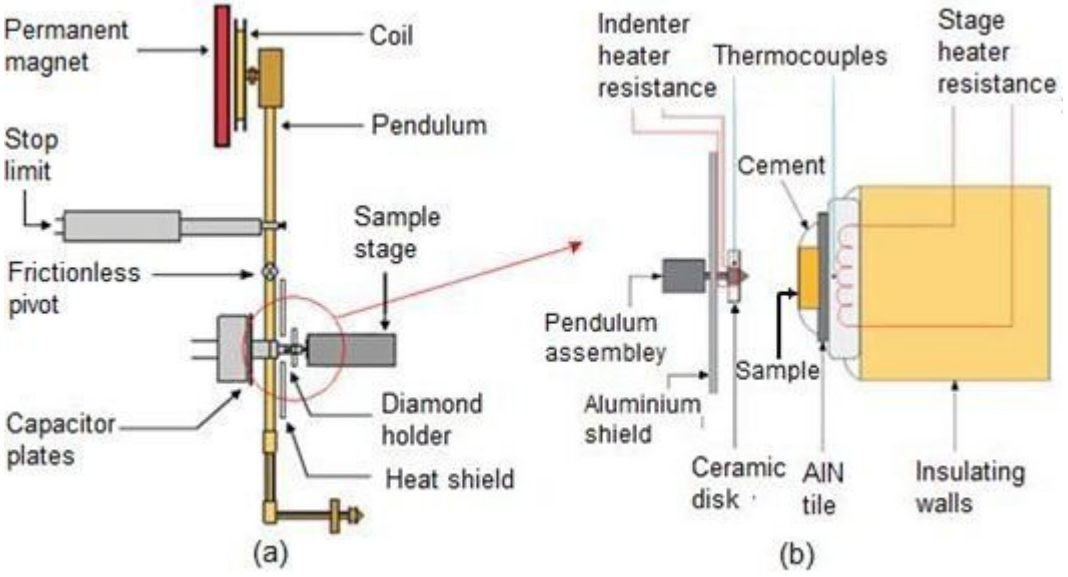

Figure 5-3 Schematic of the nanoindentation equipment Nanotest Platform 2: (a) the loading system, (b) detail of the temperature control system [88].

5.2.3 Sample preparation

The TiN_{bulk} and magnetron sputtered coatings had a mirror finish surface; hence, they did not necessitate a polishing treatment. However, the industrial cathodic arc coatings were rough and required polishing for nanoindentation. O'Hern et al.

performed nanoindentation experiments on TiN films which were polished using dimple equipment (commonly used for mechanically thinning of transmission electron microscopy specimens) fitted with a large diameter stainless steel polishing disk. This polishing technique produced smooth surface with slope of less than 2 degrees at the edge of the dimple region [105]. The authors determined that the error in the projected contact area due to the slope was less than 0.5%. In the present research the polishing was performed with diamond suspension of 0.25 μm at a small angle with regards to the initial film surface, producing a smooth flat area with a slope less than 1 degree. Therefore, the errors in the projected contact area due to polished slope are expected to be under 0.5%. The indents considered for analysis were performed on the thicker part of the film, which ensured the sampling of the material without effect from the substrate. A schematic of the geometry of the sample after polishing it is shown in Figure 5-4.

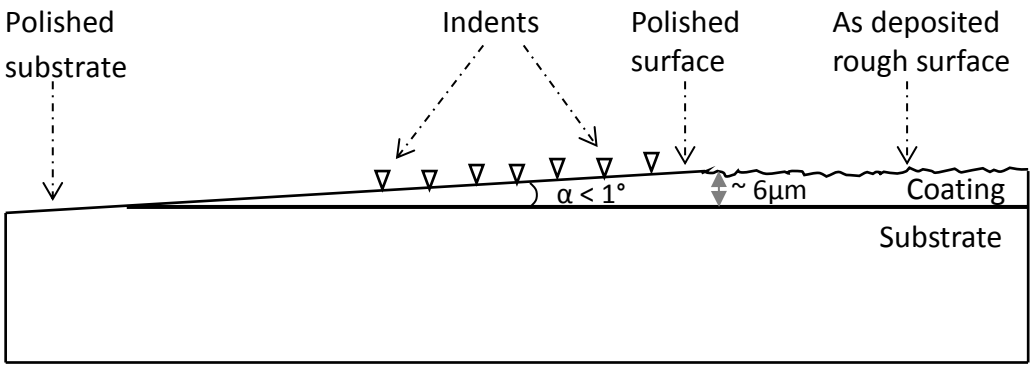

Figure 5-4 Schematic representation of the sample after polishing treatment. The indented region is highlighted by triangles.

A number of coatings were annealed in order to investigate the contribution of the deposition defects on mechanical properties and the influence of temperature on the structure. Isothermal annealing was carried out in argon atmosphere in a hot-wall quartz-tube furnace, with a constant temperature range of ± 5 °C. The coatings were subjected to temperatures of 600 °C to 800 °C for 24 hours. The heating rate was 20 K min^{-1} and the cooling was done by natural convection.

5.2.4 High temperature nanoindentation

Limitation of experimental temperature

Whereas nanoindentation at ambient temperature has become an established technique, characterisation of materials by nanoindentation at elevated

temperatures is still in its infancy. While it is convenient to measure the microhardness of materials at room temperature, it is often the corresponding high temperature microhardness which is more relevant in practical application. However, it is still very challenging to investigate these materials at their actual working temperature, which could reach more than 900 °C. In this work the maximum temperature of investigation by nanoindentation was limited to 350 °C, mainly by the stability of the diamond tip, as will be explained next. In addition, it has been shown that oxidation of these materials onsets around 500 °C for TiN and 700 °C for $Ti_{1-x}Al_xN$. As nanoindentation technique tests the surface at very shallow depths, approaching oxidation temperature increases the risk of indentation being performed in an oxide layer formed at the surface. Therefore, the data would reflect the properties of the oxide material and not of the under-layered ceramic material.

Despite the fact that the diamond is the hardest material known, it still wears out in time during indentations. The wearing process becomes more significant when indentation is performed in harder materials, as it was the case in this work. Furthermore, the wearing of the tip is accelerated by the increase in temperature, leading to a less sharp indenter tip. In this work, the geometry of the Berkovich diamond tip seemed to change at 350 °C. This change was confirmed by the different forms of the DAFs determined before and after experiments, as shown by the following relationships:

$$A(h_c)_{before} = 1512.279487 \times h_c + 17.633772 \times h_c^2$$

$$A(h_c)_{after} = 3075.953172 \times h_c + 17.976498 \times h_c^2$$

The wearing of the indenter was also reflected by fact that the hardness of the TiN_{bulk} (determined with initial DAF only) was the same at 350 °C to the one at 300 °C, as shown in Figure 5-5. The increase in hardness with the wearing of the indenter tip is attributed to the fact that a blunt tip penetrates less than a sharp tip, at the same applied load. In other words, for the same contact depth (h_c), an indentation performed with a blunt tip requires a higher load. As it is shown by the DAFs relationships, a blunter indenter yields a larger contact area for the same contact depth (h_c). If the DAF used corresponds to a sharp tip, while the

indentation is performed with a blunter tip, the contact depth would be underestimated and the resulting contact area would be smaller than in reality. A smaller contact area would mean a higher hardness, as $H = \frac{P_{max}}{A(h_c)}$.

In addition, the hardness at low load varies considerably compared to the hardness recorded for higher loads. This was attributed to the uncertainty in the real shape of the indenter. The effect of wearing of the indenter increased with decreasing indentation depth. Therefore, at very small loads the blunting of the tip may result in an exaggerated increase of hardness. This increase in hardness must be carefully distinguished from the indentation size effect. Consequently, knowing the real geometry of the indenter tip is an important prerequisite in nanoindentation [195].

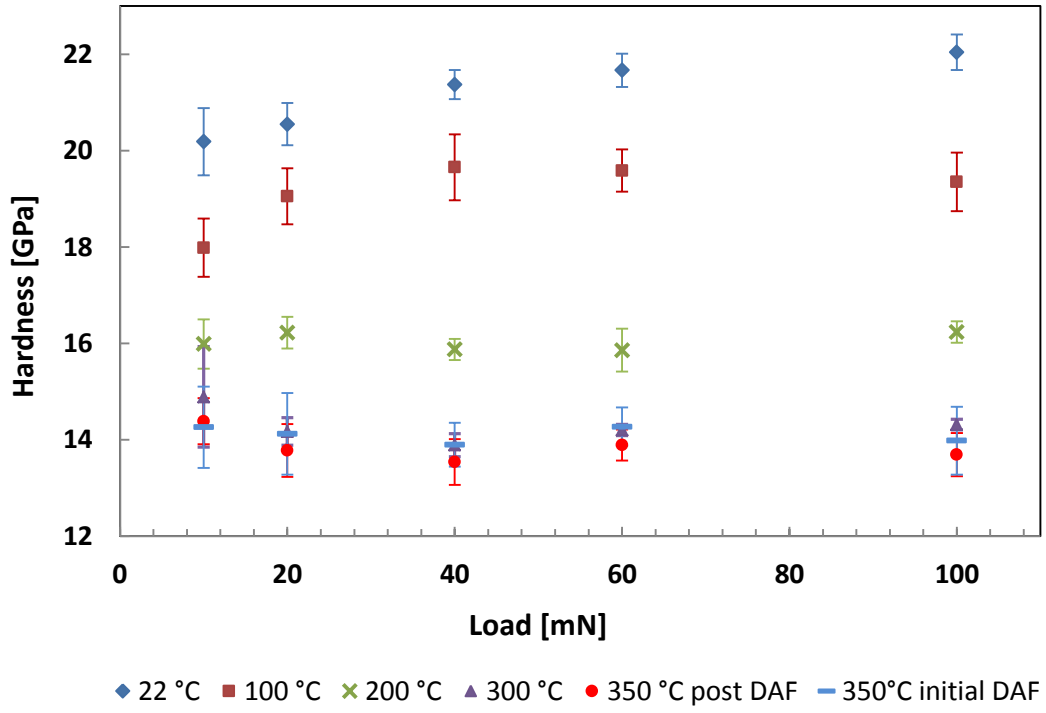

Figure 5-5 Hardness versus load for bulk single crystal (001) TiN at various temperatures. The wearing of the diamond tip led to the same or higher hardness values at 350 °C than at 300 °C. 10 indents were performed at each temperature and load.

DAF was determined before and after each set of indents done at high temperatures.

The equipment was calibrated before each series of HT indentations and a number of experiments at temperatures up to 350 °C were performed in fused silica, of

which mechanical properties variation with the temperature is well known [88, 196-199], in order to confirm the calibration.

Nanoindentation parameters for the bulk single crystal TiN

Nanoindentation experiments consisting of series of at least 10 indents have been performed at 5 temperatures: RT (22 °C), 100 °C, 200 °C, 300 °C and 350 °C, on the TiN_{bulk}. The loading rate for each indentation experiment was set that the maximum load, which was between 10 and 100 mN, was reached in 20 seconds.

Nanoindentation parameters for TiN and $Ti_{1-x}Al_xN$ films

In addition to the wearing of the tip, the influence of the thermal drift becomes more significant with decreasing the indent size. Furthermore, as already mentioned, the potential errors due to the initial depth of contact and surface roughness are more significant for indents performed at small loads. Because of the above mentioned issues, indentation experiments consisting of series of at least 10 indents have been performed on coatings RT, 100 °C, 200 °C and 300 °C, with a minimum applied load of 20 mN. Furthermore, after each high temperature series of experiments, a new DAF was determined and the results at 300 °C were reanalysed with the new DAF to assess the differences that might have arisen from the change in the tip geometry.

Magnetron sputtered coatings were indented at 50 mN load, whereas the cathodic arc evaporated films were indented at 20mN, 40 mN and 60 mN. During data analyses, the maximum loads were carefully selected to ensure that all experiments fulfil the criterion $d/t \leq 0.1$; where d is the depth of penetration of the diamond indenter into the coating and t is the thickness of the coating. The fact that the indentation depth increases with the temperature has been considered.

Thermal drift

It is crucial that the indenter and the sample have both reached stable temperatures when the experiments are started as otherwise the thermal drift can reach high enough values to render the data collected unusable. Each indentation cycle was preceded by 120 seconds thermalisation time while the sample and the indenter were in contact at a small load. During the last 60 seconds a thermal drift

measurement was performed. After thermalisation the indentation load was increased at the predetermined maximum values. The maximum load was maintained for up to 60 seconds followed by unloading at the same rate used for loading. A post-indentation thermal drift measurement was performed during unloading at 10% of the maximum load. An analysis of the influence of temperature on the post-indentation thermal drift recorded during indentation in TiN_{bulk} and TiN film is presented in the Figure 5-6, in which it can be seen that with increase in temperature the thermal drift increases. In addition, the standard deviation increases significantly with temperature. Another observation was that, the thermal drift did not follow a trend with temperature; it went up, as well as, down in values with the temperature, exhibiting a random character.

The measured average thermal drift for the TiN_{bulk} at RT was -0.02 nm/s and increased to 0.097 nm/s at 350 °C. The lowest rate of change of indentation depth with time during the loading stage of the test was encountered in experiments performed at RT and was of the order of 6 to 10 nm/s. Hence, the rate of indentation depth increase was at least two orders of magnitude larger than the instrumental drift. Above RT the thermal drift increased. However, as temperature increased, the rate of penetration of the indenter increased, so the error attributed to drift was again of the same order. Therefore, the average contribution of thermal drift to plastic depth in these experiments was very small.

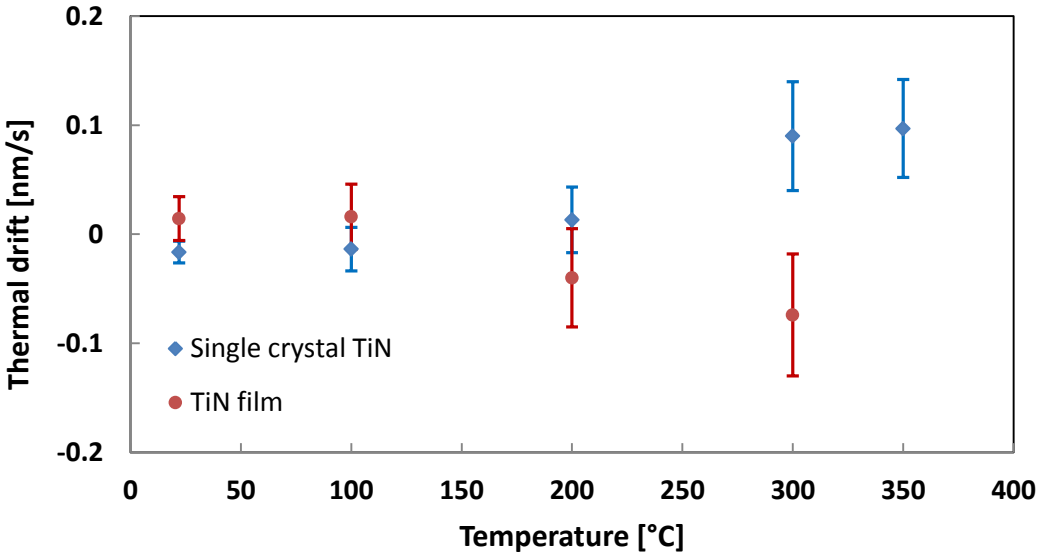

Figure 5-6 The variation of the post-indentation thermal drift with temperature extracted from 10 indentation experiments performed at each temperature on the TiN_{bulk} and TiN_{film}.

For a reliable analysis of the data, only indents which exhibited values of the thermal drift between -0.05 and 0.05 nm/s at RT and 100°C and, between -0.15 and 0.15 nm/s at 200 °C and 300 °C were considered in the analysis.

The consistency of the results obtained from nanoindentation experiments can be appreciated from the repeatability of the load-displacement data, as shown in Figure 5-7 for two series of 10 indents performed at RT and 350 °C, respectively.

The variation of $Ti_{1-x}Al_xN$ hardness and Young's modulus as a function of film composition, substrate bias and indentation temperature is presented in the results chapter.

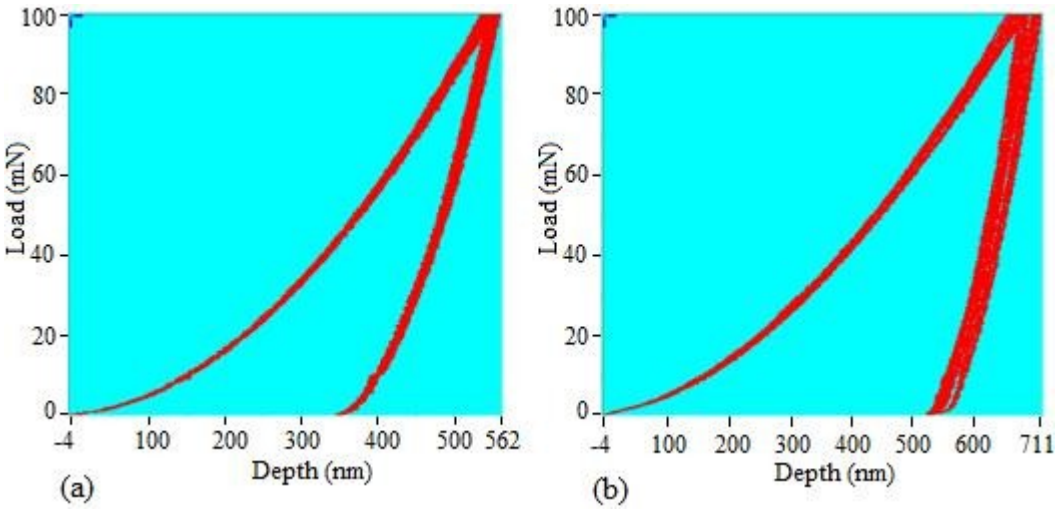

Figure 5-7 Load-displacement curves illustrating the consistency of the nanoindentation data. Series of 10 indents at 100 mN load performed on single crystal (001) TiN at 22 °C (a) and 350 °C (b). The average thermal drift was -0.008 nm/sec and +0.139 nm/sec, respectively.

5.3 Transmission Electron Microscopy

The structure of the coatings was analysed using a combination of transmission electron microscopy (TEM) and high-resolution TEM (HRTEM). The analyses were performed on JEOL 2000 and JEOL 2010 electron microscopes fitted with a LaB_6 source and operated at an accelerated voltage of 200 kV, and on FEI TITAN 80/300 TEM/STEM instrument operated at 300 kV. Bright field (BF), center dark field (CDF) and select area diffraction pattern (SADP) were used to characterise the plastic deformation under the performed nanoindents at various temperatures, the crystallography and phase transformation in studied materials.

TEM is a versatile microscopy technique used to characterise materials from atomic scale to micrometer level. It works by illuminating a very thin specimen with a broad beam of electrons (incident beam) which has a uniform intensity over the illuminated area. The electron is a negatively charged low-mass, which exhibits both, particle and wave characteristics. Because it carries a charge, it can easily be deflected by passing close to other electrons or the positive nucleus of an atom. As the electrons travel through the specimen they either interact with the atoms or they may remain unaffected. The ones which interact can change both their amplitudes and their phases as they traverse the specimen and both types of change can give rise to image contrast. The end result is a non-uniform distribution of electrons (transmitted electrons) emerging from the exit surface of the specimen. It is this non-uniform distribution that contains all the structural, chemical, and other information about the specimen.

An image is formed from the transmitted electrons, which is then magnified and focused on an imaging device (phosphorus screen or a CCD camera). A number of phenomena can be examined by TEM, including: dislocation activity, shear localization, crystallographic phase composition and crystallographic phase transformation. In the following the main TEM techniques used are briefly presented.

TEM has two modes of operation; one is imaging mode, in which the spatial distribution of scattering can be observed as contrast in images of the specimen; second is diffraction mode, in which the angular distribution of diffracted electrons can be viewed in the form of diffraction patterns (DP). The information extracted from the two modes of operation complements each other. Because of that, the image should be accompanied most of the time by the corresponding DP. In order to increase the contrast in the image and to avoid various artefacts due to the variation in thickness or buckling of the sample, a specific area of interest is selected by means of an aperture (see Figure 5-8). Under these conditions, only electron beams which are closer to the optic-axis are allowed to form images and DPs. Any electron that hits the specimen outside the area defined by the virtual aperture will hit the diaphragm when it travels onto the image plane. Such electrons will thus be excluded from contributing to the images and DPs.

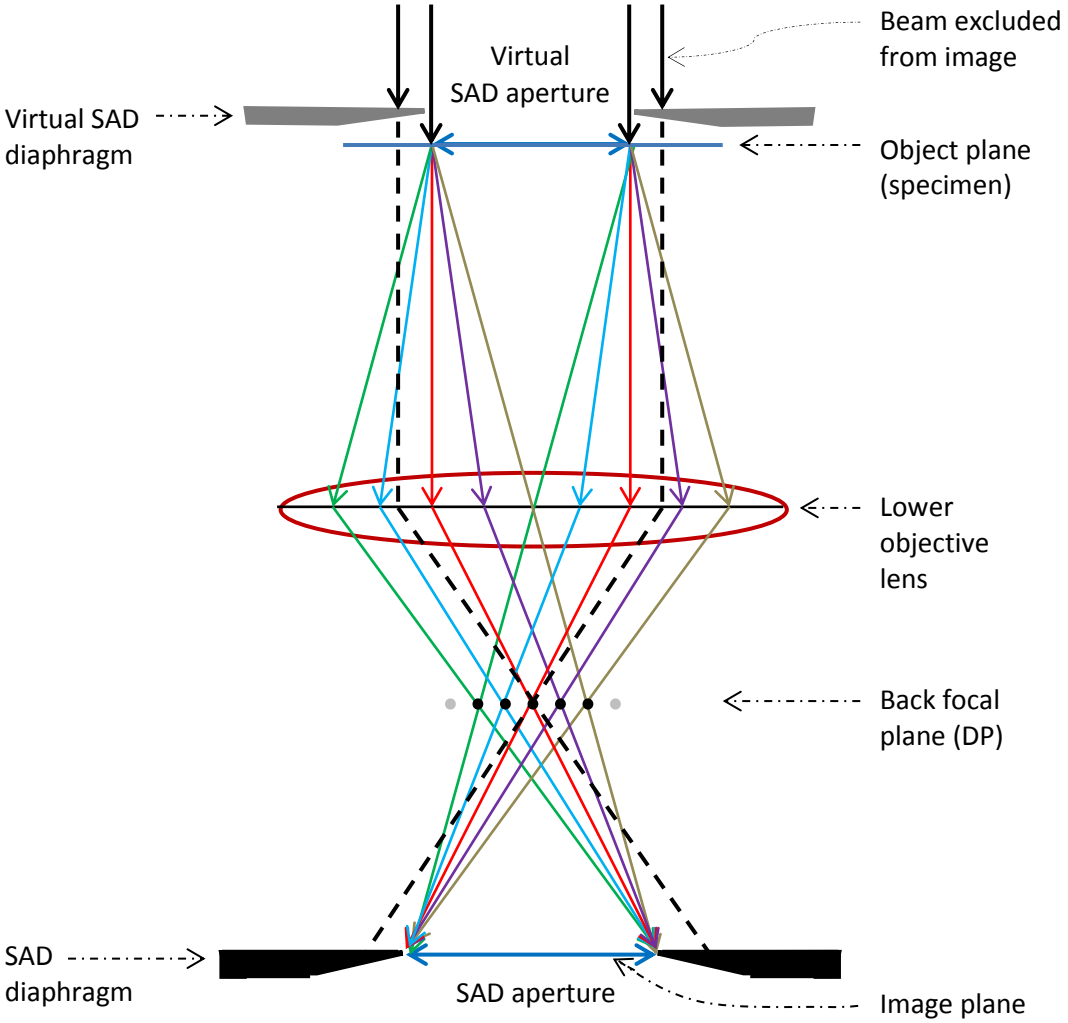

Figure 5-8 Ray diagram showing SADP formation. The selection of an area of the specimen is done by inserting an aperture in the image plane, which results in the creation of a virtual aperture in the plane of the specimen. Only electrons passing through the virtual aperture are allowed to form images and DPs [200].

Electrons passing through a thin specimen are separated by means of an aperture (objective aperture) into those that suffer no deviation from their incident direction and those scattered at variable measurable angles. Electrons, which at exit have the same initial direction, form the direct beam, whereas the other electrons form the diffracted beams. If the specimen is thin enough, it is sensible to consider that an electron either undergoes a single-scattering event or it suffers no scattering [200].

A fundamental operational step in the TEM is the use of restricting apertures (or/and an electron detector) to select which electrons will be used and thus controlling what information will be present in the image. When a selected area diffracted pattern (SADP) is projected on the screen/display, each individual beam

or a number of beams can be selected to form the final image. If the objective aperture is placed on the optic-axis to select the direct beam, a bright field (BF) image is formed by the selected electrons (Figure 5-9 A). If the objective aperture is placed off optic-axis to select a diffracted beam, a dark field image can be formed (Figure 5-9 B). If the incident electron beam is tilted to bring a diffracted beam on the optic-axis and the objective aperture is placed on the optic-axis, a centered dark field image (CDF) is formed (Figure 5-9 C).

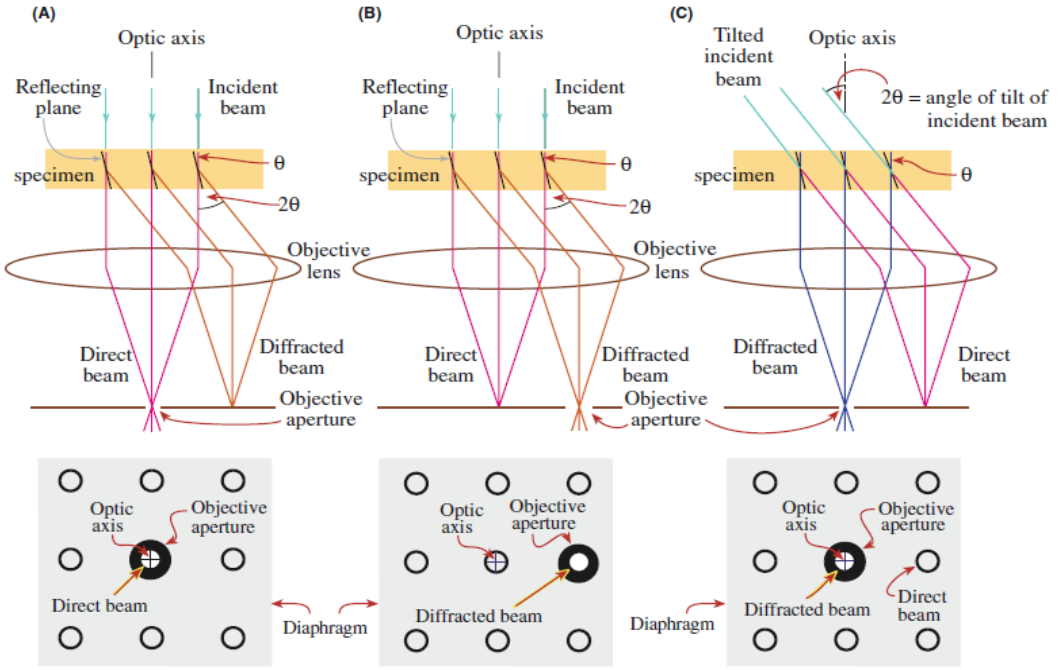

Figure 5-9 Ray diagrams showing how the objective aperture is used to produce (A) a BF image (the direct electron beam is selected), (B) a DADF image, and (C) a CDF image where the incident beam is tilted so that a particular diffracted beam is centered on the optic axis. A schematic of the DP corresponding to each case is shown below each ray diagram [200].

Alongside BF, CDF and SADP techniques, *Fresnel contrast analysis* was performed in order to image voids, microcracks, areas of porosity and to position the specimen at the right height during lattice fringes imaging. This technique makes use of the interference phenomenon which appears when electrons experience a phase shift as they pass through specimen. This phase shift occurs in any situation where the inner potential changes abruptly. In areas with constant chemistry and crystallographic structure, only the specimen thickness variation could promote an electron phase shift. The specimen thickness changes could be attributed to abrupt variations in surface topography or to voids within the foil, voids which decrease the effective thickness [200-201]. The phase shift, $\Delta\varphi$, is described by the relation:

$$\Delta\varphi = KV_0 t$$

where K is a constant, V_0 is the mean inner potential of the crystal and t is the thickness of the sample. The electrons which have suffered various phase shifts interfere with each other giving rise to fringes. The intensity of the fringes at position x, away from the phase shift is given by:

$$I(x) = 1 + \frac{\lambda \Delta}{2\pi}\varphi''(x)$$

where λ is the electrons wavelength and Δ is the defocus. When the image is in focus ($\Delta = 0$) the intensity of the fringes is unity and the Fresnel fringe contrast is not observable [201]. Therefore, to image voids or small gas-filled cavities within the thickness of the specimen, the images must be taken out of focus. An illustration of Fresnel contrast is shown in Figure 5-10.

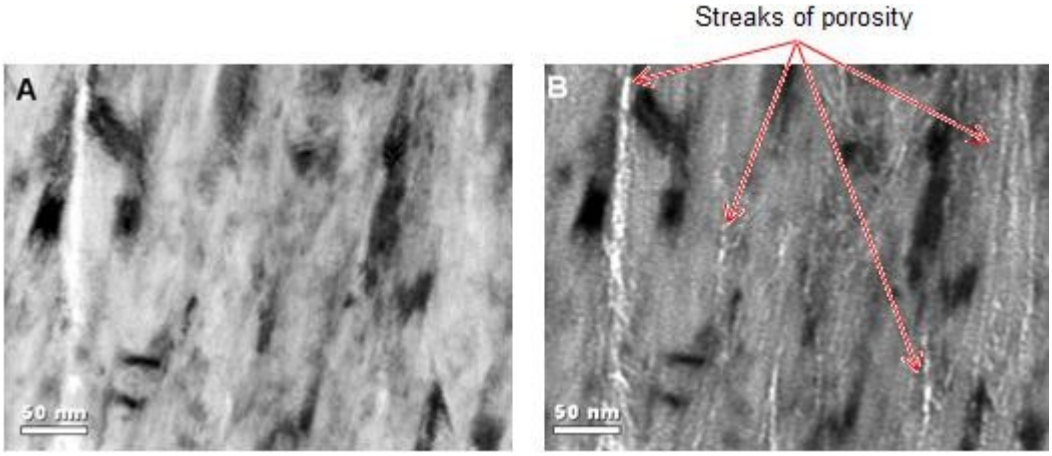

Figure 5-10 Cross section BF images (of $Ti_{0.38}Al_{0.62}N$ thin film) taken at focus (A) and underfocus (B) conditions from the same area. The porosity was barely observable in the image taken at focus condition, whereas, at the underfocused conditions, the Fresnel contrast highlighted the porosity as white streaks.

5.4 Focus ion beam

Focused ion beam (FIB) is an experimental technique particularly used in the semiconductor industry and materials science for site-specific analysis, deposition and ablation of materials. One of the most important applications of FIB systems is sample preparation for TEM.

An FIB instrument looks and operates much like a scanning electron microscope (SEM). These instruments rely on a focused beam which strikes the sample in order to create an image of the specimen; a FIB uses an ion beam, whereas, an SEM uses an electron beam. For both instruments the intensity of secondary electrons produced at each raster position of the beam is displayed to create an image of the specimen. In the FIB, secondary ions may also be detected and used to form an image of the specimen [202-204].

Accurate imaging, milling and deposition, makes FIB the only TEM sample preparation technique that can be employed on a scale ranging from a few tens of nanometres to hundreds of micrometres. Using a FIB, one is able to determine the precise location of the cross section (in the submicron range), and an arbitrary number of subsequent cross section TEM samples can be made on the same bulk, with minimum material loss. FIB enables cross sections preparation in a much shorter time than in the traditional TEM sample preparation [202].
The issue of preferential milling between different materials is nearly negligible in FIB processing. Because of that, focus ion beam is equally used for TEM sample preparation from single crystals, polycrystalline and multiphase materials containing one or more atomic species. In addition, FIB is equally suited for cross-section and plan view TEM specimen preparation [204].
In this work the *ex-situ lift out* and *in-situ lift out* (FIB techniques) were used to prepare TEM specimen. These lift-out techniques are differentiated by the way the TEM membrane is attached to the TEM grid.

Ex-situ lift-out technique

The first steps are: finding the area of interest and deposition of a metal protective layer on the surface. A stair-step trench is then milled out on one side of the deposited metal strip and a rectangular trench is milled away on the other side of the metal line (Figure 5-11 (a)), using a high beam current (15 - 21 nA) and acceleration voltage (30 kV). The lamella is subsequently thinned to ~ 1 – 2 μm with smaller ion beam current (6.5 nA). Then the stage is tilted 45°, allowing for the sample to be visualized from the lateral (see Figure 5-11 (b)). The bottom, one end and a portion of the other end of the membrane is cut. At this stage the membrane is attached to the bulk material only by a small bridge left on one side.

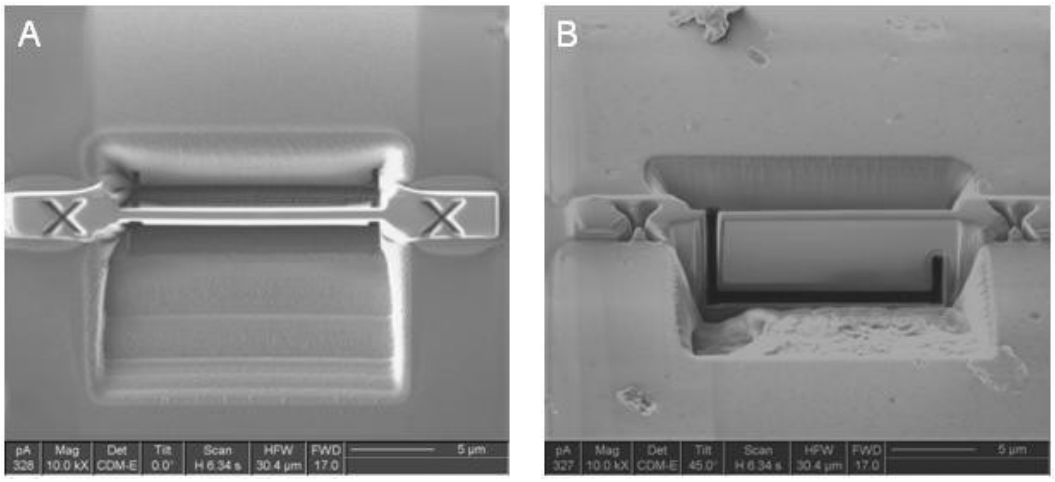

Figure 5-11 The first stages of the ex-situ lift-out technique for TEM sample preparation. (a) The crosses milled in the Pt deposited layers are required by the Wizard software which recognises their location in order to set the position and parameters of the ion beam during automatic milling. The stair-step trench and the rectangular one are milled on the either side of the Pt strip. (b) The tilted sample at 45° and the cuts which leave the sample suspended on the bulk material by a small bridge on the right side.

The sample is tilted back and thinned with a 0.92 nA followed by a 93 pA beam current at 5 kV acceleration voltage, to electron transparency (see Figura 5-12 (a)). The thickness of the sample is measured using the software tools and when it is thin enough the bridge which links the sample to the bulk is cut. The electron transparent membrane falls free in the trough or sticks to the walls of the trenches, due to electrostatic charges, as shown in Figure 5-12 (b). Once the sample is cut free, a further thinning of it cannot be performed.

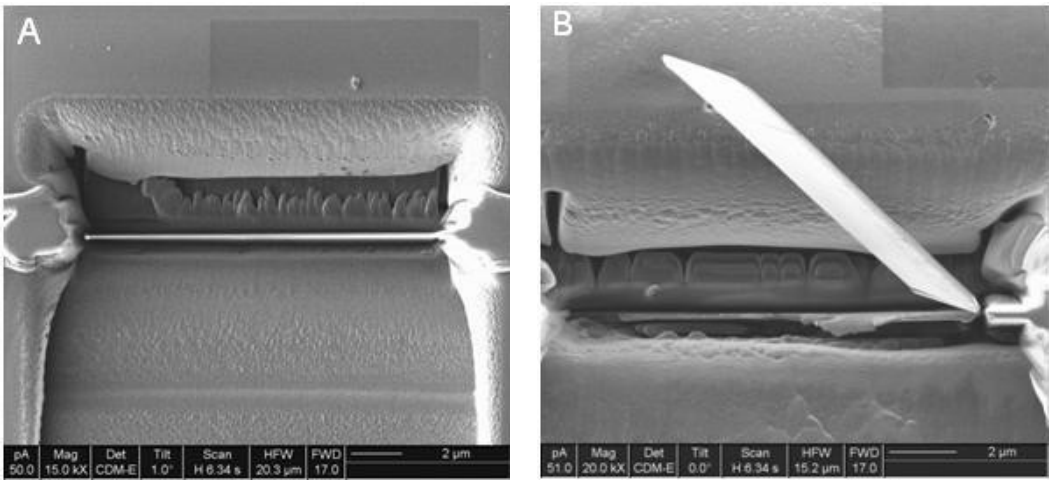

Figure 5-12 Final stages of milling in ex-situ lift-out technique. (a) The thinned sample imaged from top, before is cut free from the bulk and (b) the free standing sample lining on the rectangular trench-wall, after the bridge was cut free.

The bulk sample is removed from the FIB vacuum chamber and is viewed using on an optical microscope that has an objective lens with a large working distance, as presented in Figure 5-13.

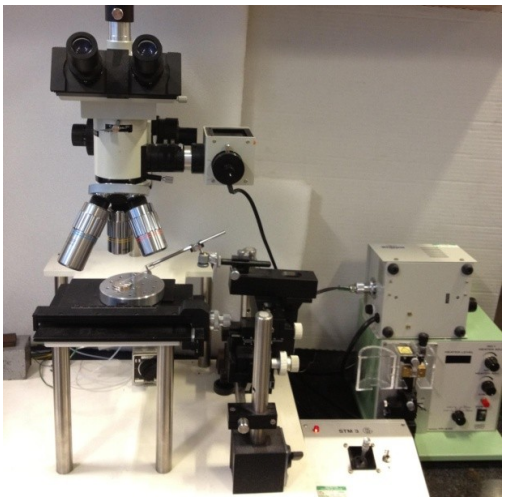

Figure 5-13 The equipment used in the ex-situ lift out TEM sample preparation for transferring the TEM sample from the bulk material to the TEM grid.

An electrical or hydraulic micromanipulator is used to transfer the TEM sample from the trough onto a TEM grid. A very sharp glass tip of the order of a few microns is inserted into the micromanipulator arm. The tip is brought in the proximity of the TEM membrane and electrostatic forces allow the membrane to stick to the glass needle [204]. The needle is gently moved in the proximity of a carbon coated TEM mesh grid where the sample is placed. However, the transfer of the sample from bulk to the TEM grid has a quite high potential risk of losing the specimen. Too much electrostatic charge can make difficult to unload the specimen on the TEM grid. Once the sample is laid on the grid it can be examined on the TEM.

The in-situ lift-out technique

The first steps of in-situ lift out technique are similar to the ex-situ lift out. The feature of interest is found and a metal layer is deposited on the surface (Figure 5-14 (a) and (b)) to protect the site of interest.

Trenches are milled on either side of metal strip with a 21 nA beam current at an acceleration voltage of 30 kV. The lamella is then thinned to ~ 2 μm and then the sample is tilted at 45°. The bottom, one end and a portion of the other end of the

lamella is cut free (Figure 5-14 (c) and (d)). A micromanipulator is used to bring a tungsten needle in the proximity of the free cut side of the specimen, as shown in Figure 5-14 (d) and (e).

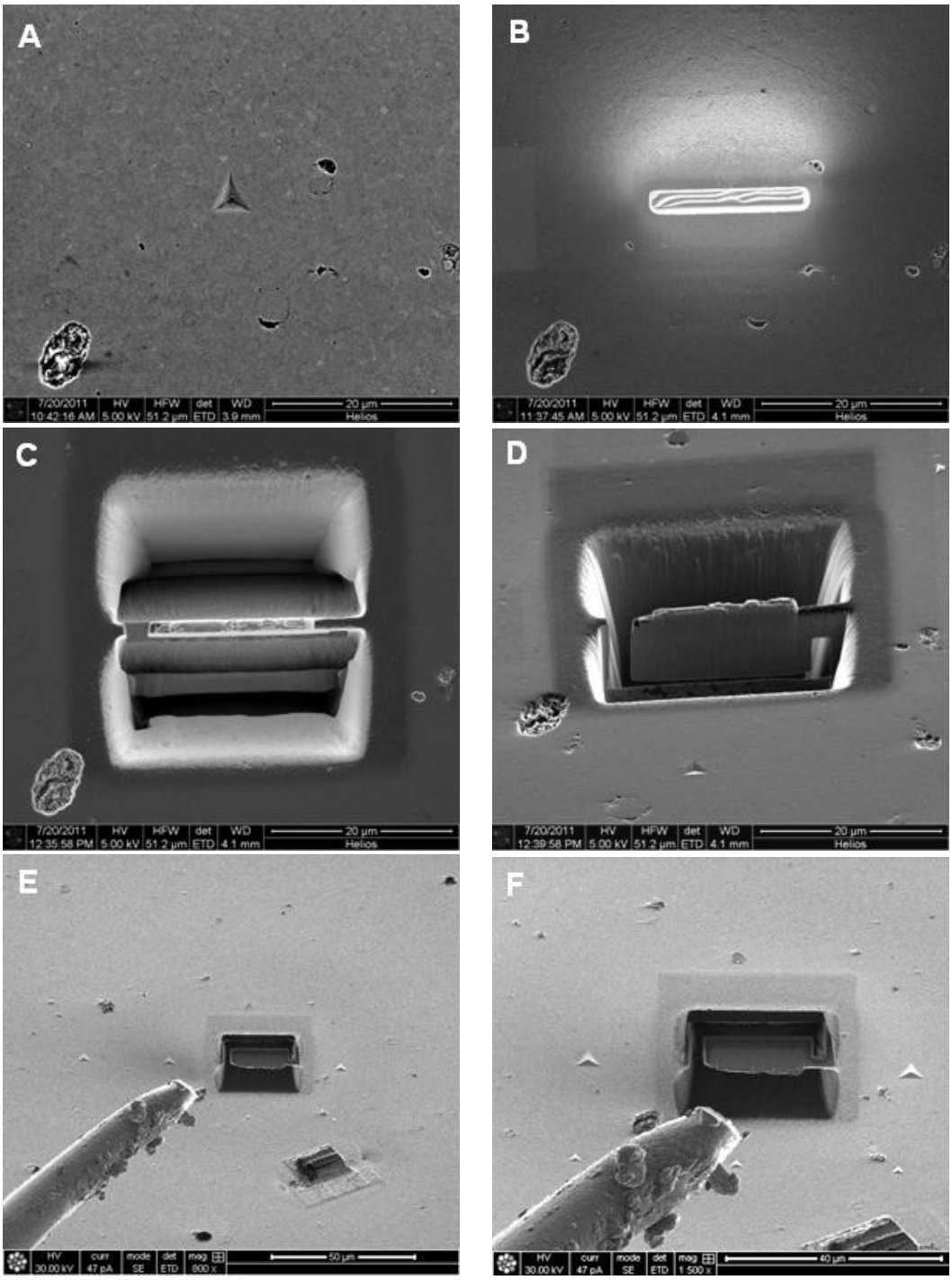

Figure 5-14 SEM images of an arc evaporated $Ti_{0.4}Al_{0.6}N$ deposited film taken on a FIB equipped with an electron gun showing the first main steps of in-situ lift out technique: (a) The spot of interest where a TEM sample will be milled is represented here by an indent; (b) A strip of Pt is deposited over the indent to preserve the surface; (c) and (d) Trenches are milled on the either side of the Pt strip and the lamella is cut in such a way that remains suspended on the bulk by a small bridge on right side; This stage of milling is imaged from the top, 0° (c) and tilted at 52° (d); (e) and (f) a tungsten needle used for extracting the sample from the crater is inserted in the proximity of the free cut side of the lamella.

The tungsten needle is gently brought in contact with the upper corner of the free side of the lamella. This operation is risky, especially in single ion beam equipment, in which the approach of the needle to the lamella is evaluated from the shadow the needle makes on the sample.

In the case of FIB equipped with an electron beam, the specimen and the needle can be imaged from the top and laterally simultaneously, which greatly eases the transfer of the sample from the bulk to the needle.

A weld is performed at the contact point and then the bridge which links the sample to the bulk is cut. These operations are illustrated in Figure 5-15.

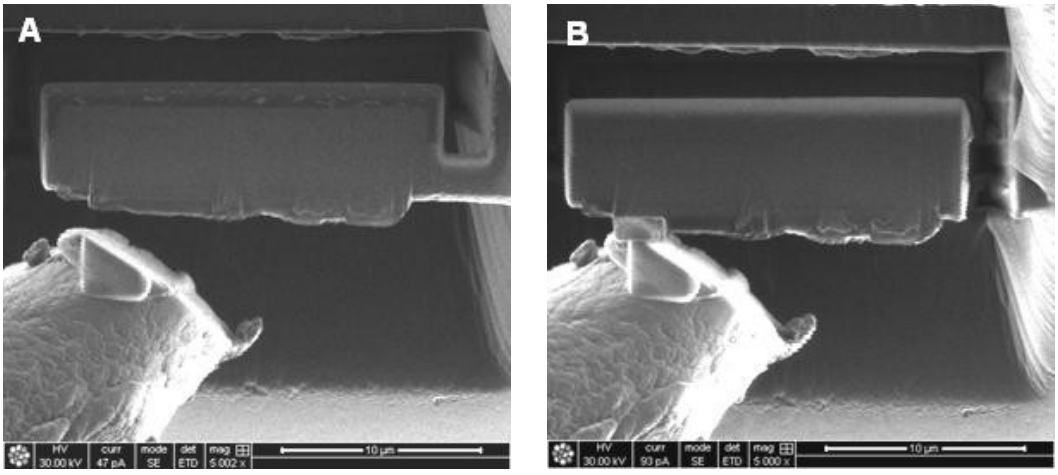

Figure 5-15 Transfer of the lamella from the bulk to the needle. (a) The needle is brought in touch with the sample and then welded by the deposition of a patch of Pt; (b) The bridge between the sample and the bulk is milled away, leaving the sample attached only on the needle. Due to the redeposition from cutting the bridge, the features on the sample are no longer visible.

At this stage the ~ 2 μm lamella is attached to the micromanipulator needle, which is lifted out from the milled crater (Figure 5-16 (a)) and is moved to a TEM grid. The sample is brought in the proximity of one side of a pillar of a TEM grid (Figure 5-16 (b)).

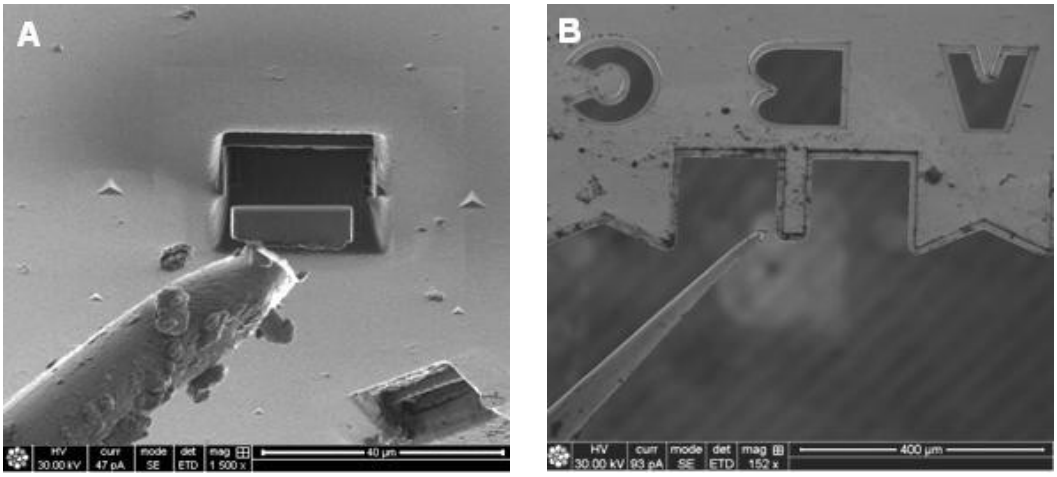

Figure 5-16 The sample is moved to the TEM grid. (a) Lifting of the specimen out from the crater, (b) low magnification SEM image showing the needle with the sample at the tip moved next to central pin of a TEM grid.

The sample is brought in contact with the grid and a weld is performed by depositing a strip of Pt (Figure 5-17 (a)). Then the weld between the needle and the sample is milled away (Figure 5-17 (b)) in order to complete the transfer of the ~ 2 μm lamella to the TEM grid.

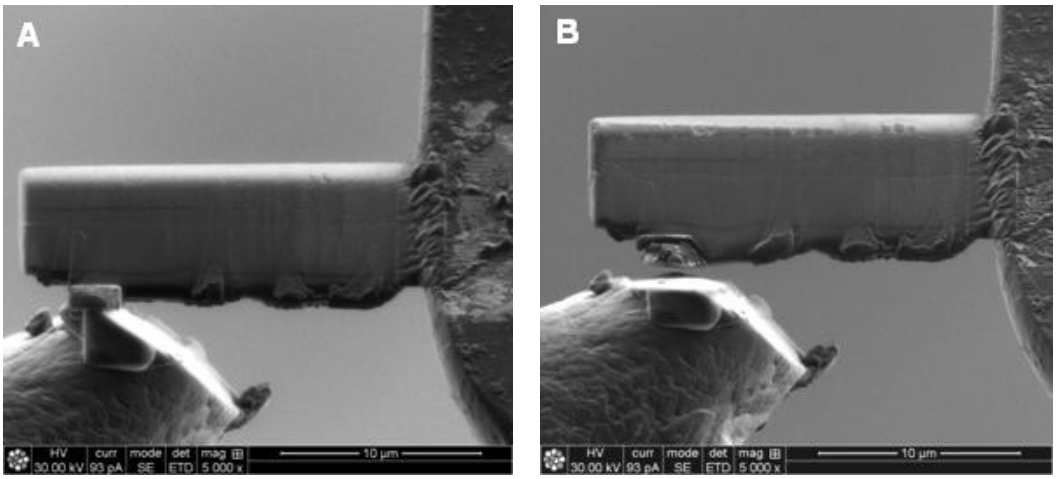

Figure 5-17 Transfer of the lamella from the needle to a TEM grid. (a) The sample is placed in contact with the grid and welded to the grid; (b) The sample is separated from the needle by cutting the bridge used for lifting up the sample.

The needle is retracted and the sampled is thinned by milling on alternate sides at maximum 2° tilting between the sample wall and the beam direction. The angle of incidence is usually set-up as small as possible so that the milled surfaces of the TEM foil are almost parallel to each other and the ion implantation is diminished [203]. As the thinning progresses, the current of the ion beam is gradually decreased from 0.92 nA at 30 kV acceleration voltage to 47 pA and 5 kV,

respectively. The current and voltage of the ion beam can be varied by using various aperture sizes and controlling the strength of the electrostatic lenses [202]. This way the beam current density (and, therefore, the beam diameter) can be varied, allowing for both, a small beam for fine milling and polishing and, a broad high current beam for fast-rough milling.

Finally the sample is tilted at 7° and then polished sidewall with a beam current of 28 pA at an acceleration voltage of 2 kV. Images of a sample during thinning stage are shown in Figure 5-18. Subsequent thinning can be performed on samples prepared by in-situ lift out technique after viewing in the TEM.

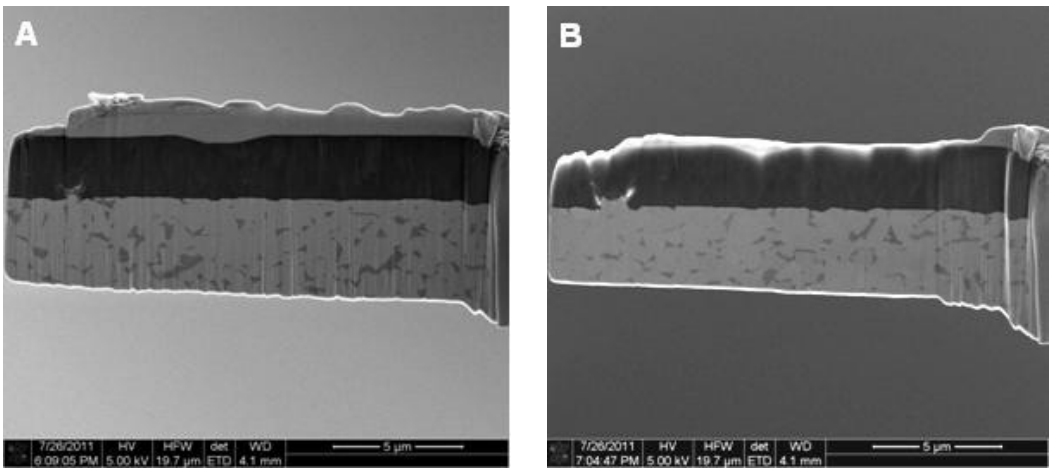

Figure 5-18 Final thinning stages. (a) A sample attached on the TEM grid at the beginning of the thinning stage. Some microstructural features as well as curtain effects from the rough milling can be seen on the side of the sample. (b) As the thinning progresses, the shape of the indent (which is the spot of interest in this case) provides an idea about when the milling should stop. The curtain effects and the Pt layer are milled out. The brightness indicates that the sample approaches the final thickness and the polishing should follow.

As the TEM sample becomes thinner, the tendency to bend or twist increases. This is particularly true for materials which exhibit high internal stresses, as it is the case for PVD deposited films. In order to somehow suppress the distortion of the TEM specimen, the sample is placed on a window milled in the TEM grid as shown in Figure 5-19. A rectangle which is approximately one micrometer wider than the sample is milled on top of one of the TEM grid pillars. Then the sample is gently parked in the milled slot and Pt welded simultaneously on both ends, as shown in Figure 5-19 (b).

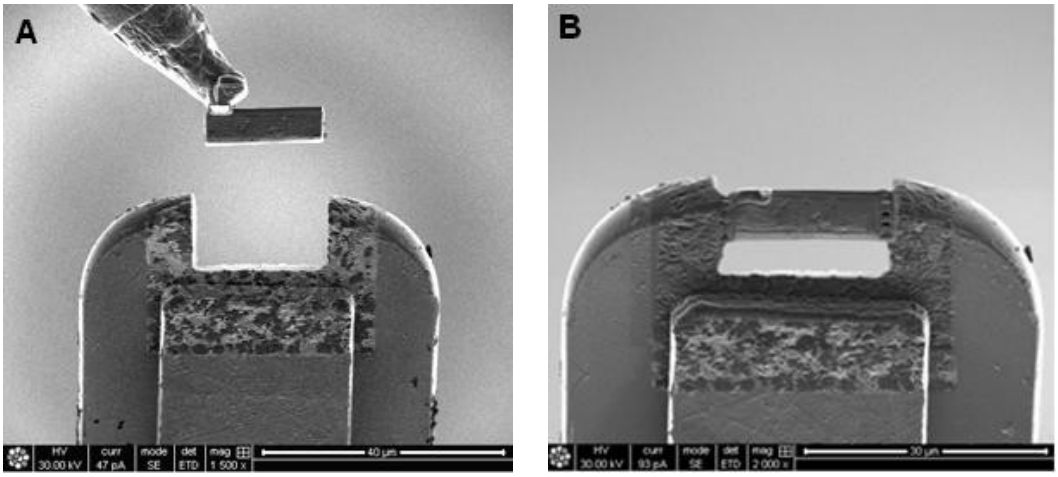

Figure 5-19 The sample is placed on a milled window in order to provide a better shape stability during final stages of milling. (a) The sample is carefully guided in the bay. (b) The sample is parked, welded on both sides and the needle is cut.

The lamella is thinned in a similar way as if the sample is placed on a side of the TEM grid. The thickness of the sample is monitored by changes in brightness of the secondary electrons image, as it is shown in Figure 5-20**.** This technique allows for larger TEM samples to be milled.

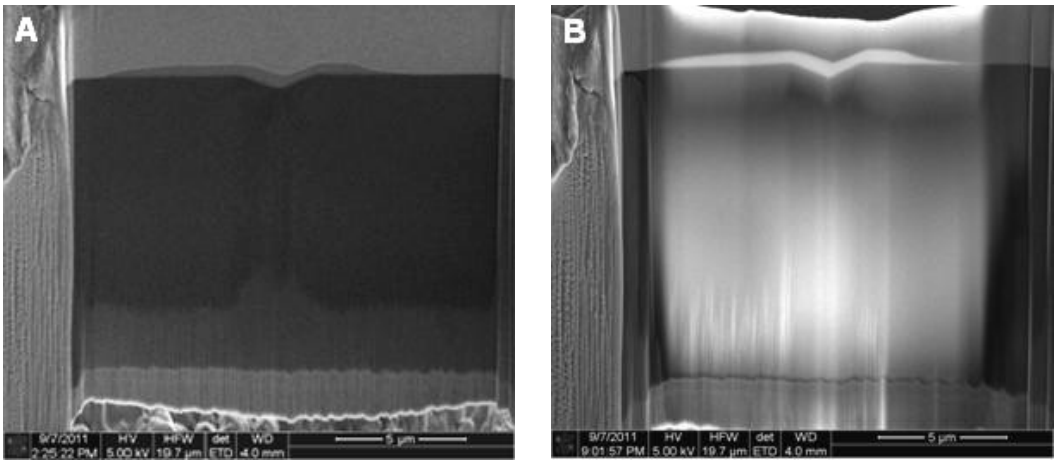

Figure 5-20 Cross section SEM images of an indent in bulk single crystal TiN. (a) The specimen before thinning (imaged at 50° tilt). The feature of interest (the indent) is clearly visible. The TEM foil before polishing (imaged at 54° tilt). The change in the brightness of a specimen can be used to monitor its thickness and therefore reduce the number of specimens that are prepared too thick for TEM analysis.

Ion beam damage during TEM sample preparation by FIB

It is recognised that FIB has become a powerful technique for TEM sample preparation. However, the awareness regarding the limitations and drawbacks of the FIB-based methods has also increased. The use of the FIB inherently involves damaging the sample, and thereby degrades the TEM resolution. The primary

damage appears in the form of amorphisation on the surface of the TEM foil, as a result of the bombardment by highly accelerated gallium ion beams. Alongside removing material by sputtering, during milling, a series of various processes occur, such as: gallium implantation, redeposition of milled material, ion beam radiation and sample alteration due to local heat [203]. These processes lead to the damage of initial crystalline structure of milled material at the surface of TEM foil. Another artefact that might be present in the FIB processed samples is thickness non-uniformities.

The main factors which influence the extent of the damaged surface layer are the beam current and voltage and, the angle of incidence of the ion beam with respect to the specimen.

Numerous efforts have been made to reduce or eliminate the damage surface of the TEM samples produced by FIB. The most promising results come from using a lower energy ion beam and a smaller angle of incidence as the TEM sample approaches the final thickness. However, a lower energy ion beam results in a lower sputtering rate (therefore, increasing the milling time). A lower sputtering rate results in a weaker signal of the detector which is translated in a lower resolution for the image formed by the ion beam. Because of that, the use of low energy beams should be restricted to final stages of thinning, in which the electron column (for FIB-SEM equipment) is of great use for monitoring the milling process. The rise of temperature at the milling point in FIB is less than 10 K [205], which is negligible for hard ceramics.

In this work, cross sectional thin foils for TEM analyses were prepared by using either a single beam FIB (FEI 200TEM) or dual FIB equipment (FEI Helios 600 Nanolab). Most TEM samples were prepared in the latter equipment. The final low current and acceleration voltage coupled with less than 2° tilting during final stages of milling ensured a minimal ion implantation and surface amorphisation of the TEM specimen.

5.5 XRD

XRD was performed to characterise the phase composition and orientation of the polycrystalline coatings. An X-ray diffraction system (PANalytical XPert Pro MPD) was employed, using CuKα radiation of wave length λ=1.540598 Å, in a 2θ

range from 30° to 110° with a step size of 0.0334° and scan time of one second per step.

The X-ray technique used was *diffractometer method*, in which monochromatic (the same wavelengths) X-ray beams are fired at the sample. The sample is rotated with respect to the beams in order to orient as many planes as possible in diffraction conditions. The intensity of the diffracted beams is measured directly by an electronic counter (detector), which collects the X-ray signal while moving on the circumference of a circle centered on the specimen. Because the samples were thin films, the X-ray signal coming from the substrate was removed prior to analyses.

6 Results and discussion

The experimental investigation began by studying the (001) TiN_{bulk}, which is the simplest system related to ternary coatings $Ti_{1-x}Al_xN$. Then, the complexity of the system was increased step by step. The second material analysed was the same composition, TiN, but polycrystalline. This was a magnetron sputtered TiN film with a (001) preferential orientation, which was epitaxially deposited on MgO substrate. By investigating the same composition (TiN) in the same crystallographic orientation but in two different structures (with and without grain boundaries), the influence of grain boundaries on mechanical properties of the TiN system could be studied. The next phase was to isolate and investigate the influence of aluminium addition in the TiN system, with regards to mechanical stability with temperature. For this, magnetron sputtered $Ti_{1-x}Al_xN$ films with various contents of aluminium (x = 0.34; x = 0.52 and x = 0.62) were tested. The complexity of the system was further increased; $Ti_{1-x}Al_xN$ coatings deposited by industrial cathodic arc technique, which is known to yield coatings with a less homogeneous structure compared to magnetron sputtered films [26, 146-147], were investigated.

The mechanical performance of materials exhibited during nanoindentation was linked to the phase composition, the crystallography and morphology, which were examined by X-ray diffraction and TEM.

6.1 Indentation study of TiN system

6.1.1 Indentation study of the bulk single crystal (001) TiN

The influence of temperature on the mechanical properties of the (001) TiN_{bulk} was studied by nanoindentation at the following temperatures: RT, 100 °C, 200 °C, 300 °C and 350 °C. A number of 10 indents were performed at every temperature. Figure 6-1 shows that the increase in temperature had a strong influence on the hardness of the TiN_{bulk}, leading to a decrease in values from 21.4 ± 0.4 GPa at RT to 13.7 ± 0.4 GPa at 350 °C.

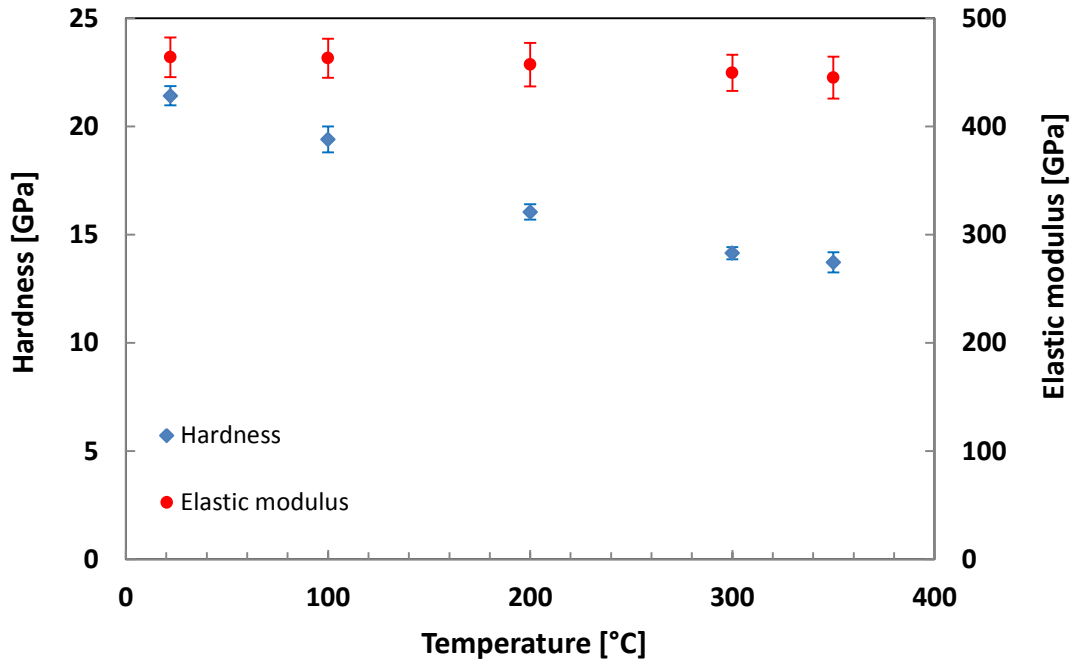

Figure 6-1.: The influence of temperature on the hardness and elastic modulus of the bulk single crystal (001) TiN. Each point represents the average data gathered from 10 indents.

The elastic modulus of the TiN_{bulk} remained stable, exhibiting a small drop in values of 4 % over the range RT – 350 °C, which is in good agreement with the literature data for other refractory materials (see Table 6-1) with similar properties (hardness and melting temperature) to TiN [206-210].

Table 6-1. The drop in the elastic modulus values over the temperature range RT – 350 °C for various refractory materials

Material	Drop in elastic modulus from RT to 350 °C [%]	Observation
TiAlN [207]	5.5	No composition stated. Fcc structure
$Ti_{0.44}Al_{0.56}N$ [211]	4.2	Fcc structure
$Ti_{0.68}Al_{0.32}N$ [211]	3.9	Fcc structure
$Ti_{0.36}Al_{0.64}N$ [211]	2.3	Wurtzite structure
Si_3N_4 [206]	2.2	
SiC [207-208]	1.6	
SiC [209]	1.3	
TiC [209]	3.5	
TiC [212]	1.7	Calculated from shear modulus vs T
BC [207-209]	1.6	
ZrC [212]	2.6	Calculated from shear modulus vs T
Al_2O_3 [208]	2.4	
Al_2O_3 [206]	3.3	
Al_2O_3 [209]	3.9	
Al_2O_3 [209]	4.6	Single crystal ruby
Al_2O_3 [209]	4.7	Single crystal sapphire
Al_2O_3 [212]	4.9	Calculated from shear modulus vs T
MgO [209]	5.8	
MgO [212]	7.1	Calculated from shear modulus vs T
Mullite [209]	1.6	
Spinel [209]	3.2	
Spinel [212]	3	Calculated from shear modulus vs T
CrO_2 [212]	4	Calculated from shear modulus vs T
ThO_2 [209]	3.7	

6.1.2 Indentation study of the magnetron sputtered TiN film

The hardness variation of the magnetron sputtered TiN film (TiN_{film}) with temperature is presented in Figure 6-2, together with data from the TiN_{bulk}. 10 indents were performed on the TiN_{film} at every temperature. At low temperatures (RT and 100 °C) the TiN_{film} had similar hardness values to the TiN_{bulk}. This was surprising, because, due to the nature of magnetron sputtering deposition, various strengthening mechanisms known to work well in bulk metals might be expected to be active in hard coatings, as well. Such strengthening mechanisms have the

role to provide obstacles for dislocation motion. This is achieved by an increased: (a) density of point and line defects generated during deposition; (b) internal boundaries between grains and columns; (c) residual compressive stresses. Therefore, the TiN_{film} was expected to have a higher hardness than the TiN_{bulk}. However, it seems that the grain boundaries and columnar morphology did not change the performance of the TiN system, at RT and 100 °C.

TEM investigation (presented in the next chapter) revealed that the TiN_{film} had a columnar structure as shown in Figure 6-7, and the average size of the columns width (determined from four TEM samples taken from various parts of the film) was around 20 nanometers (Figure 6-8). However, each column does not represent one single grain, but, it is formed from a number of grains which have a very close orientation. Therefore, the average width of grain size of the TiN_{film} is expected to be smaller than 20 nanometers.

Although, the volume of the plastic zone under the indent is bigger than 1 μm^3 and encompasses many grains (see Figure 6-9), the Hall-Petch effect does not appear to be present in this film, due to the similarity in hardness values between the TiN_{film} and the TiN_{bulk}.

These observations were all consistent with the literature data which shows that the influence of the grain size on the hardness of hard ceramics does not follow the general accepted rule that the hardness increases with smaller grain size (Hall-Petch effect), as is the case in metals [86, 96, 213-214]. This suggests the TiN hardness is dominated by the magnitude of the lattice resistance at temperatures up to 100 °C. In other words, the activation energy required for a dislocation to move over the TiN lattice at these temperatures is greater than the activation energy required to move over a grain boundary.

However, at 200 °C and 300 °C, the TiN_{film} showed a smaller drop in hardness compared to the TiN_{bulk}. The better thermal stability of the TiN_{film} could be attributed to the relative increased influence of grain boundaries on reducing the dislocation mobility at higher temperatures, compared to the TiN_{bulk}.

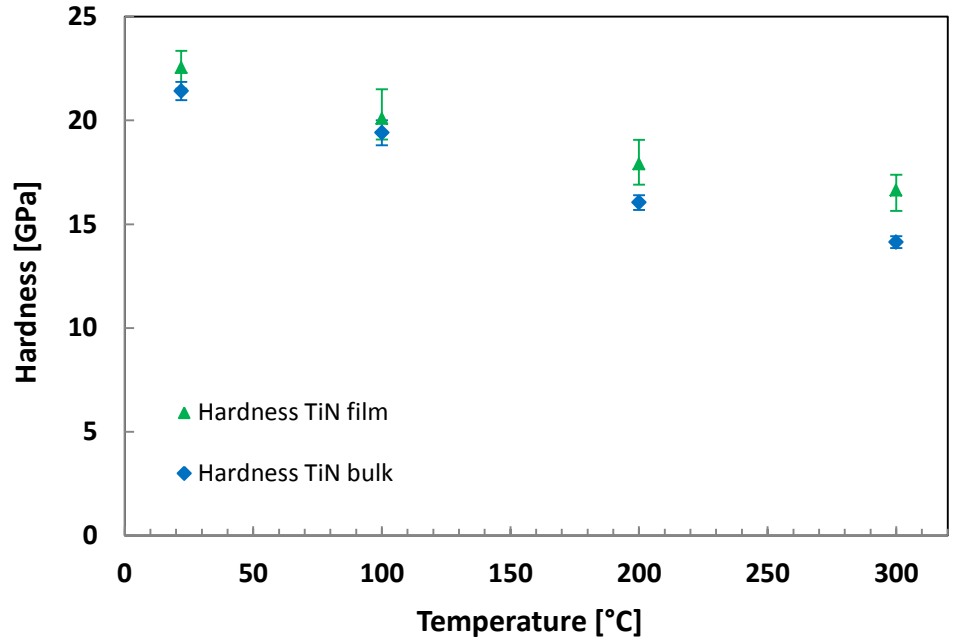

Figure 6-2 The influence of temperature on hardness of the magnetron sputtered TiN_{film} and the TiN_{bulk}. Each data point represents the average data gathered from 10 indents.

In Figure 6-3, the elastic modulus variation of the TiN_{film} with temperature is presented, alongside data corresponding to the TiN_{bulk}. Surprisingly, the elastic modulus of the TiN_{film} decreased more than that of the $TiN_{bulk,}$ with increasing temperature. The reason for this behaviour is not clear. As the elastic modulus depends on the chemical bonding, microstructural changes (for materials with the same lattice structure) generally do not have a large effect on the elastic modulus. However, in the next chapters it is shown that this film exhibit porosity, and the literature data suggests that porosity significantly reduces the elastic modulus of a material [215-216].

The influence of temperature on the hardness of the TiN_{bulk} and the TiN_{film} is plotted in Figure 6-4 alongside data obtained by Quito [2, 163] and Jindal et. al [1] from Vickers indentation of magnetron sputtered deposited TiN coatings. These results show that the hardness values of the TiN_{film} from the present work were in line with the literature data. At RT, despite the polycrystalline structure, all films had almost the same hardness as the TiN_{bulk}. This once again suggested that the hardness of TiN system was dominated by the magnitude of the lattice resistance at low temperatures.

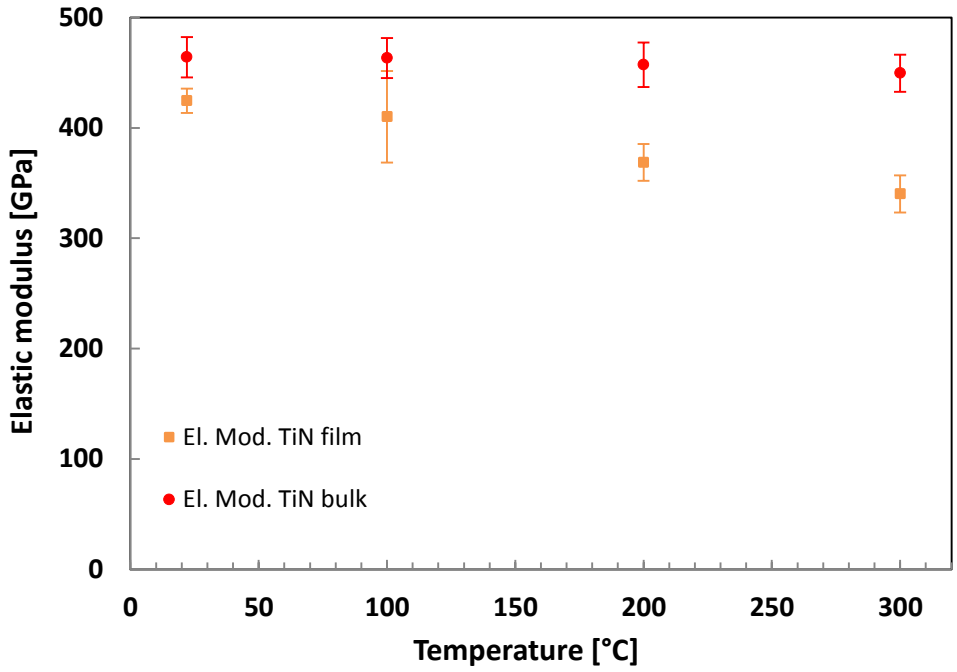

Figure 6-3 The influence of temperature on the elastic modulus of the magnetron sputtered TiN_{film} and the TiN_{bulk}. Each point on the graph represents the average data from 10 indents.

However, the relative contribution of the grain boundaries against dislocation mobility increased with the temperature, evidenced by the increase in hardness difference between the TiN films and the TiN_{bulk}. Nevertheless, with increasing temperature, hardness for materials in TiN systems decreased.

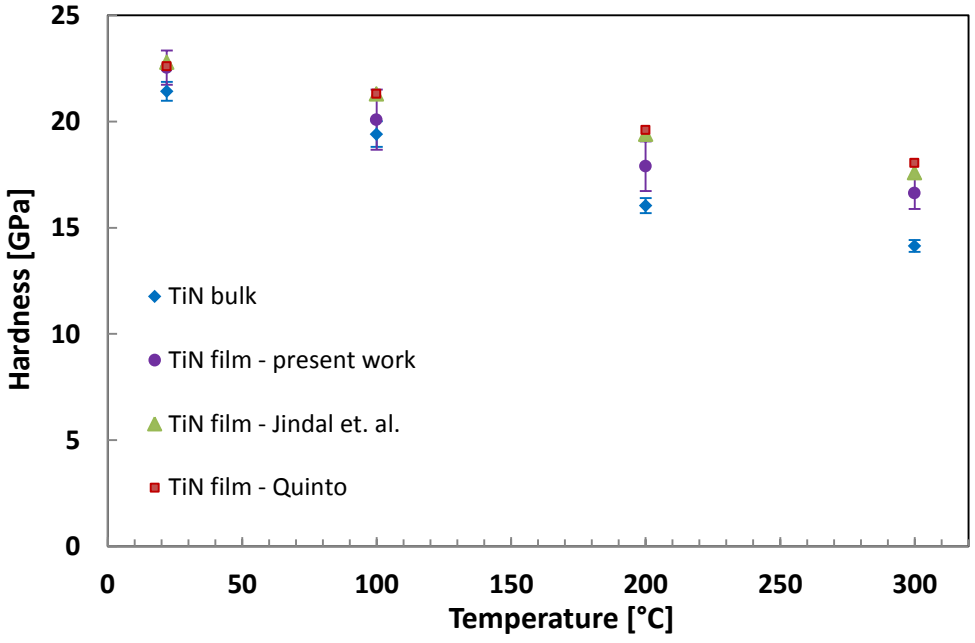

Figure 6-4 The influence of temperature on the hardness of the magnetron sputtered TiN_{film} and the TiN_{bulk} determined by nanoindentation, compared to the influence of temperature on Vickers hardness of TiN magnetron sputtered films from [1-2, 163].

6.1.3 Structural deformation of the bulk single crystal TiN

Bright field images taken at [001] zone axes from indents performed on TiN_{bulk} at RT and 350 °C are presented in Figure 6-5. The plastic flow during nanoindentation performed over the temperature range RT - 350 °C occurred primarily along {110} crystallographic planes. This is consistent with Yamamoto results from compression tests carried out at high temperature on fine-grained sintered TiN [40], which showed that the primary slip system in TiN is {110}⟨110⟩. Therefore, the drop in hardness with the temperature might be attributed to a decline in the lattice resistance to dislocation motion, translated in a change of intrinsic ease of plastic slip. The change in lattice resistance with temperature could be confirmed by an increase of the plastic zone size, which means an increase in dislocation activity (see Figure 6-5). If the dislocation activity intensify, the role of the grain boundaries becomes more relevant in dislocation motion at elevated temperatures. Therefore, lower lattice resistance would facilitate dislocation activity and pile-ups at grain boundaries. This hypothesis was confirmed by an increase in the hardness stability with temperature of the TiN_{film}, which is a material with a high density of grain boundary, as will be shown in the next chapters.

TEM investigation revealed no porosity in the structure of the TiN_{bulk}.

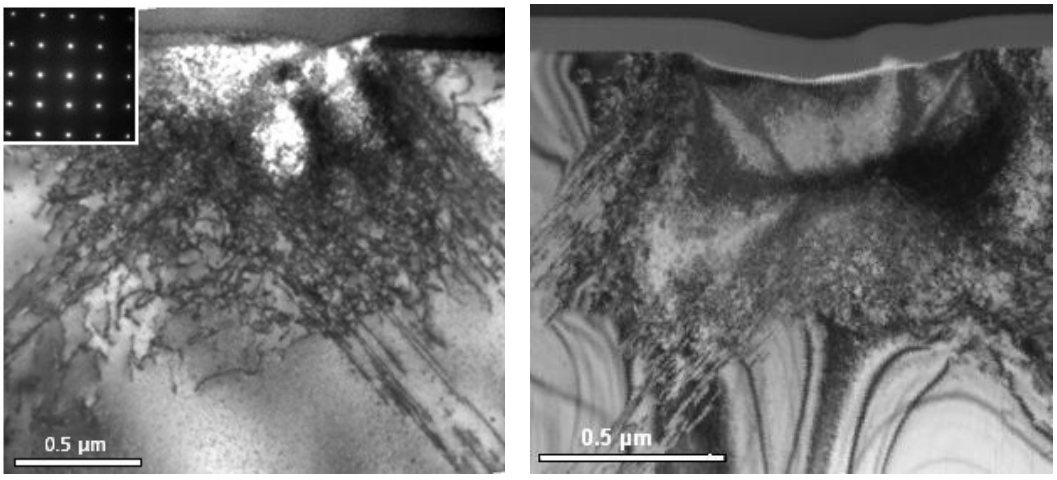

(a) (b)

Figure 6-5 Cross-section BF TEM images taken at [001] zone axis from 50 mN indents performed in the TiN_{bulk} at: (a) RT and (b) 350 °C. The dominant plastic flow during indentation occurred along the [110] slip planes.

6.1.4 Structural characterisation of the magnetron sputtered TiN film

The X-ray diffraction shows that the orientation of the TiN_{film} strongly followed the (001) orientation of single crystal MgO substrate, as shown in Figure 6-6. The main (001) peak of the TiN_{film} appeared as a distinct peak at $2\theta = 42.61°$, which is very close to the position corresponding to pure TiN ($2\theta = 42.63°$). This small shift of 0.02 ° towards lower 2θ values suggested a larger lattice that could be caused by atomic implantation processes during deposition, in which small atoms belonging to the gases used in deposition are forced in lattice interstitials [2, 97, 118, 171, 175, 217-218].

TEM analysis revealed a polycrystalline structure with columnar morphology for the TiN_{film}. The first stages of deposition were epitaxial to the MgO substrate, up to a layer thickness of around 300 nm, from which columnar structure developed, as shown in Figure 6-7. Due to high energy deposition sufficient residual ion damage was produced to disrupt the columnar structure and continuously nucleate new grains [94].

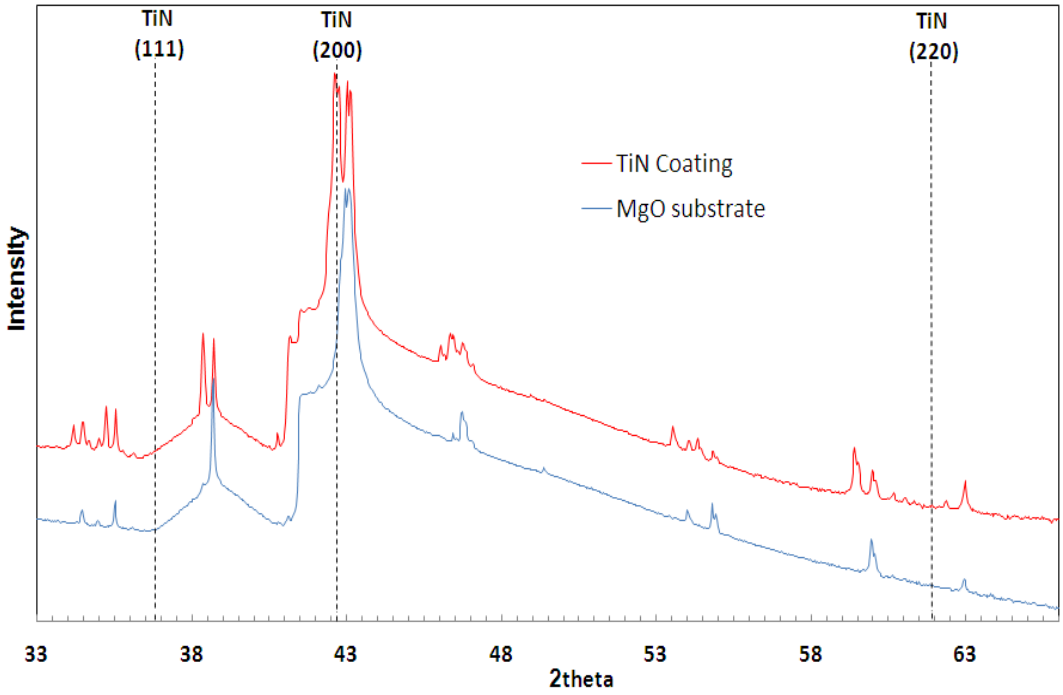

Figure 6-6 X-ray diffractograms corresponding to TiN_{film} and MgO substrate. The TiN_{film} has a strong (001) orientation

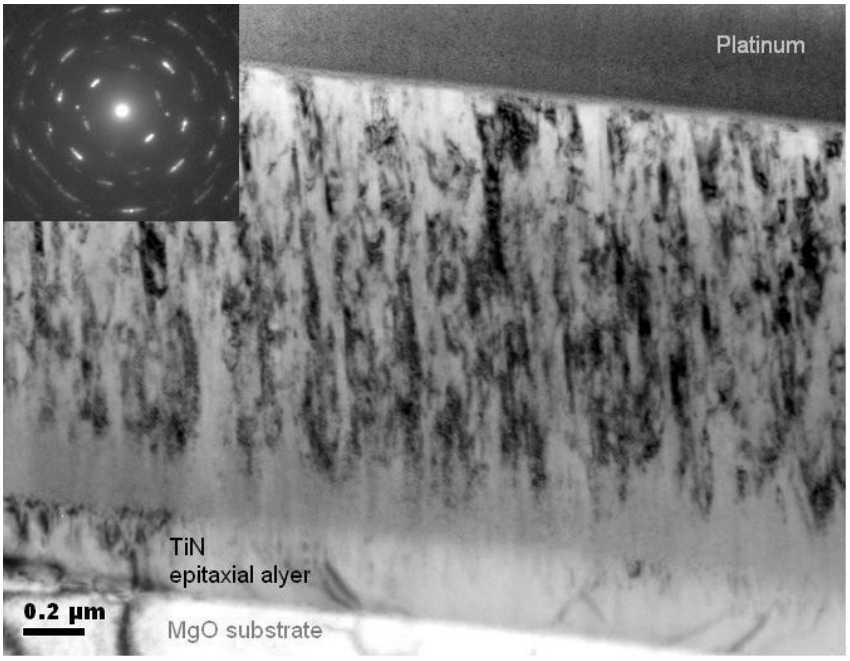

Figure 6-7 Cross-section BF TEM image of the magnetron sputtered TiN film deposited on MgO substrate, showing the columnar morphology and the epitaxial layer on the substrate.

Voids and possible bubbles of trapped gasses (Ar and N_2) gathered along the column boundaries, as shown in Figure 6-8. The porosity seemed to be attributed to the atomic shadowing during the process of texture evolution via competitive growth [219-220].

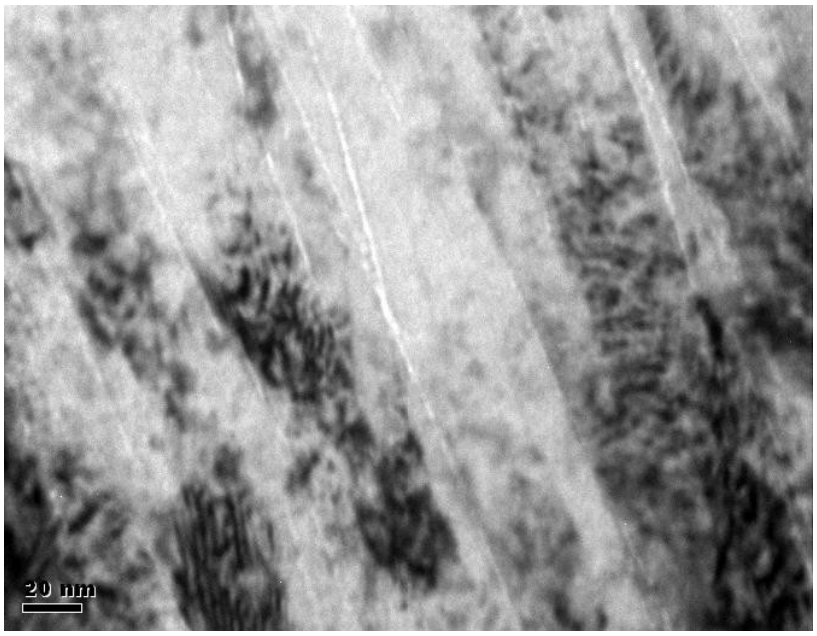

Figure 6-8 Cross-section BF TEM images of magnetron sputtered the TiN film showing seams of voids running in the film growing direction along the column boundaries.

Plastic deformation in the sense of dislocations is hard to detect in films, because of the fine columnar structure and the large number of defects that are introduced

during deposition. An example illustrating the plastic zone under an indent performed on the TiN_{film} is presented in Figure 6-9.

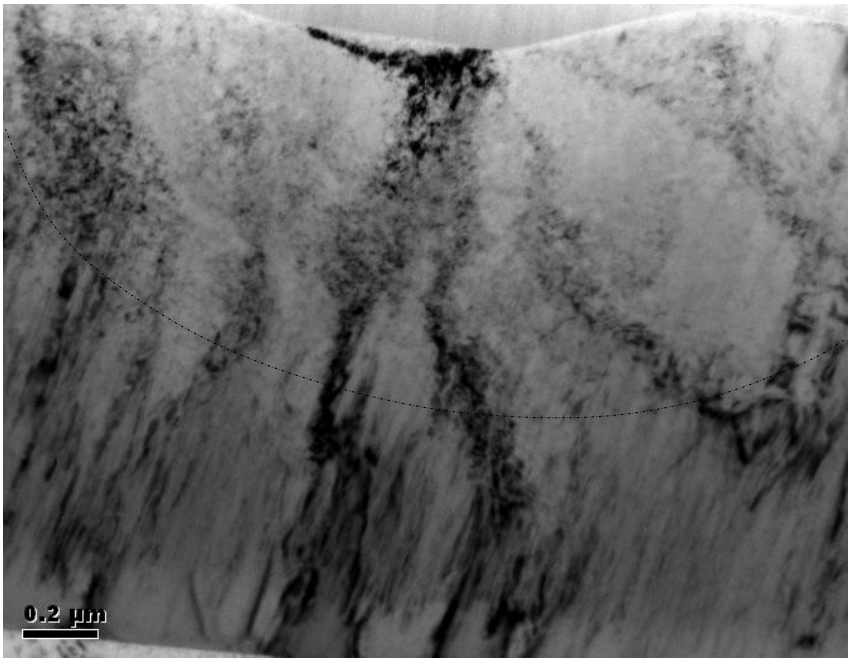

Figure 6-9 Cross-section BF image of an indent performed at RT in TiN showing the plastic zone. The dislocation activity during indentation masked the fine columnar structure, which can be seen under the plastic zone delineated by the dotted line.

6.1.5 Discussion of TiN system

The TiN_{film} had a similar hardness at RT and 100 °C to the TiN_{bulk}. However, at higher temperatures (200 °C and 300 °C), at which the lattice resistance to dislocation motion decreases (as seen in bulk single crystal TiN), the hardness of the TiN_{film} dropped less than that of the TiN_{bulk}. This behaviour suggests that, whereas the lattice resistance dropped with temperature, the relative contribution of the high density of defects (such as grain boundary, dislocations) towards an improved thermal stability increased.

As the elastic modulus depends on the chemical bonding, microstructural changes (for materials with the same chemistry and lattice structure) generally do not have a large effect on the elastic modulus. However, Yang et al. investigated the influence of porosity on the elastic modulus of α-Si_3N_4 ceramics, which have similar mechanical properties to the materials investigated in this work. They found that the increase in porosity reduces the elastic modulus. For a 0.23 volume fraction of porosity, the elastic modulus decreased to half of that for the dense material [215-216]. Jang and Matsubara confirmed that porosity significantly

reduces the elastic modulus of ceramics; the elastic modulus of thermal barrier coatings (ZrO_2–4 mol% Y_2O_3) reached half values around 20 % porosity [221]. Another factor which could have a significant influence on measured properties (elastic modulus and hardness) by high temperature nanoindentation is the thermal drift. The response of interest during indentation is the load-displacement curve illustrated in Figure 6-10.

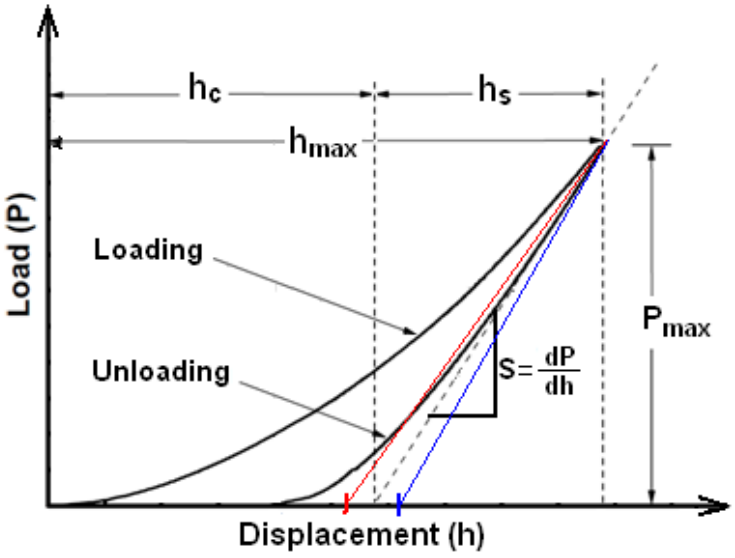

Figure 6-10 Typical load-displacement curve obtained from an instrumented nanoindentation experiment performed with a Berkovich indenter, showing important analysis parameters, from [76]. The coloured lines have been added to illustrate the effect of the thermal drift on the slope of the unloaded curved.

Oliver and Pharr [76] showed that the unloading response during indentations made by sharp-tip self-similar indenters is well described by the power law relation (3) which has the form

$$P = \alpha(h - h_f)^m$$

As explained in the experimental chapter, the above relationship can then be differentiated to obtain the initial unloading slope (stiffness). The contact depth (h_c) is determined by extrapolating the slope (the dotted line in Figure 6-10). The intersection between the slope extrapolation and displacement axes marks the h_c. From the Figure 6-10 it is seen that

$$h_c = h_{max} - h_s$$

Increasing in temperature increases the thermal drift. For a positive drift, the slope would be larger, and the slope extrapolation would intersect the displacement axes on the right of the dotted line (eg. the blue line). That means the h_c and elastic modulus would have larger values, whereas the hardness would be smaller. For a negative drift, the opposite would be true (eg. the red line). As a result, the h_s value is going to be smaller for positive drift and larger for negative drift. An example showing the error in contact depth (h_c), which is the key analysis parameter, is presented below. The dimensions in the example are similar to the ones recorded by the machine in the present work.

Table 6-2. Example showing the influence of the thermal drift on the contact depth

No drift recorded during indentation	Recorded drift of 1 nm/s x 20 sec (unloading time) = 20 nm	Error in $(h_c)^2$ value $A(h_c) = 24.5(h_c)^2$
h_{max} = 710	h_{max} = 710	**7.14%**
h_s = 180	h_s = 160	
h_c = 530	h_c = 550	

The experimental equipment takes in consideration the thermal drift, which is determined (as a value) during unloading at 10% of the maximum load. However, the Olive and Pharr algorithm based on which the h_c is calculated assumes that the measured thermal drift is constant throughout the experiment. But that might not be the case, as thermal drift can vary during the indentation experiment.

At higher temperature, the drift is expected to be higher, which results in larger errors in contact depth. Therefore, some variations in hardness and elastic modulus might be attributed to errors resulted from the thermal drift, especially at high temperatures. The nanoindentation runs which yielded strange results have been repeated in order to confirm if the results have been affected by the experimental conditions. However, due to equipment availability and the time required for such experiments, not all indentation runs which raised minor concerns were able to be repeated.

Therefore, it is suggested that, the low elastic modulus values of the TiN_{film} compared to the TiN_{bulk} could be attributed to the porosity present in the film and the influence of the thermal drift.

6.2 Indentation study of magnetron sputtered $Ti_{1-x}Al_xN$ films

The variation of mechanical properties with temperature of the ternary coatings with various aluminium contents is presented next, followed by an analysis of the influence of aluminium on the kinetics of deformation. The XRD and TEM analyses are also presented. The chapter concludes with a discussion which relates the structural changes due to the addition of aluminium in TiN lattice to the mechanical properties.

6.2.1 Influence of aluminium addition on mechanical properties of the magnetron sputtered $Ti_{1-x}Al_xN$ films

The influence of aluminium addition on the hardness of the magnetron sputtered $Ti_{1-x}Al_xN$ films, at various temperatures, is shown in Figure 6-11, alongside data corresponding to the TiN_{film}. The addition of aluminium in TiN system resulted in higher hardness, which is in line with the literature data [30, 103, 114, 125, 222]. However, the increase in hardness and its stability with the temperature was different for each $Ti_{1-x}Al_xN$ coating. The low aluminium content film ($x = 0.34$) exhibited higher hardness than the TiN_{film}, but the hardness stability with the temperature followed a similar trend to the TiN_{film}. The intermediate aluminium composition ($x = 0.52$) exhibited not only a significant increase in hardness, but the hardness stability with temperature was improved compared to the $x = 0.34$ film. The hardness dropped only 2 GPa, from 29 GPa at RT to 27 GPa at 300 °C. The rich aluminium composition ($x = 0.62$) exhibited improved hardness stability with temperature, although at significantly lower values of hardness compared to $x = 0.52$ film.

The elastic modulus of the magnetron sputtered $Ti_{1-x}Al_xN$ films versus temperature is shown in Figure 6-12, alongside data corresponding to TiN_{film}. The stability of the elastic modulus with temperature is improved by the addition of aluminium.

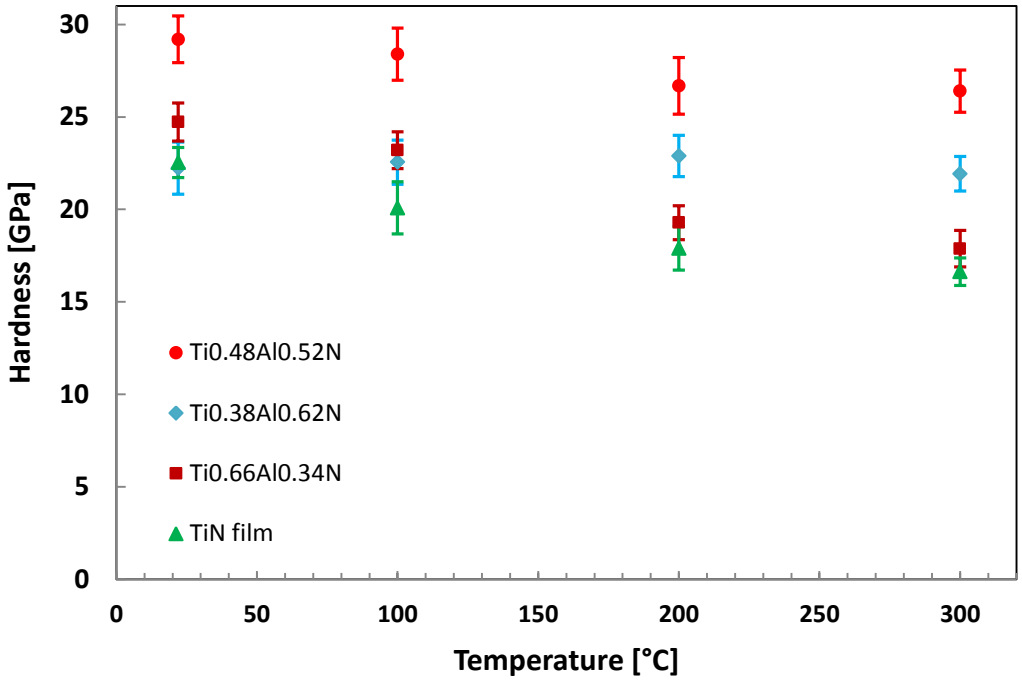

Figure 6-11 The influence of the aluminium addition on the hardness of magnetron sputtered $Ti_{1-x}Al_xN$ films as determined from nanoindentation measurements performed at various temperatures. The hardness of the TiN_{film} is plotted, as well. Each data point represents the average data gathered from 10 indents.

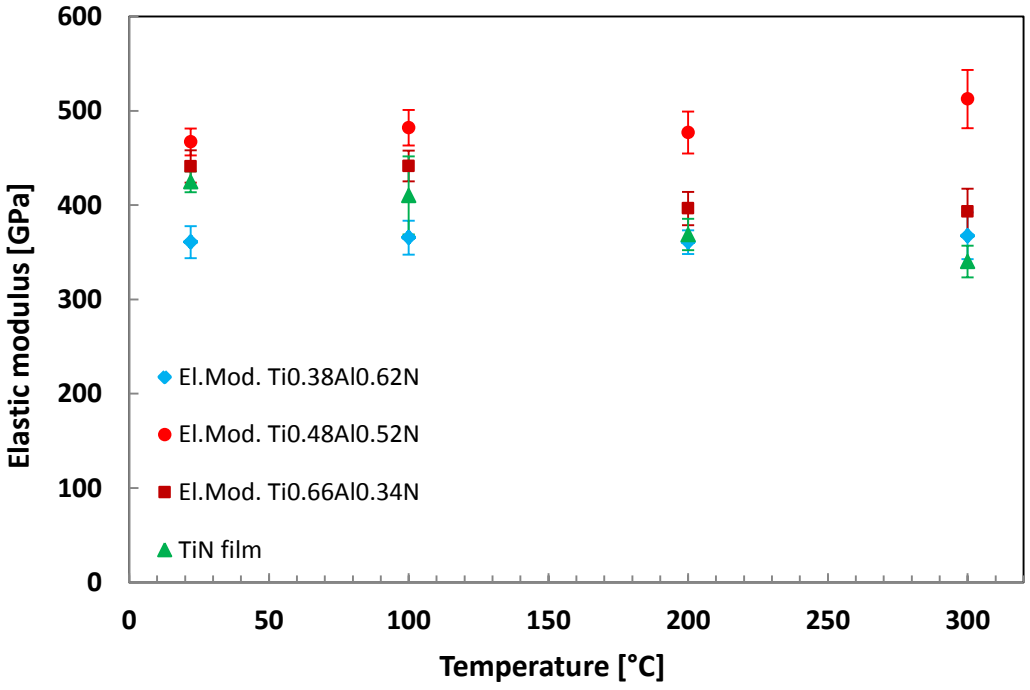

Figure 6-12 The influence of the aluminium addition on the elastic modulus of the magnetron sputtered $Ti_{1-x}Al_xN$ films and the TiN_{film} as determined from nanoindentation measurements performed at various temperatures. Each data point represents the average data from 10 indents.

It is interesting to note that the x = 0.52 film exhibited an exceptional behaviour compared to the other films; it yielded the highest hardness and elastic modulus, as well as, good thermal stability.

In order to understand the mechanical behaviour at various temperatures with aluminium addition, TEM and XRD analyses were performed. The findings from these investigations are presented in the next chapters. Based on these findings, the improved mechanical performance (attributed to the aluminium addition) with temperature is explained in chapter 6.2.7.

6.2.2 Influence of aluminium on kinetics of plastic deformation

In order to obtain insight into the operative micro-mechanisms and nature of obstacles controlling deformation-rate process over the tested temperature range of these materials, deformation kinetics analysis is carried out. The lattice resistance for hard materials, such as hard ceramic coatings, is very high [86]. Hence, it is reasonable to assume that the plastic deformation mechanism responsible for the high hardness as dislocation glide dominated by the lattice resistance [223]. Due to the small indentation scale, the deformation of materials during nanoindentation takes place mainly by plastic flow without cracking. In the present work, only a few indents exhibited cracks, and these were performed at higher loads than the indents considered for data analysis. Therefore, it is reasonable to assume that decreasing hardness of materials studied here with temperature implies decrease in the resistance to dislocation flow.

High temperature nanoindentation was employed to determine the influence of aluminium addition in TiN system on the kinetics of plastic deformation. Due to time constraints, only the TiN_{bulk} and the $Ti_{0.48}Al_{0.52}N$ coating were investigated among the range of compositions studied. These two materials were chosen because their hardness values with temperature marked the ends of the spectrum with respect to mechanical behaviour; $Ti_{0.48}Al_{0.52}N$ coating exhibited both the highest hardness and good hardness stability with temperature, whereas, TiN_{bulk} exhibited lowest hardness and poor hardness stability with temperature. Furthermore, they were the two densest materials studied here, allowing for the

investigation of their plastic deformation kinetics without substantial contribution from porosity. However, as part of future work, this investigation will be extended to all compositions.

Indentation experiments performed at three different loading rates of 0.5, 1 and 10 mN/s made it possible to determine the strain-rate sensitivity of indentation hardness. The Peierls stress of the TiN_{bulk} and the $Ti_{0.48}Al_{0.52}N$ film determined from the shear-stress versus temperature response of the material at a particular strain rate was 6 GPa and 7.2 GPa, respectively, as can be seen in Figure 6-13. The activation volume, V, of the TiN_{bulk} and the $Ti_{0.48}Al_{0.52}N$ film calculated from the slope of the plot of the shear flow stress versus natural logarithm of strain rate at a particular temperature was estimated to be 2.05 x 10^{-29} m^3 (which corresponds to 0.76 x b^3) and 3.06 x 10^{-29} m^3 (which corresponds to 1.14 x b^3), respectively. For a value of 0.3 nm used for b [176, 211], the apparent activation energy of the deformation process, Q, of the TiN_{bulk} was of the order of 0.77 eV, which corresponds to 1.24 x 10^{-19} J, whereas, for the $Ti_{0.48}Al_{0.52}N$ coating, Q was of the order of 1.37 eV, which corresponds to 2.19 x 10^{-19} J.

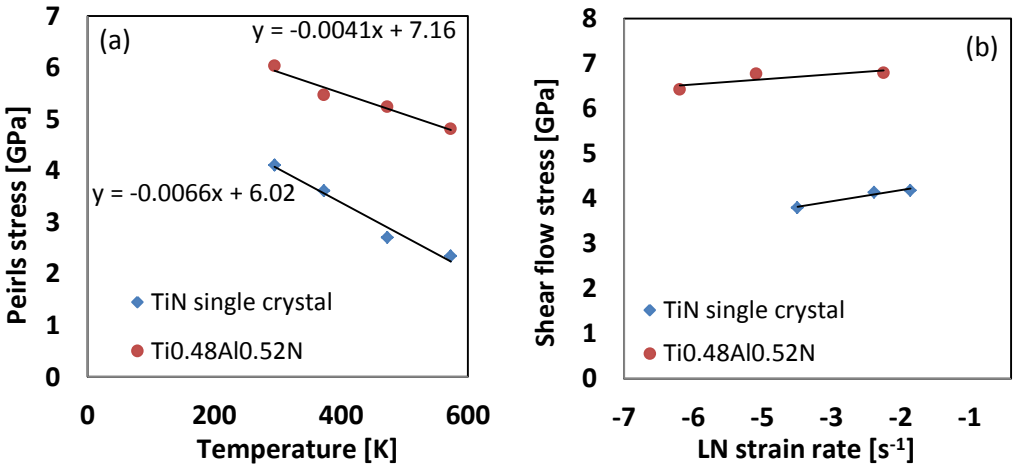

Figure 6-13 (a) The variation of the shear flow stress with temperature for the TiN_{bulk} and the $Ti_{0.48}Al_{0.52}N$ film. The extrapolation of the graph at 0 K gives the Peierls stress. (b) The variation of the shear flow stress vs LN of strain rate for the TiN_{bulk} and the $Ti_{0.48}Al_{0.52}N$ film. The slope of the plot serves for determining the activation volume of the TiN_{bulk}.

These results are reasonable and compare favourably with the literature values for various hard ceramics, such as SiC [86, 224-225], ZrB_2 [86]. The activation volume of the deformation process for both the TiN_{bulk} and the $Ti_{0.48}Al_{0.52}N$ film

was of the order of $1b^3$ indicating that lattice resistance dislocation glide is the deformation rate controlling mechanism.

The apparent activation energy of the deformation process (Q) of the x = 0.52 film was almost double compared to the activation energy of the TiN_{bulk} (with no aluminium content). This increase in the apparent activation energy of deformation process was remarkable and it seemed to be attributed to the presence of the aluminium in the structure. Such an increase in the resistance to plastic flow seems to be responsible for the significant improvement in the hardness and elastic modulus, as well as, their good thermal stability for the x = 0.52 film.

Therefore, it is sensible to conclude that the addition of aluminium in TiN structure led not only to an increase in hardness and elastic modulus, but, thermal stability of these mechanical properties was improved, as well. However, in order to understand why aluminium addition improves mechanical properties of these materials, structural investigations comprising of X-Ray diffraction and TEM analyses were performed on the magnetron sputtered $Ti_{1-x}Al_xN$ coatings.

6.2.3 Influence of aluminium addition on the phase crystallography of the magnetron sputtered $Ti_{1-x}Al_xN$ films

X-ray diffraction analysis revealed that the growth orientation of the magnetron sputtered $Ti_{1-x}Al_xN$ films was (100), which was facilitated by the (100) MgO substrate.

Due to the substitution of titanium atoms with smaller aluminium ones, the lattice parameter decreased, approaching the lattice parameter of MgO. This is shown in the XRD diffractogram by the shift of (200) peak of all ternary coatings towards higher 2θ. For example, the (200) peak of the x = 0.34 film shifted, from 42.62° (peak corresponding to TiN_{film}) to 43.01°, leading to an overlapping with the (200) peak corresponding to the MgO substrate (see Figure 6-14).

All three ternary coatings had an fcc structure. However, the x = 0.34 film exhibited only an fcc lattice corresponding to TiN, whereas, x = 0.52 film had a mixture of two fcc phases, corresponding to TiN and stabilised fcc AlN phase (AlN_{fcc}), respectively. The latter phase is highlighted in the Figure 6-14 by the red arrows, which point towards the corresponding peaks at 2θ values of 37.5°, 62.5°

and a peak-shoulder at 43.5°. The peaks of AlN_{fcc} were shifted towards lower 2θ with respect to pure fcc AlN peak positions [132, 226] (highlighted by dotted vertical lines) because of the presence of larger titanium atoms in the AlN_{fcc} lattice.

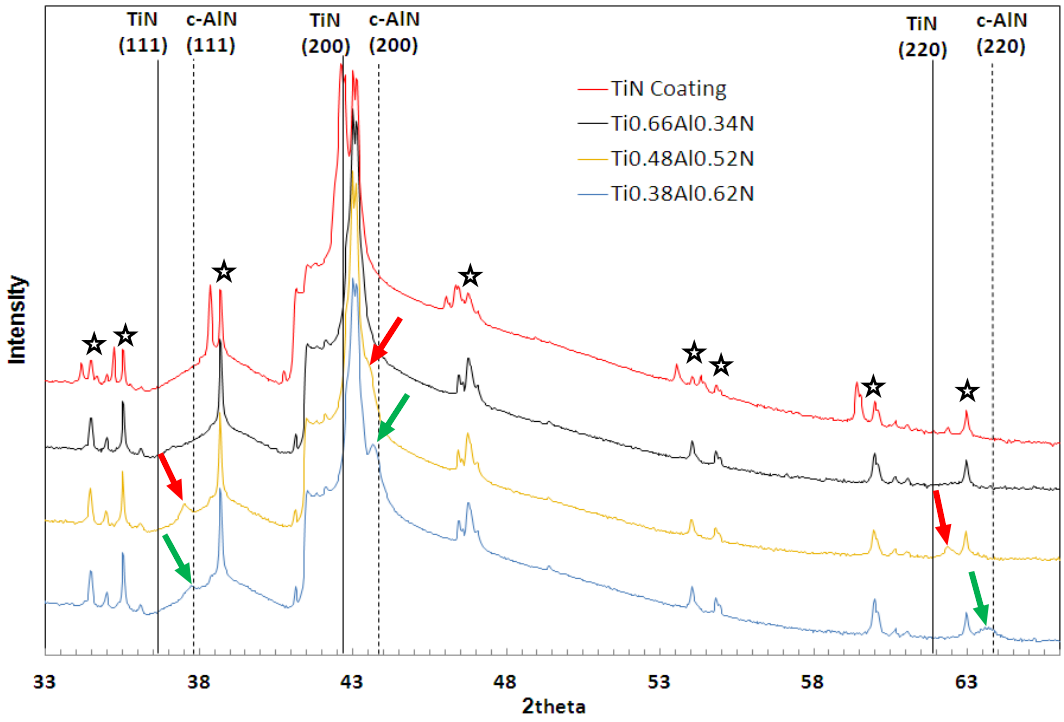

Figure 6-14 Comparative X-ray diffractograms showing the changes in the magnetron sputtered $Ti_{1-x}Al_xN$ structure with addition of aluminium. All films have an fcc lattice. Increasing the Al content led to the formation, alongside fcc TiN phase, of stabilized fcc AlN phase, which is shown by the red and green arrows for films with x = 0.52 and x = 0.62, respectively. The stars represent the peaks attributed to the substrate.

A further addition of aluminium to x = 0.62 led, alongside fcc TiN phase, to an increased in stabilised AlN_{fcc} phase, of which peaks shifted closer to the 2θ of pure fcc AlN peak positions, because of the reduced amount of titanium atoms in AlN_{fcc} lattice. Furthermore, the peak-shoulder at 2θ = 43.5° became an individual peak.

6.2.4 Influence of aluminium addition on the microstructure of the magnetron sputtered $Ti_{1-x}Al_xN$ films

Cross-section bright field images revealed that increasing the aluminium content in magnetron sputtered deposited $Ti_{1-x}Al_xN$ resulted in a finer structure, with a smaller grain size, as shown in Figure 6-15. SADPs suggested a loss in texture with aluminium addition and confirmed that all films had an fcc lattice structure.

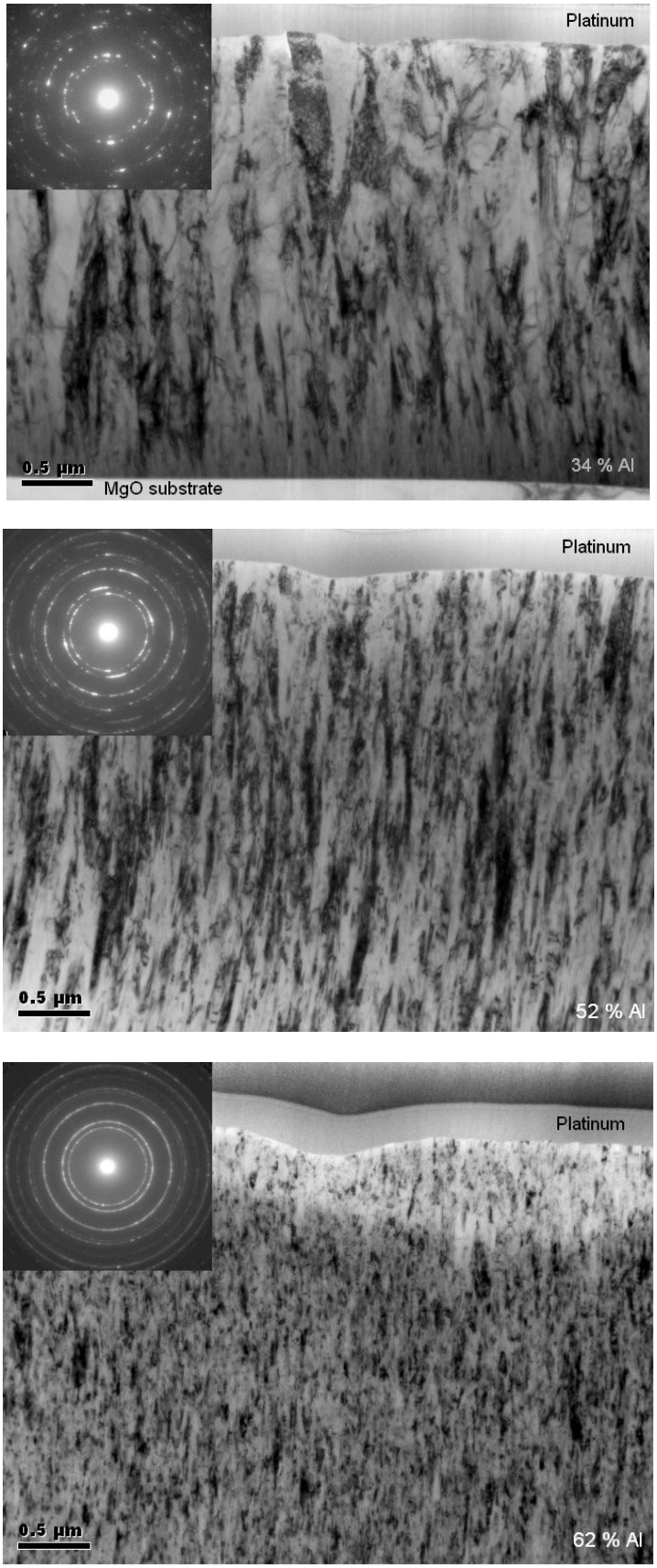

Figure 6-15 Cross-section BF images with the corresponding SADPs showing the changes in the microstructure of the magnetron sputtered $Ti_{1-x}Al_xN$ coatings as a function of Al content. The structure of the films changed from columnar to fibre, the grain size decreased and a loss in texture was evident with aluminium addition.

6.2.5 TEM evidence of cubic nanodomains and the onset of the spinodal decomposition

The secondary phase corresponding to AlN_{fcc} could not be imaged in the as deposited films. However, TEM analysis performed on the x = 0.52 film annealed at 600 °C for 24 hours revealed both crystallographic nanodomains, as shown Figure 6-16. High resolution images showed that nanodomains had the same orientation as the matrix, as can be seen Figure 6-17. Hence, the contrast could not be assigned to various orientations of the nanograins, but to local variations in chemistry.

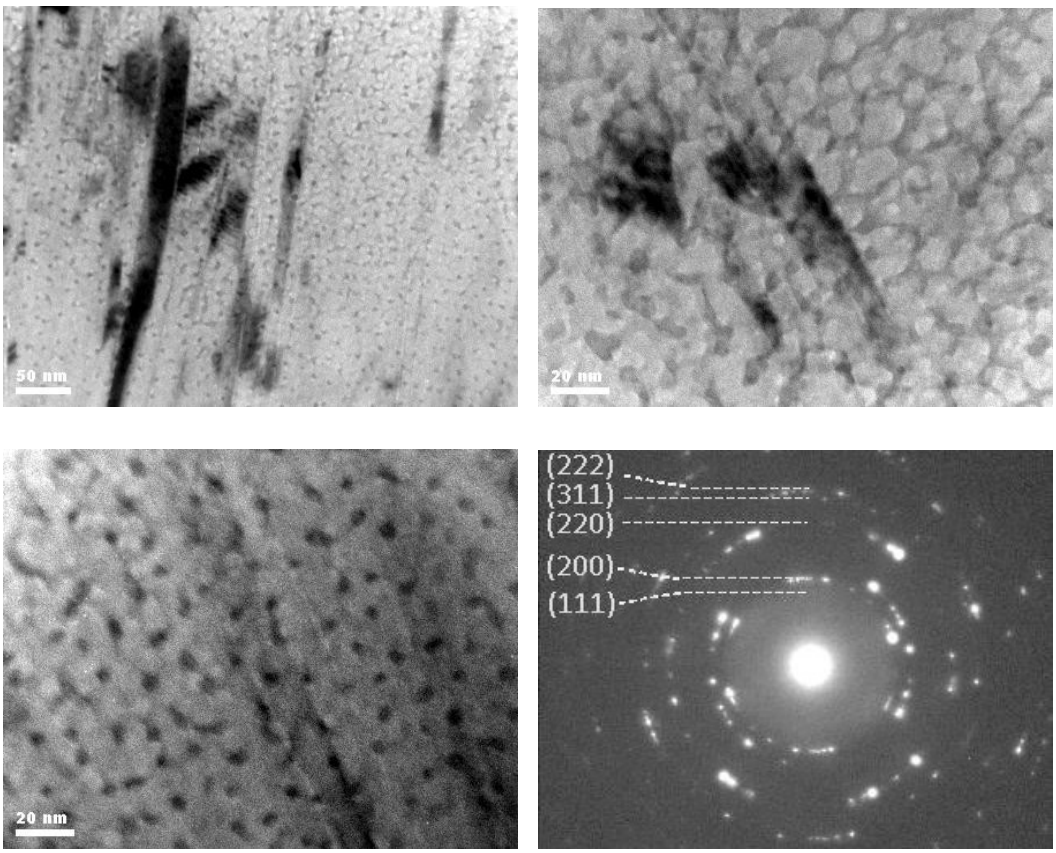

Figure 6-16 Cross-section BF images and SADP of the magnetron sputtered $Ti_{0.48}Al_{0.52}N$ film annealed at 600 °C for 24 hours. Dark nanodomains are expected to be rich in titanium, whereas the aluminium rich nanodomains are the white ones. The grey colour belongs to the matrix, from which the nanodomains had segregated. SADP exhibited a cubic crystallographic phase.

Aluminium rich nanodomains appeared as whitish spots, whereas titanium nanodomains as dark spots or as a dark network. The difference in light intensity is due to different scattering factors of these two elements, with aluminium having a lower one [227]. The grey colour seemed to be the matrix from which the two nanodomains had segregated. The continuity of the crystallographic phase through

the nanodomains suggests the presence of coherent grain boundaries between the nanodomains and the surrounding matrix. The SADPs revealed only a cubic structure. The annealed sample was too small to be analysed by XRD.

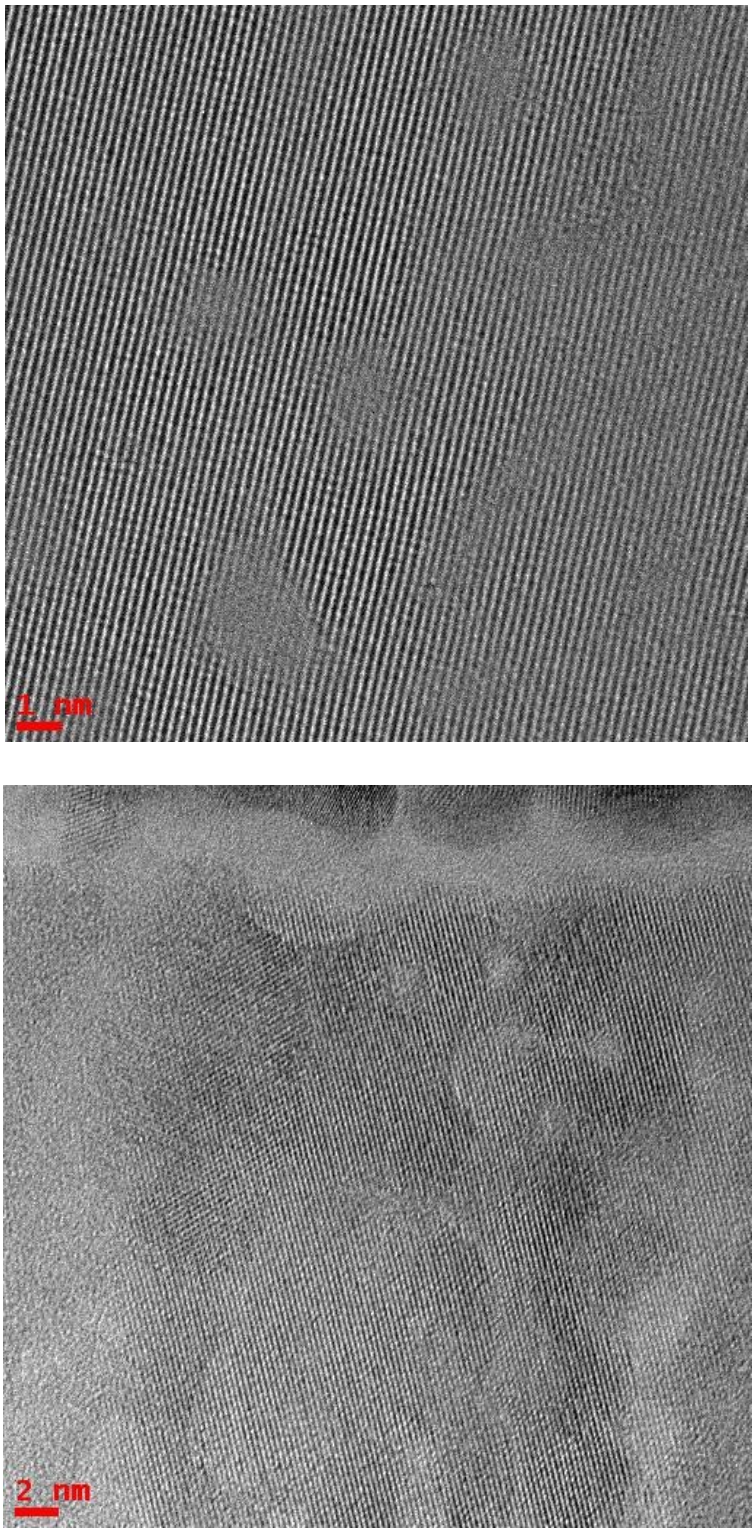

Figure 6-17 High resolution cross-section BF images of the magnetron sputtered $Ti_{0.48}Al_{0.52}N$ film annealed at 600 °C for 24 hours. The nanodomains have the same crystallographic orientation as the matrix.

Increasing the annealing temperature to 800 °C for 24 hours resulted in the onset of the spinodal decomposition. The bright field images, which were quite similar to the one taken from the sample annealed at 600 °C, showed the segregation of two phases, TiN and AlN (see Figure 6-18). However, whereas the SADP of the film annealed at 600 °C showed only a cubic structure, the SADPs from the film annealed at 800 °C exhibited rings corresponding to cubic TiN and hexagonal AlN phases. Comparative studies of diffraction patterns from various aluminium rich $Ti_{1-x}Al_xN$ compositions confirmed that the extra ring present in the film annealed at 800 °C belonged to (10-10) wurtzite structure [172].

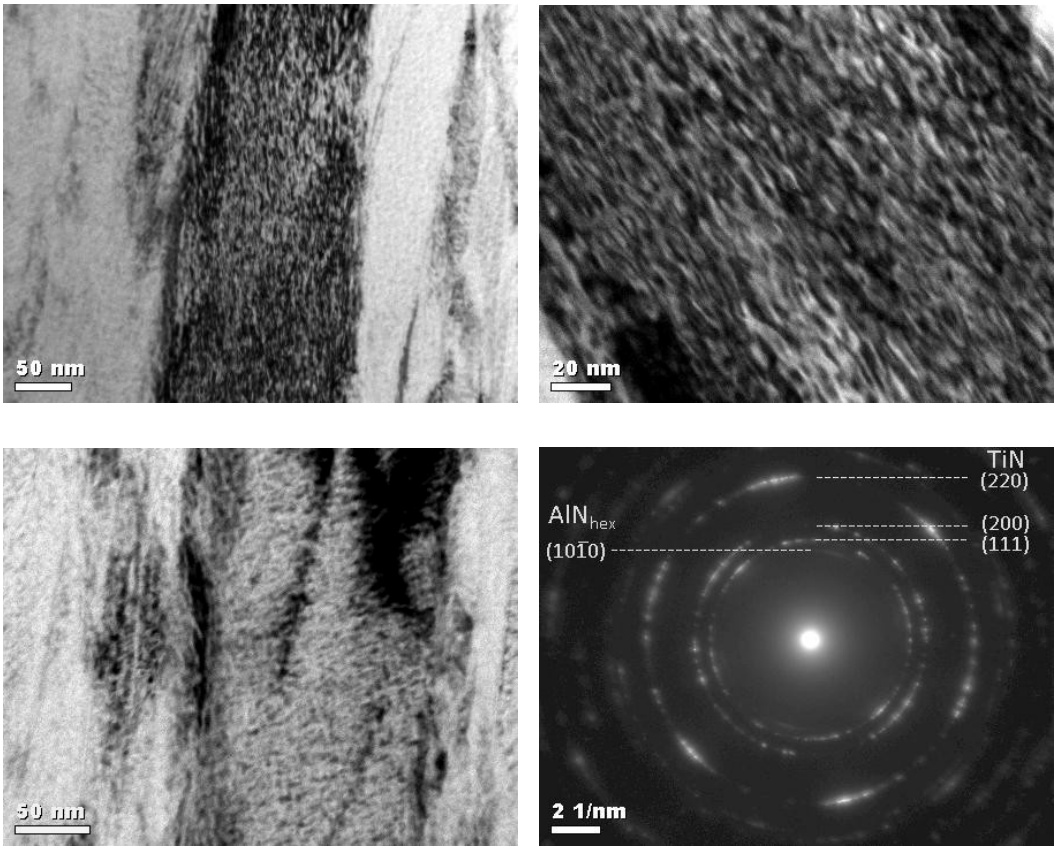

Figure 6-18 Cross-section BF images and SADP of the magnetron sputtered $Ti_{0.48}Al_{0.52}N$ film annealed at 800 °C for 24 hours. Dark nanodomains are expected to be rich in titanium, whereas the aluminium rich nanodomains are the white ones. The grey colour belongs to the matrix, from which the nanodomains had segregated. SADP showed TiN as a dominant phase and hexagonal AlN as a secondary phase.

Another observation was that the spinodal decomposition could be imaged over the whole $Ti_{0.48}Al_{0.52}N$ TEM sample annealed at 800 °C, whereas, the cubic nanodomains (TiN and AlN_{fcc}) could be imaged only in the very thin sections of the sample annealed at 600 °C, around holes.

6.2.6 Influence of aluminium addition on the porosity of the magnetron sputtered $Ti_{1-x}Al_xN$ films

The addition of aluminium to x = 0.34 did not seem to change the amount of porosity, which was mainly detected as fine lines along grain boundaries, similar to the TiN_{film} (see Figure 6-19). However, increasing the amount of aluminium to x = 0.52 seems to promote a denser structure. Although the figure presented below for x = 0.52 shows some porosity, it is not representative because this was an exception. However, this picture was chosen to emphasise the fact that, where porosity was detected (in form of white streaks) in some parts of the film, this was finer compare to the other films.

A further aluminium addition significantly increased the porosity, which is evidentiated by an increase in the pore size and the amount of pores present in x = 0.62 film. Furthermore, the lines of porosity are inter- and intra-columnar, as can be seen in Figure 6-19.

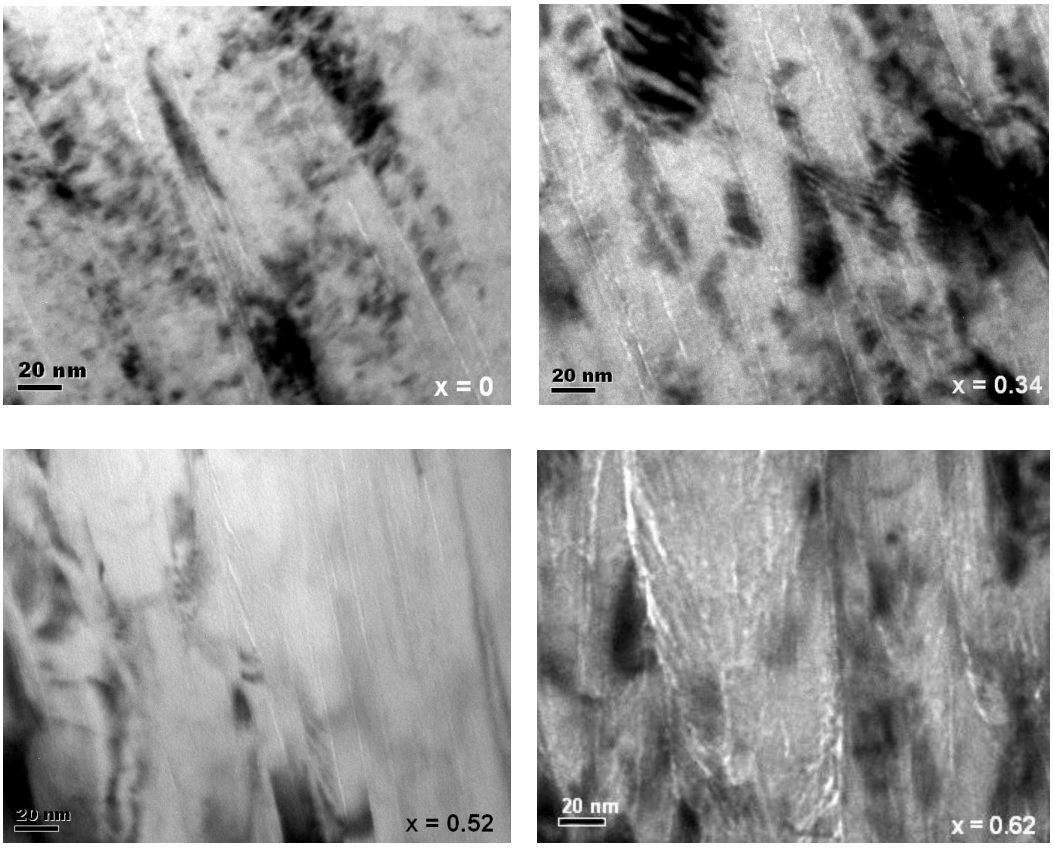

Figure 6-19 Cross-section BF image showing the porosity (in the form of white lines) of the magnetron sputtered TiN and $Ti_{1-x}Al_xN$ films. The x = 0.52 film appeared to exhibit the least porosity, whereas, the rich Al composition (x = 0.62) exhibited a significant amount of porosity intra- and inter-columnar.

6.2.7 Discussion magnetron sputtered $Ti_{1-x}Al_xN$ coatings

Addition of aluminium in TiN system led to higher hardness and elastic modulus and, more importantly, improved thermal stability of these properties. In order to understand the mechanical properties of materials and their behaviour with temperature, a number of factors should be taken in consideration, such as: grain size, porosity, atomic bonding, composition and crystallographic phases.

The influence of the grain size on the hardness of hard ceramics does not follow the general accepted rule that the hardness increases with smaller grain size, as is the case in metals [99, 213-214, 223]. This has also been confirmed in this work by showing that the presence of the grain boundaries in TiN system had a limited contribution towards hardness at ambient temperature and 100 °C. However, at 200 °C and 300 °C the lattice resistance decreased and the influence of the grain boundary increased. Therefore, the impact of the grain size (grain boundary density) of these coatings on hardness values depends on the temperature.

Porosity has been observed to reduce the hardness and elastic modulus of materials [216, 221, 228]. During indentation of a porous material, the deformation includes, alongside the plastic flow, compaction of the material. The higher the porosity, the more significant the fraction of deformation by compaction is. Furthermore, the porosity can act as crack sources, leading to deformation of the material under the indent by cracking [229]. However, data included in the analysis was extracted from small load indents which were shown to be crack free by TEM analysis. Nevertheless, the effects from microcracks cannot be ruled out completely.

Due to the difference between the atomic size (Al = 1.43 Å and Ti = 1.47 Å) and the lengths of the atomic bonding (Ti - N bond > Al - N bond [227]), replacement of titanium with aluminium results in a strained (distorted) TiN type lattice. In addition, the bond strength is expected to increase due to increase in covalency component of the atomic bonding, as aluminium has a closer electronegativity to nitrogen than titanium [103]. The increase in the bond strength with aluminium addition was confirmed in this work by showing that the Peierls stress of x = 0.52

composition was 7.2 GPa, whereas, the Peierls stress of pure TiN lattice was 6 GPa.

It has been shown that the solid solution effect due to aluminium addition in TiN lattice led to an increase in the apparent activation energy of the deformation process. This means a higher force is required to activate the plastic flow (to move dislocations over obstacle), which is translated in a higher hardness of the material.

XRD analysis revealed that the x = 0.34 film had an fcc TiN structure, whereas, the x = 0.52 and x = 0.62 films exhibited, alongside an fcc TiN structure, a stabilised AlN_{fcc} crystallographic phase.

Interpretation of the results

The x = 0.52 film exhibited high hardness and elastic modulus and, more importantly, improved thermal stability. The higher hardness and elastic modulus could be attributed to a denser structure (less porosity than x = 0.34 film) coupled with a further increase in the bond strength and the lattice strain. However, in order to understand the improved hardness stability with temperature, a closer look at the changes in the lattice structure, due to the replacement of almost 50 at % titanium with aluminium, is required.

XRD analysis revealed the as deposited x = 0.52 and x = 0.62 films exhibited stabilised AlN_{fcc} as a secondary phase. The presence of this phase in the as deposited films came as a surprise because the literature data show that the AlN_{fcc} phase can form either by (1) epitaxial deposition of nanolayers of AlN_{fcc} on TiN [227, 230], (2) during the spinodal decomposition of aluminium rich $Ti_{1-x}Al_xN$ films [109, 126, 130], and (3) during the phase transition from wurtzite AlN at high pressure [132]. In order to understand how the secondary phase AlN_{fcc} formed in the as deposited magnetron sputtered x = 0.52 and x = 0.62 films, a simple explanation is suggested next.

The maximum lattice distortion due to the replacement of titanium atoms with aluminium ones is expected to be reached for an atomic stoichiometric composition Ti:Al = 50:50, for an ideal homogeneous distribution of atomic species, as it is shown schematically in Figure 6-20.

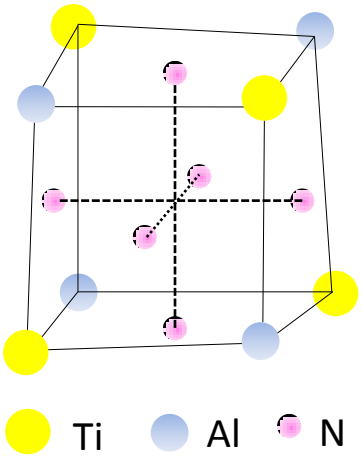

Figure 6-20 Schematic representation of the ideal distribution of atomic species in a distorted lattice of $Ti_{0.5}Al_{0.5}N$. The distortion from a perfect cube is greatly exaggerated.

However, due to inherent differences in the vapour production from the targets, vapour transport through the "vacuum" towards the substrate and vapour condensation onto the substrate, it is expected a less uniform distribution of atomic species [176]. Therefore, in some parts of the deposited film the aluminium concentration can be slightly higher, leading to the formation of the fcc lattice with more Al atoms than Ti ones. This lattice corresponds to stabilised AlN_{fcc}.

The pure AlN_{fcc} lattice is almost 4% smaller than TiN one [227]. However, phases present in $Ti_{1-x}Al_xN$ films are not in their pure form as TiN and AlN_{fcc}. Due to the replacement of titanium atoms with smaller aluminium ones, the actual lattice parameter of TiN(+Al) phase is expected to be smaller than that of pure TiN. In a similar manner, replacement of aluminium atoms in an AlN_{fcc} lattice with bigger titanium atoms results in a larger lattice parameter compared to pure AlN_{fcc}. As a result, the gap difference between the lattice parameters of the two fcc phases present in the structure is expected to be smaller than 4%. The distortion and the dimensional variation of the lattice due to these atomic substitutions are schematically presented in Figure 6.20.

The lattice mismatch is accommodated by distortion of the lattices in order to form coherent grain boundaries between nanodomains, leading to a coherent strained lattice structure.

In addition, another factor that might contribute to the high temperature performance improvement of these ternary coatings could be attributed to, presumably, the different critical resolved shear stresses of TiN and AlN_{fcc} phases.

However, AlN_{fcc} is a metastable phase and it has been obtained in nanometre domains only, which makes it difficult to determine its mechanical properties. Therefore, the presence in the structure of both fcc crystallographic phases, TiN and stabilised AlN_{fcc} seems to have an important role in improved hardness stability with temperature for the x = 0.52 film.

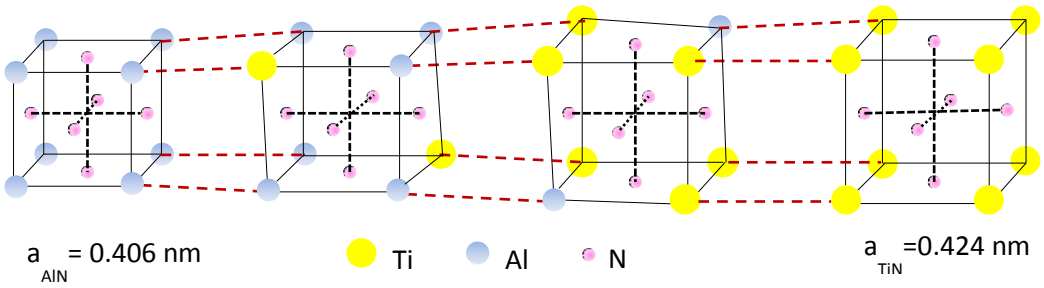

Figure 6-21 Schematic representation of the lattice distortion as a result of the size difference between the metalic species. The second left lattice suggests that when the concentration of Al atoms reaches a certain level, stabilised AlN_{fcc} lattice form. The intermediate phases, which are ternary compositions, are the ones expected to be present in the structure. The difference between their lattice parameters is expected to be smaller than 4%.

A further addition of aluminium to x = 0.62 resulted in more AlN_{fcc} nanodomains, which were expected to lead to a more strained lattice structure, compared to the x = 0.52 film. The increase in coherency strain due to the presence of the two lattices resulted in a better thermal stability.

Therefore, it is suggested that for good hardness stability with temperature of these ternary coatings the presence of both fcc crystallographic phases, TiN and stabilised AlN_{fcc}, is required.

The hardness and elastic modulus values of the x = 0.62 film were smaller compared to the x = 0.52 film. The lower values of the x = 0.62 film were attributed to significantly increased porosity, which was inter- and intra-columnar, as shown in Figure 6-19.

6.3 Indentation study of arc evaporated $Ti_{1-x}Al_xN$ films

Due to the deposition process, the structure of cathodic arc evaporated $Ti_{1-x}Al_xN$ films, which are used industrially, is less homogeneous compared to magnetron sputtered films [26, 146]. The former are known to have large structural defects, such as droplets, which affect the mechanical properties of these films [147].

The industrial cathodic arc evaporated $Ti_{1-x}Al_xN$ (x = 0.44; x = 0.6; x = 0.7) coatings were initially investigated at room temperature, to acquire a good understanding of their mechanical properties with the aluminium content and deposition bias. Then the investigation at high temperature of x = 0.6 film was performed by nanoindentation at 100 °C, 200 °C and 300 °C.

6.3.1 Room temperature mechanical properties of the industrial cathodic arc evaporated $Ti_{1-x}Al_xN$ as a function of aluminium concentration and deposition bias

The hardness of the cathodic arc deposited $Ti_{1-x}Al_xN$ films increased with substrate bias, as presented in Figure 6-22, which is in line with the literature data [231]. However, the extent of the increase in hardness was different for each coating; the substrate bias had the least effect on the hardness of x = 0.7 film and the strongest effect on the hardness of x = 0.6 film. The hardness of the latter film increased significantly, from 20.5 GPa at 20 V bias to 28 GPa at 40 V bias.

For films deposited at 20 V bias, addition of aluminium yielded lower hardness values. However, at higher deposition bias, x = 0.44 to x = 0.6 films exhibited similar hardness values. An increase in aluminium content to x = 0.7 resulted in lower hardness values at all three deposition biases.

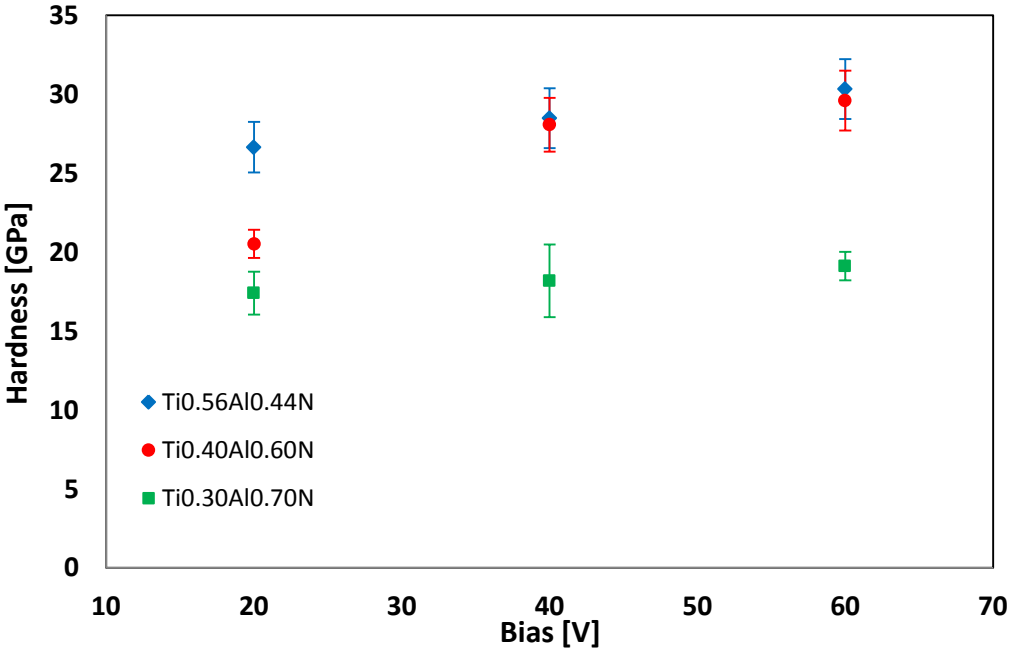

Figure 6-22 The hardness variation of cathodic arc deposited $Ti_{1-x}Al_xN$ films with substrate bias and aluminium content. Each data point with corresponding standard deviation are calculated from 10 indents.

The elastic modulus of cathodic arc evaporated $Ti_{1-x}Al_xN$ coatings exhibited small variations with deposition bias, as shown in Figure 6-23. The x = 0.44 films exhibited the highest elastic modulus and its values showed a slight decrease with increase in bias. On the contrary, the x = 0.6 and x = 0.7 films showed a slight increased elastic modulus values with bias.

It is noticed that aluminium addition lowered the elastic modulus values, irrespective of the deposition bias. A similar effect of aluminium content on elastic modulus has been shown by Horling et al. [30] and Santana et al. [172].

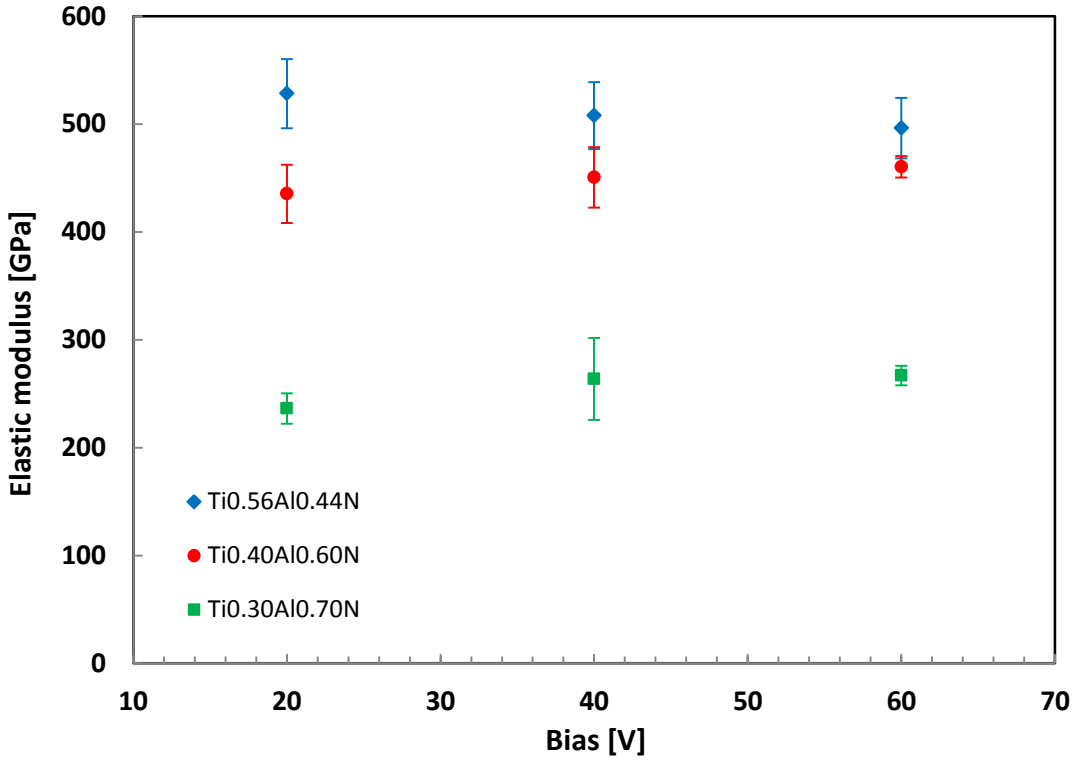

Figure 6-23 The elastic modulus variation of cathodic arc deposited $Ti_{1-x}Al_xN$ films with substrate bias and aluminium content. Each data point represents the average data gathered from 10 indents.

In order to understand and explain why and how the addition of aluminium and the substrate bias changed mechanical properties of the cathodic arc evaporated films, phase composition and structural analyses of these materials were performed by XRD and TEM. The structural investigation is presented next for each composition, starting with low aluminium content.

6.3.2 $Ti_{0.56}Al_{0.44}N$

Variation of phase composition with substrate bias

X-ray diffraction analysis revealed that the x = 0.44 films deposited at low and intermediate bias (20 V and 40 V) had a similar fcc TiN phase crystallography, with preferential (200) orientation, as shown in Figure 6-24. A further increase in deposition bias to 60 V promoted, alongside TiN phase, a secondary phase corresponding to stabilised cubic AlN_{fcc} lattice, phase highlighted by the diffraction peak at $2\theta = 43.8°$. In addition, (111) TiN diffraction peak at $2\theta = 36.8°$ spread towards larger two theta angles in a similar manner to (200) peak, which suggested an overlap with the peak corresponding to (111) AlN_{fcc} phase. This observation is in agreement with Santana et al. work, in which an XRD diffraction pattern (see Figure 6-25) from a similar cathodic arc composition ($Ti_{0.6}Al_{0.4}N$) film deposited at a higher bias (100 V) was discussed [232].

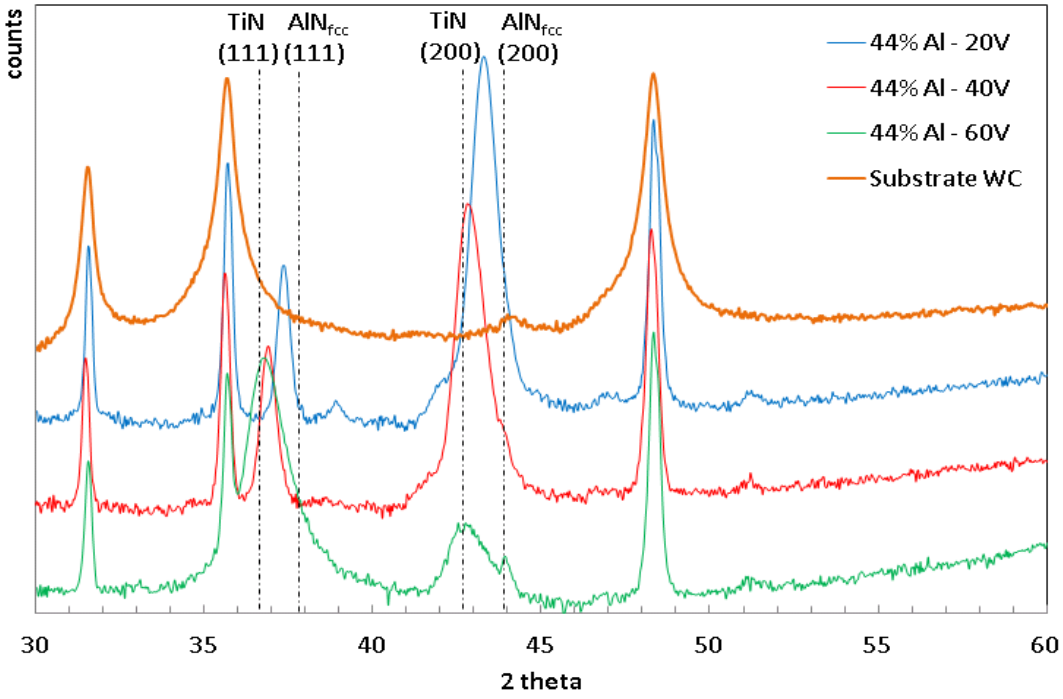

Figure 6-24 Comparative X-ray-diffraction patterns from cathodic arc $Ti_{0.56}Al_{0.44}N$ films deposited at three biases, together with the diffraction pattern corresponding to the WC (6% Co) substrate. The expected positions for reflections from pure NaCl-structure TiN are shown.

Alongside the formation of secondary phase, the growing orientation of the film changed from (200) to (111) with increasing deposition bias, which is in line with literature data [117, 171-173]. This effect is also illustrated in Santana et al. work, in Figure 6-25.

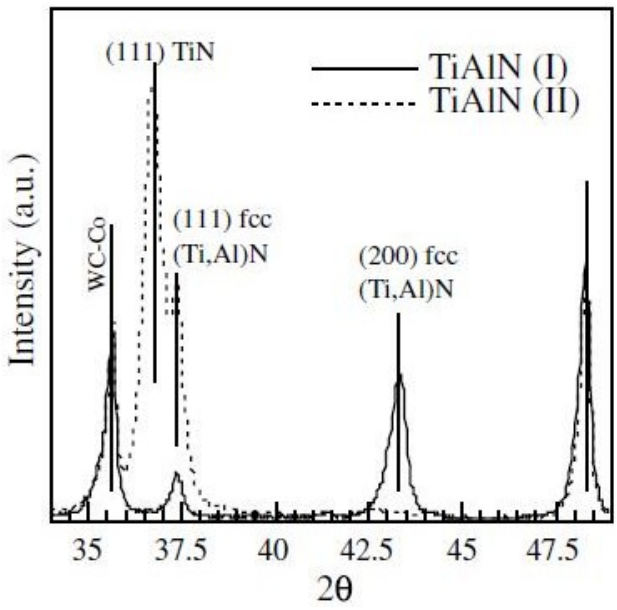

Figure 6-25 X-ray diffraction spectra from cathodic arc $Ti_{0.6}Al_{0.4}N$ deposited at low (I) and high (II) bias (100 V) from [232]. The dotted diffractogram corresponds to the film deposited at high bias and presented a peak at 37.36° which appears to come from TiAlN composition which has an AlN_{fcc} phase.

On the one hand, the diffraction peaks of the film deposited at low bias were shifted to higher 2θ with respect to the positions corresponding to pure TiN (highlighted by black dotted vertical lines in Figure 6-24.). Larger 2θ angles suggest a smaller lattice parameter. The shrinkage of the lattice is attributed to the substitution of titanium atoms with smaller aluminium ones [5, 103, 114]. On the other hand, increasing in deposition bias shifted the peaks to smaller 2θ, which correspond to a higher lattice parameter. Therefore, the lattice parameter (reflected by the 2θ position of the peak) is influenced by both aluminium content and bias [118].

The increase in lattice parameter with bias has been attributed to the implantation of gas atoms in the interstices of the lattice [2, 97, 118, 171, 175, 217-218]. Because of that, films synthesized at high deposition energy are reported to exhibit high internal compressive stresses [117, 174]. In the same time, the change in orientation with the deposition bias seems to be linked to the interstices of the lattice, as well. Higher bias promotes (111) growth orientation [117, 172-173, 175]. This orientation has been shown to exhibit the highest volume of interstitial voids, which accommodate the implanted gas atomic species in the structure [175].

Variation of crystallography with substrate bias

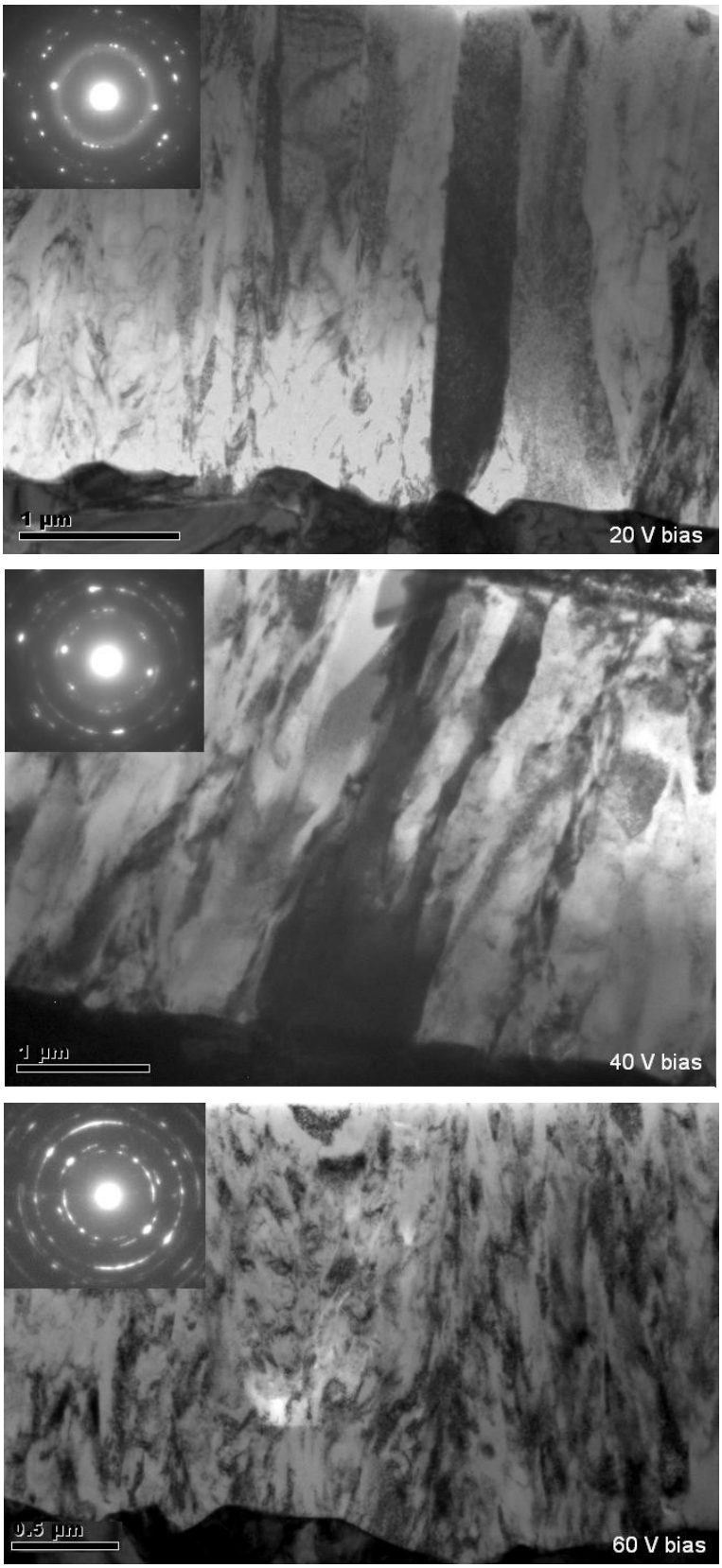

Figure 6-26 Bright field cross-section TEM images with corresponding SADPs of $Ti_{0.56}Al_{0.44}N$ films deposited at: 20 V bias, 40 V bias, 60 V bias. The increase in bias leads to a loss in texture and a smaller grain size.

The film deposited at the lowest bias (20 V) presented a well-developed columnar morphology, with some columns grown from the film-substrate interface up to the coating surface (see Figure 6-26 (a)). Throughout the film thickness the columns exhibit a slight rotation around the [001] growth direction. SADP confirmed the XRD findings that the $Ti_{0.56}Al_{0.44}N$ films exhibited fcc B1 NaCl structure at all three deposition biases.

Bright field images showed that higher bias promoted a denser structure, with a smaller grain size and a less well defined columnar morphology evidenced by continuous renucleation (Figure 6-26). The transition of SADPs from a spot pattern to a ring one confirmed a loss in texture with deposition energy.

An interesting feature presented by the film deposited at the highest bias (60 V) was a nanolayered structure superimposed on the columnar structure, as shown in Figure 6-27. These nanolayers seemed to be formed due to the rotation of the sample holder with respect to aluminium and titanium targets. In the next chapter it will be shown that the presence of these nanolayers seems to be linked to the formation of the rock-salt structure AlN_{fcc} as a secondary phase.

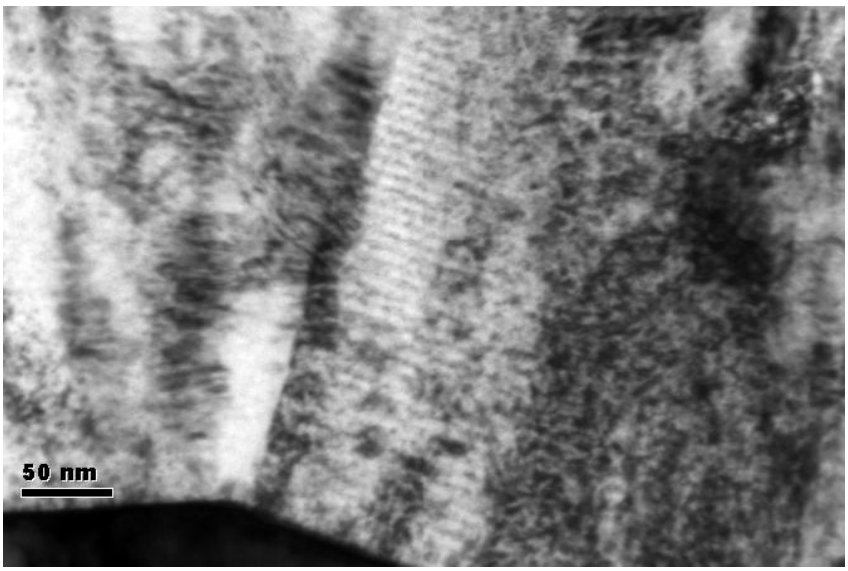

Figure 6-27 Bright field cross section TEM images of cathodic arc $Ti_{0.56}Al_{0.44}N$ deposited at 60 V bias showing a nanolayered structure alongside the columnar one.

Film porosity

The porosity of the x = 0.44 films was mainly concentrated around the droplets. With the increase in bias the size of the droplets seemed to decrease, as shown in Figure 6-28.

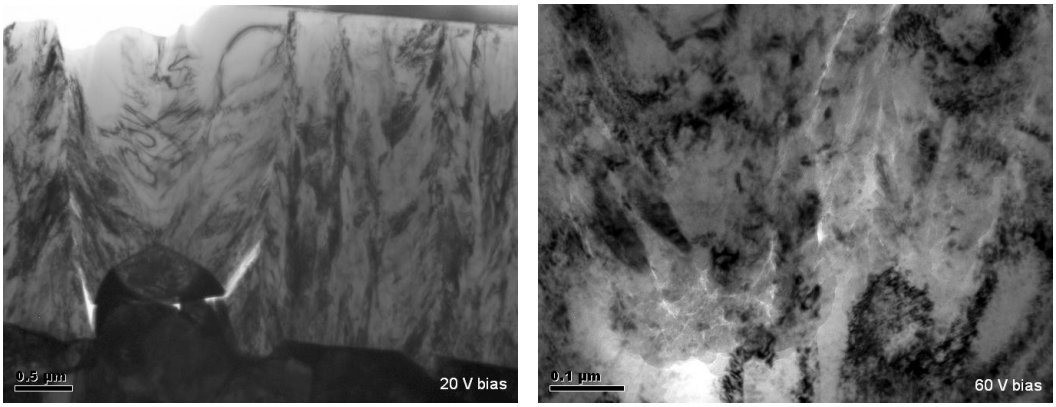

Figure 6-28 Bright field cross-section TEM images showing droplets in the structure of $Ti_{0.56}Al_{0.44}N$ films deposited at 20V bias and 60V bias

Discussion of $Ti_{0.56}Al_{0.44}N$ films

The increase in hardness of x = 0.44 films with bias (see Figure 6-22) seems to be attributed to the fact that, higher bias promoted a denser structure with fewer droplets. In addition, the shift of diffraction peaks to lower 2θ angles with bias suggests an increase in compressive stresses, stresses which are expected to contribute to an increase in hardness [231]. Furthermore, increasing in bias led to a change in the growing orientation from (200) to (111), and, literature data shows that the latter orientation exhibits higher hardness [117, 172]. Another contributor to high hardness of the film deposited at 60 V bias seemed to be the presence of the secondary phase corresponding to AlN_{fcc} lattice.

Despite the fact that higher bias yielded a denser structure, the elastic modulus of x = 0.44 films decreased slightly with bias. This is in line with Ahlgren et al. [117] and Santana et al. [172] results, which show that the elastic modulus of a cathodic arc film of a similar composition to the one discussed here is lower for (111) orientation compared to (200) one.

6.3.3 $Ti_{0.40}Al_{0.60}N$

Variation of phase composition with substrate bias

The x = 0.6 film exhibited a phase transition with an increase in substrate bias from 20 V to 60 V, as shown in Figure 6-29. The film synthesised at 20 V bias exhibited a mixture of two crystallographic phases: the main one corresponding to TiN and the secondary one corresponding to hexagonal AlN. The latter phase was evidenced by the presence of individual peaks at 2θ of 32.6 and 58.3 degrees. These peaks were shifted towards smaller 2θ with respect to pure AlN_{hex} phase due to the presence of larger titanium atoms in the AlN_{hex} lattice, which results in a larger lattice [233]. In addition, as already mentioned, these films were expected to have residual compressive stresses [117], which shifted the diffraction peaks to even smaller 2θ.

Increasing the bias to 40 V led to the deposition of films which exhibited only one crystallographic phase corresponding to fcc TiN. A further increase in deposition bias to 60 V led, alongside fcc TiN phase, to the formation of stabilised AlN_{fcc} as a secondary phase. The presence of the latter phase is marked by a pronounced shoulder at 2θ = 43.9 degrees. The diffraction peaks corresponding to AlN_{fcc} phase were shifted to larger two theta angles compared to x = 0.44 films, due to an increased amount of aluminium, as shown in Figure 6-30.

The (111) TiN diffraction peak moved towards larger 2θ angles in a similar manner to (200) peak, which suggested an overlap with the peak corresponding to (111) AlN_{fcc} phase. These features are very much like the ones presented by the x = 0.44 film deposited at the same bias, as shown in Figure 6-30.

Similar to x = 0.44 film, the increase in bias promoted (111) crystallographic orientation.

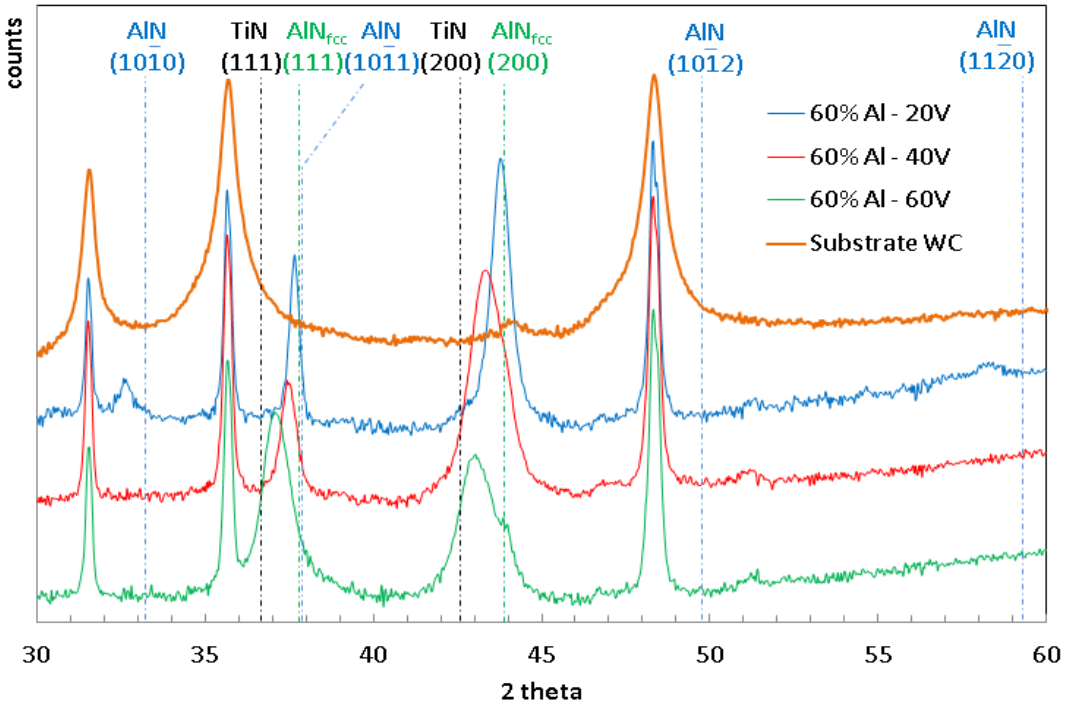

Figure 6-29 Comparative X-ray-diffraction patterns from cathodic arc $Ti_{0.4}Al_{0.6}N$ films deposited at three biases, together with the diffraction pattern corresponding to the WC (6% Co) substrate. The expected position for reflections from pure NaCl-structure TiN and wurtzite structure AlN are shown.

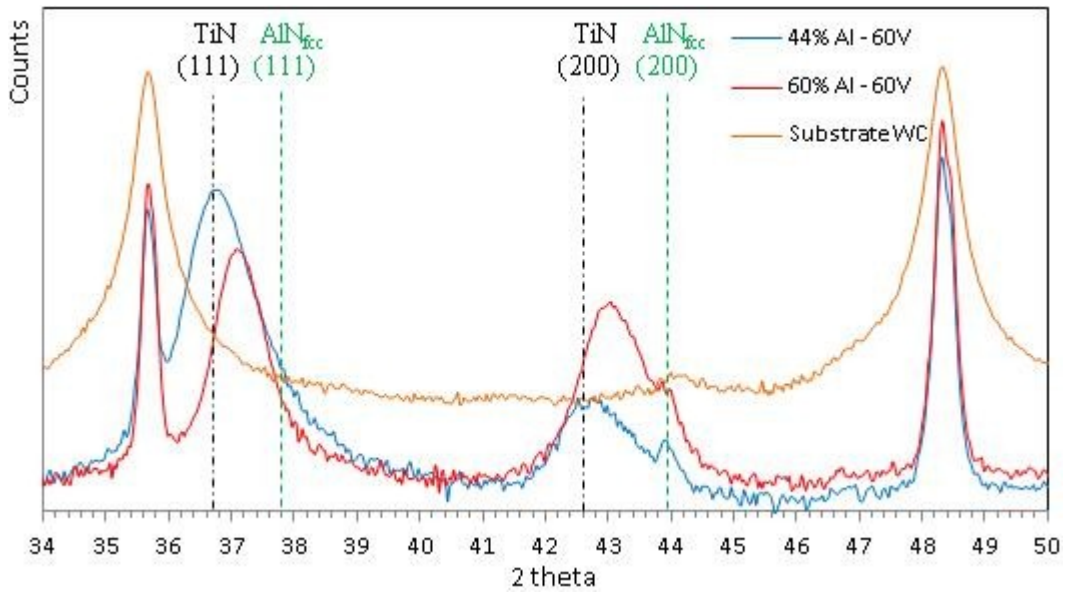

Figure 6-30 Comparative X-ray-diffraction patterns from cathodic arc films $Ti_{0.56}Al_{0.44}N$ and $Ti_{0.4}Al_{0.6}N$ deposited at 60 V bias, showing the structural similarities between the two films. Alongside is plotted the diffraction pattern corresponding to the WC (6% Co) substrate. The expected position for reflections from pure NaCl-structure TiN and stabilised cubic AlN_{fcc} are shown. The shoulder and the peak at two theta 43.9° correspond to (200) $AlN_{fcc.}$ Furthermore, the (111) TiN peaks were asymmetric and extended towards larger two theta. This asymmetry suggested the presence of (111) AlN_{fcc} which overlapped with the (111) TiN.

Variation of morphology with the substrate bias

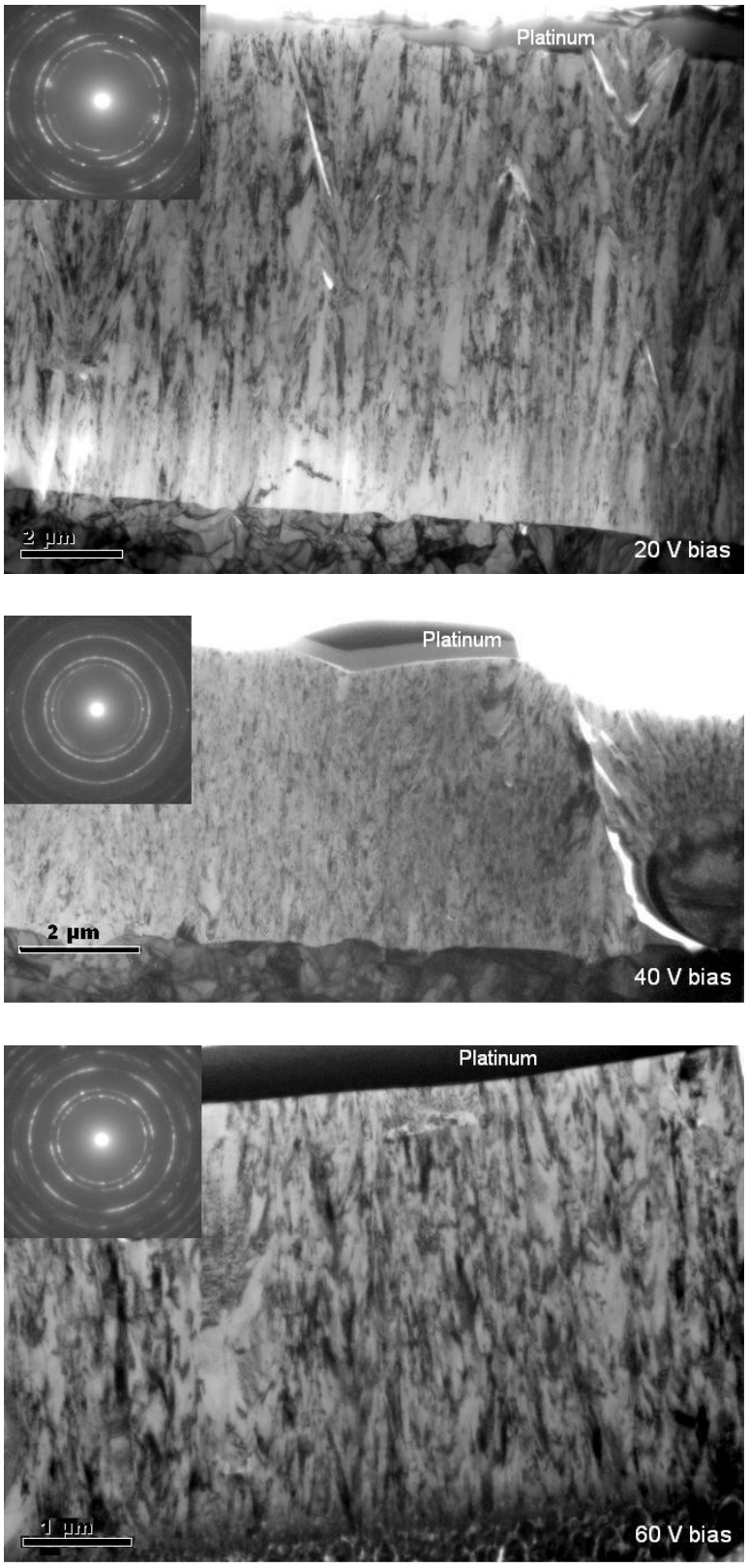

Figure 6-31 Bright field cross-section TEM images with corresponding SADPs of $Ti_{0.40}Al_{0.60}N$ films deposited at 20 V bias, 40 V bias and 60 V bias. The increase in bias promotes a denser structure with fewer defects and a smaller grain size.

The x = 0.6 film deposited at 20 V bias exhibited an open columnar morphology with significant porosity, due to the shadowing effect of the growing columns (see Figure 6-31). Increasing the deposition bias promoted a denser structure with continuous columnar renucleation and a smaller grain size.

SADP confirmed the XRD results that the x = 0.6 film deposited at 20 V exhibited a secondary phase which corresponds to AlN_{hex}. However, increasing the bias to 40 V decreased the amount of secondary phase; faint rings corresponding to hexagonal phase were still present in SADP. This suggested the presence of a very small amount of AlN_{hex}, which seems to be under the detection capability of XRD equipment used. A further increase in the deposition bias to 60 V completely suppressed the formation of the AlN_{hex} phase, as illustrated in Figure 6-32.

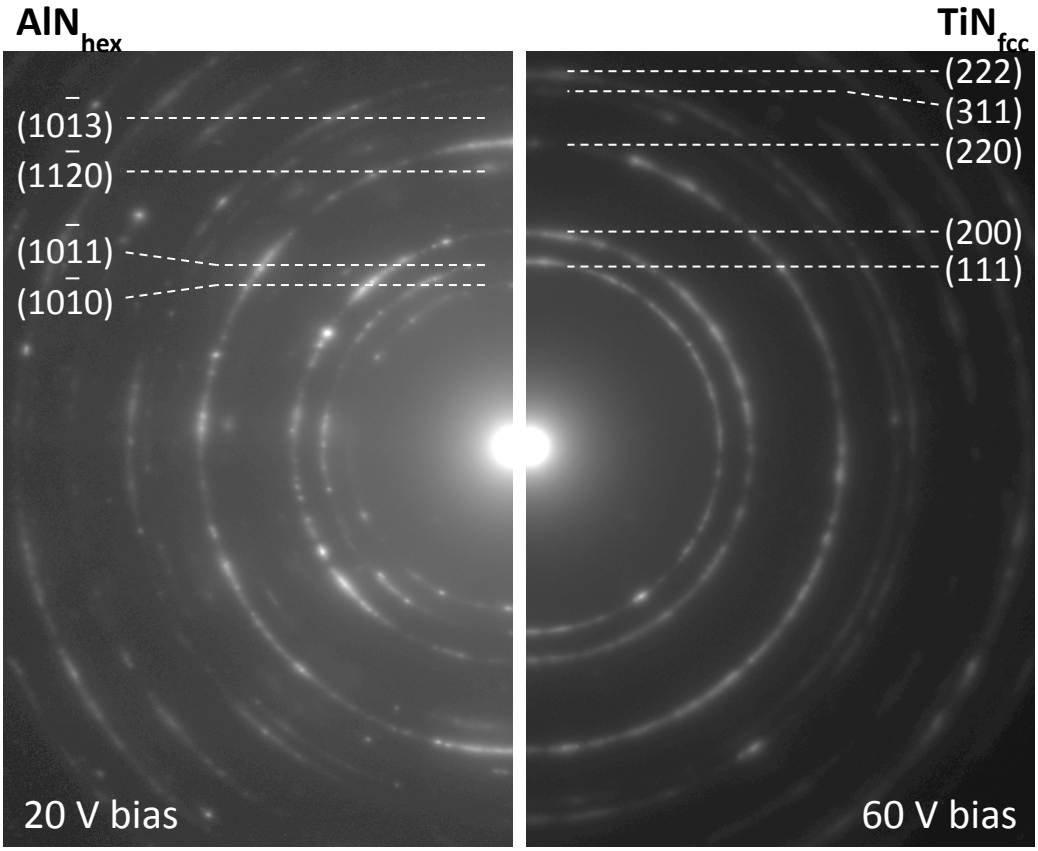

Figure 6-32 The area diffraction pattern of the $Ti_{0.40}Al_{0.60}N$ film deposited at 20 V bias exhibited rings corresponding to two crystallographic phases: hexagonal AlN and fcc TiN. The film deposited at 60 V bias exhibited only fcc TiN phase.

The x = 0.6 film deposited at 20 V bias exhibited big droplets which disrupted the texture throughout the film thickness, as shown in Figure 6-33. Increasing in deposition energy led to coatings with a denser structure, although droplets were still present in the film.

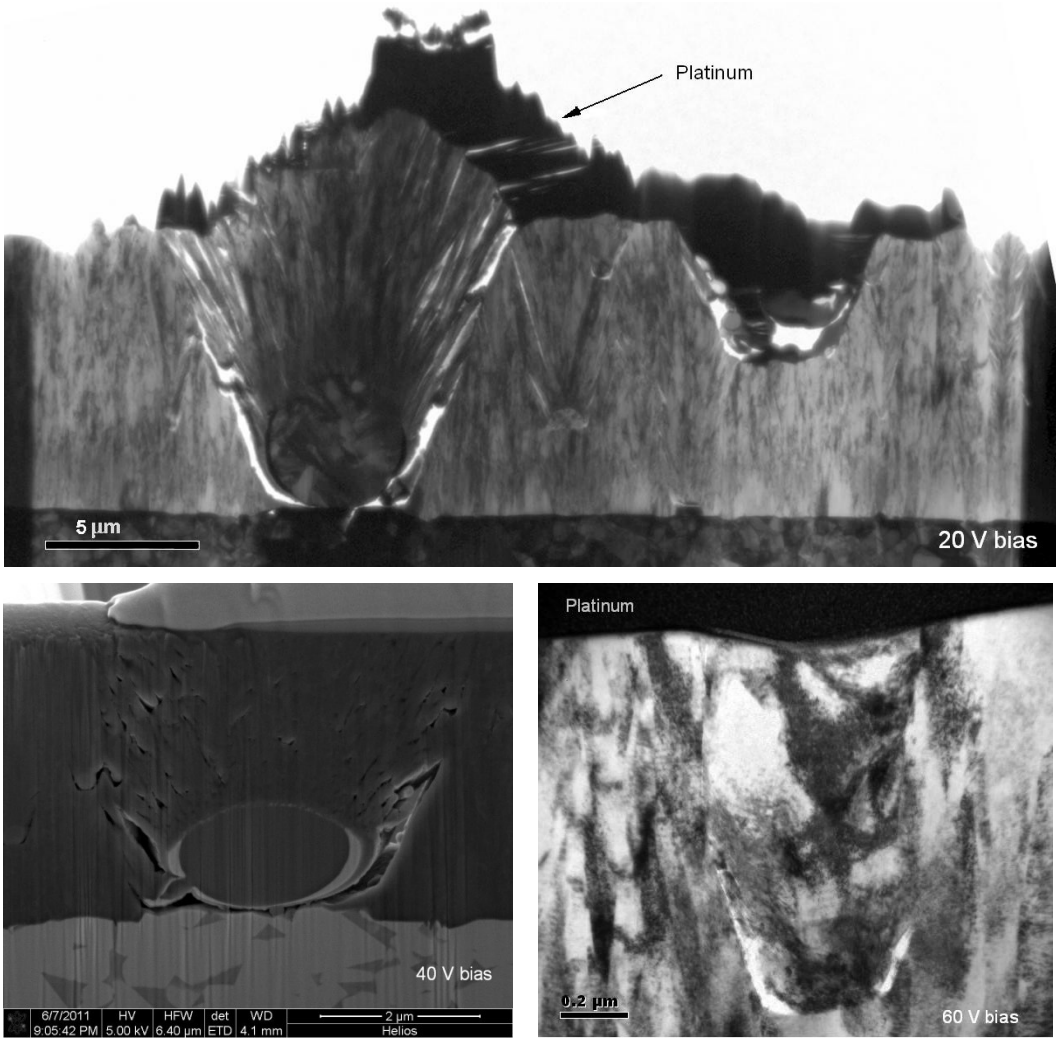

Figure 6-33 Big droplets disrupt the growth throughout the film thickness of the $Ti_{0.40}Al_{0.60}N$ films. The TEM foil of the film deposited at 20 V was made from unpolished film in order to highlight the origin of the surface roughness. If a droplet is big, it creates a large nucleation site, which outgrowths compared to the rest of the film and it swells, leading to significant shadowing which results in big voids. The film deposited at 40 V bias had big droplets as well, as shown in SEM image taken at 60 ° during FIB milling. Due to the high energy of deposition, the film deposited at 60 V substrate bias exhibited smaller droplets and the shadowing effect is reduced in the subsequent deposition stages.

The x = 0.6 coating deposited at 60 V revealed a nanolayered structure superimposed on the underlying columnar structure (see Figure 6-34). Similar nanolayers, but not to the extent presented by this film were found in the x = 0.44 coating deposited at the same bias (60 V). This feature is expected to come from

the local change in the chemistry of the film due to the rotation of the substrate holder with respect to Ti and Al targets during deposition [232]. However, the films with the same compositions, but deposited at lower biases, did not show such features and did not exhibit the AlN_{fcc} secondary phase either.

This variation in chemistry, which led to the formation of nanolayers, seemed to have promoted the formation of the secondary phase corresponding to AlN_{fcc} lattice. Literature data has shown that the high-pressure rocksalt structure of AlN_{fcc} can be stabilised in nanolayers of maximum 2 [227] to 3 nanometers [230]. However, the nanolayers discussed in literature were pure TiN and AlN_{fcc}, whereas, in the present work the nanolayers are 10 – 15 nanometers and have ternary compositions. The AlN_{fcc} lattice is expected to form in rich aluminium nanolayers, which appeared slightly lighter than the titanium rich nanolayers [227]. Hence, there seems to be a link between the formation of nanolayers and the presence of AlN_{fcc} type phase.

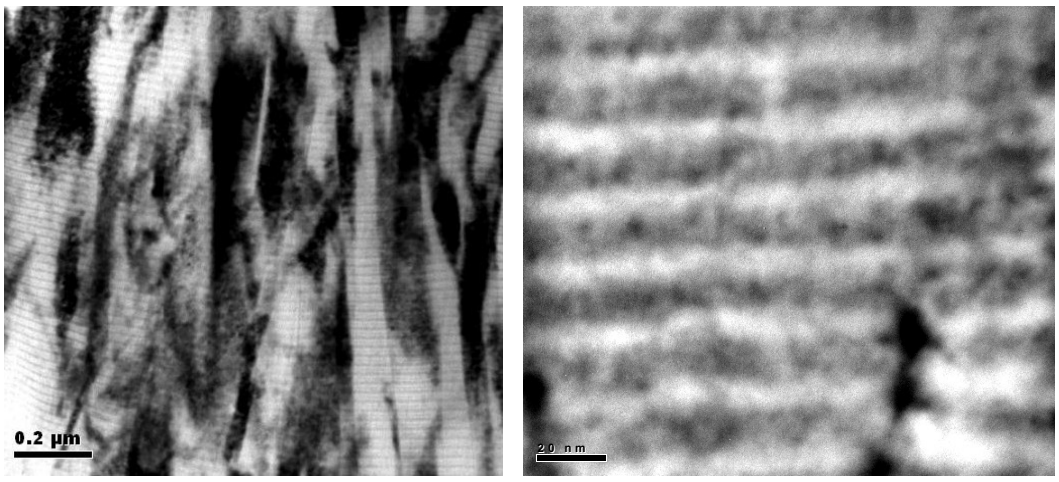

Figure 6-34 Bright field cross section TEM images of $Ti_{0.40}Al_{0.60}N$ deposited at 60 V bias showing the nanolayered structure superimposed on the underlying columnar structure

Discussion of $Ti_{0.4}Al_{0.6}N$ films

The low hardness of the x = 0.6 film deposited at 20V bias compared to the one exhibited by films deposited at 40V and 60V was attributed to porous structure and the presence of the softer AlN_{hex} phase. Increasing the bias to 40 V led to a denser structure with a smaller grain size and suppressed the formation of AlN_{hex} phase, resulting in a significant increase in hardness values (Figure 6-22). A

further increase in bias to 60 V resulted in slightly improved hardness values, which seemed to be attributed to the formation of the secondary phase corresponding to AlN_{fcc} lattice.

The small increase in elastic modulus values with bias could be attributed to the densification of the film at higher deposition energy. These explanations are in line with the literature data, in which it has been shown that porosity reduces the hardness and elastic modulus of materials [216, 221, 228].

6.3.4 $Ti_{0.30}Al_{0.70}N$

Variation of phase composition with substrate bias

The x = 0.7 films exhibited a completely different phase structure compared to x = 0.44 and x = 0.6 coatings. Films deposited at 20 V and 40 V bias exhibited only hexagonal AlN phase, as illustrated in Figure 6-35. Increasing the bias to 60 V yielded a film with a mixture of two crystallographic phases, in which the AlN_{hex} type of lattice was the dominant phase and fcc TiN lattice was the secondary phase.

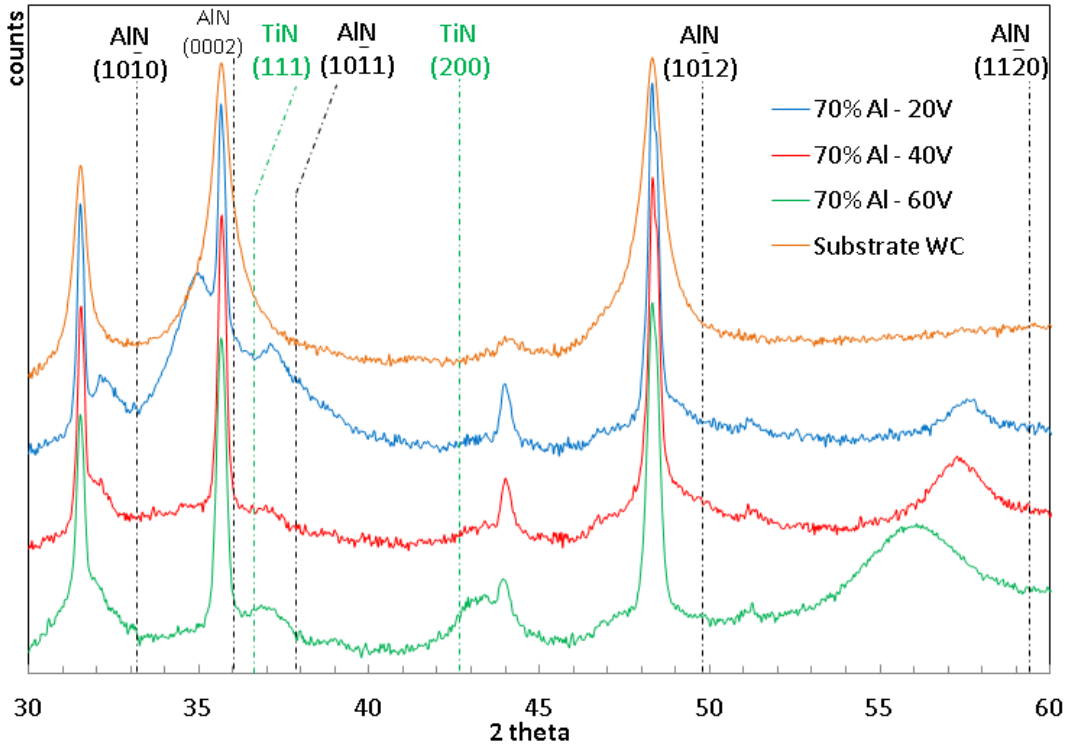

Figure 6-35 Comparative X-ray-diffraction patterns from cathodic arc $Ti_{0.3}Al_{0.7}N$ films deposited at three biases, together with the diffraction pattern corresponding to the WC (6% Co) substrate. The expected position for reflections from pure NaCl-structure TiN and wurtzite structure AlN are shown.

The predominant AlN_{hex} phase in the x = 0.7 films is in agreement with the literature data [176, 234], in which it has been shown that the aluminium solubility limit in the cubic phase $Ti_{1-x}Al_xN$ is around the concentration range of x = 0.64 to 0.7.

Once again, the shift of the peaks with respect to pure AlN_{hex} and TiN crystallographic phases was explained by the mutual substitution of metallic atoms in the two types of lattice, which result in both a larger AlN_{hex} and a smaller TiN lattice.

Variation of $Ti_{0.3}Al_{0.7}N$ crystallography with substrate bias

The influence of deposition energy on the structure of rich aluminium coatings is shown in Figure 6-36. Increasing the deposition bias from 20 V to 40 V yielded a denser structure with a smaller grain size and fewer defects. A further increase in bias to 60 V led, surprisingly, to an increase in the size of the droplets, which promoted big disruptions in the structure (see Figure 6-36 (c)).

Selected area diffraction patterns suggested that the crystallography of the films deposited at 20 V and 40 V bias was only AlN_{hex} phase, whereas, the film deposited at 60 V exhibited a secondary phase, corresponding to fcc TiN (see Figure 6-37). These findings are in agreement with the XRD results.

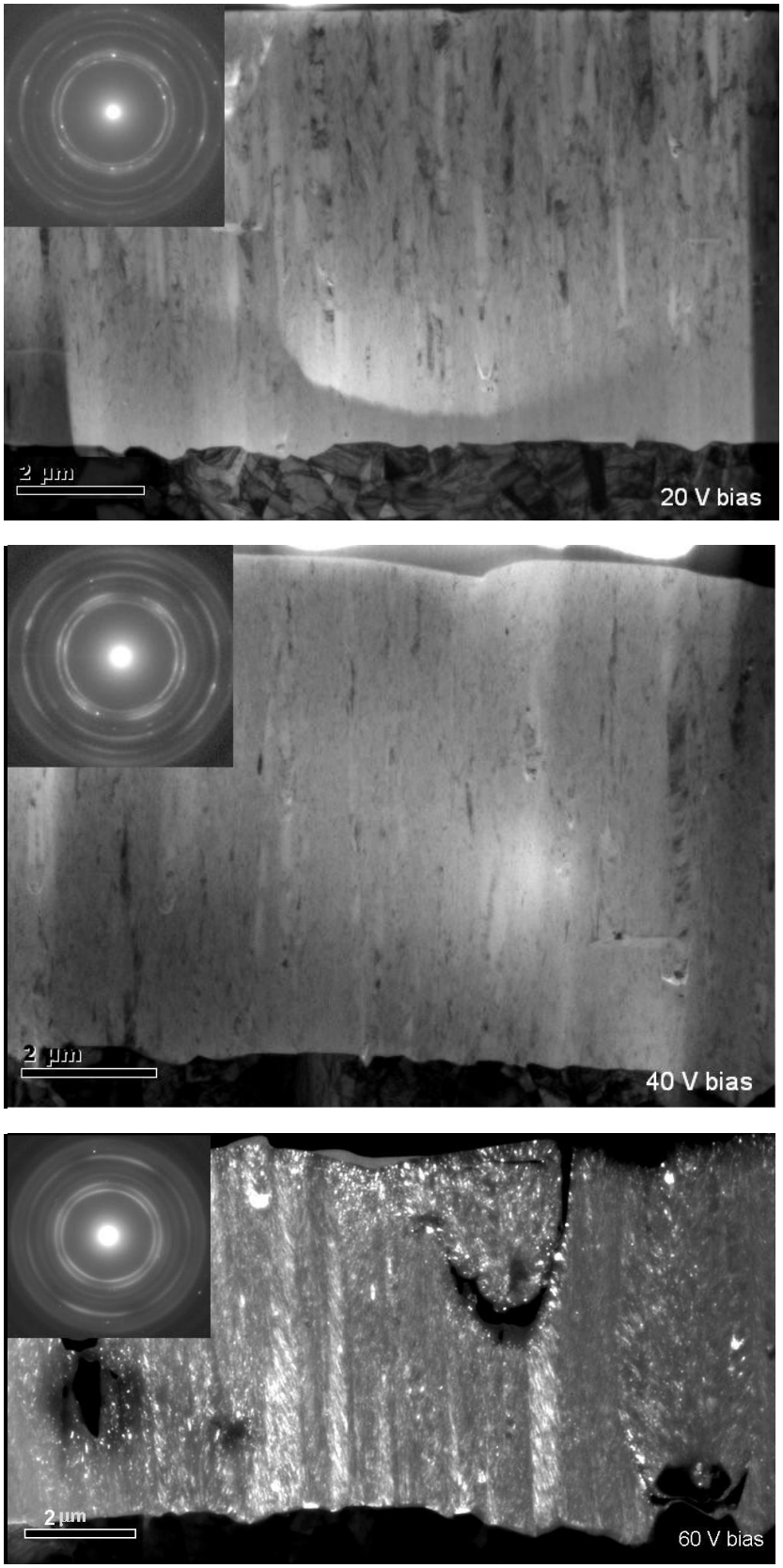

Figure 6-36 Cross section TEM images with corresponding SADPs of $Ti_{0.30}Al_{0.70}N$ films. The film deposited at 20 V bias shows a fine structure in the first stages of deposition, followed by a columnar morphology. The film deposited at 40 V bias exhibited a finer structure, with a few small columns. Increasing the deposition bias to 60 V led to a structure with big defect due to the droplets, as exemplified in the DF image.

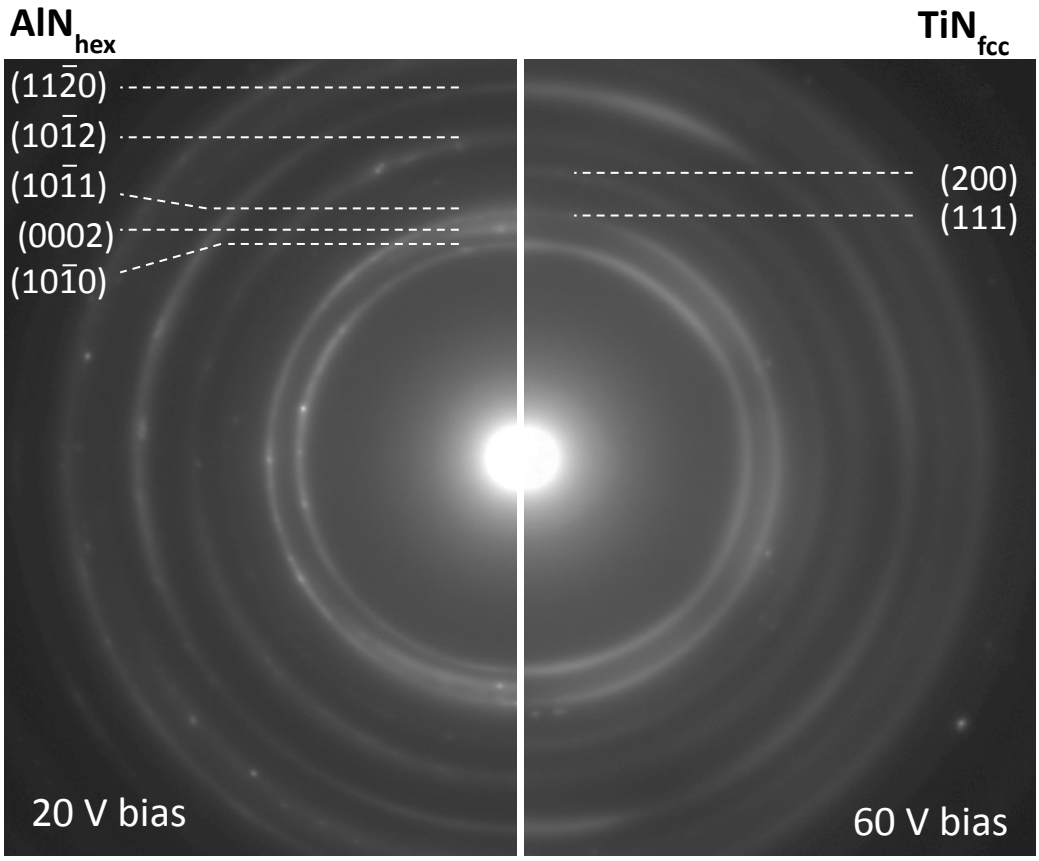

Figure 6-37 Select area diffraction pattern of the $Ti_{0.30}Al_{0.70}N$ film deposited at 20 V bias exhibited rings corresponding only to hexagonal AlN phase. The film deposited at 60 V bias exhibited a secondary phase corresponding to fcc TiN.

In addition, the SADP of the film deposited at 60 V bias corresponded to a nanocrystalline structure, which was confirmed by high resolution TEM analysis, as shown is Figure 6-38.

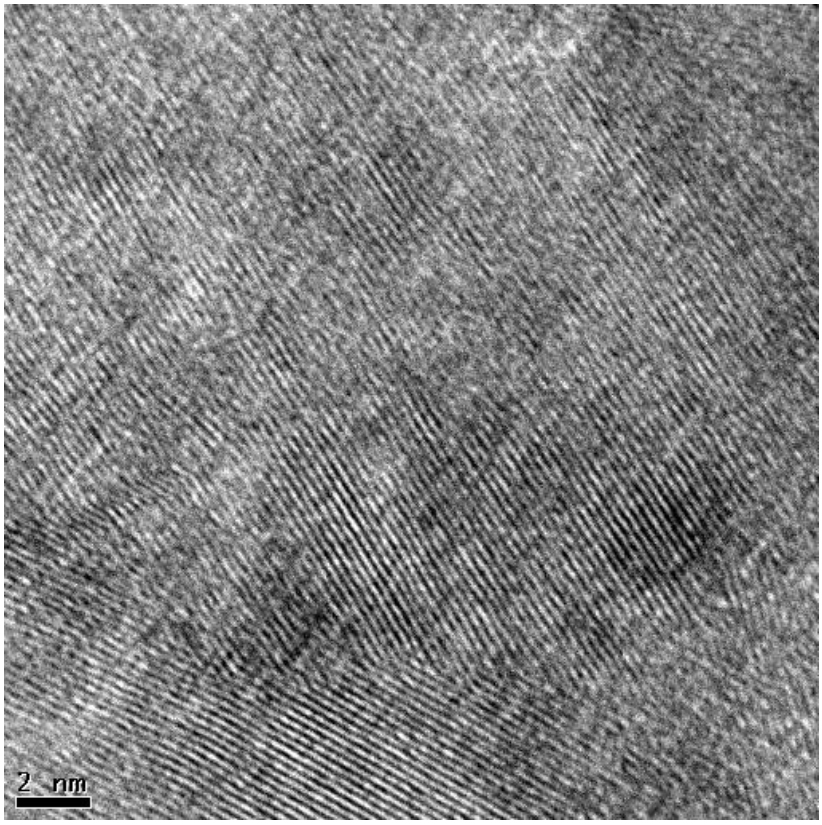

Figure 6-38 HRTEM image of the $Ti_{0.30}Al_{0.70}N$ film deposited at 60 V bias, which shows grains of a few nanometers size.

Discussion of $Ti_{0.3}Al_{0.7}N$ films

The slight increase in hardness and elastic modulus with increase in the deposition bias seemed to be attributed, once again, to a denser structure. However, the film deposited at 60 V bias exhibited a less dense structure. The slight increase in hardness for this film (see Figure 6-22) seemed to be caused by the formation of the harder TiN phase alongside AlN_{hex} one. In addition, a higher bias led to higher internal compressive stresses, as observed by a stronger shift of the diffraction peaks to lower two theta angles. The internal compressive stresses are expected to contribute to an increase in hardness values.

Summary – bias influence on room temperature properties and structure of cathodic arc $Ti_{1-x}Al_xN$

It has been shown that higher bias led to a denser structure with a less columnar morphology. These finding are in good agreement with literature data. Sato et al.

showed that increase in bias from 20V to 100V disrupts the columnar structure of $Ti_{1-x}Al_xN$ ($x = 0.45 \div 0.6$) and increases internal compressive stresses [231]. These structural changes are explained by the severe kinetic restraints in the mobility of ad-atoms. The kinetic limitations stem from the actual deposition technique, during which the ions together with a small amount of neutral particles (atoms, molecules) arrive at the growing film with energies above the lattice displacement energies, breaking the bonds between atoms at the surface. This process carries various names in the literature: as plasma immersion ion implantation [235] or knock-on implantation [165] or shot-peening [236]. In order to initiate this process the bombarding ion must have more than some threshold energy. A higher bombarding energy reflected by higher bias leads to higher penetration depth of ions. The penetration is accompanied by the interruption of the columnar structure and nucleation of new grains, as well as a build-up of higher compressive stresses [165]. This could explain why the films deposited at 60 V bias have a less columnar crystallography and a smaller grain size than those deposited at 20 V bias.

In addition, higher bias promoted the formation of TiN phase and stabilised cubic AlN_{fcc} phase. Furthermore, bias promoted (111) orientation of films with predominantly fcc structure. Moreover, the increased shift of diffraction peaks to lower two theta angles with the increase in deposition bias is indicative of larger residual compressive stresses at higher bias [231, 237]. All these transformations attributed to an increase in the deposition bias were shown to lead to higher hardness and explained the small variation of elastic modulus values for these films.

6.3.5 The influence of aluminium content on the structure of the cathodic arc $Ti_{1-x}Al_xN$ films

In the previous chapter the influence of deposition bias on the structure of cathodic arc films was presented. In the following, the influence of the aluminium content on the structure of these films is discussed.

The addition of aluminium in cathodic arc evaporated $Ti_{1-x}Al_xN$ films deposited at the same bias yielded a smaller lattice parameter, as reflected by the shift of the diffraction peaks to larger two theta angles with aluminium content (Figure 6-39).

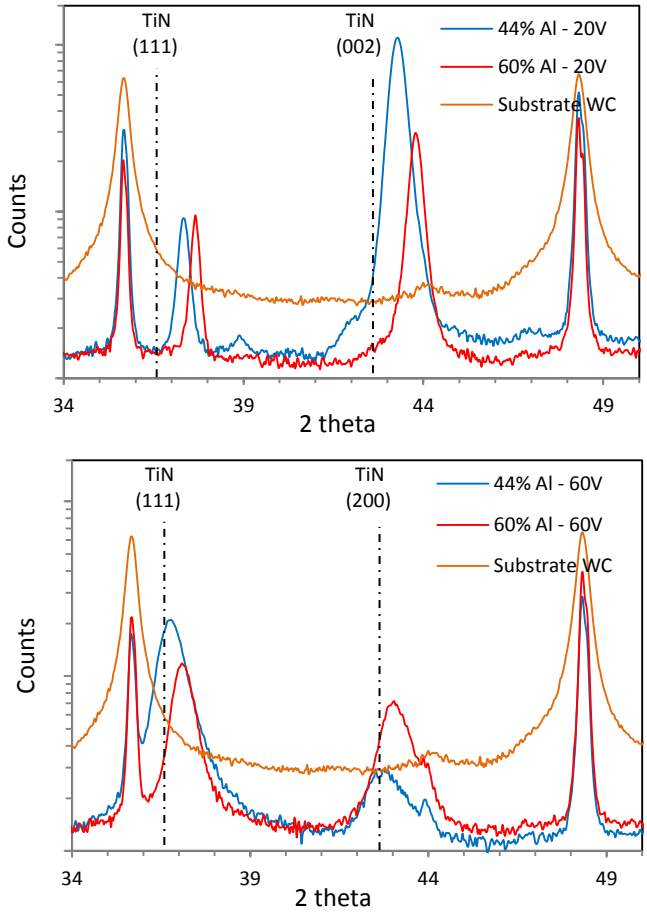

Figure 6-39 X-rays diffractogram of x = 0.44 and x = 0.6 films deposited at 20 V and 60 V bias. An Increase in the aluminium content shifts the peaks to larger two theta angles, corresponding to a smaller lattice.

Furthermore, the addition of aluminium yielded a less columnar structure and a smaller grain size. In addition, the phase crystallography changed from cubic TiN structure to hexagonal AlN. These structural changes are presented in Figure 6-40, Figure 6-41 and Figure 6-42 for films deposited at 20 V, 40 V and 60 V, respectively.

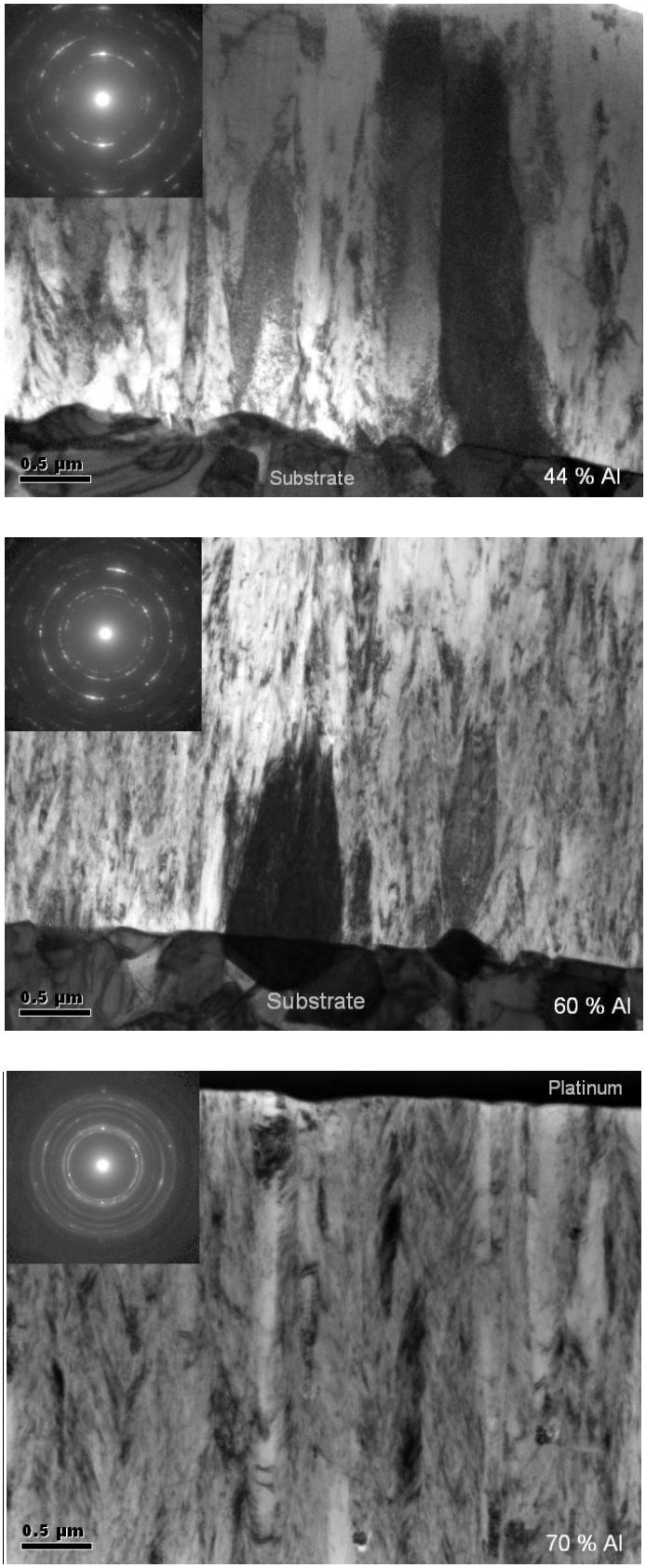

Figure 6-40 BF cross-section TEM images of cathodic arc evaporated $Ti_{1-x}Al_xN$ films deposited at 20 V bias showing changes in the microstructure with aluminium addition. The morphology changes from columnar to fibre. Aluminium addition led to a smaller grain size and a loss in texture, as well as, to the formation of hexagonal AlN.

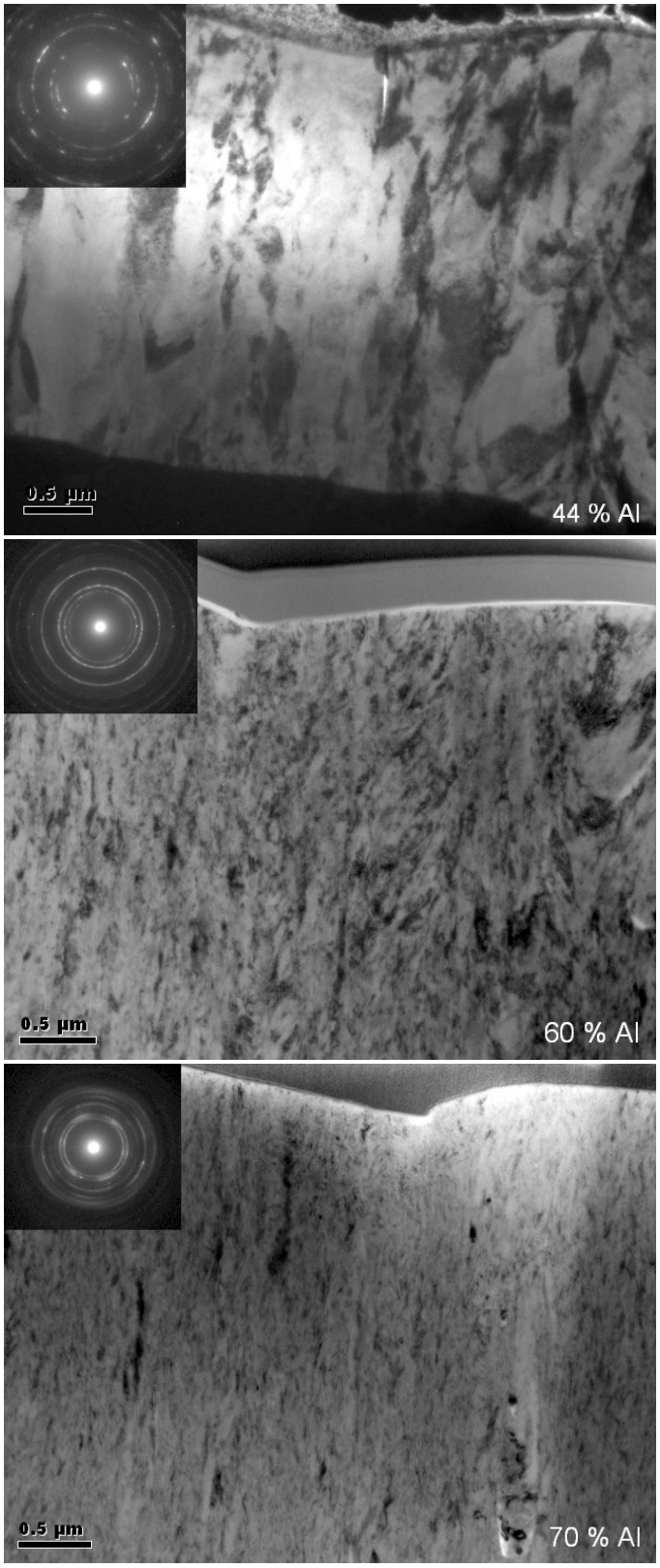

Figure 6-41 BF cross-section TEM images of cathodic arc evaporated $Ti_{1-x}Al_xN$ films deposited at 40 V bias showing changes in the microstructure with aluminium addition. The morphology changes from columnar to fibre and SADP suggests a smaller grain size and/or a loss in texture, as well as the transition from fcc TiN phase to hexagonal AlN with aluminium addition.

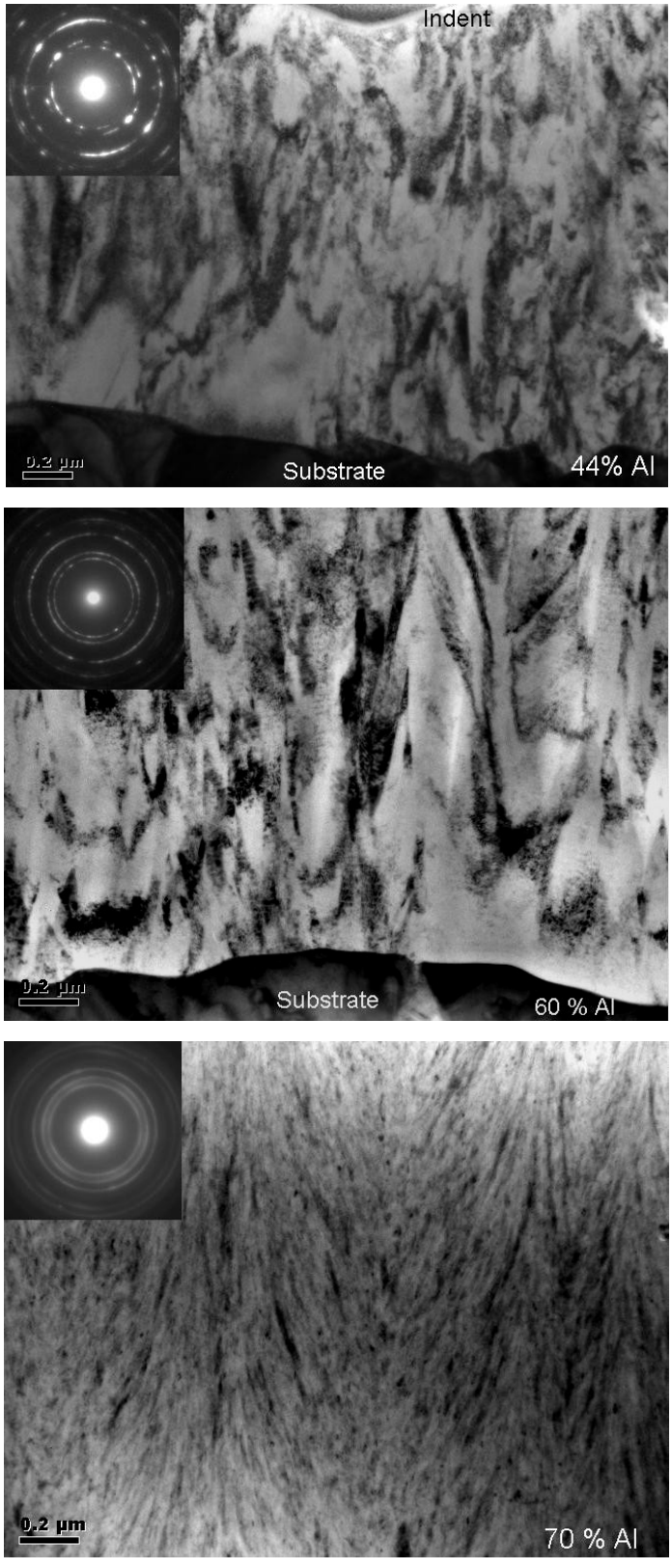

Figure 6-42 BF cross-section TEM images of cathodic arc evaporated $Ti_{1-x}Al_xN$ films deposited at 60 V bias showing changes in the microstructure with aluminium addition. The low aluminium content film has a fibre structure with big grains, whereas, the rich aluminium film has a very fine structure, corresponding to a nanocrystalline material.

Changes in the phase composition of the films deposited at the same bias with the amount of aluminium are summarised in Table 6-3.

Table 6-3 Variation in the phase composition for $Ti_{1-x}Al_xN$ films, deposited at the same bias, with the content of aluminium. The * is attached to the minority phase.

Aluminium content	Crystallographic phases present in films deposited at		
	20 V bias	40 V bias	60 V bias
x = 0.44 ($Ti_{0.56}Al_{0.44}N$)	TiN_{fcc}	TiN_{fcc}	$TiN_{fcc} + AlN_{fcc}^*$
x = 0.6 ($Ti_{0.40}Al_{0.60}N$)	$TiN_{fcc} + AlN_{hex}^*$	$TiN_{fcc} + AlN_{hex}^*$	$TiN_{fcc} + AlN_{fcc}^*$
x = 0.7 ($Ti_{0.30}Al_{0.70}N$)	AlN_{hex}	AlN_{hex}	$AlN_{hex} + TiN_{fcc}^*$

Discussions

The low hardness values of x = 0.7 coatings compared to the x = 0.6 and x = 0.44 films was attributed to the fact that the aluminium rich film exhibited mainly hexagonal AlN phase structure, whereas, in the other two compositions the dominant phase was cubic TiN. The hexagonal AlN phase is softer than the TiN one [230, 233]. The hardness of x = 0.7 films are in good agreement with literature values for hardness of TiAlN films with AlN lattice, around 18 GPa [233].

The elastic modulus decreased with the aluminium content, which is in line with the results found by Horling et al. [30], Mayrhofer et al. [176] and Santana et al. [172].

It is observed that increasing the addition of aluminium resulted in a loss in texture and a smaller grain size, in a similar manner found in other work [172, 233]. Lattice distortion induced by energetic particles arriving at the growing coating surface would be more easily accommodated in a material with lower elastic modulus [2].

6.3.6 High temperature indentation study of cathodic arc $Ti_{1-x}Al_xN$ films

The influence of temperature on the hardness of the cathodic arc $Ti_{0.4}Al_{0.6}N$ films deposited at 20 V and 60 V bias is presented in Figure 6-43, alongside data corresponding to magnetron sputtered TiN, $Ti_{0.48}Al_{0.52}N$ and $Ti_{0.38}Al_{0.62}N$ films. The cathodic arc film deposited at the highest bias (60 V) exhibited room temperature hardness similar to magnetron sputtered x=0.52 film and significantly higher than magnetron sputtered x=0.62 film. However, the hardness of the cathodic arc film showed a significant drop with temperature, from 29 ± 1.4 GPa at room temperature to 21 ± 1.1 GPa at 300 °C, whereas, the magnetron sputtered films exhibited stable hardness over the same temperature range. A similar drop in hardness for TiAlN coatings was found by Fox-Rabinovich and co-workers [207].

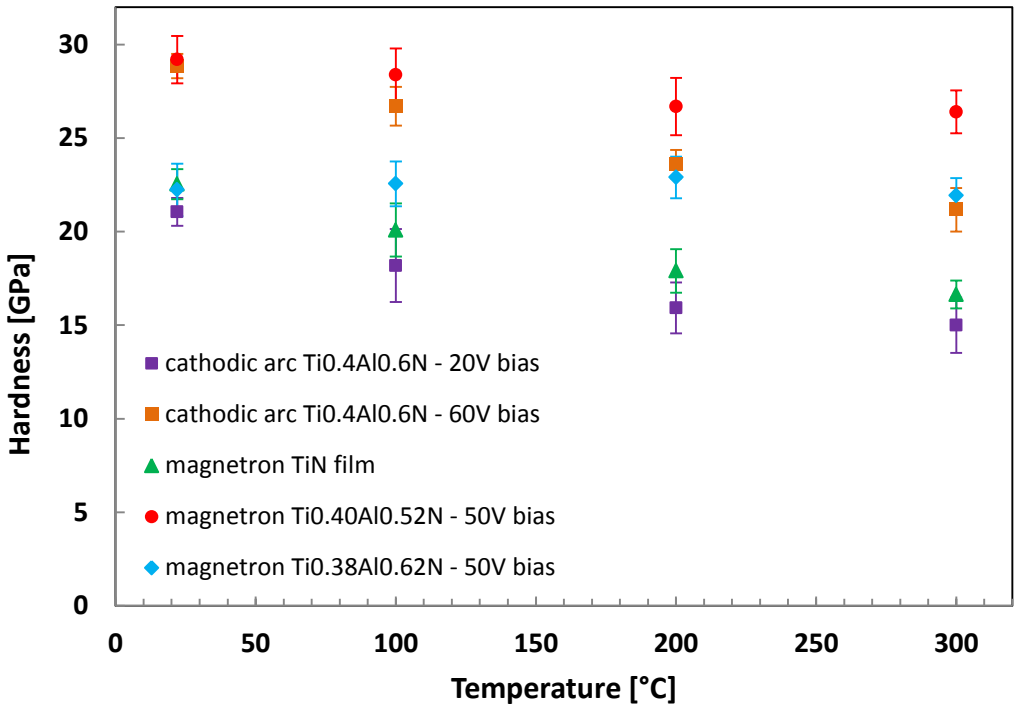

Figure 6-43 The influence of the temperature on the hardness of the cathodic arc evaporated $Ti_{0.4}Al_{0.6}N$ films deposited at two bias values. The data corresponding to magnetron sputtered films of similar composition and magnetron sputtered TiN film are also presented for a direct comparison. Each data point represents the average values of 10 indents.

The poor hardness stability with temperature of the cathodic arc film presented here was unexpected because this film exhibited a mixture of two crystallographic phases, TiN and stabilised cubic AlN_{fcc}, which were responsible for good hardness stability with temperature for magnetron sputtered films. An explanation that could account for the drop in hardness with temperature would have been: the

cathodic arc film might have developed the hexagonal AlN phase during indentation at high temperature. However, TEM analyses of the sample held at 300 °C for 24 hours revealed the same morphology and B1 NaCl structure (Figure 6-44) presented by the film before indentation. Furthermore, room temperature hardness of the film did not change after high temperature nanoindentation. This suggests that there were no permanent structural changes during indentation at high temperature and the process which led to drop in hardness with temperature is reversible.

The major difference between the structure of coatings synthesised by cathodic arc evaporation and magnetron sputtered deposition is the presence of droplets in cathodic arc films. These droplets are clusters of atoms or molecules which have mainly the chemistry of the metal cathode from which were ejected. These droplets are expected to significantly soften with temperature. Therefore, these structural defects might be the cause of the drop in hardness of this film with temperature. In addition, the cathodic arc films have different phases and orientations than the magnetron ones. However, conclusive evidence could not be found to explain the poor thermal stability of hardness for this film, and this would be the subject of further work.

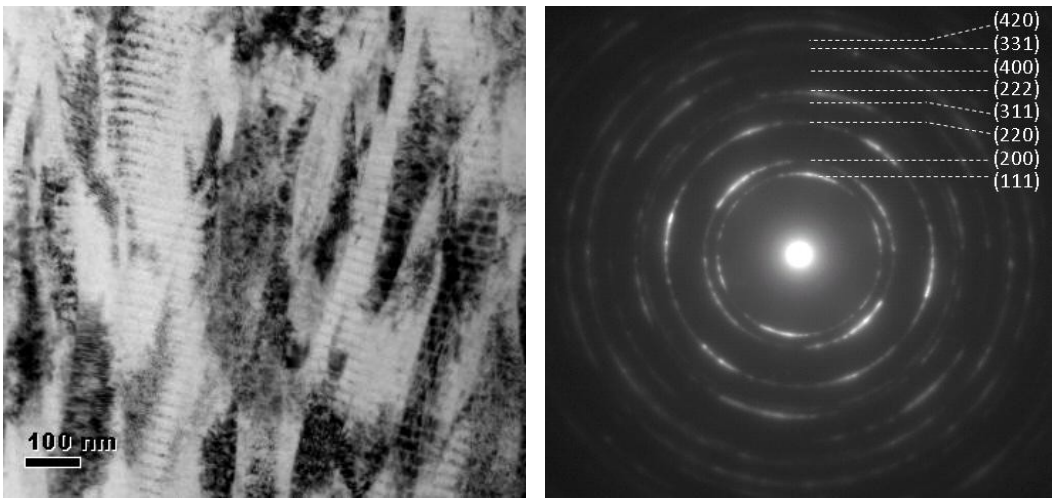

Figure 6-44 Bright field cross section TEM image and SADP of $Ti_{0.40}Al_{0.60}N$ (deposited at 60 V bias) after indentation at 300°C for 24 hours. The morphology was similar to the as deposited film, with the nanolayered structure superimposed on the underlying columnar structure. The crystal structure was the same, B1 NaCl lattice, as illustrated by the diffraction rings. There could not be detected any presence (formation) of hexagonal AlN phase.

The film deposited at low bias (20 V) showed a similar trend in hardness with temperature to the film deposited at 60 V bias, although at significantly lower hardness values. This film was even softer than the magnetron sputtered TiN film, and its low hardness seemed to be attributed to significant porosity (Figure 6-33) and the presence of AlN hexagonal phase (Figure 6-32).

The increase in temperature led to a drop on the elastic modulus of the cathodic arc $Ti_{0.4}Al_{0.6}N$ films, as presented in Figure 6-45. However, the film deposited at 60 V bias showed a better stability of elastic modulus with temperature, compared to the film deposited at 20 V bias. Similar values and variations of the elastic modulus of TiAlN with temperature to the one exhibited by the film deposited at 60 V bias was observed in Fox Rabinovich et al. work [207].

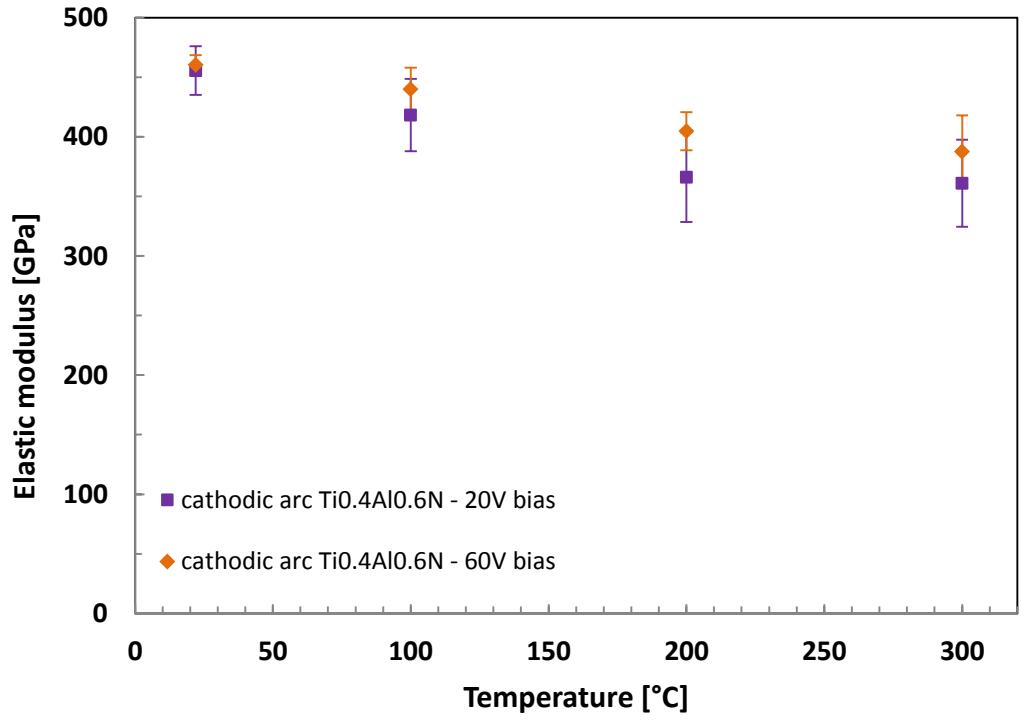

Figure 6-45 The influence of the temperature on the elastic modulus of the cathodic arc evaporated $Ti_{0.4}Al_{0.6}N$ films deposited at two bias values. Each data point represents the average data gathered from 10 indents.

7 Conclusions and further work

7.1 Conclusions

An investigation into the effect of the temperature on the hardness and elastic modulus of the bulk single crystal TiN, magnetron sputtered single crystal TiN coating deposited on MgO, magnetron sputtered $Ti_{1-x}Al_xN$ coatings deposited on MgO and arc evaporated $Ti_{1-x}Al_xN$ industrial coatings deposited on WC-Co(6%) has been conducted. Nanoindentation data acquired over a temperature range (room temperature to 350 °C) was used to extract fundamental deformation rate-controlling parameters such as activation volume, activation energy and Peierls stress, demonstrating the usefulness of the indentation as an effective experimental technique for investigating kinetics of plastic deformation in ceramics at moderately elevated temperatures. TEM analysis combined with XRD measurements were conducted for detailed structural investigations.

Mechanical properties of the (001) TiN_{bulk} were shown to be strongly influenced by temperature. The hardness dropped from 21 GPa at room temperature to 14 GPa at 350 °C, whereas, the elastic modulus remained relatively constant, recording a drop of 4 % over the same temperature range. The deformation behaviour of TiN occurred mainly by slip along {011} crystallographic planes at all tested temperatures, which suggested that the drop in hardness with the temperature was attributed to a change of ease of plastic slip (decrease in the lattice resistance).

The magnetron sputtered TiN film exhibited similar hardness values at low temperatures (room temperature and 100 °C) to the TiN_{bulk}. The fact that the high density of defects present in the film did not improve its hardness suggests that, the hardness of these materials is dominated by the magnitude of the lattice resistance at low temperatures. However, at 200 °C and 300 °C, temperatures at which the lattice resistance to dislocation motion is significantly reduced, the drop in hardness of TiN film was smaller compared to the TiN_{bulk}. The improved thermal stability of the film was attributed to the influence of the grain boundary at high temperatures. Therefore, the impact of the grain size (grain boundary density) of these coatings on hardness values depends on the temperature.

Addition of aluminium in the system was shown to significantly increase the hardness of these materials. Furthermore, the mechanical stability with temperature was markedly improved, as has been shown by the magnetron sputtered compositions in which approximately half of titanium atoms were replaced by aluminium atoms ($Ti_{0.48}Al_{0.52}N$, $Ti_{0.40}Al_{0.60}N$). These compositions exhibited, in the as deposited state, a mixture of two fcc crystallographic nanodomains with lattices corresponding to TiN and stabilised cubic AlN phases. Literature data suggests that the stabilised AlN_{fcc} phase can form either by (1) epitaxial deposition of nanolayers of AlN_{fcc} on TiN [227, 230], (2) during the spinodal decomposition of aluminium rich $Ti_{1-x}Al_xN$ films [109, 126, 130], and (3) during the phase transition from wurtzite AlN at high pressure [132]. However, in this work it has been shown that the stabilised AlN_{fcc} phase can be form during deposition. A thermal treatment at only 600 °C for 24 hours of $Ti_{0.48}Al_{0.52}N$ film led to multiplication of this phase, whereas, annealing at 800 °C led to the formation of hexagonal AlN phase. Direct observation of stabilised AlN_{fcc} nanodomains was possible by high resolution TEM.

The good mechanical stability with temperature of $Ti_{0.48}Al_{0.52}N$ and $Ti_{0.40}Al_{0.60}N$ films seems to be attributed to stresses generated by the lattice distortion required to form continuous boundaries between the nanodomains. In addition, it is suggested that, if the stabilised cubic AlN has different slip systems to TiN (nonisostructural phases), different slip systems would prevent the dislocation from moving easily through the interfaces between the phases. That could be another factor that might contribute to the improved mechanical properties of the systems exhibiting the two fcc phases. However, AlN_{fcc} is a metastable phase and it has been obtained in nanometre domains only, which makes it difficult to determine its mechanical properties.

Porosity did not seem to affect the mechanical stability with temperature for $Ti_{0.48}Al_{0.52}N$ and $Ti_{0.40}Al_{0.60}N$ films. However, it had a noticeable contribution towards their hardness and elastic modulus values. The latter film had lower hardness and elastic modulus than the former one, due to an increased porosity.

Analyses based on the nanoindentation data revealed that the apparent activation energy of the deformation process of the magnetron sputtered $Ti_{0.48}Al_{0.52}N$ is

almost double ($Q = 2.19 \times 10^{-19}$ J) compared to the apparent activation energy of the TiN_{bulk} ($Q = 1.24 \times 10^{-19}$ J). This increase in the apparent activation energy of deformation process is remarkable and seems to be attributed mainly to the presence of the aluminium in the structure. Such an increase in the resistance to plastic flow seems to be responsible for the significant improvement in the mechanical properties of the $Ti_{0.48}Al_{0.52}N$ magnetron sputtered film.

Mechanical properties of industrial cathodic arc $Ti_{0.4}Al_{0.6}N$ films were strongly influenced by temperature. The variation of hardness with the temperature for $Ti_{0.4}Al_{0.6}N$ followed a similar descending trend as for magnetron sputtered TiN_{film}.

The deposition bias had a strong influence on room temperature hardness and elastic modulus of industrial cathodic arc $Ti_{1-x}Al_xN$ films ($x = 0.44, 0.6, 0.7$). The increase in deposition bias led to a denser structure and higher stresses, which yielded higher hardness. Furthermore, higher bias promoted TiN and stabilised cubic AlN_{fcc} crystallographic phase and (111) orientation.

The increase in aluminium content led to a finer microstructure. In the case of arc evaporated coatings, low aluminium films ($x = 0.44$) exhibited a polycrystalline structure with well-defined columns, whereas rich aluminium films ($x = 0.7$) exhibited a nanocrystalline structure with fibre morphology. The former composition exhibited only B1 NaCl lattice structure, whereas, the latter exhibited a mixture of two crystallographic phases; where wurtzite AlN was the dominant phase and TiN was the minority phase.

The temperature on the nanoindentation investigation was limited at 350 °C for the TiN bulk and at 300 °C for the films, due to the instability of the diamond tip. It has been shown that the geometry of the indenter tip changed significantly around 350 °C. Because of that, the analysis of the indents performed at maximum temperatures has been done using a diamond area function determined immediately after the high temperature experiment.

Based on the research presented here it can be concluded that the addition of aluminium in TiN lattice increases the lattice resistance. In addition, for improved thermal stability of hardness and elastic modulus of $Ti_{1-x}Al_xN$ coatings, it is

required the presence of both cubic crystallographic nanodomains: TiN and stabilised AlN_{fcc}.

7.2 Further work

The hardness and elastic modulus of the bulk single crystal TiN have been determined for (001) facet. It would be interesting to determine these properties by nanoindentation in other orientations, as well, especially on (111) direction, which is has been shown in literature to yield then highest hardness. In addition, micropillar compression could be performed on various facets of the bulk single crystal TiN, and then the results could be compared. This way, a thorough characterisation of single crystal TiN could be made.

TEM investigation showed that the magnetron sputtered $Ti_{0.48}Al_{0.52}N$ annealed at 600 °C presented cubic nanodomains TiN and AlN_{fcc}. It is proposed, as a next step, to determine the hardness and elastic modulus of this film at various temperatures by nanoindentation, in order to investigate the influence of the nanodomains on the mechanical properties.

The poor thermal stability of industrial cathodic arc evaporated $Ti_{0.40}Al_{0.60}N$ needs to be understood. One major factor that affects the properties of these films is constituted by droplets. In order to isolate and investigate the influence of droplets on mechanical properties, it is suggested an investigation of filtered cathodic arc films, which have a reduced level and size of droplets in the structure. In the same time, the influence of temperature on the mechanical properties of cathodic arc $Ti_{1-x}Al_xN$ films with a lower aluminium content (x = 0.4) needs to be investigated.

Micropillar compression could also be used to investigate the influence of temperature on mechanical properties of these materials, and then the results could be compared to the one obtained by nanoindentation.

Another avenue into the investigation of deformation behaviour at temperature of these films would be by in-situ TEM nanoindentation. This technique could provide insight into the formation of cubic nanodomains TiN and AlN_{fcc} , as well as, the onset of the spinodal decomposition.

Cathodic arc films $Ti_{0.48}Al_{0.52}N$ and $Ti_{0.40}Al_{0.60}N$ deposited at high bias developed a nanolayers structure. This feature is expected to come from the local change in the chemistry of the film due to the rotation of the substrate holder with respect to Ti and Al targets during deposition. Such a variation in chemistry seemed to have promoted the formation of a secondary phase with AlN_{fcc} lattice, alongside TiN lattice. The co-existence of both types of lattice was shown to improve mechanical properties of these materials. By varying the rotation of the substrate holder during deposition, the thickness of the nanolayers might be varied. This could be a way to further tailor mechanical properties of these materials and to improve their practical performance.

It has been shown that by extending the analysis of the nanoindentation data obtained at various temperatures and strain rates, the Peierls' stress and fundamental deformation parameters (activation energy and activation volume) of hard ceramics could be estimated. In the present work the Peierls' stress and fundamental deformation parameters for the bulk single crystal TiN and magnetron sputtered $Ti_{0.48}Al_{0.52}N$ have been determined. As a next step, this analysis will be performed for the rest of the compositions studied here. Taking this further, it is possible to determine these characteristics for other similar materials, which could then be compared with literature data.

8 References

1. Jindal, P.C., Santhanam, A.T., Schleinkofer, U., Shuster, A.F., *Performance of PVD TiN, TiCN, and TiAlN coated cemented carbide tools in turning.* International Journal of Refractory Metals and Hard Materials, 1999. **17**(1-3): p. 163-170.
2. Quinto, D., G. Wolfe, and P. Jindal, *High Temperature microhardness of hard coatings produced by physical and chemical vapor deposition.* Thin Solid Films, 1987. **153**(1-3): p. 19-36.
3. Munz, W.D., *Titanium Aluminum Nitride Films: a New Alternative to Titanium Nitride Coatings.* Journal of vacuum science & technology. B, Microelectronics and nanometer structures, 1986. **4**(6): p. 2717.
4. Zhang, S., Zhu, W., *TiN coating of tool steels: a review.* Journal of materials processing technology, 1993. **39**: p. 165.
5. Knotek, O., M. Bohmer, and T. Leyendecker, *On structure and properties of sputtered Ti and Al based hard compound films.* Journal of Vacuum Science & Technology A: Vacuum, Surfaces, and Films, 1986. **4**(6): p. 2695-2700.
6. Söderberg, S., M. Sjöstrand, and B. Ljungberg, *Advances in coating technology for metal cutting tools.* Metal Powder Report, 2001. **56**(4): p. 24-30.
7. Ting, C.Y. and M. Wittmer, *The use of titanium-based contact barrier layers in silicon technology.* Thin Solid Films, 1982. **96**(4): p. 327-345.
8. Rha, S-K., Lee, W-J., Lee, S-Y., Hwang, Y-S., Lee, Y-J., Kim, D-I., Kim, D-W., Chun, S-S, Park, C-O., *Improved TiN film as a diffusion barrier between copper and silicon.* Thin Solid Films, 1998. **320**(1): p. 134-140.
9. Kim, J.Y., Kim, H.K., Kim,Y., Kim, Y.D., Jeon,H., *Compositional variations of TiAlN films deposited by metalorganic atomic layer deposition method.* Japanese Journal of Applied Physics Part 1-Regular Papers Short Notes & Review Papers, 2002. **41**(2A): p. 562-565.
10. Roquiny, P., Bodart, F., Terwagne, G., *Colour control of titanium nitride coatings produced by reactive magnetron sputtering at temperature less than 100° C.* Surface & coatings technology, 1999. **116**: p. 278.
11. Tamura, Y., Yokoyama, A., Watari, F., Kawasaky, T., *Surface properties and biocompatibility of nitrided titanium for abrasion resistant implant materials.* Dental Materials Journal, 2002. **21**(4): p. 355-372.
12. Piscanec, S., Ciacchi, L.C., Vesselli, E., Comelli, G., Sbaizero, O., Meriani, S., De Vita, A., *Bioactivity of TiN-coated titanium implants.* Acta materialia, 2004. **52**(5): p. 1237.
13. Czarnowska, E., Wierzchon, T., Maranda-Niebala, A., *Properties of the surface layers on titanium alloy and their biocompatibility in in vitro tests.* Journal of materials processing technology, 1999. **92**(93): p. 190.
14. Czarnowska, E., Wierzchon, T., Maranda-Niebala, A., Karczmarewicz, E., *Improvement of titanium alloy for biomedical applications by nitriding and carbonitriding processes under glow discharge conditions.* Journal of materials science. Materials in medicine, 2000. **11**(2): p. 73.
15. Groessner-Schreiber, B., Neybert, A., Muller, W-D., Hopp, M., Griepentrog, M., Lange, K-P., *Fibroblast growth on surface-modified dental implants: an in vitro study.* Journal of biomedical materials research, 2003. **64**(4): p. 591.
16. SECO, *Cutting tools*. 2011.
17. BBC. *Olimpic Torch 2012*. 2012 [cited 2012 2012]; Available from: www.bbc/news.com.

18. Wittmer, M., Noser, J., Melchior, H., *Oxidation kinetics of TiN thin films.* Journal of applied physics, 1981. **52**: p. 6659.
19. Chen, H.Y., Lu, F.H., *Oxidation behavior of titanium nitride films.* Journal of vacuum science & technology. B, Microelectronics and nanometer structures, 2005. **23**(4): p. 1006.
20. Ichimura, H., Kawana, A., *High-temperature oxidation of ion-plated TiN and TiAlN films.* Journal of materials research, 1993. **8**(5): p. 1093.
21. Panjan, P., Navinsek, B., Cvelbar, A., Zalar, A., Milosev, I., *Oxidation of TiN, ZrN, TiZrN, CrN, TiCrN and TiN/CrN multilayer hard coatings reactively sputtered at low temperature.* Thin Solid Films, 1996. **281**(282): p. 298.
22. Beensh-Marchwicka, G., Krol-Stepniewska, L., Posadowski, W., *Structure of thin films prepared by the cosputtering of titanium and aluminum or titanium and silicon.* Thin Solid Films, 1981. **82**(4): p. 313.
23. Jehn, H.A., Hofmann, S., Ruckborn,V-E., Munz, W-D., *Morphology and Properties of Sputtered(Ti, Al) N Layers on High Speed Steel Substrates as a Function of Deposition Temperature and Sputtering Atmosphere.* Journal of vacuum science & technology. B, Microelectronics and nanometer structures, 1986. **4**(6): p. 2701.
24. Wahlström, U., Hultman, L., Sundgren, J-E., Abidi, F., Petrov, I., Greene, J.E., *Crystal growth and microstructure of polycrystalline $Ti_{1-x}Al_xN$ alloy films deposited by ultra-high-vacuum dual-target magnetron sputtering.* Thin Solid Films, 1993. **235**(1-2): p. 62.
25. Prange, R., Cremer, R., Neuschutz, D., *Plasma-enhanced CVD of (Ti, Al) N films from chloridic precursors in a DC glow discharge.* Surface & coatings technology, 2000. **133**: p. 208.
26. Knotek, O., Munz, W-D., Leyendecker, T., *Industrial Deposition of Binary, Ternary, and Quaternary Nitrides of Titanium, Zirconium, and Aluminum.* Journal of vacuum science & technology. B, Microelectronics and nanometer structures, 1986. **5**(4): p. 2173.
27. Horling, A., Hultman, L., Oden, O., Sjolen, J., Karlsson, L., *Thermal stability of arc evaporated high aluminum-content $Ti_{1-x}Al_xN$ thin films.* Journal of vacuum science & technology. B, Microelectronics and nanometer structures, 2002. **20**(5): p. 1815.
28. Leyendecker, T., Lemmer, O., Esser, S., Ebberink, J., *The development of the PVD coating TiAlN as a commercial coating for cutting tools.* Surface and Coatings Technology, 1991. **48**(2): p. 175-178.
29. Roos, J.R., Celis, J.P., Veltrop, H., Vancoille, E., Boelens, S., Jungblut, F., Ebberink, J., Homberg, H., *Interrelationship between processing, coating properties and functional properties of steered arc physically vapour deposited (Ti,Al)N and (Ti,Nb)N coatings.* Thin Solid Films, 1990. **193-194**(Part 1): p. 547-556.
30. Hörling, A., Hultman, L., Oden, O., Sjolen, J., Karlsson, L., *Mechanical properties and machining performance of Ti1− xAlxN-coated cutting tools.* Surface & coatings technology, 2005. **191**(2-3): p. 384.
31. Yang, Q., He, C., Zhao, L.R., Immarigeon, J-P., *Preferred orientation and hardness enhancement of TiN/CrN superlattice coatings deposited by reactive magnetron sputtering.* Scripta Materialia, 2002. **46**(4): p. 293-297.
32. Blaha, P., Redinger, J., Schwarz, K., *Bonding study of TiC and TiN. II. Theory.* Physical review. B, Condensed matter, 1985. **31**(4): p. 2316.
33. Ahuja, R., Eriksson, O., Wills, J.M., Johansson, B., *Structural, elastic, and high-pressure properties of cubic TiC, TiN, and TiO.* Physical review. B, Condensed matter, 1996. **53**(6): p. 3072.

34. Wachtman, J.B., Cannon, W.R., Mattheuson, M.J., *Mechanical properties of ceramics*. 2009.
35. R. W. Cahn, P.H., E. J. Kramer, *Materials science and technology, a compresive treatement*. Vol. 11. 2006. 20.
36. William Jr, D., *Callister, and David G. Rethwisch, Fundamentals of Materials Science and Engineering: An Integrated Approach*. 2007, Wiley.
37. K.Kendall, *Complexities of Compression Failure.* Proc. R. Soc. London, 1978. **361**(361): p. 254 -263.
38. Lee, B.J., S. Ahzi, and R.J. Asaro, *On the plasticity of low symmetry crystals lacking five independent slip systems.* Mechanics of Materials, 1995. **20**(1): p. 1-8.
39. Bhakhri, V., Wang, J., Uh-rehman, N., Ciurea, C., Giuliani, F., Vandeperre, L. J., *Instrumented nanoindentation investigation into the mechanical behavior of ceramics at moderately elevated temperatures.* Journal of Materials Research, 2012. **27**(1): p. 65-75.
40. Yamamoto, R., Murakami, S., Maruyama, K., *High-temperature mechanical properties of hot-pressed TiN with fine grain size.* Journal of materials science, 1998. **33**(8): p. 2047.
41. Heard, H.C. and C.F. Cline, *Mechanical behaviour of polycrystalline BeO, Al₂O₃ and AlN at high pressure.* Journal of materials science, 1980. **15**(8): p. 1889-1897.
42. Hull, D., Bacon, D. J., *Introduction to Dislocations*. four ed. 2001.
43. Karman, T.v., *Z. Ver. DeutscherIngen., 55 (1911), p. 1749.* 1911.
44. Chen, W. and G. Ravichandran, *Dynamic compressive failure of a glass ceramic under lateral confinement.* Journal of the Mechanics and Physics of Solids, 1997. **45**(8): p. 1303-1328.
45. Chen, W. and G. Ravichandran, *Failure mode transition in ceramics under dynamic multiaxial compression.* International Journal of Fracture, 2000. **101**(1): p. 141-159.
46. Lankford, J., Predebon, W.W., Staehler, J.M., Subhush, G., Pletka, B.J., Anderson, C.A., ., *The role of plasticity as a limiting factor in the compressive failure of high strength ceramics.* Mechanics of Materials, 1998. **29**(3–4): p. 205-218.
47. Horii, H. and S. Nemat-Nasser, *Brittle Failure in Compression: Splitting, Faulting and Brittle-Ductile Transition.* Philosophical Transactions of the Royal Society of London. Series A, Mathematical and Physical Sciences, 1986. **319**(1549): p. 337-374.
48. Ashby, M.F. and C.G. Sammis, *The damage mechanics of brittle solids in compression.* Pure and Applied Geophysics, 1990. **133**(3): p. 489-521.
49. Atkins, A.G. and D. Tabor, *Hardness and deformation properties of solids at very high temperatures.* Journal Name: Proc. Roy. Soc. (London), Ser. A; Journal Volume: Vol: 292; Other Information: Orig. Receipt Date: 31-DEC-66, 1966: p. Medium: X; Size: Pages: 441-59.
50. Veyssière, P., S. Kirby, and J. Rabier. 1980, HAL - CCSD.
51. Wakai, F., S. Sakaguchi, and Y. Matsuno, *Superplasticity of yttria-stabilized tetragonal ZrO2 polycrystals.* Journal Name: Adv. Cer. Mat.; (United States); Journal Volume: 1, 1986: p. Medium: X; Size: Pages: 259-263.
52. Wakai, F. and H. Kato, *Superplasticity of TZP/Al sub 2 O sub 3 composite.* Journal Name: Advanced Ceramic Materials; (USA); Journal Volume: 3:1, 1988: p. Medium: X; Size: Pages: 71-76.

53. Cannon, R.M., W.H. Rhodes, and A.H. Heuer, *Plastic Deformation of Fine-Grained Alumina (Al2O3): I, Interface-Controlled Diffusional Creep.* Journal of the American Ceramic Society, 1980. **63**(1-2): p. 46-53.
54. Heuer, A.H., N.J. Tighe, and R.M. Cannon, *Plastic Deformation of Fine-Grained Alumina (Al2O3): II, Basal Slip and Nonaccommodated Grain-Boundary Sliding.* Journal of the American Ceramic Society, 1980. **63**(1-2): p. 53-58.
55. Folweiler, R.C., *Creep Behavior of Pore Free Polycrystalline Aluminum Oxide.* Journal of applied physics, 1961. **32**(5): p. 773-778.
56. Cannon, W.R. and O.D. Sherby, *Creep Behavior and Grain-Boundary Sliding in Polycrystalline A12O3.* Journal of the American Ceramic Society, 1977. **60**(1-2): p. 44-47.
57. Waku, Y., Nakagawa, N., Wakamoto, T., Ohtsubo, H., Shimizu, K., Kohtoku, Y., *High-temperature strength and thermal stability of a unidirectionally solidified Al2O3/YAG eutectic composite.* Journal of materials science, 1998. **33**(5): p. 1217-1225.
58. McColm, I., *Ceramic hardness.* 1990.
59. Hockey, B.J., *Plastic deformation of aluminum oxide by indentation and abrasion (Plastic deformation of aluminum oxide by indentation and abrasion at room temperature, using transmission electron microscopy).* AMERICAN CERAMIC SOCIETY, JOURNAL., 1971. **Vol. 54** (5): p. 223-231
60. Lawn, B.R.E., A G ; Marshall, D B, *Elastic/plastic indentation damage in ceramics. The median/radial crack system.* J.AM.CERAM.SOC. J. Am. Ceram., 1980. **Vol. 63**(9/10): p. 574 -581.
61. Nakano K, T.I., Shin Takeuchi, *Hardness Anisotropy of Single Crystals of IVa-Diborides.* Japanese Journal of Applied Physics, 1973. **12**(2): p. 186 - 189.
62. Krajcinovic, D. and A. Stojimirovic, *Deformation processes in semi-brittle polycrystalline ceramics.* International Journal of Fracture, 1990. **42**(1): p. 73-86.
63. Davidge, R.W., *Mechanical behaviour of ceramics*. 1979, Cambridge : Cambridge University Press.
64. C. Gurney, J.Hunt, *Quasi-static crack propagation,Proc. R. Soc. London, vol. 299, no. 1459,* p. 508-524, 1967.
65. Puttick, K.E., *Energy scaling, size effects and ductile-brittle transitions in fracture* J. Phys. D: Appl. Phys., 1979. **12**(3): p. L19 - L23.
66. Östlund, F., Howie, P. R., Ghisleni, R., Korte, S., Leifer, K., Clegg, W.J., Michler, J., *Ductile–brittle transition in micropillar compression of GaAs at room temperature.* Philosophical Magazine, 2010. **91**(7-9): p. 1190-1199.
67. Lloyd, S.J., J.M. Molina-aldareguia, and W.J. Clegg, *Deformation under nanoindents in sapphire, spinel and magnesia examined using transmission electron microscopy.* Philosophical Magazine A, 2002. **82**(10): p. 1963-1969.
68. Uchic, M.D., Dimiduk, D.M., Florando, J.N., Nix, W.D., *Sample Dimensions Influence Strength and Crystal Plasticity.* Science, 2004. **305**(5686): p. 986-989.
69. Uchic, M.D. and D.M. Dimiduk, *A methodology to investigate size scale effects in crystalline plasticity using uniaxial compression testing.* Materials Science and Engineering: A, 2005. **400–401**(0): p. 268-278.
70. Volkert, C.A. and E.T. Lilleodden, *Size effects in the deformation of sub-micron Au columns.* Philosophical Magazine, 2006. **86**(33-35): p. 5567-5579.
71. Michler, J., Wasmer, K., Meier, S., Ostlund, F., *Plastic deformation of gallium arsenide micropillars under uniaxial compression at room temperature.* Applied physics letters, 2007. **90**(4): p. 043123-043123-3.
72. F. O¨stlund, K. Rzepiejewska-Malyska, K. Leifer, L.M. Hale, Y. Tang, R. Ballarini, W.W. Gerberich, J. Michler., *Brittle-to-Ductile Transition in Uniaxial Compression*

of Silicon Pillars at Room Temperature. Adv. Funct. Mater, 2009. **19**(15): p. 2439 -2444.
73. Korte, S. and W.J. Clegg, *Discussion of the dependence of the effect of size on the yield stress in hard materials studied by microcompression of MgO.* Philosophical Magazine, 2010. **91**(7-9): p. 1150-1162.
74. Korte, S. and W.J. Clegg, *Micropillar compression of ceramics at elevated temperatures.* Scripta Materialia, 2009. **60**(9): p. 807-810.
75. Soler, R., Molina-Aldareguia, J.M., Segurado, j., Lorca, J., Merino, R.i., Orere, V.M., *Micropillar compression of LiF [111] single crystals: Effect of size, ion irradiation and misorientation.* International Journal of Plasticity, 2012. **36**(0): p. 50-63.
76. Oliver, W. and G. Pharr, *Improved technique for determining hardness and elastic modulus using load and displacement sensing indentation experiments.* Journal of materials research, 1992. **7**(6): p. 1564-1583.
77. Schuh, C.A., Alan C. , *Application of nucleation theory to the rate dependence of incipient plasticity during nanoindentation* Journal of Materials Research, 2004. **19**(7): p. . 2152-2158.
78. Schuh, C.A., J.K. Mason, and A.C. Lund, *Quantitative insight into dislocation nucleation from high-temperature nanoindentation experiments.* Nat Mater, 2005. **4**(8): p. 617-621.
79. Schuh, C.A. and T.G. Nieh, *A nanoindentation study of serrated flow in bulk metallic glasses.* Acta materialia, 2003. **51**(1): p. 87-99.
80. Greer, A.L., Castellero, A., Madge, S.V., Walker, I.T., Wilde, J.R., *Nanoindentation studies of shear banding in fully amorphous and partially devitrified metallic alloys.* Materials Science and Engineering: A, 2004. **375–377**(0): p. 1182-1185.
81. Rao, R., Brandby, J.E., Ruffel, S., Williams, J.S., *Nanoindentation-induced phase transformation in crystalline silicon and relaxed amorphous silicon.* Microelectronics Journal, 2007. **38**(6–7): p. 722-726.
82. Jang, J., Lance, M.J., Wen, S., Tsui, T.Y., Pharr, G.M., *Indentation-induced phase transformations in silicon: influences of load, rate and indenter angle on the transformation behavior.* Acta materialia, 2005. **53**(6): p. 1759-1770.
83. Jang, J., G.M. Pharr, *Influence of indenter angle on cracking in Si and Ge during nanoindentation.* Acta materialia, 2008. **56**(16): p. 4458-4469.
84. Syed Asif, S.A. and J.B. Pethica, *Nanoindentation creep of single-crystal tungsten and gallium arsenide.* Philosophical Magazine A, 1997. **76**(6): p. 1105-1118.
85. Bhakhri, V. and R. Klassen, *Investigation of high-temperature plastic deformation using instrumented microindentation tests. Part I<i>The deformation of three aluminum alloys at 473 K to 833 K</i&gt.* Journal of materials science, 2006. **41**(8): p. 2259-2270.
86. V. Bhakhri, J.W., Naeem Ur-rehman, Constantin Ciurea, Finn Giuliani, Luc J. Vandeperre, *Instrumented nanoindentation investigation into the mechanical behavior of ceramics at moderately elevated temperatures. Journal of Materials Research, 27 , pp 65-75 doi:10.1557/jmr.2011.246* Journal of Materials Research, 2012. **27** p. pp 65-75
87. Wheeler, J.M., R.A. Oliver, and T.W. Clyne, *AFM observation of diamond indenters after oxidation at elevated temperatures.* Diamond and Related Materials, 2010. **19**(11): p. 1348-1353.
88. Everitt, N.M., M.I. Davies, and J.F. Smith, *High temperature nanoindentation – the importance of isothermal contact.* Philosophical Magazine, 2010. **91**(7-9): p. 1221-1244.
89. Kelly A., M.N.H., *Strong solids*. 3 ed. 1986: Clarendon Press.

90. Dieter, G.E., *Mechanical Metallurgy, ,* ed. SI Metric Edition. 1988.
91. Hugosson, H.W., Janssson, U., Johansson, B., Eriksson, O., *Restricting dislocation movement in transition metal carbides by phase stability tuning.* Science, 2001. **293**(5539): p. 2434-2437.
92. Wang, Y., Wong, M.S., Chia,W.J., Rechner,J., Sproul, W.D., *Synthesis and characterization of highly textured polycrystalline AlN/TiN superlattice coatings.* Journal of Vacuum Science & Technology A: Vacuum, Surfaces, and Films, 1998. **16**: p. 3341.
93. Vepřek, S., Nesladek, P., Niederhofer, A., Glatz, F., Jilek, M., Sima, M., *Recent progress in the superhard nanocrystalline composites: towards their industrialization and understanding of the origin of the superhardness.* Surface and Coatings Technology, 1998. **108–109**(0): p. 138-147.
94. Hultman, L., Hakasson, G., Wahlstrom, U., Sundgren, J.E., Petrov, I., Abidi, F., Greene, J.E., *Transmission electron microscopy studies of microstructural evolution, defect structure, and phase transitions in polycrystalline and epitaxial Ti1-xAlxN and TiN films grown by reactive magnetron sputter deposition.* Thin Solid Films, 1991. **205**(2): p. 153-164.
95. McDonald, N.R., Wallwork, G.R., *The reaction of nitrogen with titanium between 800 and 1200°C.* Oxidation of metals, 1970. **2**(3): p. 263-283.
96. Toth, L.E., *Transition metal carbides and nitrides*. Vol. 7. 1971: Academic Press New York.
97. Petrov, I., Hultman, L., Helmersson, U., Greene, J., *Microstructure modification of TiN by ion bombardment during reactive sputter deposition.* Thin Solid Films, 1989. **169**(2): p. 299-314.
98. Powder Diffraction File, c.-., Issued by Joint Committee on Powder Diffraction Standards, Swarthmore, PA,. 1989.
99. Toth, L.E., *Transition Metal Carbides and Nitrides*. Vol. 7. 1971: Academic Press New York London. 279.
100. Wikipedia, *Crystal structure of NaCl with coordination polyhedra*. 2012. p. Crystal structure of NaCl with coordination polyhedra.
101. Johansson, B.O.S., J.-E.; Greene, J. E.; Rockett, A.; Barnett, S. A.; , *Growth and properties of single crystal TiN films deposited by reactive magnetron sputtering.* Journal of Vacuum Science & Technology A: Vacuum, Surfaces, and Films, 1985. **vol.3**(no.2): p. 303-307.
102. Stanislav, J., J. Sikac, and M. Cermak, *Properties of magnetron-deposited polycrystalline TiN layers.* Thin Solid Films, 1990. **191**(2): p. 255-273.
103. Zhou, M., Makino, Y., Nose, M., Nogi, K., *Phase transition and properties of Ti-Al-N thin films prepared by r.f.-plasma assisted magnetron sputtering.* Thin Solid Films, 1999. **339**(1-2): p. 203-208.
104. Ljungcrantz, H., Oden, M., Hultman, L., Greene, J.E., Sundgren, J.E., *Nanoindentation studies of single-crystal (001)-,(011)-, and (111)-oriented TiN layers on MgO.* Journal of applied physics, 1996. **80**: p. 6725.
105. O'Hern, M.E., R.H. Parrish, and W.C. Oliver, *Evaluation of mechanical properties of TiN films by ultralow load indentation.* Thin Solid Films, 1989. **181**(1–2): p. 357-363.
106. Shojaei, O.R., Karimi, A., *Comparison of mechanical properties of TiN thin films using nanoindentation and bulge test.* Thin Solid Films, 1998. **332**(1-2): p. 202.
107. Müller, D. and E. Fromm, *Mechanical properties and adhesion strength of TiN and Al coatings on HSS, steel, aluminium and copper characterized by four testing Methods.* Thin Solid Films, 1995. **270**(1-2): p. 411-416.

108. Karimi, A., Shojaei, O.R., Kruml,J.L., Martin,J.L., *Characterisation of TiN thin films using the bulge test and the nanoindentation technique.* Thin Solid Films, 1997. **308-309**: p. 334-339.
109. Mayrhofer, P.H., C. Mitterer, and J. Musil, *Structure–property relationships in single- and dual-phase nanocrystalline hard coatings.* Surface and Coatings Technology, 2003. **174–175**(0): p. 725-731.
110. Adibi, F., Petrov, I., Hultman, L., Wahlstrom, U., Shimizu, T., McIntyre, D., Greene, J.E., Sundgren, J.E., *Defect structure and phase transitions in epitaxial metastable cubic TiAlN alloys grown on MgO (001) by ultra-high-vacuum magnetron sputter deposition.* Journal of applied physics, 1991. **69**: p. 6437.
111. Anders, A., *Atomic scale heating in cathodic arc plasma deposition.* Applied physics letters, 2002. **80**: p. 1100.
112. Holleck, H., *Metastable coatings — Prediction of composition and structure.* Surface and Coatings Technology, 1988. **36**(1–2): p. 151-159.
113. Rachbauer, R., *Comparative microstructural investigations of Ti-Al-N thin films alloyed with Y or Nb*, Thesis, 2008. p. 85.
114. Kimura, A., Hasegawa, H., Yamada, K., Suzuki, T., *Metastable Ti1−xAlxN films with different Al content.* Journal of materials science letters, 2000. **19**(7): p. 601-602.
115. Hultman, L., *Thermal stability of nitride thin films.* Vacuum, 2000. **57**(1): p. 1-30.
116. McIntyre, D., Greene, J.E., Hakansso, G., Sundgren, J.E., Munz, W.D., *Oxidation of metastable single-phase polycrystalline Ti 0.5 Al 0.5 N films: Kinetics and mechanisms.* Journal of applied physics, 1990. **67**(3): p. 1542.
117. Ahlgren, M. and H. Blomqvist, *Influence of bias variation on residual stress and texture in TiAlN PVD coatings.* Surface and Coatings Technology, 2005. **200**(1-4): p. 157-160.
118. Håkansson, G., Sundgren, J.E., McIntyre, D., Greene, J.E., Munz, W.D., *Microstructure and physical properties of polycrystalline metastable Ti0.5Al0.5N alloys grown by d.c. magnetron sputter deposition.* Thin Solid Films, 1987. **153**(1-3): p. 55-65.
119. Kramer, B.M., Judd, P.K., *Computational design of wear coatings.* Journal of vacuum science & technology. B, Microelectronics and nanometer structures, 1985. **3**(6): p. 2439.
120. König, W., R. Fritsch, and D. Kammermeier, *New Approaches to Characterizing the Performance of Coated Cutting Tools.* CIRP Annals - Manufacturing Technology, 1992. **41**(1): p. 49-54.
121. Witthaut, M., Cremer, R., Alexander von Richthofen, Neuschutz, D., *Improvement of the oxidation behavior of Ti1-xAlxN hard coatings by optimization of the Ti/Al ratio.* Fresenius' journal of analytical chemistry, 1998. **361**(6): p. 639.
122. Hofmann, S. and H.A. Jehn, *Selective oxidation and chemical state of Al and Ti in (Ti, Al)n coatings.* Surface and Interface Analysis, 1988. **12**(6): p. 329-333.
123. Alexander von Richthofen, Cremer, R., Witthaut, M., Domnick, R., Neuschutz, D., *Composition, binding states, structure, and morphology of the corrosion layer of an oxidized Ti0.46Al0.54N film.* Thin Solid Films, 1998. **312**(1-2): p. 190-194.
124. Hofmann, S., Jehn, H.A., *Selective oxidation and chemical state of Al and Ti in (Ti, Al)N coatings.* Surface and Interface Analysis, 1988. **12**(1): p. 329-333.
125. Tanaka, Y., Gur, T.M., Kelly, M., Hangstrom,S.B., Ikeda,T., Wakihira, K., Satoh, H., *Properties of ($Ti_{1-x}Al_x$)N coatings for cutting tools prepared by the cathodic arc ion plating method*. 1992: AVS.

126. Rachbauer, R., Stergar, E., Massl, S., moser, M., Mayerhofer, P.H., *Three-dimensional atom probe investigations of Ti-Al-N thin films.* Scripta Materialia, 2009. **61**(7): p. 725-728.
127. Porter, D.A., Easterling.K,E., *Phase transformations in metals and alloys*. 1992.
129. Musil, J. and H. Hrubý, *Superhard nanocomposite Ti1-xAlxN films prepared by magnetron sputtering.* Thin Solid Films, 2000. **365**(1): p. 104-109.
130. Mayrhofer, P.H., Horling, A., \karlsson, L., Sjolen, J., Larsson, T., Mitterer, C., Hultman, L., *Self-organized nanostructures in the Ti–Al–N system.* Applied physics letters, 2003. **83**(10): p. 2049.
131. Horling A., K.L., Mayrhofer P. H., Mittere C., Frederick M. J., Ramanath G., Oden M., Hultman L., *Phase transformation in Ti1-xAlxN thin films.*
132. Xia, Q., H. Xia, and A.L. Ruoff, *Pressure induced rocksalt phase of aluminum nitride: A metastable structure at ambient condition.* Journal of applied physics, 1993. **73**(12): p. 8198-8200.
133. Christensen, N.E., Gorczyca, I., *Calculated structural phase transitions of aluminum nitride under pressure.* Physical review. B, Condensed matter, 1993. **47**(8): p. 4307.
134. Van Camp, P.E., Van Doren, P.E., devreese, J.T., *High-pressure properties of wurtzite-and rocksalt-type aluminum nitride.* Physical review. B, Condensed matter, 1991. **44**(16): p. 9056.
135. Johansson, L.I., Stefan, P.M., Sheck, M.L., Christensen, A.N., *Valence-band structure of TiC and TiN.* Physical review. B, Condensed matter, 1980. **22**(2): p. 1032.
136. Yoshida, T., Kawasaki, A., Nakagawa, K., Akashi, K., *The synthesis of ultrafine titanium nitride in an r.f. plasma.* Journal of materials science, 1979. **14**(7): p. 1624-1630.
137. Pierson, H.O., *Handbook of refractory carbides and nitrides: properties, characteristics, processing, and applications*. 1996, New Jersey: Noyes Publications.
138. Du, L., Edgar, J.H., Kenik, E.A., Meyer, H.M., *Sublimation growth of titanium nitride crystals.* Journal of materials science. Materials in electronics. **21**(1): p. 78.
139. Graziani, T. and A. Bellosi, *Densification and characteristics of TiN ceramics.* Journal of materials science letters, 1995. **14**(15): p. 1078-1081.
140. Ratsch, C., *Nucleation theory and the early stages of thin film growth.* Journal of vacuum science & technology. A. Vacuum, surfaces, and films, 2003. **21**(5): p. S96.
141. Movchan, B. and A. Demchishin, *Study of the structure and properties of thick vacuum condensates of nickel, titanium, tungsten, aluminium oxide and zirconium dioxide.* PHYS METALS METALLOGR, 1969. **28**(4): p. 83-90.
142. Thornton, J.A., *High rate thick film growth.* Annual review of materials research, 1977. **7**(1): p. 239.
143. Thornton, J.A., *Influence of apparatus geometry and deposition conditions on the structure and topography of thick sputtered coatings.* Journal of Vacuum Science and Technology, 1974. **11**(4): p. 666-670.
144. Messier, R., A.P. Giri, and R.A. Roy, *Revised structure zone model for thin film physical structure.* Journal of Vacuum Science & Technology A: Vacuum, Surfaces, and Films, 1984. **2**(2): p. 500-503.
145. PalDey, S., Deevi, S.C., *Single layer and multilayer wear resistant coatings of (Ti, Al) N: a review.* Materials science & engineering. B, Solid-state materials for advanced technology, 2003. **342**(1-2): p. 58.

146. Lugscheider, E., Barimani, C., Wolff, C., Guerreiro, S., Doepper, G., *Comparison of the structure of PVD-thin films deposited with different deposition energies.* Surface and Coatings Technology, 1996. **86-87**(Part 1): p. 177-183.
147. Boxman, R.L. and S. Goldsmith, *Macroparticle contamination in cathodic arc coatings: generation, transport and control.* Surface and Coatings Technology, 1992. **52**(1): p. 39-50.
148. Anders, A., *Approaches to rid cathodic arc plasmas of macro-and nanoparticles: a review.* Surface & coatings technology, 1999. **120**: p. 319.
149. Kang, G.H., H. Uchida, and E.S. Koh, *Macroparticle-free TiN films prepared by arc ion-plating process.* Surface and Coatings Technology, 1994. **68-69**: p. 141-145.
150. Sanders, D.M., Anders, A., *Review of cathodic arc deposition technology at the start of the new millennium.* Surface & coatings technology, 2000. **133**: p. 78.
151. Brown, I.G., *Cathodic arc deposition of films.* Annual review of materials science, 1998. **28**(1): p. 243.
152. Jüttner, B., *Characterization of the cathode spot.* IEEE transactions on plasma science, 1987. **15**(5): p. 474.
153. Aksenov, I.I., Belous, V.A., Padalka, V.G., Khoroshikh, V.M., *Transport of plasma streams in a curvilinear plasma-optics system.* Plasma physics reports, 1978. **4**: p. 758.
154. Boxman, R. and S. Goldsmith, *Principles and applications of vacuum arc coatings.* IEEE transactions on plasma science, 1989. **17**(5): p. 705-712.
155. Bunshah, R.F., *Handbook of Deposition Technologies for Films and Coatings - Science, Technology and Applications (2nd Edition)*. 1994.
156. Smith, D.L., *Thin-film deposition: principles and practice*. 1995.
157. Chen, L., Moser, M., Du, Y., Mayerhofer, P.H., *Compositional and structural evolution of sputtered Ti-Al-N.* Thin Solid Films, 2009. **517**(24): p. 6635.
158. Rachbauer, R., *Comparative microstructural investigations of Ti-Al-N thin films alloyed with Y or Nb*. 2008, University of Leoben: Leoben.
159. Täschner, C., Ljungberg, B., Hoffmann, B., Vogt, C., Leonhardt, A., *Deposition of TiN, TiC and Ti1−xAlxN coatings by pulsed d.c. plasma enhanced chemical vapour deposition methods.* Surface and Coatings Technology, 2001. **142–144**(0): p. 823-828.
160. Kyrylov, O., Cremer, R., Neuschutz, D., Prange, R., *Correlation between plasma conditions and properties of (Ti,Al)N coatings deposited by PECVD.* Surface and Coatings Technology, 2002. **151–152**(0): p. 359-364.
161. Török, E., Perry, A.J., Chollet, L., Sproul, W.d., *Young's modulus of TiN, TiC, ZrN and HfN.* Thin Solid Films, 1987. **153**(1–3): p. 37-43.
162. Hibbs, M.K., Johansson, B.O., Sundgren, J.E., Hlemersson, U., *Effects of substrate temperature and substrate material on the structure of reactively sputtered TiN films.* Thin Solid Films, 1984. **122**(2): p. 115-129.
163. Quinto, D.T., *Mechanical property and structure relationships in hard coatings for cutting tools.* Journal of Vacuum Science & Technology A: Vacuum, Surfaces, and Films, 1988. **6**(3): p. 2149-2157.
164. Mayrhofer, P.H., Kunc, F., Musil, J., Mitterer, C., *A comparative study on reactive and non-reactive unbalanced magnetron sputter deposition of TiN coatings.* Thin Solid Films, 2002. **415**(1–2): p. 151-159.
165. Davis C.A, *A simple model for the formation of compressive stress in thin films by ion bombardment.* Thin Solid Films, 1993. **226**(1): p. 30-34.
166. Buckle, H., J. Westbrook, and H. Conrad, *The science of hardness testing and its research applications.* American Society for Metals, Materials Park, Ohio, 1973.

167. Chen, J. and S.J. Bull, *On the factors affecting the critical indenter penetration for measurement of coating hardness.* Vacuum, 2009. **83**(6): p. 911-920.
168. Bull, S.J. and D.S. Rickerby, *New developments in the modelling of the hardness and scratch adhesion of thin films.* Surface and Coatings Technology, 1990. **42**(2): p. 149-164.
169. Ding, X.Z., Zeng, X.T., Liu, Y.C., Wei, J., *Influence of Substrate Hardness on the Properties of PVD Hard Coatings.* Synthesis and reactivity in inorganic and metal-organic chemistry, 2008. **38**(2): p. 156.
170. Suzuki, T., D. Huang, and Y. Ikuhara, *Microstructures and grain boundaries of (Ti,Al)N films.* Surface and Coatings Technology, 1998. **107**(1): p. 41-47.
171. Falub, C.V., Karimi, A., Ante, M., Klass, W., *Interdependence between stress and texture in arc evaporated Ti–Al–N thin films.* Surface and Coatings Technology, 2007. **201**(12): p. 5891-5898.
172. Santana, A.E., Karimi, A., Derflinger, V.H., Schutze, A., *Thermal Treatment Effects on Microstructure and Mechanical Properties of TiAlN Thin Films.* Tribology Letters, 2004. **17**(4): p. 689-696.
173. McKenzie, D.R., Yin, Y., McFall, W.D., Hoang, N.H., *The orientation dependence of elastic strain energy in cubic crystals and its application to the preferred orientation in titanium nitride thin films.* Journal of physics. Condensed matter, 1996. **8**: p. 5883.
174. Santana, A.E., Karimi, A., Derflinger, V.H., Schutze, A., *Relating hardness-curve shapes with deformation mechanisms in TiAlN thin films enduring indentation.* Materials Science and Engineering: A, 2005. **406**(1–2): p. 11-18.
175. Goldfarb, I., Pelleg, J., Zevin. L., Croitoru, N., *Lattice distortion in thin films of IVB metal (Ti, Zr, Hr) nitrides.* Thin Solid Films, 1991. **200**(1): p. 117-127.
176. Mayrhofer, P.H., D. Music, and J.M. Schneider, *Influence of the Al distribution on the structure, elastic properties, and phase stability of supersaturated $Ti_{1-x}Al_xN$.* Journal Name: Journal of Applied Physics; Journal Volume: 100; Journal Issue: 9; Other Information: DOI: 10.1063/1.2360778; (c) 2006 American Institute of Physics; Country of input: International Atomic Energy Agency (IAEA), 2006: p. Medium: X; Size: page(s) 094906-094906.5.
177. Mayrhofer, P.H., C. Mitterer, and H. Clemens, *Self-Organized Nanostructures in Hard Ceramic Coatings.* Advanced Engineering Materials, 2005. **7**(12): p. 1071-1082.
178. Beake, B.D., Fox-Rabonovich, G.D., Veldhuis, S.C., Goodes, S.R., *Coating optimisation for high speed machining with advanced nanomechanical test methods.* Surface & coatings technology, 2009. **203**(13): p. 1919.
179. Shand, M.A., *The chemistry and technology of magnezia*. 2006: John Wiley and Sons.
180. Holleck, H., *Material selection for hard coatings.* Journal of Vacuum Science & Technology A: Vacuum, Surfaces, and Films, 1986. **4**(6): p. 2661-2669.
181. Goldman, A., *Modern Ferrite Technology* 1990 ed. 1990, New York: Van Nostrand Reinhold,. 458.
182. Pethicai, J.B., R. Hutchings, and W.C. Oliver, *Hardness measurement at penetration depths as small as 20 nm.* Philosophical Magazine A, 1983. **48**(4): p. 593-606.
183. Stilwell, N. and D. Tabor, *Elastic recovery of conical indentations.* Proceedings of the Physical Society, 1961. **78**: p. 169.
184. Doerner, M.F. and W.D. Nix, *A method for interpreting the data from depth-sensing indentation instruments.* Journal of Materials Research, 1986. **1**(4): p. 601-609.

185. M.F. Doerner, D.S.Gardner, W.D.Nix, *Plastic properties of thin films on substrates as measured by submicron indentation hardness and substrate curvature techniques.* Journal of Materials Research, 1986. **1**(6): p. 845-851.
186. Sneddon, I.N., *The relation between load and penetration in the axisymmetric boussinesq problem for a punch of arbitrary profile.* International Journal of Engineering Science, 1965. **3**(1): p. 47-57.
187. Swain, M.V., Menick, J., *Errors associated with depth-sensing microindentation tests.* Journal of Materials Research, 1995. **10** (6): p. 1491-1501.
188. Menčík, J., *Determination of mechanical properties by instrumented indentation.* Meccanica, 2007. **42**(1): p. 19-29.
189. Walter, C., Antretter, T., Daniel, R., Mitterer, C., *Finite element simulation of the effect of surface roughness on nanoindentation of thin films with spherical indenters.* Surface and Coatings Technology, 2007. **202**(4–7): p. 1103-1107.
190. Fischer-Cripps, A.C., *Nanoindentation*. third, ed. third. 2011, New York: Springer. 280.
191. Siddhartha Pathak, D.S., Roger Doherty and Surya R. Kalidindi, *Importance of surface preparation on the nano-indentation stress-strain curves measured in metals.* Journal of Materials Research, 2009. **24** (3): p. 1142-1155.
192. Langitan, F.B. and B.R. Lawn, *Hertzian Fracture Experiments on Abraded Glass Surfaces as Definitive Evidence for an Energy Balance Explanation of Auerbach's Law.* Journal of applied physics, 1969. **40**(10): p. 4009-4017.
193. Chaudhri, M.M., Winter, M., *The load-bearing area of a hardness indentation.* Journal of Physics D: Applied Physics, 1988. **21**(2): p. 370-374.
194. McElhaney, K.W.Vlassak, J. J.; Nix, W. D., *Determination of indenter tip geometry and indentation contact area for depth-sensing indentation experiments.* 1998.
195. Grau, P., Berg, G., Franzel,W., Meinhard, H., *Recording hardness testing. Problems of measurement at small indentation depths.* physica status solidi (a), 1994. **146**(1): p. 537-548.
196. C.A. Schuh, C.E.Packard, A.C.und, *Nanoindentation and contact-mode imaging at high temperatures.* Journal of Materials Research, 2006. **21**(3): p. 725 - 736.
197. Beake, B.D. and J.F. Smith, *High-temperature nanoindentation testing of fused silica and other materials.* Philosophical Magazine A, 2002. **82**(10): p. 2179-2186.
198. Beake, B.D., S. R. Smith, J. F., *Nanoscale materials testing under industrially relevant conditions: high-temperature nanoindentation testing.* ZEITSCHRIFT FUR METALLKUNDE 2003. **94**(7): p. 789 -801.
199. N. SHINKAI, R.C.B., G. E. RINDONE, *Fracture Toughness of Fused SiO2 and Float Glass at Elevated Temperatures.* Journal of the American Ceramic Society, 1981. **64**(7): p. 426 -430.
200. Williams, D.B. and C.B. Carter, *The Transmission Electron Microscope Transmission Electron Microscopy*. 2009, Springer US. p. 3-22.
201. Cowley, J.M., ed. *Diffraction physics*. 1975, North-Holland Pub. Co. (Amsterdam and New York). 410.
202. Reyntjens. S, Puers.R., *A review of focused ion beam applications in microsystem technology.* Journal of Micromechanics and Microengineering, 2001. **Vol. 11**(4): p. 287-300.
203. Kato, N.I., *Reducing focused ion beam damage to transmission electron microscopy samples.* J Electron Microsc (Tokyo) 2004. **53**(5): p. 451-458.
204. Giannuzzi, L.A. and F.A. Stevie, *A review of focused ion beam milling techniques for TEM specimen preparation.* Micron, 1999. **30**(3): p. 197-204.

205. T. Ishitani, T.Yaguchi, *Cross-Sectional Sample Preparation by Focused Ion Beam:A Review of Ion-Sample Interaction.* MICROSCOPY RESEARCH AND TECHNIQUE, 1996. **35**: p. 320-333.
206. Shimada, M., Matsushita, K., Kuratani, S., Okamoto, T., Koizumi, M., Tsukuma, K., Tsukidate, T., *Temperature Dependence of Young's Modulus and Internal Friction in Alumina, Silicon Nitride, and Partially Stabilized Zirconia Ceramics.* Journal of the American Ceramic Society, 1984. **67**(2): p. C-23-C-24.
207. Fox-Rabinovich, G.S., Beake, D.B., Endrino, J.L., Veldhuis, S.C., Parkinson, R., Shuster, L.S., Migranov, M.S., *Effect of mechanical properties measured at room and elevated temperatures on the wear resistance of cutting tools with TiAlN and AlCrN coatings.* Surface and Coatings Technology, 2006. **200**(20–21): p. 5738-5742.
208. Matsumoto, T., Nose, T., Nagata, Y., Kawashima, K., Yamada, T., Nakano, H., Nagai, S., *Measurement of High-Temperature Elastic Properties of Ceramics Using a Laser Ultrasonic Method.* Journal of the American Ceramic Society, 2001. **84**(7): p. 1521-1525.
209. Wachtman, J.B. and D.G. Lam, *Young's Modulus of Various Refractory Materials as a Function of Temperature.* Journal of the American Ceramic Society, 1959. **42**(5): p. 254-260.
210. Soga, N. and O.L. Anderson, *High-Temperature Elastic Properties of Polycrystalline MgO and Al2O3.* Journal of the American Ceramic Society, 1966. **49**(7): p. 355-359.
211. Werchota, M., *Investigation of fundamental deformation parameters on TiAlN films of dufferent chemical composition and crystallographic structure using high-temperature nanoindentation*, in *Physical Metallurgy and Materials Testing*. 2010, Montanuniversitat Leoben: Leoben. p. 105.
212. Frost, H.J., Ashby, M.F., *Deformation-mechanism maps: The plasticity and creep of metals and ceramics*. 1 ed. 1982 Pergamon Press (Oxford Oxfordshire and New York).
213. Krell, A., *A new look at the influences of load, grain size and grain boundaries on the room temperature hardness of ceramics.* International Journal of Refractory Metals and Hard Materials, 1998. **16**(4–6): p. 331-335.
214. Rice, R.W., C.C. Wu, and F. Boichelt, *Hardness–Grain-Size Relations in Ceramics.* Journal of the American Ceramic Society, 1994. **77**(10): p. 2539-2553.
215. Yang, J.-F., Ohji, T., Kanzaki, s., Diaz, A., Hampshire, S., *Microstructure and Mechanical Properties of Silicon Nitride Ceramics with Controlled Porosity.* Journal of the American Ceramic Society, 2002. **85**(6): p. 1512-1516.
216. Rice, R.W., *Porosity of ceramics*. 1998: M. Dekker (New York). xii, 539.
217. Kanamori, S., *Investigation of reactively sputtered TiN films for diffusion barriers.* Thin Solid Films, 1986. **136**(2): p. 195-214.
218. Pelleg, J., Zevin, L.Z., Lungo, S., Croitoru, N., *Reactive-sputter-deposited TiN films on glass substrates.* Thin Solid Films, 1991. **197**(1–2): p. 117-128.
219. Müller, K.-H., *Ion-beam-induced epitaxial vapor-phase growth: A molecular-dynamics study.* Physical Review B, 1987. **35**(15): p. 7906-7913.
220. Banerjee, R., R. Chandra, and P. Ayyub, *Influence of the sputtering gas on the preferred orientation of nanocrystalline titanium nitride thin films.* Thin Solid Films, 2002. **405**(1-2): p. 64-72.
221. Jang, B.-K. and H. Matsubara, *Influence of porosity on hardness and Young's modulus of nanoporous EB-PVD TBCs by nanoindentation.* Materials Letters, 2005. **59**(27): p. 3462-3466.

222. Ding, X., Bui, C.T., Zeng, X.T., *Abrasive wear resistance of Ti1− xAlxN hard coatings deposited by a vacuum arc system with lateral rotating cathodes.* Surface & coatings technology, 2008. **203**(5-7): p. 680.
223. Vineet, B., Wang, J., Uh-rehman, N., Ciurea, C., Giuliani, F., Vandeperre, L. J., *Instrumented nanoindentation investigation into the mechanical behavior of ceramics at moderately elevated temperatures. Journal of Materials Research, 27 , pp 65-75 doi:10.1557/jmr.2011.246* Journal of materials research, 2012. **27** p. pp 65-75
224. Fujita, S., K. Maeda, and S. Hyodo, *Dislocation glide motion in 6H SiC single crystals subjected to high-temperature deformation.* Philosophical Magazine A, 1987. **55**(2): p. 203-215.
225. Pirouz, P., J.L. Demenet, and M.H. Hong, *On transition temperatures in the plasticity and fracture of semiconductors.* Philosophical Magazine A, 2001. **81**(5): p. 1207-1227.
226. *Fiala, Central Research Institute, Skoda, Czechoslovachia, Private communication*. 1973.
227. Madan, A., Kim, I.W., Cheng, S.C., Yashar, P., Dravid, V.P., Barnet, S.A., *Stabilization of Cubic AlN in Epitaxial AlN/TiN Superlattices.* Physical Review Letters, 1997. **78**(9): p. 1743-1746.
228. Luo, J. and R. Stevens, *Porosity-dependence of elastic moduli and hardness of 3Y-TZP ceramics.* Ceramics International, 1999. **25**(3): p. 281-286.
229. Finn, G., *Deformation of hard materials*, in *Materials Science and Metallurgy*. 2005, University of Cambridge: Cambridge. p. 158.
230. Setoyama, M., Nakayama, A., TAnaka, M., Kitagawa, N., Nomura, T., *Formation of cubic-AlN in TiN/AlN superlattice.* Surface and Coatings Technology, 1996. **86–87, Part 1**(0): p. 225-230.
231. Sato, K., Ichimia, N., Kondo, A., Tanaka,Y., *Microstructure and mechanical properties of cathodic arc ion-plated (Al,Ti)N coatings.* Surface and Coatings Technology, 2003. **163–164**(0): p. 135-143.
232. Santana, A.E., Karimi, A., Derflinger, V.H., Schutze,A., *Microstructure and mechanical behavior of TiAlCrN multilayer thin films.* Surface and Coatings Technology, 2004. **177–178**(0): p. 334-340.
233. Kimura, A., Hsegawa, H., Yamada, K., Suzuki, T., *Effects of Al content on hardness, lattice parameter and microstructure of $Ti_{1-x}Al_xN$ films.* Surface and Coatings Technology, 1999. **120–121**(0): p. 438-441.
234. Suzuki, T., Makino, Y., SAmadi, M., Miyake, S., *Microstructure and secular instability of the ($Ti_{1-x}Al_x$) N films prepared by ion-beam-assisted-deposition.* Journal of materials science, 2000. **35**(16): p. 4193.
235. Lieberman, M.A., *Model of plasma immersion ion implantation.* Journal of applied physics, 1989. **66**(7): p. 2926-2929.
236. D'Heurle, F.M. and J.M.E. Harper, *Note on the origin of intrinsic stresses in films deposited via evaporation and sputtering.* Thin Solid Films, 1989. **171**(1): p. 81-92.
237. Mittemeijer, E.J. and P. Scardi, *Diffraction analysis of the microstructure of materials*. Vol. 68. 2004: Springer Verlag.